

STRENGTHENING OF RC  
BEAMS USING ANCHORED NSM BARS

STRENGTHENING OF REINFORCED  
CONCRETE BEAMS USING ANCHORED NEAR  
SURFACE MOUNTED BARS

By

DAVID ANTHONY PETRINA  
B.ENG. & MGT.

A Thesis

Submitted to the School of Graduate Studies

in Partial Fulfillment of the Requirements

for the Degree

Masters of Applied Science

McMaster University

© Copyright by David Anthony Petrina, June 2009

---

MASTER OF APPLIED SCIENCE (2009)  
(Engineering)

McMaster University  
Hamilton, Ontario

TITLE:                   Strengthening of Reinforced Concrete Beams  
                              using Anchored Near Surface Mounted Bars

AUTHOR:                David Anthony Petrina, B.Eng. & Mgt. (McMaster University)

SUPERVISOR:          Professor A.G. Razaqpur

NUMBER OF PAGES:    xi, 208

# Abstract

To delay the onset of delamination and to ensure the CFRP continues to supply strength after initial delamination of reinforced concrete beams strengthened with near surface mounted CFRP bars, a new mechanical anchoring system was developed and tested in this investigation. The anchors were integrally connected to the CFRP bars and extracted from a proprietary product commonly known as NEFMAC. The anchored bars were installed by cutting grooves into the concrete cover, boring holes at anchor locations and using epoxy to bond the strengthening bars to the groove surfaces.

A total of seven simply-supported reinforced concrete beams were tested in four-point bending to study the effectiveness of the proposed anchoring system. One beam served as a control specimen, two beams were strengthened with unanchored near surface mounted bars and the remaining four beams were strengthened with the anchored bars. As an exploratory study two of the four anchored beams were also strengthened with anchored near surface mounted CFRP transverse bars to determine if the system is an acceptable substitute for internal steel stirrups.

Results of this study reveal that the anchors can delay delamination and after initial delamination, the anchored beams continued to carry the applied load whereas the unanchored beams lost strength immediately following concrete cover delamination. Although there was not a significant gain in flexural capacity in the anchored beams relative to the unanchored beams, the improved ductility provided by the new system shows promise. Further investigation is needed to determine the number of anchors needed, depth of penetration, size and location of such anchors to achieve composite behaviour between the strengthening bars and the reinforced concrete section.

# Acknowledgements

I would like to thank my supervisor, Professor and Chair, Dr. A.G. Razaqpur of the Civil Engineering Department at McMaster University, for his continual support, encouragement and guidance over the past two years of study. Specifically for the thorough teachings he provided, the time he invested even in the midst of a chaotic schedule and the heart-felt sincerity to help me achieve my goals in a timely fashion.

I would like to also thank both the secretarial and technical staff in the Civil Engineering Department. The family atmosphere is always welcoming and it separates our department from any other. Tatiana, Rebecca and Carol thank you for all the help you provide on a daily basis, which sometimes is overlooked. Kent, Rhys, Bernard and Dave thank you for all the assistance in the lab. The early mornings, late nights and specimen preparations helped me accomplish my experimental work on schedule.

Finally, and foremost, I would like to thank my family and friends that have demonstrated incredible patience throughout my academic career. For the past seven years, schooling always took precedence to help me achieve my professional goals aspirations and dreams, and now I hope to return the favour. To my Strič Drago, thank you for your words of wisdom that resonate with me every day of my life, which help me to always do my best. To my brothers, Adam and Anthony, who were always there to make me smile when challenges arose. To my loving wife, Kristy, and 'moj mali' Niko thank you for all the sacrifices in time you endured and all the support you provided. Words cannot express how thankful and lucky I am to have you two in my life. To moj momma i tata, thank you for always wanting the best for me and teaching me how to get there. Your daily sacrifices were limitless, but necessary to help me along my way and I hope to one day return what you have so graciously done for me.

# Table of Contents

<b>1. Introduction.....</b>	<b>1</b>
1.1. General .....	1
1.2. Objectives and Scope .....	3
<b>2. Literature Review.....</b>	<b>5</b>
2.1. General .....	5
2.2. Constituent Materials Characteristics.....	6
2.2.1. Fibre Reinforced Polymers .....	6
2.2.2. Carbon FRP.....	8
2.2.3. Glass FRP .....	9
2.2.4. Aramid FRP .....	10
2.2.5. The Polymeric Matrix.....	11
2.3. Structural Strengthening using FRP Materials .....	13
<b>3. Experimental Program .....</b>	<b>29</b>
3.1. General .....	29
3.2. Test Specimens .....	30
3.3. Material Properties from Ancillary Tests.....	30
3.3.1. Longitudinal and Transverse Steel.....	31
3.3.2. CFRP Reinforcement.....	33
3.3.3. Concrete.....	36
3.3.4. Two Component Epoxy.....	41
3.4. Details of Test Beams .....	43
3.4.1. Dimensions and Geometry of Beams .....	43
3.4.2. Design and Detailing .....	43
3.5. Construction of Test Beams .....	53
3.6. Test Equipment and Instrumentation .....	56
3.7. Test Setup .....	63
3.8. Loading and Data Acquisition .....	65
<b>4. Experimental Results .....</b>	<b>66</b>
4.1. General .....	66
4.2. Control Beam.....	66
4.3. Type 1 Beams .....	73
4.4. Type 2 Beams .....	88
4.5. Type 3 Beams .....	102
4.6. Summary of Results .....	118

<b>5.</b>	<b>Analysis and Discussion of Test Results.....</b>	<b>120</b>
5.1.	General .....	120
5.2.	Ultimate Flexural Capacity.....	121
5.3.	Interfacial Shear .....	130
5.3.1.	Interfacial Shear Stresses based on Experimental Data.....	131
5.4.	Refined Analysis of Stresses at the NSM Bars-Concrete Interface .....	146
5.4.1.	Interfacial Shear Stresses Based on Refined Analysis .....	147
5.4.2.	Peeling or Normal Interfacial Stresses .....	152
5.5.	Concrete Cover Failure Analysis .....	159
5.6.	Shear Strengthening using the NSM system .....	174
<b>6.</b>	<b>Summary, Conclusions &amp; Recommendations.....</b>	<b>177</b>
6.1.	Summary.....	177
6.2.	Conclusions.....	179
6.3.	Recommendations for Future Work.....	181
<b>7.</b>	<b>References.....</b>	<b>183</b>
<b>A.</b>	<b>Design Calculations .....</b>	<b>187</b>
A.1.	General .....	187
A.2.	Steel Material Properties Observed in Beam Testing .....	188
A.3.	Control Beam.....	193
A.4.	CFRP Strengthened Beams .....	200

# List of Figures

Figure 1.1: Near-Surface Mounted Versus Externally-Bonded Strengthening .....	3
Figure 2.1: Various Lamina Configurations .....	7
Figure 2.2: Tensile Stress Strain Relationship for Various Fibres.....	8
Figure 2.3: Schematic of (a) Thermoplastic polymer and (b) Thermosetting polymer.....	12
Figure 2.4: Summarized Failure Mechanisms (De Lorenzis and Teng, 2006) .....	27
Figure 3.1: Primary Longitudinal Steel Tensile Test Results .....	32
Figure 3.2: Internal Steel Stirrup Tensile Test Results.....	32
Figure 3.3: NEFMAC (a) Typical Grid, (b) Grid Joint Close-up .....	34
Figure 3.4: NEFMAC Cutting Procedure for Obtaining the NSM Bars .....	34
Figure 3.5: Cut NEFMAC.....	35
Figure 3.6: Shear and Flexural NEFMAC CFRP Reinforcement.....	36
Figure 3.7: Concrete Cylinder Measurement Locations.....	37
Figure 3.8: Concrete Compression Test Results after 28 Days .....	39
Figure 3.9: Concrete Compression Test Results after 35 Weeks.....	39
Figure 3.10: Concrete Compression Test Results after 51 Weeks.....	40
Figure 3.11: Concrete Compression Test Results after 56 Weeks .....	40
Figure 3.12: Control Beam (a) Profile Details, (b) Cross Sectional Details.....	46
Figure 3.13: Type 1a and 1b (a) Profile Details, (b) Cross Sectional Details.....	48
Figure 3.14: Type 2a and 2b (a) Profile Details, (b) Cross Sectional Details.....	50
Figure 3.15: Type 3a and 3b (a) Profile Details, (b) Cross Sectional Details.....	52
Figure 3.16: Typical Longitudinal Grooves for Type 2 and 3 Beams.....	54
Figure 3.17: Longitudinal Grooves during Primer Application.....	55
Figure 3.18: Longitudinal Grooves During Epoxy Application and Final NSM Bars Disposition .....	56
Figure 3.19: Foil Strain Gauges Installed on CFRP Bar .....	57
Figure 3.20: Strain Gauge Locations for Control Beam.....	58
Figure 3.21: Strain Gauge Locations for Type 1 Beams .....	59
Figure 3.22: Strain Gauge Locations for Type 2 Beams .....	60
Figure 3.23: Strain Gauge Locations for Type 3 Beams .....	61
Figure 3.24: Typical String Potentiometer Locations for all the Tested Beams.....	62
Figure 3.25: Beams Test Set-up (North-South Profile).....	63
Figure 3.26: Beams Test Set-up (West-East Profile) .....	64
Figure 4.1 Typical Crack Pattern along the Eastern Shear Span of the Control Beam at 50% of Maximum Load.....	67
Figure 4.2: Concrete Crushing in Constant Moment Region of the Control Beam.....	68

Figure 4.3: Buckled Compression Steel at Failure of the Control Beam .....	68
Figure 4.4: Control Beam Load-Midspan Displacement.....	69
Figure 4.5: Control Beam Deflection .....	70
Figure 4.6: Control Beam Longitudinal Steel Bar Strain 390 mm from Supports.....	71
Figure 4.7: Control Beam Longitudinal Steel Bar Strain within Max. Moment Region ..	72
Figure 4.8: Control Beam Steel Stirrup Strain 390 mm from Supports .....	72
Figure 4.9: Reinforcement Delamination Initiation for Beam 1a .....	74
Figure 4.10: Reinforcement Delamination Initiation for Beam 1b .....	75
Figure 4.11: Delaminated Reinforcement for Beam 1a.....	75
Figure 4.12: Delaminated Reinforcement for Beam 1b.....	76
Figure 4.13: Delaminated Reinforcement for Beam 1a at Failure .....	76
Figure 4.14: Delaminated Reinforcement for Beam 1b at Failure .....	77
Figure 4.15: Type 1 Beams Load-Midspan Displacement .....	78
Figure 4.16: Type 1a Beam Deflection.....	79
Figure 4.17: Type 1b Beam Deflection .....	79
Figure 4.18: Type 1 Beams Longitudinal Steel Strain 390 mm from Supports.....	80
Figure 4.19: Type 1 Beams Longitudinal Steel Strain under Point Loads .....	81
Figure 4.20: Type 1 Beams Longitudinal NSM Bars Strain under East Point Load .....	81
Figure 4.21: Type 1 Beams Longitudinal NSM Bars Strain under West Point Load .....	82
Figure 4.22: Type 1 Beams Longitudinal NSM Bars Strain 200 mm from East Bar End .....	84
Figure 4.23: Type 1 Beams Longitudinal NSM Bars Strain 200 mm from West Bar End .....	84
Figure 4.24: Type 1 Beams Longitudinal Steel Strain at Mid-Span .....	85
Figure 4.25: Type 1 Beams Longitudinal CFRP Strain at Mid-Span.....	86
Figure 4.26: Type 1 Beams Steel Stirrup Strain 390 mm from East Support.....	87
Figure 4.27: Type 1 Beams Steel Stirrup Strain 390 mm from West Support .....	87
Figure 4.28: Reinforcement Delamination Initiation in Beam 2a .....	89
Figure 4.29: Reinforcement Delamination Initiation in Beam 2b.....	89
Figure 4.30: Sheared Anchor Pegs along North CFRP Bar in Beam 2a .....	90
Figure 4.31: Sheared Anchor Pegs along North CFRP Bar in Beam 2b .....	90
Figure 4.32: Delaminated Reinforcement in Beam 2a at Failure.....	91
Figure 4.33: Close-Up of Sheared Anchor in Beam 2b.....	91
Figure 4.34: Type 2 Beams Load-Midspan Displacement .....	93
Figure 4.35: Type 2a Beam Deflection.....	93
Figure 4.36: Type 2b Beam Deflection .....	94
Figure 4.37: Type 2 Beams Longitudinal Steel Strain 390 mm from Supports.....	94
Figure 4.38: Type 2 Beams Longitudinal Steel Strain under Point Loads .....	96
Figure 4.39: Type 2 Beams Longitudinal CFRP Strain under East Point Load .....	96
Figure 4.40: Type 2 Beams Longitudinal CFRP Strain under West Point Load .....	97
Figure 4.41: Type 2 Beams Longitudinal CFRP Strain 200 mm from East Bar End .....	98
Figure 4.42: Type 2 Beams Longitudinal CFRP Strain 200 mm from West Bar End .....	98
Figure 4.43: Type 2 Beams Longitudinal Steel Strain at Mid-Span .....	99
Figure 4.44: Type 2 Beams Longitudinal CFRP Strain at Mid-Span.....	100
Figure 4.45: Type 2 Beams Steel Stirrup Strain 390 mm from East Support.....	101

Figure 4.46: Type 2 Beams Steel Stirrup Strain 390 mm from West Support .....	101
Figure 4.47: Reinforcement Delamination Initiation for Beam 3a .....	103
Figure 4.48: Reinforcement Delamination Initiation for Beam 3b .....	103
Figure 4.49: Anchors Pulled from Concrete Core in Beam 3a .....	104
Figure 4.50: Anchors Pulled from Concrete Core in Beam 3b .....	104
Figure 4.51: Beam 3a at Failure due to NSM Reinforcement Delamination.....	105
Figure 4.52: Beam 3b at Failure due to NSM Reinforcement Delamination .....	105
Figure 4.53: Type 3 Beams Load-Midspan Displacement .....	106
Figure 4.54: Type 3a Beam Deflection.....	107
Figure 4.55: Type 3b Beam Deflection .....	107
Figure 4.56: Type 3 Beams Longitudinal Steel Strain 390 mm from Supports.....	109
Figure 4.57: Type 3 Beams Longitudinal Steel Strain under Point Loads .....	109
Figure 4.58: Type 3 Beams Longitudinal CFRP Strain under East Point Load .....	110
Figure 4.59: Type 3 Beams Longitudinal CFRP Strain under West Point Load .....	110
Figure 4.60: Type 3 Beams Longitudinal CFRP Strain 200 mm from East Bar End ....	112
Figure 4.61: Type 3 Beams Longitudinal CFRP Strain 200 mm from West Bar End ...	112
Figure 4.62: Type 3 Beams Longitudinal Steel Strain at Mid-Span .....	113
Figure 4.63: Type 3 Beams Longitudinal CFRP Strain at Mid-Span.....	113
Figure 4.64: Type 3 Beams Steel Stirrup Strain 390 mm from East Support.....	114
Figure 4.65: Type 3 Beams Steel Stirrup Strain 390 mm from West Support .....	115
Figure 4.66: Type 3 Beams Transverse CFRP Strain 250 mm from East Support.....	116
Figure 4.67: Type 3 Beams Transverse CFRP Strain 500 mm from East Support.....	116
Figure 4.68: Intersecting Cracks along Transverse NSM Bars in Beam 3a .....	117
Figure 4.69: Intersecting Cracks along Transverse NSM Bars in Beam 3b .....	117
Figure 5.1: Maximum Recorded Strains in CFRP Bars in Beam 1a.....	126
Figure 5.2: Maximum Recorded Strains in CFRP Bars in Beam 1b.....	126
Figure 5.3: Maximum Recorded Strains in CFRP Bars in Beam 2a.....	127
Figure 5.4: Maximum Recorded Strains in CFRP Bars in Beam 2b.....	127
Figure 5.5: Maximum Recorded Strains in CFRP Bars in Beam 3a.....	128
Figure 5.6: Maximum Recorded Strains in CFRP Bars in Beam 3b.....	128
Figure 5.7: Load-Midspan Deflection for Beams 1a, 2a and 3a .....	129
Figure 5.8: Interfacial Shear and Normal Stress Distribution in the Concrete Cover ....	131
Figure 5.9: Infinitesimal Element of CFRP Bar Free-Body Diagram.....	132
Figure 5.10: Shear Stress along the CFRP Reinforcement for Beam 1a.....	134
Figure 5.11: Shear Stress along the CFRP Reinforcement for Beam 1a.....	134
Figure 5.12: Shear Stress along the CFRP Reinforcement for Beam 1b.....	135
Figure 5.13: Shear Stress along the CFRP Reinforcement for Beam 1b.....	135
Figure 5.14: Shear Stress along the CFRP Reinforcement for Beam 2a.....	136
Figure 5.15: Shear Stress along the CFRP Reinforcement for Beam 2a.....	136
Figure 5.16: Shear Stress along the CFRP Reinforcement for Beam 2b.....	137
Figure 5.17: Shear Stress along the CFRP Reinforcement for Beam 2b.....	137
Figure 5.18: Shear Stress along the CFRP Reinforcement for Beam 3a.....	138
Figure 5.19: Shear Stress along the CFRP Reinforcement for Beam 3a.....	138

Figure 5.20: Shear Stress along the CFRP Reinforcement for Beam 3b.....	139
Figure 5.21: Shear Stress along the CFRP Reinforcement for Beam 3b.....	139
Figure 5.22: Interfacial Shear Stresses and Anchor Tributary Areas.....	144
Figure 5.23: Equilibrium of a NSM Strengthened RC Beam and its Concrete Cover....	146
Figure 5.24: Free-Body Diagram as a Basis for Täljsten Interfacial Stress .....	147
Figure 5.25: Interfacial Shear Stress along NSM Bar for Beams 1a and 1b .....	151
Figure 5.26: Interfacial Shear Stress along NSM Bar for Beams 2a and 2b .....	151
Figure 5.27: Interfacial Shear Stress along NSM Bar for Beams 3a and 3b .....	152
Figure 5.28: Free-Body Diagram as a Basis for Täljsten Peeling Stress.....	153
Figure 5.29: Interfacial Normal Stress along NSM Bar for Beams 1a and 1b .....	158
Figure 5.30: Interfacial Normal Stress along NSM Bar for Beams 2a and 2b .....	158
Figure 5.31: Interfacial Normal Stress along NSM Bar for Beams 3a and 3b .....	159
Figure 5.32: Principle Stresses at Location of Delamination Initiation .....	160
Figure 5.33: Directions of Positive Stresses for Principal Stresses Calculation.....	162
Figure 5.34: Kupfer and Gerstle Failure Envelope .....	164
Figure 5.35: Mohr-Coulomb Failure Criterion .....	165
Figure 5.36: Mohr-Coulomb Failure Envelope.....	167
Figure 5.37: Stress Concentrations due to Developing Stress Overlaps .....	168
Figure 5.38: Normal Stress Distribution at the NSM Bar End .....	169
Figure 5.39: Tensile Stress Linear Approximation at NSM Bar End.....	173
Figure 5.40: Strain Developed in Transverse Reinforcement for Beam 3a.....	176
Figure 5.41: Strain Developed in Transverse Reinforcement for Beam 3b.....	176
Figure A.1: Back Calculation using the Equivalent Stress Block Method.....	191
Figure A.2: Equivalent Stress Block Method Design of Control Beam.....	194
Figure A.3: Strain Compatibility for Design of Control Beam.....	195
Figure A.4: Elastic bending moment and shear diagrams for a simply-supported beam	198
Figure A.5: Equivalent Stress Block Method Design of Strengthened Beams.....	202
Figure A.6: Strain Compatibility for Design of Strengthened Beams.....	203

# List of Tables

Table 2.1: Physical Properties of Commercially Available Carbon Fibres .....	9
Table 2.2: Physical Properties of Commercially Available Glass Fibres.....	10
Table 2.3: Physical Properties of Commercially Available Aramid Fibres .....	10
Table 2.4: Thermosetting Physical Properties .....	12
Table 3.1: Summary of Steel Properties Based on Tensile Testing .....	33
Table 3.2: Summary of Concrete Properties Based on Compressive Tests.....	41
Table 3.3: BASF MBrace Primer and Saturant Properties .....	42
Table 3.4: Summary of all Material Properties based on Ancillary Tests.....	44
Table 4.1: Summary of Experimental Testing .....	118
Table 5.1: Experimental versus Theoretical Ultimate Moments of Tested Beams.....	122
Table 5.2: Interfacial Shear Stress in Test Beams.....	141
Table 5.3: Summary of Approximated Interfacial Shear Stresses along Failure Plane ..	144
Table 5.4: Approximated Normal Stresses provided by NSM Anchors and the Corresponding Axial Stress in the Anchors.....	145
Table 5.5: Approximated vs. Täljsten Shear Stresses at Delamination.....	150
Table 5.6: Concrete State of Stress near the Bar End and at the Onset of Delamination	161
Table 5.7: Principal Stresses of Concrete at Delamination Initiation .....	163
Table 5.8: Prediction of Concrete Cover Failure based on the Kupfer and Gerstle Failure Envelope .....	163
Table 5.9: Prediction of Concrete Cover Failure Based on the Mohr-Coulomb Failure Envelope .....	166
Table 5.10: Vertical Tensile/ Compressive Resultant Forces for Test Beams .....	171
Table A.1: Summary of Steel Reinforcement Yield Strain from Beam Tests .....	189
Table A.2: Summary of Yield Strain Statistics from Beam Tests .....	189

# Chapter 1

## Introduction

### **1.1. General**

One of the most promising strengthening techniques to rehabilitate aging reinforced concrete (RC) structures that has attracted the attention of researchers is near-surface mounted (NSM) strengthening. This strengthening technique involves the cutting of grooves into the tensile face of a beam or slab, normally in the concrete cover, and the placement of the NSM reinforcing bars into these grooves. The bars are bonded to the concrete by cementitious grout or epoxy.

The NSM technique originated in Europe in the 1950's to increase the strength of RC structures. Steel bars were inserted in grooves cut into the concrete cover of RC flexural members and a cement grout was used to bond the bars to concrete (De Lorenzis, 2006). However, conventional/ black steel NSM reinforcement created difficulties due to corrosion experienced by these relatively unprotected bars. Hence, black steel was replaced by stainless steel and more recently by fibre reinforced polymer (FRP) bars.

FRP offers numerous advantages compared to steel reinforcement due to its corrosion resistance and high strength-to-weight ratio. To replace the NSM steel bars by the stronger FRP materials, more advanced adhesive compounds need to be developed to effectively transfer the stresses from the FRP strengthening system to the RC element. Modern epoxies are the alternative to the mortar or cement used to bond steel bars to the

---

concrete due to their superior mechanical properties relative to the traditional cementitious materials (De Lorenzis 2006). Nevertheless, the combination of high strength FRP and epoxy has created its own challenges which must be overcome prior to the field application of the new system.

The effectiveness of the strengthening system is dependant on many factors, but the prevention of delamination at the adhesive/ concrete interface is a crucial factor. Delamination refers to the separation of the NSM reinforcing bars from the RC member and is generally characterized by a bond failure at the epoxy/ concrete interface or FRP/ epoxy interface. Premature delamination at any one of the interfaces limits the amount of interfacial stresses that can be transferred from the RC element to the NSM system and it usually leads to complete separation. As will be discussed later in this thesis, to prevent, or rather delay, delamination, a few techniques have been reported and most are generally based on techniques developed to prevent delamination of externally-bonded (EB) FRP laminates. Figure 1.1 schematically compares NSM strengthening to externally-bonded strengthening. A popular method is the application of FRP sheet U-jackets which are wrapped around the tension face of flexural elements and then bonded to the tension face of the beam web. This technique works relatively well provided the surface concrete to which the jacket is bonded is undamaged and is able to transfer the resulting interfacial shear and normal stresses. Additionally, the U-jacket is restricted to RC beams and does not permit the strengthening of slab elements. Another method is the use of ‘mechanical-interlocking grooves’ where horizontal epoxy-filled grooves positioned within the concrete cover intersect the primary NSM grooves and act as anchors to the FRP reinforcement. Although this method can be used to strengthen slab elements, if the interfacial failure occurs within the concrete cover the entire system is lost when the cover delaminates and separates. Consequently, there is need for the development of an anchor system that does not rely solely on the concrete cover to transfer the stresses from the NSM bars to the RC member.

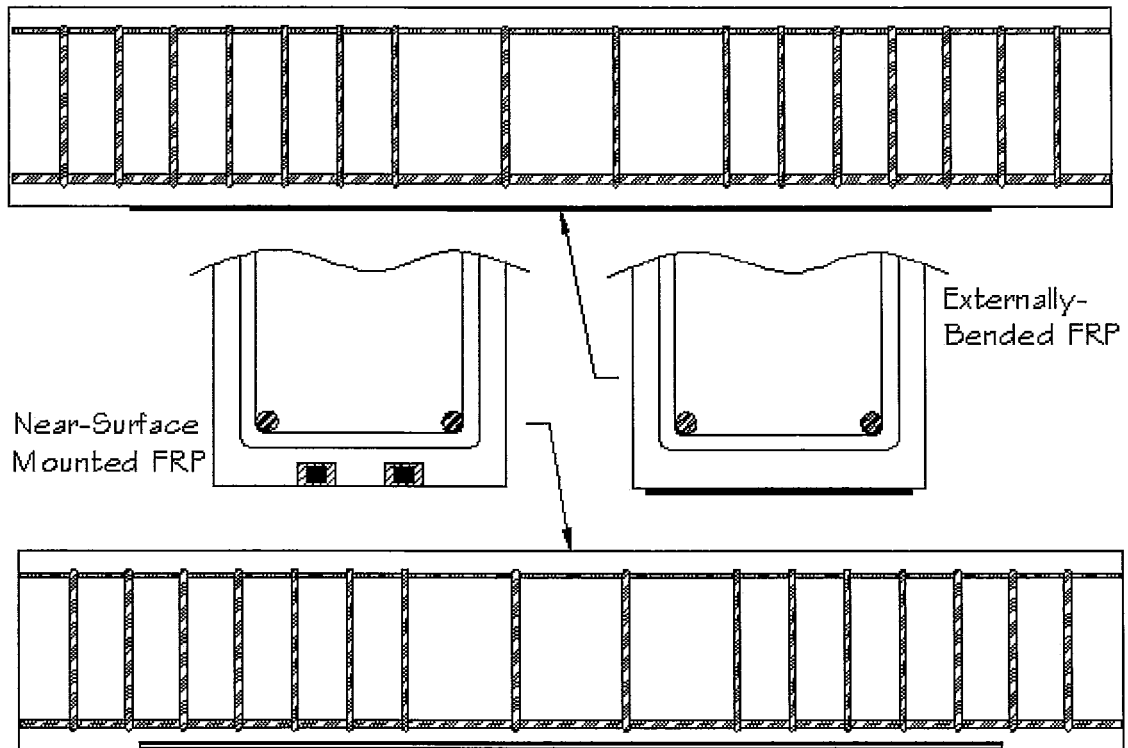


*Figure 1.1: Near-Surface Mounted Versus Externally-Bonded Strengthening*

## 1.2. Objectives and Scope

In light of the above introduction and the problems associated with existing anchoring systems for NSM FRP bars, the objectives of this study are:

- To develop a new NSM FRP anchoring system for delaying the delamination of NSM reinforcement in RC members.
- To investigate, via laboratory tests, the effectiveness of the new anchoring system. The NSM system effectiveness will be investigated by applying the new technique to standard RC beams to increase associated flexural strength.
- To apply the same technique to RC beams strengthened with NSM FRP bars to increase their shear capacity.
- To analyze the behaviour of RC beams involving the proposed anchoring system and to make recommendations for further improvements.

---

The study scope is limited to rectangular RC beams strengthened with NSM carbon fibre-reinforced polymer (CFRP) bars. All the test beams will be under-reinforced before and after the applications of the NSM CFRP reinforcing system and will all be designed to fail in flexure. Although the behaviour of a NSM shear strengthening system will be investigated, the pertinent strengthened beams will still be designed to fail in flexure. The NSM shear strengthened beams will be investigated to determine if the proposed NSM system would be an acceptable replacement for conventional internal steel stirrups. The studied parameters include the presence/ absence of anchors and the replacement of some steel stirrups by NSM CFRP bars involving the proposed anchor system.

# Chapter 2

## Literature Review

### **2.1. General**

Methods for strengthening existing reinforced concrete structures have been extensively studied over the past half a century. After the introduction of advanced composite materials in construction over the past 20 years, strengthening techniques have evolved from surface bonded FRP laminates to near-surface mounted FRP bars. The purpose of these studies has been the understanding of the behaviour of the strengthened members under increased applied loads and their modes of failure. Through a proper understanding of the failure mechanisms of these members, the feasibility and effectiveness of each strengthening technique can be established. Although the NSM technique is a relatively recent development, it has become one of the most promising techniques for strengthening RC and masonry structures due to the many advantages it offers relative to other externally bonded FRP systems.

The following chapter will describe the constituent materials used to construct a NSM system and the main challenges associated with NSM design, namely, the preservation of reinforcement bond to the RC element. The high strength of the FRP material creates challenges to efficiently transfer stresses from the strengthening system to the RC element. The positioning of the FRP bars within the unconfined concrete cover, which inevitably cracks and spawls, accelerates the tendency of cover

delamination. As the cover detaches, or delaminates, from the RC members, the gained strength from the NSM system is lost. To understand the delamination mechanisms and their causes, measures for delaying and/ or preventing it, have been studied by numerous researchers. The following literature review will briefly describe the nature of these studies and their results and conclusions.

## **2.2. *Constituent Materials Characteristics***

### **2.2.1. Fibre Reinforced Polymers**

Fibre Reinforced Polymers (FRP) are primarily made up of two components: reinforcing fibres and the matrix. Fibre bundles are bound together by the matrix which transfers stresses between the fibres. Generally, fibre laminas are stacked and combined to form a laminate or a composite section. Such sections may be in the form of thin laminate sheets or strips, round or square bars, rectangular grids or full size flanged members. Each lamina can be constructed in a variety of different ways which will affect the mechanical properties of the composite as illustrated in Figure 2.1 (Mallick, 1988).

Uni-directional continuous and discontinuous lamina contain ‘long’ and ‘short’ strands of fibre, respectively, running along a single direction. Uni-directional fibres are anisotropic or highly dependant on the direction of the applied load. Like wood, the fibres are strongest if the load is applied along the same direction as the fibre length and much weaker transversely. A bi-directional continuous system has fibres running in both directions, thus it could be equally strong in both the longitudinal and transverse directions. Random discontinuous lamina contain ‘short’ fibres in different directions and they approach a nearly isotropic material.

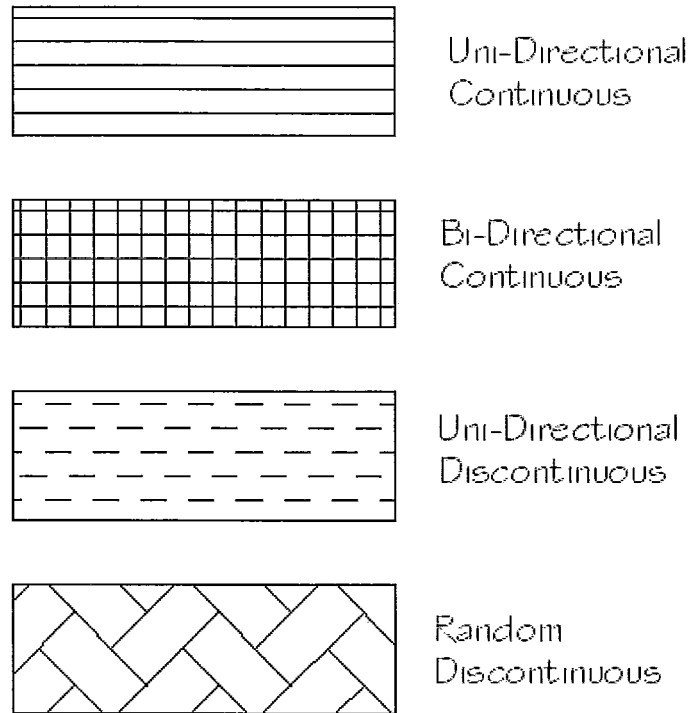


**Figure 2.1: Various Lamina Configurations**

Fibres can be constructed from a large array of materials; however, carbon, glass and aramid are the most common for structural elements. Figure 2.2 summarizes the stress-strain relationships for high strength and high modulus carbon; S and E glass; and Kevlar 49, which is an organic or aromatic compound (Mallick, 1988). It is apparent that fibres ultimate strength and elastic modulus vary over a wide range, but the linear-elastic stress-strain relation is common amongst all the listed fibres and is a common assumption for FRP design.

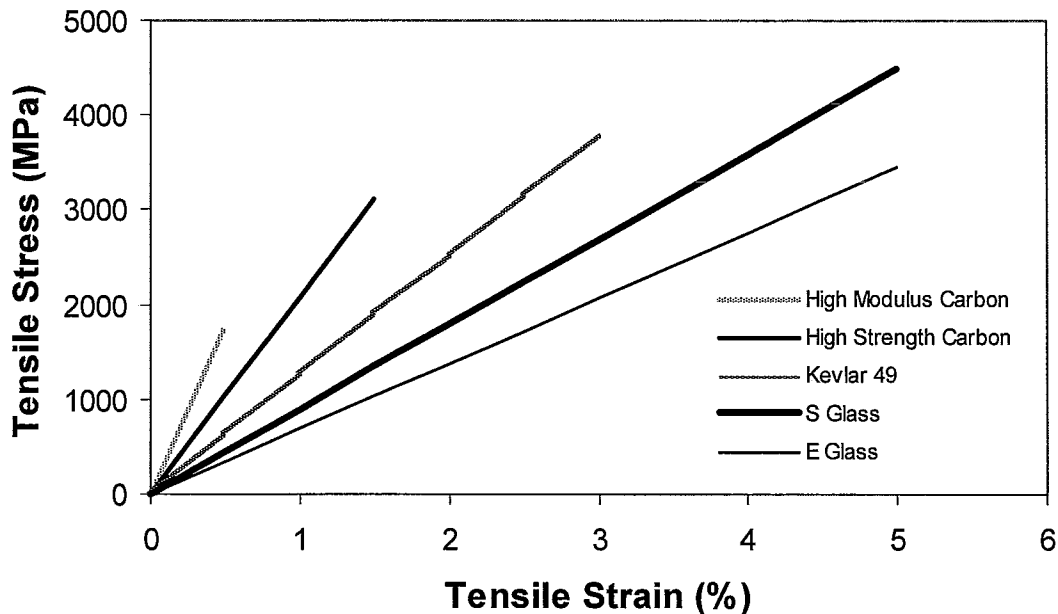


*Figure 2.2: Tensile Stress Strain Relationship for Various Fibres*

### 2.2.2. Carbon FRP

Carbon fibres are commercially available and amongst the more popular type of reinforcing material used in structural composites. Their tensile modulus ranges from approximately 270 to 517 GPa. Advantages of carbon filaments are their high tensile strength to weight ratio, very low coefficient of linear thermal expansion, resistance to corrosion and high fatigue strengths. Some disadvantages include their low impact resistance, high electrical conductivity and high costs. Carbon fibres contain a blend of amorphous and graphitic carbon. The graphitic carbon is laid in planes held together by strong covalent forces which contribute to carbon's anisotropic behavior, while weak vander Waals bonds hold the planes together. The strong covalent bonds are responsible for the fibres high tensile strength. Table 2.1, outlines some of the physical properties of commercially available carbon reinforcing fibres (Mallick, 1988). Note that carbon fibres are either made from pitch or from polyacrylonitrile (PAN).

*Table 2.1: Physical Properties of Commercially Available Carbon Fibres*

Fibre	Typical Diameter (µm)	Specific Gravity	Tensile Modulus (GPa)	Tensile Strength (GPa)	Strain to Failure (%)	Poisson's ratio
PAN – Carbon						
T-300 by Amoco	7 (round)	1.76	228	3.2	1.4	0.2
AS by Hercules Inc.	7 (round)	1.77	220	3.1	1.2	0.2
T-40 by Amoco	6 (round)	1.81	276	5.65	2	0.2
HMS by Hercules Inc.	7 (round)	1.85	344.5	2.34	0.58	0.2
GY-70 by Celanese	8.4 (bilobal)	1.96	483	1.52	0.38	0.2
Pitch-Carbon						
P-55 by Amoco	10	2	380	1.9	0.5	0.2
P-100 by Amoco	10	2.15	690	2.2	0.31	0.2

### 2.2.3. Glass FRP

Glass fibres, like carbon fibres, are commercially available and are popular in composite design. Principle advantages include low cost, high tensile strength, high chemical resistance and excellent insulating properties. Disadvantages are low tensile modulus, relatively high specific gravity when compared to other commercial fibres, sensitivity to abrasion when handled, relatively low fatigue resistance and high hardness, which wears on tools during the manufacturing processes. Due to its severe hardness, if glass is subjected to cyclic loading, glass fibres will continually slide by one another and reduce their tensile strength over time. Additionally, glass fibres can experience static fatigue in the presence of water. Water will bleach out the alkalis from the surface of the fibres and deepen surface flaws, thus reducing the tensile strength of the fibres. Unlike carbon, the internal molecular structure of glass is composed of long three-dimensional networks of silicone, oxygen and other atoms arranged in a random fashion which allows

glass to behave as an isotropic material. Table 2.2 presents two commercially available glass fibres and their associated physical properties (Mallick, 1988).

*Table 2.2: Physical Properties of Commercially Available Glass Fibres*

<b>Fibre</b>	<b>Typical Diameter (µm)</b>	<b>Specific Gravity</b>	<b>Tensile Modulus (GPa)</b>	<b>Tensile Strength (GPa)</b>	<b>Strain to Failure (%)</b>	<b>Poisson's ratio</b>
E glass	10 (round)	2.54	72.4	3.45	4.8	0.2
S glass	10 (round)	2.49	86.9	4.3	5	0.22

#### 2.2.4. Aramid FRP

Relative to carbon and glass fibres, aramid fibres have the lowest specific gravity, the highest strength to weight ratio and are the only organic fibres that are used in structural design. Some disadvantages include low compressive strength which leads to a high degree of longitudinal strain when the material is compressed, and manufacturing difficulty. A significant advantage is the stiffness of the fibre. The repeating aromatic ring gives aramid greater stiffness and better chemical and thermal stability when compared to other nylons. Similar to the carbon filaments, aramids are anisotropic along the longitudinal direction and unlike glass, aramid fibres do not exhibit any reaction to water. Since aramid is an organic compound, they react with ultraviolet light, however, the problem can be mitigated using ultraviolet light absorbing fillers added to the matrix. Table 2.3 lists the physical properties of a commercially available aramid fibre (Mallick, 1988).

*Table 2.3: Physical Properties of Commercially Available Aramid Fibres*

<b>Fibre</b>	<b>Typical Diameter (µm)</b>	<b>Specific Gravity</b>	<b>Tensile Modulus (GPa)</b>	<b>Tensile Strength (GPa)</b>	<b>Strain to Failure (%)</b>	<b>Poisson's ratio</b>
Kevlar 49 by DuPont	11.9 (round)	1.45	131	3.62	2.8	0.35

Currently, glass and carbon are the most common types of FRP used in structural repair and as internal reinforcement in new concrete structures.

### **2.2.5. The Polymeric Matrix**

There are mainly two types of polymeric matrix materials: thermoset polymers and thermoplastic polymers which are shown schematically in Figure 2.3. Thermoplastic polymers, illustrated in Figure 2.3a, have molecules that are held in place by weak intermolecular forces such as vander Waals and hydrogen bonds, thus, with the application of pressure and heat they can be temporarily broken. After the molecules cool they can be realigned and form a new solid shape. Thermosetting polymer molecules, illustrated in Figure 2.3b, are chemically joined with a cross link forming a strong, three dimensional network structure. Once these cross links are established during polymerization, the thermosetting polymer cannot be reformed with the use of heat and pressure (Mallick, 1988).

Thermoset polymers are generally used as the matrix material in fibre-reinforced composites because of their lower molecular weight, low viscosity, chemical stability, thermal stability and most importantly they exhibit less creep and stress relaxation compared to thermoplastic polymers. Thermosetting polymers disadvantages include limited storage life at room temperature, longer fabrication times and low impact strength (Mallick, 1988). Table 2.4 summarizes some of the physical properties of thermosetting polymers that are widely used in fibre-reinforced composites (Moukwa, 1996).

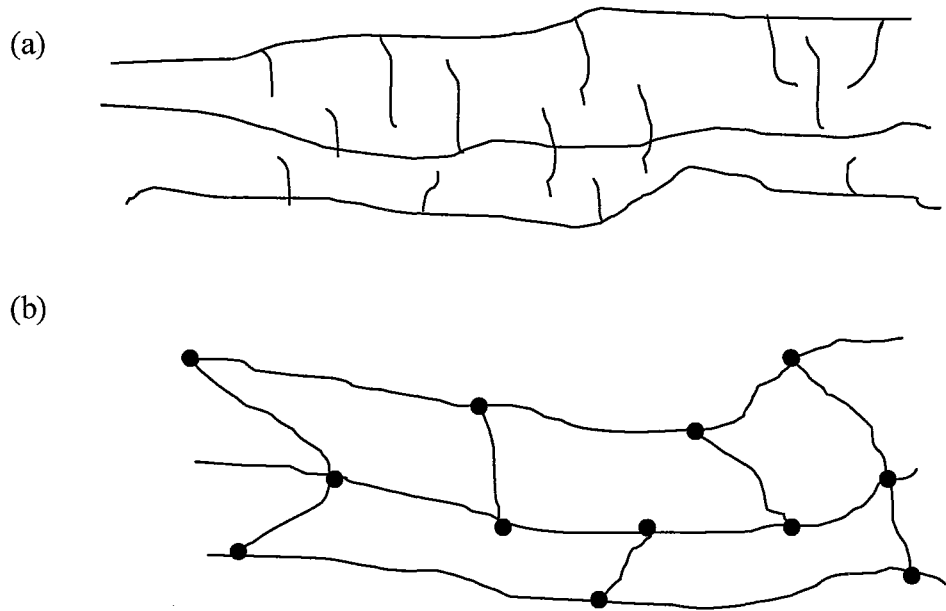


Figure 2.3: Schematic of (a) Thermoplastic polymer and (b) Thermosetting polymer

Table 2.4: Thermosetting Physical Properties

Resin	Density (kg / m <sup>3</sup> )	Tensile (MPa)	$\epsilon_u$ (%)	E (GPa)	Long term use temp. (°C)
Polyester	1.2	50-65	2-3	3	120
Vinylester	1.15	70-80	4-6	3.5	140
Epoxy	1.1-1.4	50-90	2-8	3	120-200
Phenolic	1.2	40-50	1-2	3	120-150

It is important to point out that FRP composites are made of one or more of the aforementioned fibres immersed in a polymeric matrix. Many properties of the composite, including its strength and elastic modulus, depend on the volumetric ratio of the fibre in the composite. Typically, for the FRP used in construction, the fibre ratio varies between 0.5 and 0.8.

---

### **2.3. Structural Strengthening using FRP Materials**

Due to the absence of design guidelines, NSM strengthening knowledge and literature is limited compared to the strengthening technique involving externally bonded FRP material, which follows design guidelines issued by the Canadian Standards Association Standard S806-02 (CSA, 2002) and the ACI 440 technical committee (ACI Technical Committee 440, 2002). These design guidelines are commonly used as a basis to design NSM systems, however, many issues specific to NSM systems are not addressed by them. The bonding characteristics between concrete and the FRP material vary from one system to the next. For externally bonded systems the laminate is bonded to a single concrete surface whereas the NSM system is bonded to three to four surfaces within a concrete groove. This difference in bonded surfaces between the two systems has lead researchers to state that NSM reinforcement is less prone to debonding from the concrete substrate (De Lorenzis and Teng, 2006). Although intuitively this may be the case, understanding the bond and quantifying the bond strength between the FRP and the RC element comprises a significant portion of the existing research on concrete members externally strengthened by FRP. For designing NSM strengthening systems, there is no readily available and widely accepted empirical or theoretical formula to estimate the loading that will initiate delamination; only strategies are available to mitigate the onset of this catastrophic failure mechanism.

To construct an effective NSM strengthened system, FRP reinforcements must be able to transfer its developed longitudinal stresses to the RC flexural member in order to ensure composite action. Premature delamination, however, separates the strengthening reinforcement from the concrete before a significant fraction of the usable strength of the FRP is developed. The factors which contribute to the phenomenon of delamination in NSM FRP strengthened members have been studied in a number of investigations.

De Lorenzis et al. (2000) investigated the strengthening of RC structures with NSM FRP rods. Each of the four full-scale specimens were 4575 mm long with the

---

following T-beam cross sectional dimensions: height of 405 mm, flange thickness of 100 mm, web width of 150 mm and flange width of 380 mm. The specimens consisted of an unstrengthened control beam and three strengthened beams using NSM CFRP rods. Two beams were strengthened with sandblasted CFRP rods each fitted with two #3 (3/8") or two #4 (4/8" or 1/2") rods while the final beam was fitted with two #4 deformed GFRP rods. All the grooves were square in cross section with side-length of 19 mm and 25 mm for the #3 and #4 rods, respectively. They found that the specimens strengthened with two NSM CFRP #3 and #4 rods each increased the load carrying capacity by 30% and 44.3%, respectively, relative to the corresponding unstrengthened or control specimen. Both CFRP beams failed due to the debonding of the NSM reinforcement, thus since bond was the controlling failure mechanism, increasing the amount of NSM reinforcement did not produce a proportional gain in capacity.

De Lorenzis and Nanni (2001) investigated shear strengthening of RC beams with NSM CFRP rods. Each of the 8 full scale T-shaped beams were 3000 mm long with the following cross sectional dimensions: height of 405 mm, flange thickness of 100 mm, web width of 150 mm and flange width of 380 mm. The specimens consisted of six beams with no internal steel shear reinforcement and the remaining two with internal steel stirrups at a spacing that did not satisfy the ACI 318 Code (1995) requirements. The beams were designed with equal flexural reinforcement and allowed to fail in shear despite the NSM shear strengthening. The following parameters were examined during the experiment: spacing of the NSM FRP bars (178 mm and 127 mm), inclination of the NSM FRP shear resisting bars (vertical and 45°), anchorage of the NSM bars in the flange using epoxy filled drilled holes, and the presence of internal steel stirrups. Each NSM CFRP reinforcing bar was 9.5 mm in diameter and was inserted within a 19 mm wide by 19 mm deep vertical groove extending along the full height of the beam web. In the absence of internal steel shear reinforcement, they found as high as 106% increase in the beams capacity compared to the control beam without shear reinforcement. In the beams with internal shear reinforcement, the NSM technique increased the capacity 35%

---

relative to the companion beam with stirrups but without NSM FRP bars. Generally, in the NSM reinforced beams the governing failure mode was the splitting of the epoxy cover, but when the specimens involved anchorage of the NSM bars in the flange or ‘closely’ spaced 45° NSM reinforcement, the failure mechanism changed to the splitting of the concrete cover along the longitudinal reinforcement. Finally, they reported that NSM shear reinforcement, unlike internal steel shear reinforcement, are not able to restrain the longitudinal steel reinforcement subjected to dowel forces thus it does not enhance the dowel forces, contribution to the overall shear strength of the beam.

De Lorenzis and Nanni (2002) conducted an experimental study on the bond between NSM FRP rods and concrete. They constructed 22 inverted-T test specimens that were 1220 mm long with the following cross sectional dimensions: height of 255 mm, flange thickness of 100 mm, web width of 155 mm and flange width of 255 mm. Each specimen was saw-cut and outfitted with a hinge at the mid-span to ensure the beam cracked at the mid-span location. The hinge forced the compressive resultant to act through its centroid and thus the moment arm was known at any given load. The test parameters included the bonded length of the NSM reinforcement (6, 12, 18 and 24 times the diameter of the bar), diameter of the NSM reinforcement (9.5 and 13 mm), type of NSM material (glass and carbon), type of NSM surface configuration (deformed and sandblasted) and the size of the groove. They found that the deformed rods had better bond performance than the sandblasted rods. When the groove size was increased, thus increasing the cover thickness, the bond strength was greater, and the governing failure mechanism was bar pull-out or epoxy cover splitting. As the groove size was increased, some specimens failure mode shifted from either bar pull-out or epoxy cover splitting to failure in the surrounding concrete. The optimal square groove size found for 9.5 and 13 mm diameter deformed bars were 19 and 25 mm, respectively. The ultimate load carrying capacity increased with increase in the NSM reinforcement bonded length and in most cases, with the exception of the smaller 9.5 mm CFRP deformed bar, bond stress distribution at ultimate was not uniform.

---

Hassan and Rizkalla (2003) investigated the bond in concrete structures strengthened with NSM CFRP strips. Each of the nine simply supported specimens were 2500 mm long with the following T-beam cross sectional dimensions: height of 300 mm, flange thickness of 50 mm, web width of 150 mm and flange width of 250 mm. The specimens consisted of one unstrengthened control beam and eight beams strengthened with NSM CFRP strips. The 1.2 mm wide by 25 mm high CFRP strips were inserted inside a single 5 mm wide by 25 mm deep groove along the mid-width of the bottom face of the beam. The test parameter was the embedment length of the NSM CFRP reinforcing strip (150, 250, 500, 750, 850, 950, 1050 and 1200 mm). They found that ultimate load carrying capacity increased by as much as 53% and the groove dimensions used were capable of preventing epoxy cover failure. The beam with 850 mm embedment exhibited the same bending capacity as the specimens with 950, 1050 and 1200 mm embedment, indicating the critical embedment length to be 850 mm. Localized debonding failure was observed at bar cut-off locations due to concentrated shear stresses and within the region of maximum moment due to wide flexural cracks. Through their analytical model produced after the laboratory tests, they found that the development length of strips increased when the internal steel reinforcement ratio increased. Additionally, the development length was found to decrease with increases of either concrete compressive strength and/or groove width.

Teng et al. (2003) conducted an experimental study on the debonding failures of RC beams strengthened with NSM CFRP strips. A total of five specimens were constructed, each being 3200 mm long with cross sectional dimensions of 150 mm wide by 300 mm high. The specimens consisted of one unstrengthened control beam and four beams strengthened with one NSM strip. The 5 mm wide by 16 mm high strips were inserted into an 8 mm wide by 22 mm deep groove along the mid-width of the beam bottom face. The test parameter was the length of embedment of the NSM CFRP reinforcement (500, 1200, 1800 and 2900 mm). They found for the specimens of 1200 and 1800 mm embedment, the governing failure mechanism was the debonding of the

---

concrete cover, while for the specimen with 2900 mm embedment the governing failure mode was concrete crushing. After analyzing the FRP strain and bond stress distribution, they reported debonding propagation from the bar cutoff section to the section of maximum moment for the beams with 500, 1200, 1800 mm embedment. Conversely, in the beam with 2900 mm embedment, the debonding propagated from the maximum moment region to the cutoff region as a secondary mechanism after the governing mechanism, concrete crushing had occurred. Prior to the flexural tests, they conducted tensile pull tests using various NSM bar embedment lengths and noted that the bond stress distribution developed in pull tests could not be used to predict flexural bond stresses. The reasons are the presence of flexural and flexural-shear cracks which alter the distribution, the curvature of the beam and the generated dowel forces due to bond cracks.

Barros and Fortes (2004) examined the flexural strengthening of RC beams with NSM CFRP reinforcing strips. A total of eight specimens were constructed each 1500 mm long with nominal cross sectional dimensions of 100 mm wide by 175 mm high. The test specimens consisted of four beams strengthened with NSM CFRP strips and the remaining four being unstrengthened and serving as control specimens. The 2 mm wide by 10 mm high strips were inserted into a 4 mm wide by 12 mm deep groove along the mid-width of the bottom face of the beam when a single strip was used, along 1/3 points when two strips were used and along 1/4 points when three strips were used. The test parameters were the amounts of steel and NSM CFRP reinforcement. It was the objective of the investigation to double the flexural strength of each control specimen by adding a particular amount of NSM reinforcement. It was observed that three of the four strengthened beams failed due to the debonding of the concrete cover. Portions of the detached layer extended above the level of the primary tensile reinforcement. The average increase in the ultimate load was 91% compared to the corresponding control specimen, and the CFRP reinforcements reached 62 to 91% of its ultimate strain. The authors suggest that their observed force-strain relationships consisted of three quasi-

---

linear segments: the first segment ranged from zero load to the cracking load, the second from the cracking load to the yielding load of the conventional reinforcement, and the third from the yielding load to the load corresponding to the initiation of slippage at the FRP-concrete interface. In the first segment all materials behaved linearly, along the second segment the concrete had cracked, internal steel reinforcement was behaving linearly while there was minimal slipping of the CFRP reinforcement, and along the final segment the steel had yielded and the slipping of the CFRP increased until failure was reached.

Barros et al. (2004) conducted tests using NSM CFRP strengthening techniques. The tests consisted of three test series involving three types of RC elements. The first series involved eight 1000 mm tall RC columns designed to fail in flexure with cross sectional dimensions of 200 mm by 200 mm. The tensile faces of the column were strengthened with three 10 mm deep by 2 mm wide CFRP strips inserted within 15 mm deep by 5 mm wide grooves spaced evenly at 1/4 points across the width of the strengthened face. Four control columns were initially tested under eight load cycles varying between +/-2.5 mm and +/-20.0 mm axial displacement, in increments of +/-2.5 mm at a displacement rate of 150  $\mu\text{m/s}$ . Subsequently these columns were strengthened with NSM bars and re-tested to failure. The performance of these strengthened columns was compared to that of another four similarly strengthened columns which did not involve pre-testing. They found that strain values of the CFRP strips approached their rupture strains, yielding an average increase of 92% and 34% in the columns load carrying capacity for the columns constructed with 4 No. 10 and 4 No. 12 internal steel reinforcements, respectively.

The second series of testing involved the construction of eight 1500 mm long RC beams designed to fail in flexure with nominal cross sectional dimensions of 175 mm high by 100 mm wide. The eight specimens consisted of four strengthened beams and the remaining four being the companion unstrengthened control specimens. The tensile

---

face of each beam specimen was strengthened with one, two or three 10 mm deep by 2 mm wide CFRP strips inserted within the 12 mm deep by 4 mm wide grooves spaced evenly at 1/2, 1/3 or 1/4 points of the bottom face of each beam, depending on the number of strips used. The objective of this test program was to double the load carrying capacity of the beam specimens by varying the amount of steel and the amount of CFRP used. They observed that the average increase of ultimate strength and average increase of cracking load was 91% and 51%, respectively. They also found that the NSM strengthening on average increased the load corresponding to the maximum serviceable deflection by 32% and the load corresponding to the onset of internal steel yielding by 39%.

The third series involved the construction of five 900 mm long RC beams designed to fail in shear with cross sectional dimensions of 150 mm wide by 150 mm high. The five beams consisted of a single control beam, a beam with steel stirrups, a beam using an externally bonded CFRP sheet and the remaining two beams were strengthened with NSM CFRP strips. The two beams strengthened with NSM CFRP strips used the same strips and groove dimensions as in the second series; however, they differed by the orientation of the installed NSM reinforcement along the beam (vertical or 45°) versus the horizontal. The objective of this test program was to double the load carrying capacity of the beam specimens by varying the amount of steel and the amount of CFRP used. They observed that the ultimate strength of the strengthened beams increased ranging from 50 to 77% with respect to the unstrengthened control beam. Additionally, the strengthened beams illustrated larger deflections at their associated ultimate loads than the control beam ranging from 118% to 294%, indicating a high level of deformability at failure amongst the strengthened beams.

De Lorenzis et al. (2004) conducted an experimental and analytical study on the anchorage length of NSM FRP bars for concrete strengthening. A total of thirty-four tests were conducted using a simple C-shaped concrete block to anchor the FRP

---

reinforcing bar. The test variables included the groove-filling material (epoxy paste and a cement-based expansive paste), bonded length of the FRP bar (4, 12 and 24 times the diameter of the reinforcing bar), groove size (ranging from 1.24 – 2.50 times the actual diameter of the reinforcing bar), surface configuration of the FRP bar (spirally wound and ribbed) and groove surface condition (roughened and smooth). They found that the epoxy paste offers superior mechanical performance when compared to the cement-based expansive paste due to the higher tensile strength of the epoxy. For the tests conducted, the optimal groove size was two times the diameter of the reinforcing bar as it delayed the occurrence of epoxy splitting. As the bonded length increased, the average bond strength decreased due to the non-uniform distribution of the bond stresses along the bonded length. They found it difficult to directly compare spirally wound and ribbed surface configurations due to the difference in bar diameters, however, spirally wound yielded the highest average bond strength along the bonded length of the reinforcing bar. Roughened groove surfaces failed in all cases at higher ultimate loads and the smooth grooves illustrated a more ductile bond-slip behavior.

El-Hacha and Rizkalla (2004) conducted an experimental study on flexural strengthening by NSM FRP bars and externally bonded FRP strips. Each of the 8 T-beam specimens was 2700 mm long with the following cross sectional dimensions: height of 300 mm, flange thickness of 50 mm, web width of 150 mm and flange width of 300 mm. The specimens consisted of one control specimen, three beams strengthened with NSM CFRP bars, one beam strengthened with NSM GFRP strip and the remaining three specimens externally strengthened with either CFRP or GFRP strips. Among the four beams involving NSM FRP, groove dimensions and number of bars installed along the beam were varied. Additionally, to compare the effectiveness of the NSM strengthening system, they constructed externally bonded specimens with an equal amount of FRP reinforcement as in the NSM FRP strengthened beams. They found that the use of NSM FRP reinforcement increased the flexural stiffness and ultimate load carrying capacity of the specimens. The strengthened beams behaved similar to the

---

unstrengthened control specimen prior to cracking, but after cracking their stiffness increased, deflections were limited and crack widths were reduced. The beams strengthened with the NSM system were able to achieve higher ultimate load compared to the beams strengthened with the externally bonded FRP strips. The increase in strength between the two systems for type 1 and type 2 configurations were 79% and 25%, respectively, illustrating the significance of concrete-FRP bond area for developing the reinforcement stresses.

Hassan and Rizkalla (2004) investigated the bond mechanism of NSM FRP bars for strengthening concrete structures. Each of the 8 simply supported specimens were 2500 mm long with the following T-beam cross sectional dimensions: height of 300 mm, flange thickness of 50 mm, web width of 150 mm and flange width of 250 mm. The specimens consisted of one control beam and seven beams strengthened with NSM CFRP bars. The 9.5 mm diameter CFRP bars were inserted within a single 18 mm wide by 30 mm deep groove centered along the beam soffit. The test variables included the use of various embedment lengths (150, 550, 800 and 1200 mm) and the comparison of two different epoxies (Duralith-gel and Kemko 040 bonding adhesive). They found that the development length of 150 mm provided insignificant increases in flexural stiffness due to premature pull-out failure. For this particular test the most efficient embedment length was 800 mm (80 times the bar diameter) while an increase to a 1200 mm embedment length increased the maximum tensile stress of the bar by less than 7.5%. Neglecting the results of the beams with 150 mm embedment length, all the other beams experienced increased load carrying capacities ranging from 20 to 41% in comparison to the control specimen. All the beams, with the exception of the 150 mm embedment length, failed by the debonding of the concrete cover. The failure occurred along the bottom of the internal steel reinforcement, indicating that the configuration of the internal steel reinforcement significantly influences the debonding location due to shear stresses concentration. They concluded that rupture in the NSM CFRP bars is not likely to occur no matter the embedment length as only 40 – 45% of the ultimate rupture strain was

---

achieved and the type of epoxy had no effect on the ultimate carrying capacity of the specimen. They stated that increasing the groove width and/or using a high strength concrete, the concrete resistance to split failure could be increased. Based on their analytical model, they recommend a minimum clear spacing between grooves of twice the diameter of the bar, regardless of the groove width and a minimum edge distance of four times the diameter of the bar.

Jung et al. (2005) examined the flexural behavior of RC beams strengthened by NSM CFRP reinforcement. Each of the 8 rectangular RC beams were 3000 mm long and having a 300 mm deep by 200 mm wide cross section. The specimens consisted of an unstrengthened control specimen, two beams strengthened with externally bonded CFRP sheets or strips and the remaining five strengthened with the NSM bars or strips. Of the five NSM beams, two beams used mechanical interlocking grooves which involved cutting grooves perpendicular to the longitudinal NSM CFRP bar or strip. The following parameters were examined during the tests: type of CFRP reinforcement (externally bonded versus NSM), shape of the NSM reinforcement (strip and round bar) and the application of the mechanical interlocking grooves. They found prior to cracking all the strengthened specimens exhibited behaviour similar to the unstrengthened control beam, however, after cracking the strengthened beams behaved stiffer than the control. The externally bonded and NSM reinforced beams exhibited ultimate load increases ranging 30 – 47% and 39 – 65%, respectively, compared to the control specimen. The governing failure mechanism for the NSM reinforcement was the debonding of the bars from the concrete cover, thus with the application of the mechanical interlocking epoxy-filled grooves, they were able to increase the beam capacity by 15% compared to the conventionally placed NSM specimens.

Kang et al. (2005) conducted an experimental and analytical study on the flexural behaviour of RC beams strengthened with NSM CFRP laminates. They constructed 5 prismatic test specimens that were 3000 mm long and having a cross section of 300 mm

---

high by 200 mm wide. The five beams consisted of one control beam and four specimens strengthened with NSM CFRP strips. The test parameters included the varying of the groove depth (15 and 25 mm) and groove spacing (60 and 120 mm). Based on their results, the authors derived an analytical model which produced results similar to the recorded data. Upon variation of the groove depth they found that there is a critical groove depth after which no additional capacity could be gained. Additionally, the analytical results revealed a critical edge distance of at least 40 mm for the NSM reinforcing bars.

Yost et al. (2007) conducted an experimental study on the flexural behaviour of concrete beams strengthened with NSM CFRP strips. They constructed 15 prismatic test specimens that were 2743 mm long and the beams were divided into three groups of five beams, where each beam in a given group had the same cross sectional dimensions and steel reinforcement ratio. The beam heights were all 190 mm while the widths were 152.4, 229 and 305 mm for each of the three groups. The NSM CFRP strips were 15 mm deep by 2.5 mm wide and were inserted longitudinally within a groove measuring 19 mm deep by 6.4 mm wide located along the beam center line when a single strip was installed or at 1/3 points when two strips were installed. All of the beams were designed to fail in flexure and the test parameters were the amount of internal reinforcing steel (0.353, 0.470 and 0.684 times the balanced reinforcement ratio) and the amount of CFRP reinforcement (1 or 2 strips). The test results indicated that all the beams strengthened with one NSM strip failed with the CFRP rupturing and all the beams strengthened with two NSM strips failed by the steel first yielding and then the concrete crushing. Thus, for all the specimens strengthened with a single CFRP strip 100% of the rupture strain was achieved and no apparent slip was noted for beams reinforced with two CFRP strips. They found that the thin rectangular CFRP cross section combined with a roughened surface texture provided an effective force transfer with the epoxy. Compared to the unstrengthened control beam, the strengthened beams showed increases in yield strength and ultimate

---

strength ranging 9 – 30% and 10 – 78%, respectively. On the other hand deflection ductilities decreased in the CFRP strengthened beams.

Choi et al. (2008) conducted an experimental study on partially bonded NSM CFRP bars in reinforced concrete T-beams. Each of the 9 specimens were 3500 mm long with the following cross sectional dimensions: height of 300 mm, flange thickness of 50 mm, web width of 150 mm and flange width of 400 mm. The specimens consisted of a control specimen, 4 non-prestressed NSM CFRP reinforcements and 4 prestressed NSM CFRP bars. Among the four beams in each of the two test series, four unbonded lengths, centered along the beam mid-span, were investigated. The unbonded lengths were 2100, 1700, 1300 and 0 mm. Each beam was reinforced with a single 7.9 mm diameter CFRP bar inserted within a 15 mm wide by 25 mm deep groove running along the length of the beam. They found that both the prestressed and non-prestressed fully bonded reinforcement systems were effective in increasing the ultimate strength by 56% when compared to the companion unstrengthened or control beam. The prestressed and non-prestressed strengthening systems reduced the ultimate deflection of the beam to 48 mm and 86 mm, respectively compared to the ultimate deflection of approximately 109 mm for the control specimen. Additionally, the ultimate deflection increased and the ultimate load decreased with increasing unbonded length, but for the partially bonded prestressed beams, deformability was greatly improved without significant reductions in ultimate strength. The failure mode was changed from FRP rupture to concrete crushing in the partially bonded non-prestressed beams and all prestressed beams failed due to FRP rupture. They finally concluded that the partially bonded specimens had greater concrete strain at mid-span due to greater beam deflections relative to the fully bonded beams.

Perera et al. (2008) investigated the effects of bond length, bar size, bar surface texture, groove size and concrete strength on the bond between NSM CFRP bars and the surrounding concrete. Their experimental program consisted of 6 test series of 4 bond specimens per series. The specimens were 110 mm x 220 mm in cross section and 750

---

mm long, containing a practical percentage of internal reinforcing steel and designed not to fail in shear, flexure or compression before bond failure. They found that the ultimate load of the specimen could be increased by increasing the bond length up to approximately 20 times the diameter ( $20d_b$ ) of the bar, for bond lengths greater than that, the ultimate load remained constant. Failure mechanisms within the epoxy cover were avoided in the specimens with larger groove dimensions (i.e. making the groove twice the size of the bar versus 1.5 times). Bond performance was improved with the bars of 'rougher' surface texture, indicating that surface texture has a significant influence on bond behavior. Through slip measurement and bond stress distribution they concluded that with small bond lengths a significant portion of the total bond length is active throughout the entire loading duration and stresses are nearly constant at any given load level compared to longer bond lengths.

Finally, Soliman et al. (2008) conducted an experimental and analytical investigation of RC beams strengthened in bending with NSM CFRP bars. Each of the 10 RC specimens were 2600 mm long with a rectangular cross section of the following dimensions: height of 300 mm and width of 200 mm. The specimens were tested using two internal steel reinforcement ratios 0.80% (series A) and 0.40% (series B) while varying the bonded length of the bar. Four bond lengths were tested for series A and B specimens consisting of 12, 24, 48 and 60 times the diameter of the NSM CFRP bar, while the remaining two beams were used as control specimens. The strengthened beams were reinforced with a single 9.5 mm diameter CFRP bar inserted within a 19 mm wide by 19 mm deep groove running along the length of the beam where the unbonded length was centered at the beam mid-span. They observed that all the strengthened beams failed due to the separation of the concrete cover initiated at the CFRP cut-off points near the beam supports. Beams in series A all showed increases in ultimate load carrying capacity with the exception of the one with the smallest bonded length of 12 times the bar diameter, where only the yielding load was increased by 16% compared to the companion control specimen. They found that increases in flexural strength among series A beams

---

were greatest up to the bonded length of 48 times the bar diameter. Series B beams exhibited increases in strength, compared to their associated control beam, of 22%, 32%, 71% and 75% when the bonded lengths was increased from 12 to 60 times the bar diameter as stated earlier. All strengthened beams behaved similarly to the unstrengthened control beams following the debonding of the NSM CFRP bar.

To summarize the literature reviewed in this chapter, most of the research has been focused on understanding and characterizing bond development between the NSM system and the RC element. Intuitively, and from a design perspective, a longer development length is better, nevertheless researchers continue to work on finding methods for quantifying a minimum length necessary to develop the strength of the NSM FRP bars. It is commonly reported that rupture strain of the FRP material cannot be reached due to failures at either the bar/ epoxy interface or at the epoxy/ concrete interface. Although failures can occur at various other interfaces, which are summarized in Figure 2.4, the latter two failures seem to be the most common in the reported literature. Figure 2.4 outlines the variety of observed failure mechanisms during testing which include failure at the bar/ epoxy interface, cohesive failure in the epoxy, failure at the epoxy/ concrete interface, cohesive failure in the concrete, epoxy splitting, a combination of epoxy and concrete split failure along inclined planes, a combination of epoxy and concrete split failure along inclined planes, where the split is not visible in the epoxy cover, and concrete fracture at the cross sectional edge (De Lorenzis and Teng, 2006). Delamination failures typically initiate near the NSM bar ends and propagate toward the centre of the beams due to high interfacial shear stresses; however, there are some reported cases where delamination first initiated near the beam midspan due to the curvature of the beam.

Various measures have been investigated to help delay NSM reinforcement delamination and bond failure. The use of ‘rough’ textured NSM bars helps in the development of the bond between the bar and the epoxy. By increasing the groove size

or effectively increasing the layer of epoxy surrounding the bar, the risk of a cohesive failure within the epoxy is reduced. Bar spacing and edge distance are also significant in delaying premature delamination. Analogous to internal steel reinforcement spacing, longitudinal and radial stresses must be permitted to develop between the NSM reinforcement and the surrounding concrete to produce composite action. If the radial stresses from adjacent bars overlap, pull-out failure (or bar/ epoxy interfacial failure) may occur. Also if the radial stresses overlap, the concrete between bars could fail cohesively. If the radial stresses spread to the section free edges, cover splitting can occur (MacGregor and Bartlett, 2000).

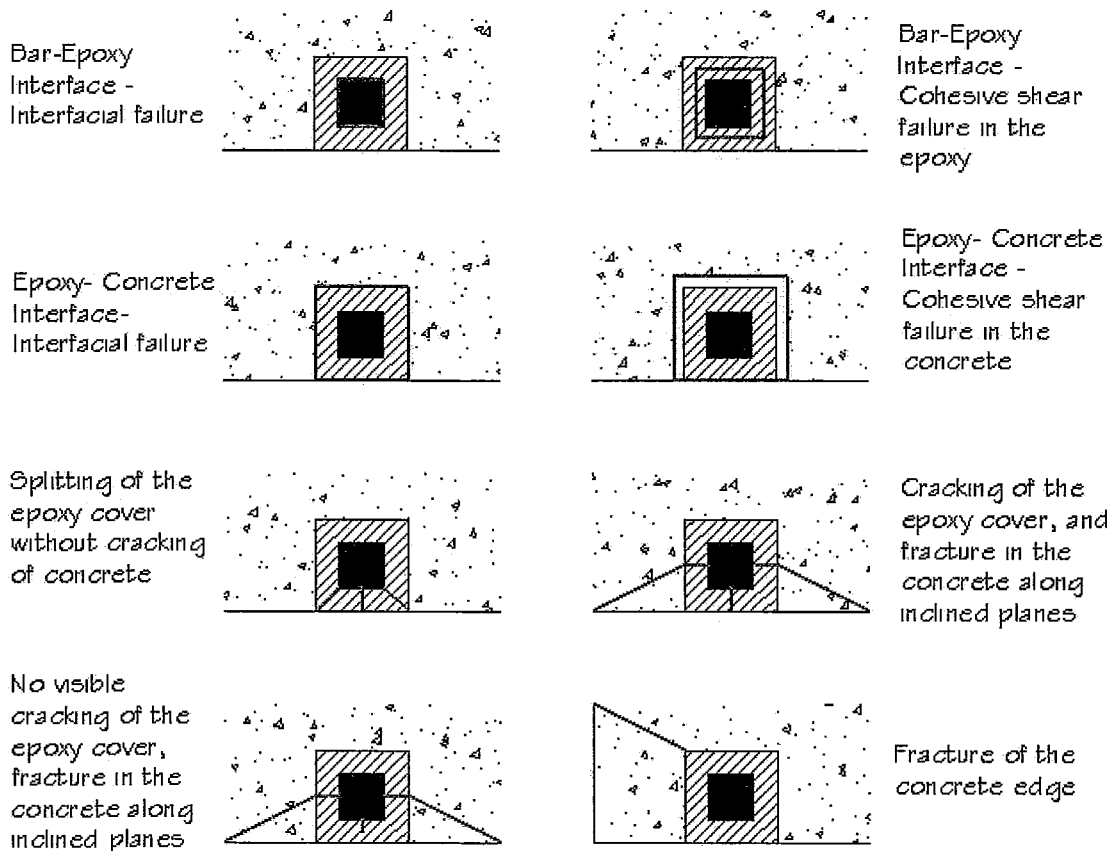


**Figure 2.4: Summarized Failure Mechanisms (De Lorenzis and Teng, 2006)**

NSM bar size is critical because relatively smaller FRP bars are easier to develop relative to larger bars. Larger bars need larger groove sizes which necessitates removal of more

---

concrete cover, and this induces larger stresses in the concrete surrounding the groove and increases the likelihood of either the concrete or the epoxy failure prior to achieving the bar rupture strain.

Intuitively, as the amount of NSM or internal steel is increased, the beam failure mode may be shifted from tension to compression failure, and the effectiveness of the NSM strengthening with respect to its usable strength is reduced. In spite of the variety of factors influencing the strength of the NSM reinforced members, and the various techniques applied to achieve strength gain, many investigators have reported strength gains and improved deflection control with NSM strengthening. However, all the techniques have not been equally efficient due to premature delamination, therefore, prevention of premature delamination remains the subject of on-going research in this field.

# Chapter 3

## Experimental Program

### **3.1. General**

The main objective of this experimental study is to investigate a new anchoring system for delaying delamination of NSM CFRP bars used to strengthen RC elements. The anchors are formed integrally with the CFRP reinforcement and extend into the core of the RC beam. The NSM bars will be placed within grooves cut into the concrete cover where a two-part epoxy will be used to bond the NSM reinforcement to the concrete. It is also intended to investigate the application of a similar system to resist applied shear forces. NSM CFRP anchored bars will be installed on the vertical faces of the test beams to carry 50% of the shear force resisted by the shear reinforcement in these beams.

Single span simply-supported beams will be tested to investigate the strength gain achieved by the CFRP strengthened beams. In each case two nominally identical beams will be tested to obtain a greater level of confidence in the repeatability of the observed behaviour. As a reference for comparison, one beam will serve as control specimen reinforced with only longitudinal and transverse steel. The remaining six will all be strengthened with NSM CFRP reinforcement and internally with 50% of the longitudinal steel used in the control beam. Two of the six beams will be reinforced with NSM CFRP bars without anchors and the remaining four with similar bars but with anchors. By

---

replacing 50% of the longitudinal steel with CFRP bars, the anchors could be readily embedded in the RC beams. Of the four beams with the anchors, two will be strengthened with NSM transverse bars to resist the applied shear. The transverse bars would have anchors to help them develop their strength over the relatively short height of the beams. The NSM transverse bars will be placed along half of the beam length and in that half the transverse reinforcement will alternate between steel stirrups and NSM bars. The objective of the exercise is to investigate the effectiveness of the NSM bars as external transverse reinforcement.

### 3.2. Test Specimens

Seven single-span beams each with a total length of 3175 mm, a span of 2500 mm, and a cross section of 275 mm x 450 mm will be tested. The beams are categorized as follows:

- a) **Control Beam:** One control beam (under-reinforced), used as a reference to the remaining six RC beams strengthened with CFRP bars.
- b) **Type 1 (a & b) Beams:** Two replicate CFRP beams (under-reinforced) reinforced with NSM CFRP bars without anchors.
- c) **Type 2 (a & b) Beams:** Two replicate CFRP beams (under-reinforced) reinforced with NSM CFRP bars with integral CFRP anchors.
- d) **Type 3 (a & b) Beams:** Two replicate CFRP beams (under-reinforced) reinforced with NSM CFRP bars with integral anchors for increased flexural and shear resistance. The CFRP shear strengthening system is only applied over half of each beam and is achieved by replacing every other internal steel stirrup with a NSM transverse bar on each face of the beam. The other half is reinforced with closed steel stirrups at the designed spacing.

### 3.3. Material Properties from Ancillary Tests

Three materials are used in this experimental program; namely, concrete, steel reinforcing bars and CFRP bars. Most of their properties would be obtained from

---

---

ancillary tests, however, in the case of the FRP, the manufacturer's recommended values would be used. The use of the recommended values is not expected to affect the conclusions of the presented flexural tests because rupture of the FRP is not anticipated in any of the test beams. The ancillary tests include tensile tests for both the longitudinal and transverse steel reinforcement and compression testing of the concrete cylinders.

### 3.3.1. Longitudinal and Transverse Steel

Deformed longitudinal and transverse steel bars were used in all seven beams. All the main flexural steel consisted of deformed No. 20 reinforcing bars while No. 10 hanger bars were used for fabricating the steel cage. The steel stirrups consisted of deformed No. 15 steel bar. All the reinforcing steel was specified to have a nominal yield strength of 400 MPa and all preliminary design calculations were based on the specified strength. Steel reinforcement coupons were tested using a 600 kN universal testing machine and strains were measured by means of an electronic extensometer. Three No. 20 and three No. 15 coupons were tested to determine the tensile behaviour of the longitudinal and transverse steel, respectively. The steel strains and the associated forces were recorded using a data acquisition system. The steel stress was calculated based on the initial cross-sectional area of the bar.

It is evident from Figure 3.1 and Figure 3.2 that neither bar size had a distinct yield point; therefore, the 0.2% offset method was utilized to find the yield strength and elastic modulus of these bars. The method involves offsetting the initial strain to 0.2% (zero stress) and drawing a secant line with a slope equal to that of the initial tangent modulus of the curve. The point at which the secant intersects the stress-strain curve is taken as the yield strength of the material. The secant lines are omitted from Figure 3.1 and Figure 3.2 to better illustrate the recorded stress-strain relationships.

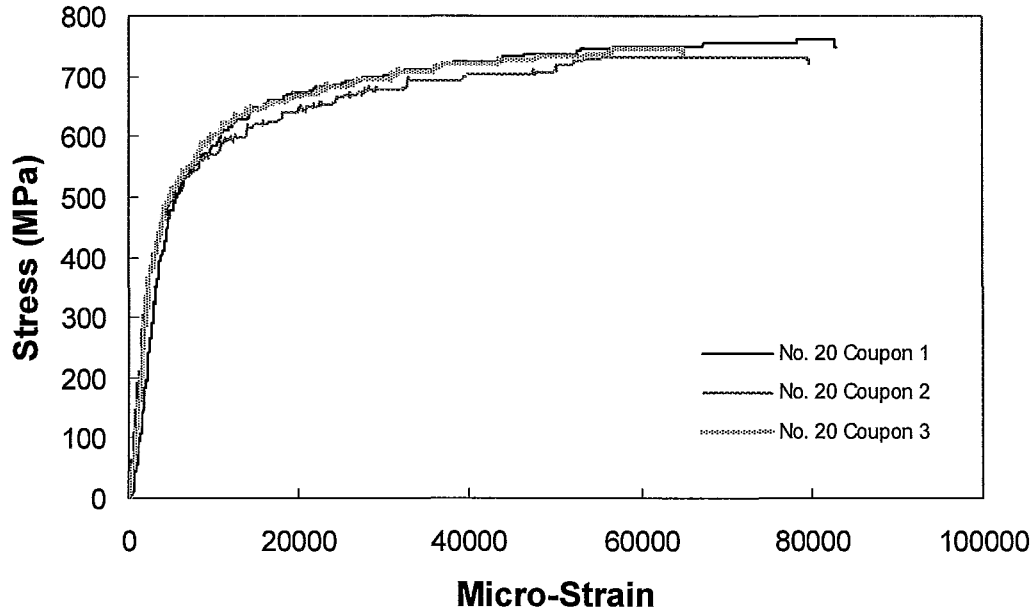


Figure 3.1: Primary Longitudinal Steel Tensile Test Results

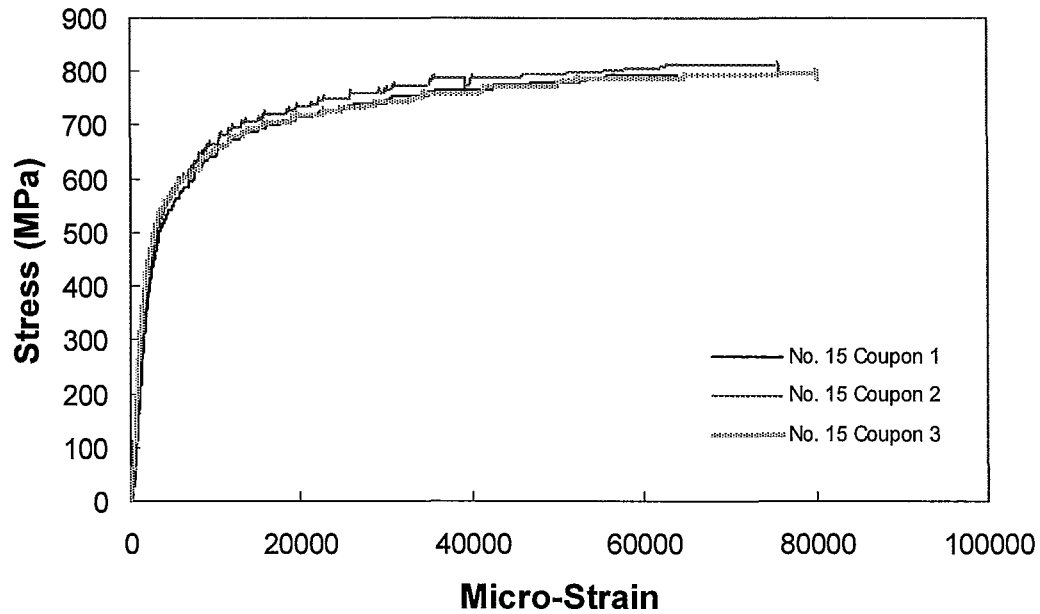


Figure 3.2: Internal Steel Stirrup Tensile Test Results

Table 3.1 summarizes the results of the tensile tests on the six steel coupons. The average yield strength of the longitudinal and the transverse shear reinforcement were determined to be 481 MPa and 569 MPa, respectively. The average elastic modulus based on the slope of the secant is shown in Table 3.1. Since the 0.2% offset procedure was completed to estimate the yield strengths of the steel coupons the corresponding yield strain,  $\epsilon_y$ , will be estimated by dividing the yield strength by the elastic modulus determined with the 0.2% offset method.

**Table 3.1: Summary of Steel Properties Based on Tensile Testing**

<b>Reinforcement Type</b>	<b>Test No.</b>	<b><math>f_y</math> (MPa)</b>	<b><math>\epsilon_y</math></b>	<b><math>f_u</math> (MPa)</b>	<b><math>\epsilon_u</math></b>	<b><math>E_s</math> (MPa)</b>
Longitudinal Steel (No. 20 Bar)	1	489	0.0026	755	0.083	186726
	2	470	0.0025	730	0.080	184727
	3	485	0.0025	738	0.065	194623
<b>AVERAGE</b>		<b>481</b>	<b>0.0026</b>	<b>741</b>	<b>0.076</b>	<b>188692</b>
Transverse Steel Stirrups (No. 15 Bar)	4	563	0.0036	785	0.064	156944
	5	578	0.0031	803	0.076	185732
	6	565	0.0026	791	0.080	219088
<b>AVERAGE</b>		<b>569</b>	<b>0.0030</b>	<b>793</b>	<b>0.073</b>	<b>187255</b>

### 3.3.2. CFRP Reinforcement

The CFRP rectangular reinforcing bars were obtained by cutting the ribs of a CFRP grid or mesh commonly known as NEFMAC (New Fibre Composite Material For Advanced Concrete). NEFMAC is a proprietary product distributed by Autocon Composites Inc. of Toronto, Ontario. A schematic cross section and intersection details of the grid can be seen in Figure 3.3 (Karbhari, 1994). At rib intersections the carbon lamina overlaps each other alternating between the crossing orthogonal layers. The use of this product permitted the quick construction of both types of NSM CFRP reinforcing bars (i.e. longitudinal bars with anchors and without anchors). The cutting technique used to develop the NSM bars with anchors for type 2 and 3 beams is shown in Figure 3.4. For the bars used in type 1 beams, which involved CFRP bars with no anchors, the

protruding ribs or anchors were simply cut flush with the longitudinal bar. Figure 3.5 shows a typical NSM bar with anchors.

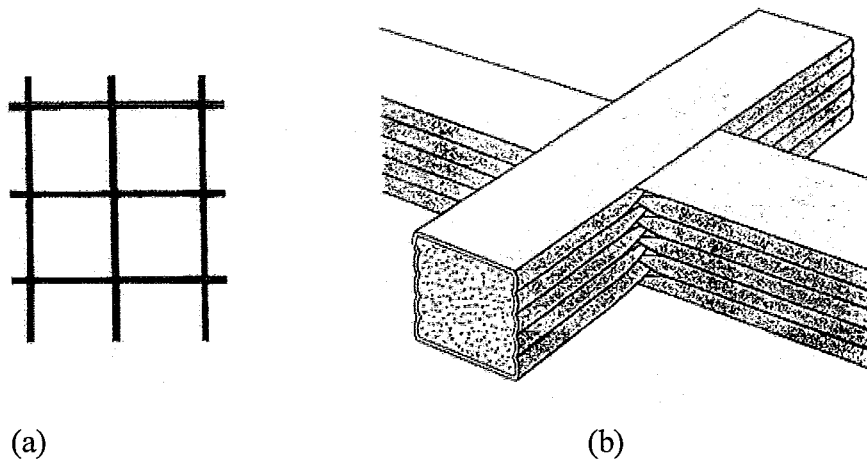


**Figure 3.3: NEFMAC (a) Typical Grid, (b) Grid Joint Close-up**

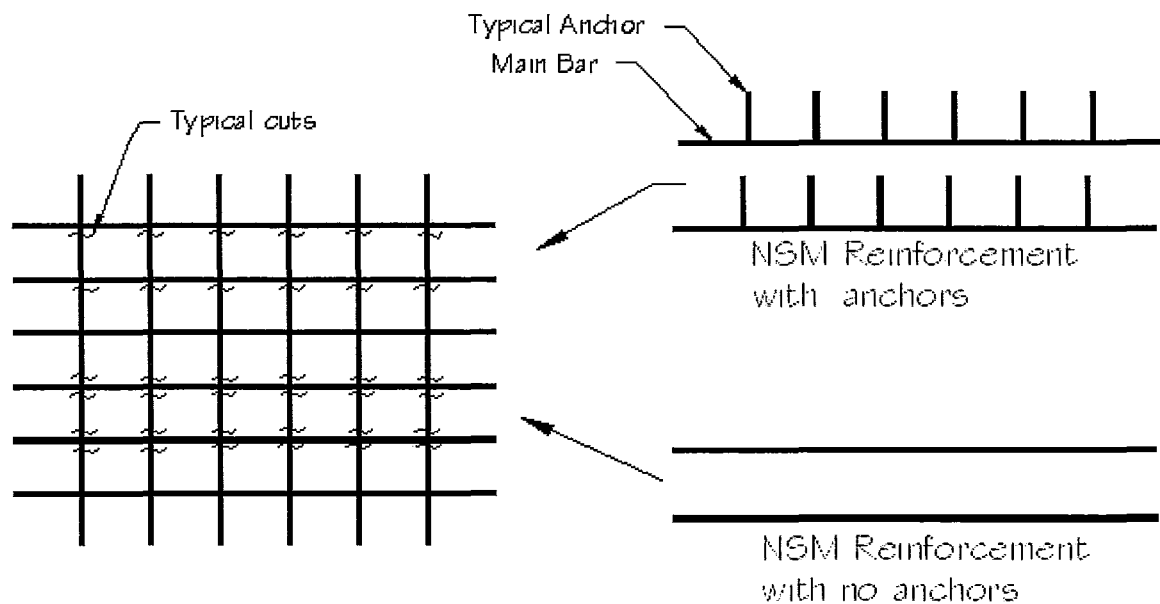


**Figure 3.4: NEFMAC Cutting Procedure for Obtaining the NSM Bars**

In all applications the grids consisted of bars with nominal cross sectional dimensions of 15 mm by 10 mm or a cross sectional area of 148 mm<sup>2</sup>. The bar size is classified as C19 by the manufacturer. The grids had 110 mm spacing in one direction

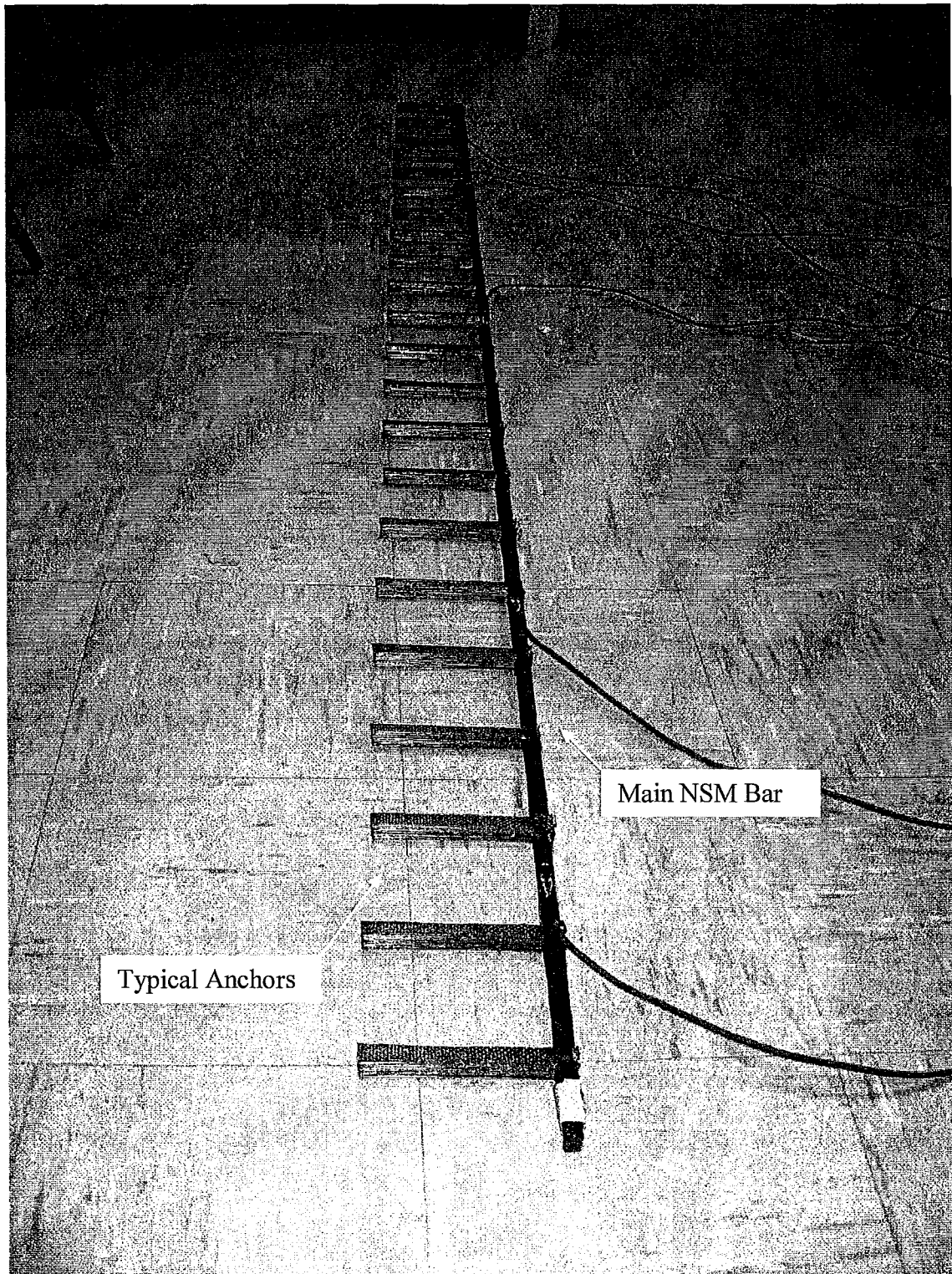


*Figure 3.5: Cut NEFMAC*

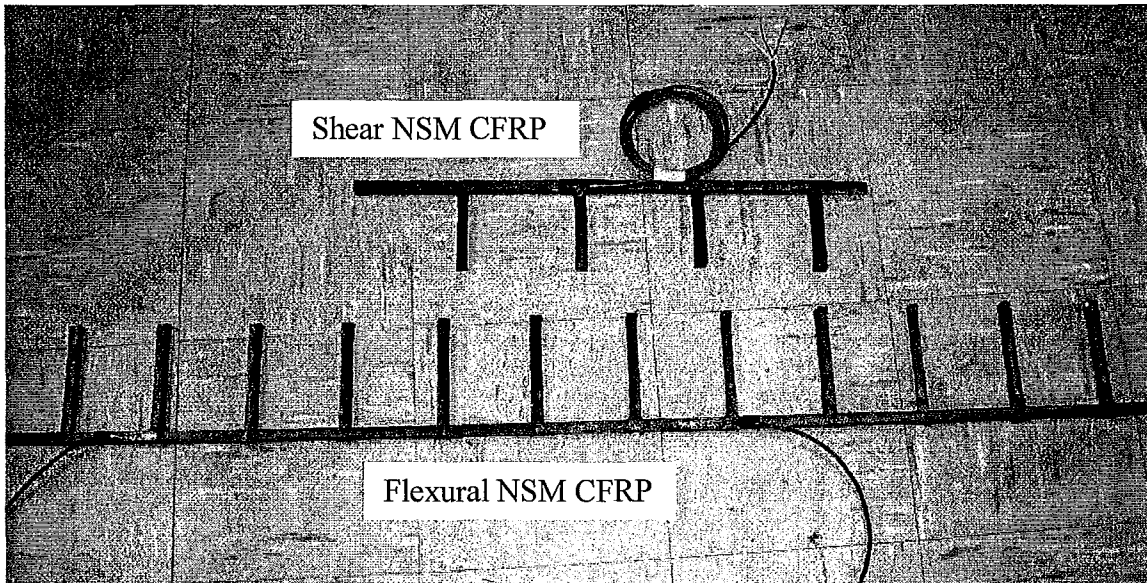


*Figure 3.6: Shear and Flexural NEFMAC CFRP Reinforcement*

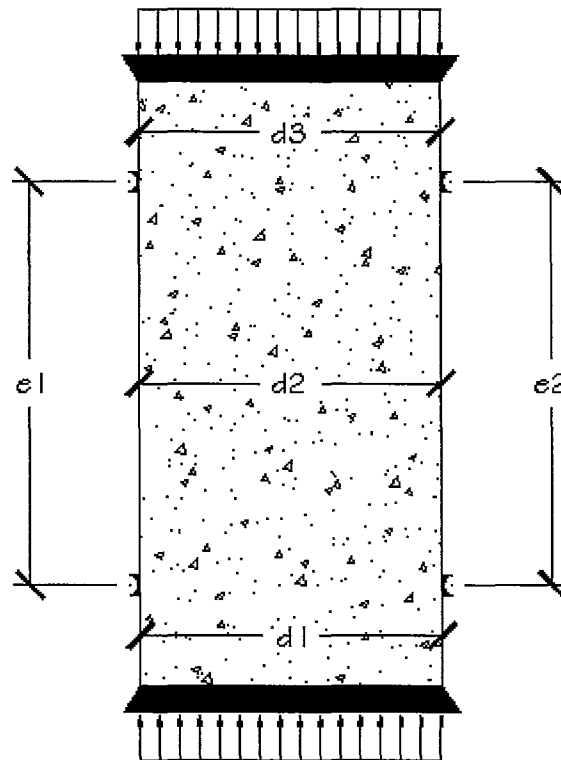
and 85 mm in the perpendicular direction. Due to lack of proper grips or chucks at the Applied Dynamics Laboratory, the NEFMAC grids were not tested to obtain their properties; instead the required properties were obtained from the standard specifications recommended by the manufacturer. According to those specifications, the tensile strength and elastic modulus of the C19 NEFMAC grid are 1200 MPa and 100 GPa, respectively.

Figure 3.6 shows the typical NEFMAC NSM bars used as shear and flexural reinforcement. The cables seen attached to the CFRP bars are soldered to foil strain gauges along the longitudinal axis of the bar which will be discussed in detail in subsequent sections of this chapter.

### 3.3.3. Concrete

The concrete was cast in a single batch seven months prior to testing. Concrete with specified compressive strength ( $f'_c$ ) of 35MPa, slump of 75 mm and maximum aggregate size of 15 mm was ordered from the Lafarge ready mix plant. During the casting of the beams, a total of 17 standard concrete cylinders (150 x 150 x 300 mm)

were concurrently cast and cured under the same conditions as the test specimens. To obtain a smooth and level surface, all the cylinders were capped with sulfur compounds prior to compressive testing. Five cylinders were tested after 28 days, four cylinders at weeks 35, 51 and 56, for a total of twelve additional cylinders. The latter times correspond to the age of concrete at the time of testing beam types 1, 2 and 3, respectively. The four cylinders for each beam type were tested to establish the concrete stress-strain relationship and modulus of elasticity,  $E_c$ , at the time of testing of the associated beams. The cross-sectional area of the cylinders was calculated based on the average value of three diameters along the cylinder height, Figure 3.7, measured using a pair of calipers. The relative displacements were measured using a mechanical



*Figure 3.7: Concrete Cylinder Measurement Locations*

extensometer at two locations and the corresponding strain was calculated by averaging the two readings and multiplying it by a calibration factor. The cylinders were tested using a 300,000 lbf compression machine. Data was manually recorded at increments of

5,000 lbf between 0 to 50,000 lbf and at increments of 10,000 lbf from 50,000 lbf to failure.

Since the collected data was in US customary units, they were converted to SI units and are plotted in Figure 3.8 through Figure 3.11. It should be noted that because of the relatively high strength of concrete, the descending branch of the stress-strain curves could not be captured with the testing machine that was used. In some of the stress-strain curves unexpected behaviour is noted where recorded strain values suddenly ‘jump’ to higher levels without a proportional increase in load. This is due to the manual operation of the mechanical extensometer. During the cylinder testing a constant pressure could not be maintained when trying to hold the extensometer in contact with the demec disks; the contact pins would slip and this led to erroneous readings. The concrete strength and elastic modulus obtained from the cylinder compression tests are summarized in Table 3.2. Note the nearly 10% increase in the compressive strength from the age of 28 days to 56 weeks. The modulus of elasticity values in the table are based on the secant modulus which is the slope of a secant line connecting two points on the stress-strain curve. As specified by the ASTM C469 (ASTM, 2006), the first point corresponds to the stress level at 50 micro-strain and the second point corresponds to a stress level equal to 40 per cent of the maximum stress. Table 3.2 compares the modulus of elasticity thus calculated with the empirical formula used in the CSA A23.3-04 (CSA, 2004), which for concrete of compressive strength between 20 and 40 MPa is given by,

$$E_c = 4500\sqrt{f'_c} \quad (3.1)$$

The simplified equation given by the A23.3-04 agrees relatively well with the experimental elastic modulus as can be observed in Table 3.2. Additionally, the modulus of rupture of the concrete was calculated in accordance with the CSA A23.3-04 which is given by,

$$f_r = 0.6\lambda\sqrt{f'_c} \quad (3.2)$$

where  $f_r$  represents the modulus of rupture or tensile strength of concrete in bending and  $\lambda$  is a modification factor for the density of the concrete used. The concrete used in the

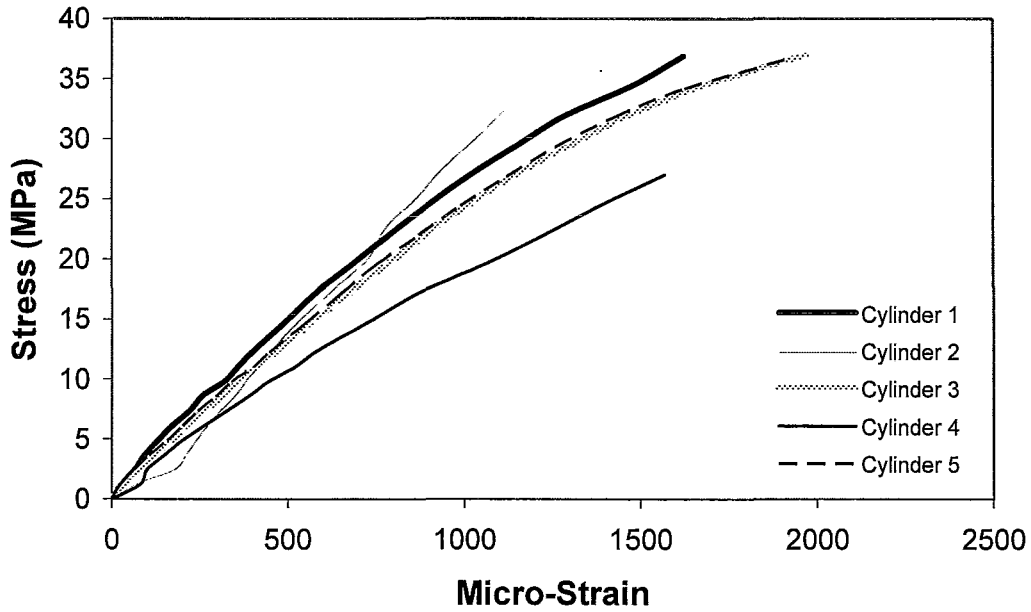


Figure 3.8: Concrete Compression Test Results after 28 Days

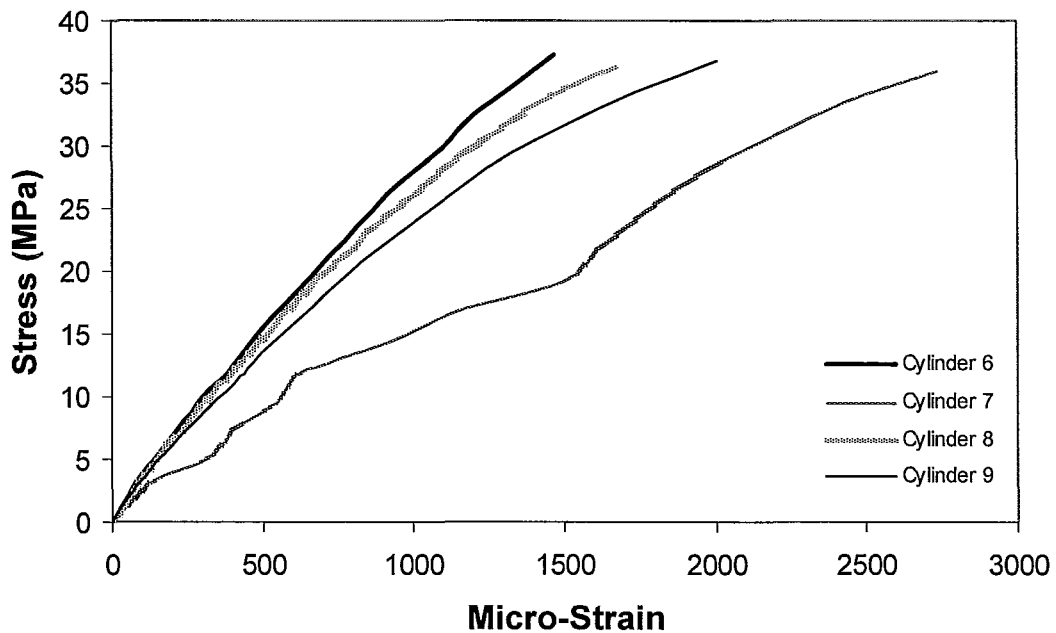


Figure 3.9: Concrete Compression Test Results after 35 Weeks

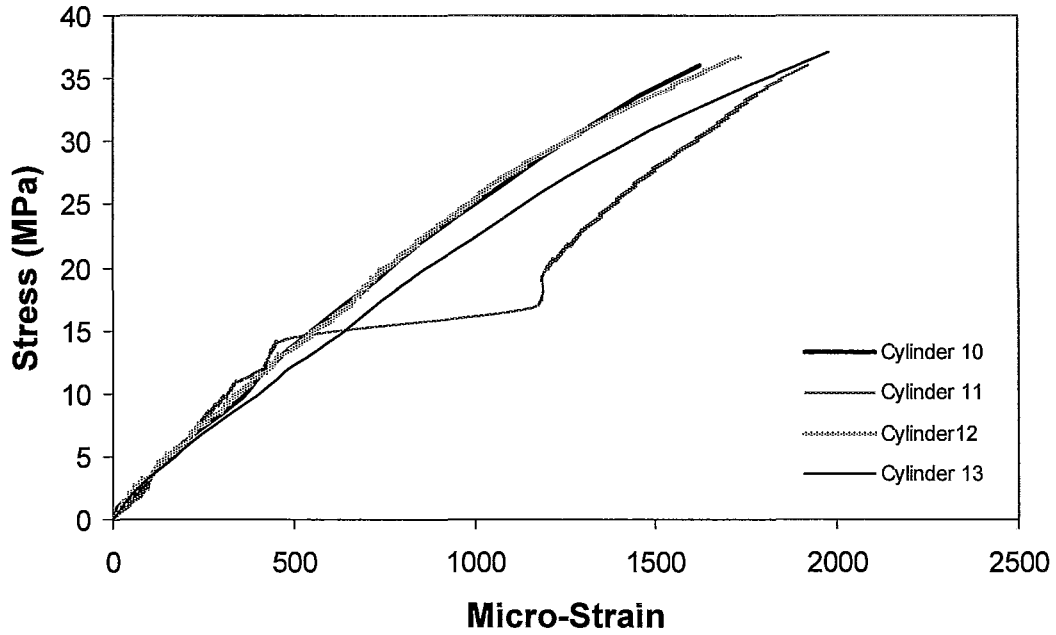


Figure 3.10: Concrete Compression Test Results after 51 Weeks

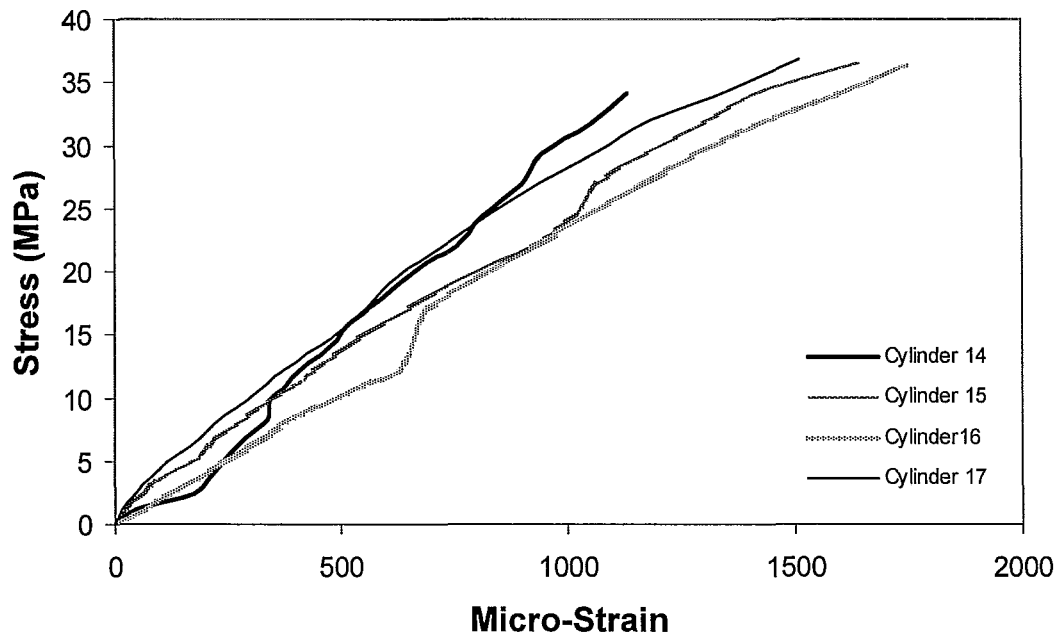


Figure 3.11: Concrete Compression Test Results after 56 Weeks

present investigation is normal density concrete, therefore  $\lambda$  is equal to one. Henceforth, the average compressive strengths for each beam type will be used to discuss their experimental results and to compare their theoretical capacity and behaviour with their experimental counterparts.

*Table 3.2: Summary of Concrete Properties Based on Compressive Tests*

Age	Specimen	Experimental		CSA A23.3-94	
		$f'_c$ (MPa)	$E_c$ (MPa)	$E_c$ (MPa)	$f_t$ (MPa)
28 days	1	37.0	29215	27379	3.7
	2	33.3	29109	25968	3.5
	3	37.1	25335	27409	3.7
	4	29.6	22276	24483	3.3
	5	37.5	25690	27557	3.7
	<b>AVERAGE</b>	<b>34.9</b>	<b>26325</b>	<b>26559</b>	<b>3.5</b>
35 weeks	6	38.3	30395	27863	3.7
	7	39.6	18652	28318	3.8
	8	38.3	29219	27849	3.7
	9	38.2	25770	27813	3.7
	<b>AVERAGE</b>	<b>38.6</b>	<b>26009</b>	<b>27961</b>	<b>3.7</b>
51 weeks	10	40.8	25614	28751	3.8
	11	41.3	29977	28919	3.9
	12	40.4	26147	28602	3.8
	13	40.4	22703	28602	3.8
	<b>AVERAGE</b>	<b>40.7</b>	<b>26110</b>	<b>28719</b>	<b>3.8</b>
56 weeks	14	42.3	31118	29267	3.9
	15	42.6	25283	29371	3.9
	16	41.8	25282	29094	3.9
	17	40.8	28736	28744	3.8
	<b>AVERAGE</b>	<b>41.9</b>	<b>27605</b>	<b>29119</b>	<b>3.9</b>

### 3.3.4. Two Component Epoxy

A two-part epoxy was used to bond the NSM bars and the anchors to the RC beams. The mixing procedures and surface preparation requirements were followed as specified by the manufacturer to ensure a good bond to the concrete surface. Prior to the application of the two-part epoxy, a primer was applied to the surfaces of the grooves cut into the surface of the concrete for the placement of the NSM bars. The epoxy and

*Table 3.3: BASF MBrace Primer and Saturant Properties*

Properties		MB Primer	Mbrace® Saturant
<b>Tensile Properties</b>	Yield Strength	14.5 MPa	54.0 MPa
	Strain at Yield	2.00%	2.50%
	Elastic Modulus	717 MPa	2034 MPa
	Ultimate Strength	17.2 MPa	55.2 MPa
	Rupture Strain	40.00%	3.50%
	Poisson's Ratio	0.48	0.4
<b>Compressive Properties</b>	Yield Strength	26.2 MPa	85.2 MPa
	Strain at Yield	4.00%	5.00%
	Elastic Modulus	670 MPa	2620 MPa
	Ultimate Strength	28.3 MPa	86.2 MPa
	Rupture Strain	10%	5%
<b>Flexural Properties</b>	Yield Strength	24.1 MPa	138 MPa
	Strain at Yield	4.00%	3.80%
	Elastic Modulus	595 MPa	3724 MPa
	Ultimate Strength	24.1 MPa	138 MPa
	Rupture Strain	Large Deformation-No Rupture	5%
<b>Colour</b>	Part A	Amber	Blue
	Part B	Clear	Clear
	Mixed	Amber	Blue
<b>Mix</b>	Mixed Weight	1103 g/L	984 g/L
	Density	1102 kg/m <sup>3</sup>	983 kg/m <sup>3</sup>
	Mixed Ratio	3:1 (Part A: Part B) by Volume	3:1 (Part A: Part B) by Volume
		100:30 (Part A: Part B) by Weight	100:34 (Part A: Part B) by Weight

primer used are MBrace Saturant and MB Primer, respectively. The following table summarizes the epoxy and the primer properties taken from the manufacturers specifications (BASF, 2007).

### **3.4. Details of Test Beams**

As mentioned earlier, the seven test beams were cast at the same time. For easy reference, the beams are divided into 4 groups as follows one control beam reinforced with only transverse and longitudinal steel; beam type 1, which denotes the two beams with flexural NSM without anchors; beam type 2, which denotes the two beams strengthened with flexural NSM with anchors; and finally beam type 3, which comprises the two beams strengthened with the flexural NSM bars with anchors and with transverse NSM bars with anchors. Each beam type consists of two nominally identical replicate specimens designated as 'a' and 'b'. More details of the test beams are given in the following sections.

#### **3.4.1. Dimensions and Geometry of Beams**

Figure 3.12 shows the typical dimensions of the test beams, with total lengths of 3175 mm and a span length of 2500 mm. The length was selected based on lab space limitations and past test specimens tested by others (Soliman, 2008) to study near surface retrofitted beams. The cross sections of all the beams were 275 x 450 mm. The width of the web was chosen based on the longitudinal steel and CFRP reinforcement spacing requirements. The height of the section was based on the provision of adequate shear capacity.

#### **3.4.2. Design and Detailing**

The test beams were designed in accordance with the CSA Standard A23.3-04 and the NSM reinforcement was designed following current research literature and the ACI 440.2R-02 (ACI, 2002). Although the preliminary design was based on a set of

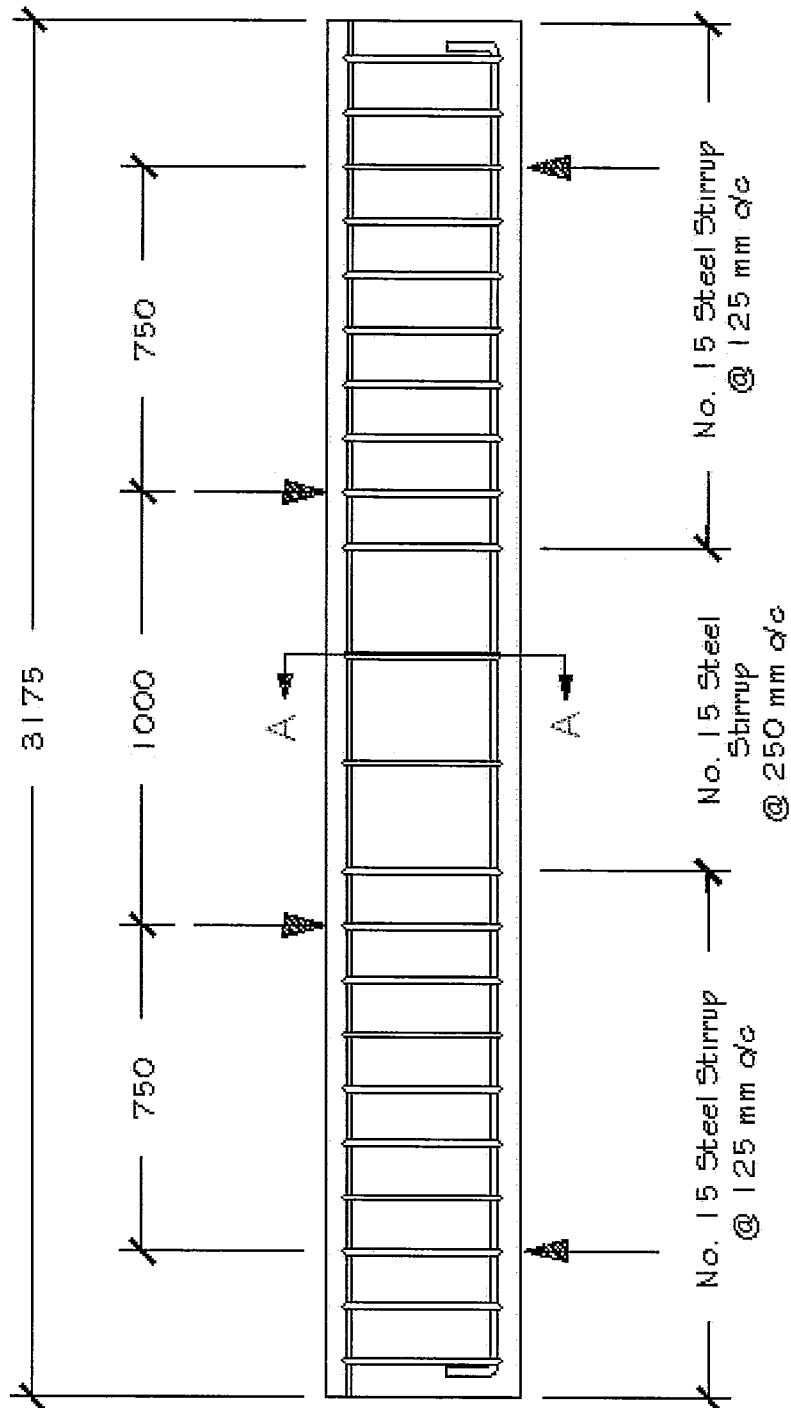
---

assumed material properties, the actual material properties as described in Section 3.3 are summarized in Table 3.4.

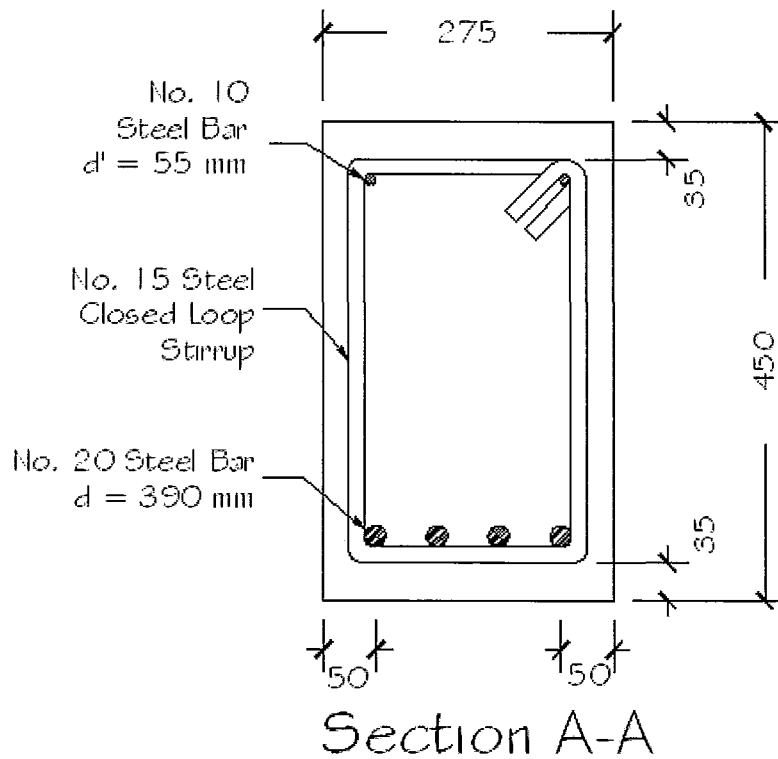
**Table 3.4: Summary of all Material Properties based on Ancillary Tests**

Material	Beam	Property	Magnitude		
Concrete	Control	$f'_c$	MPa	38.6	
		$E_c$	MPa	26009	
		$f_t$	MPa	3.7	
	1a & 1b	$f'_c$	MPa	38.6	
		$E_c$	MPa	26009	
		$f_t$	MPa	3.7	
		2a & 2b	$f'_c$	MPa	40.7
			$E_c$	MPa	26110
			$f_t$	MPa	3.8
	3a & 3b	$f'_c$	MPa	41.9	
		$E_c$	MPa	27605	
		$f_t$	MPa	3.9	
Steel	Longitudinal Reinforcement for all Beams	$f_y$	MPa	481	
		$\epsilon_y$	mm/mm	0.0026	
		$f_u$	MPa	741	
		$\epsilon_u$	mm/mm	0.076	
		$E_s$	MPa	188692	
	Transverse Reinforcement for all Beams	$f_y$	MPa	569	
		$\epsilon_y$	mm/mm	0.0030	
		$f_u$	MPa	793	
		$\epsilon_u$	mm/mm	0.073	
		$E_s$	MPa	187255	
CFRP Reinforcement	All Beams	$f_u$	MPa	1200	
		$\epsilon_u$	mm/mm	0.012	
		$E_f$	MPa	100000	

The beams were designed to fail in flexure and not in shear, therefore, the shear reinforcement was doubled compared to the amount needed to resist the maximum expected shear; which corresponds to the load inducing a moment equal to the moment capacity of the beam. Figure 3.12 through Figure 3.15 illustrate the reinforcement details of all the test beams. Full design calculations are provided in Appendix A.



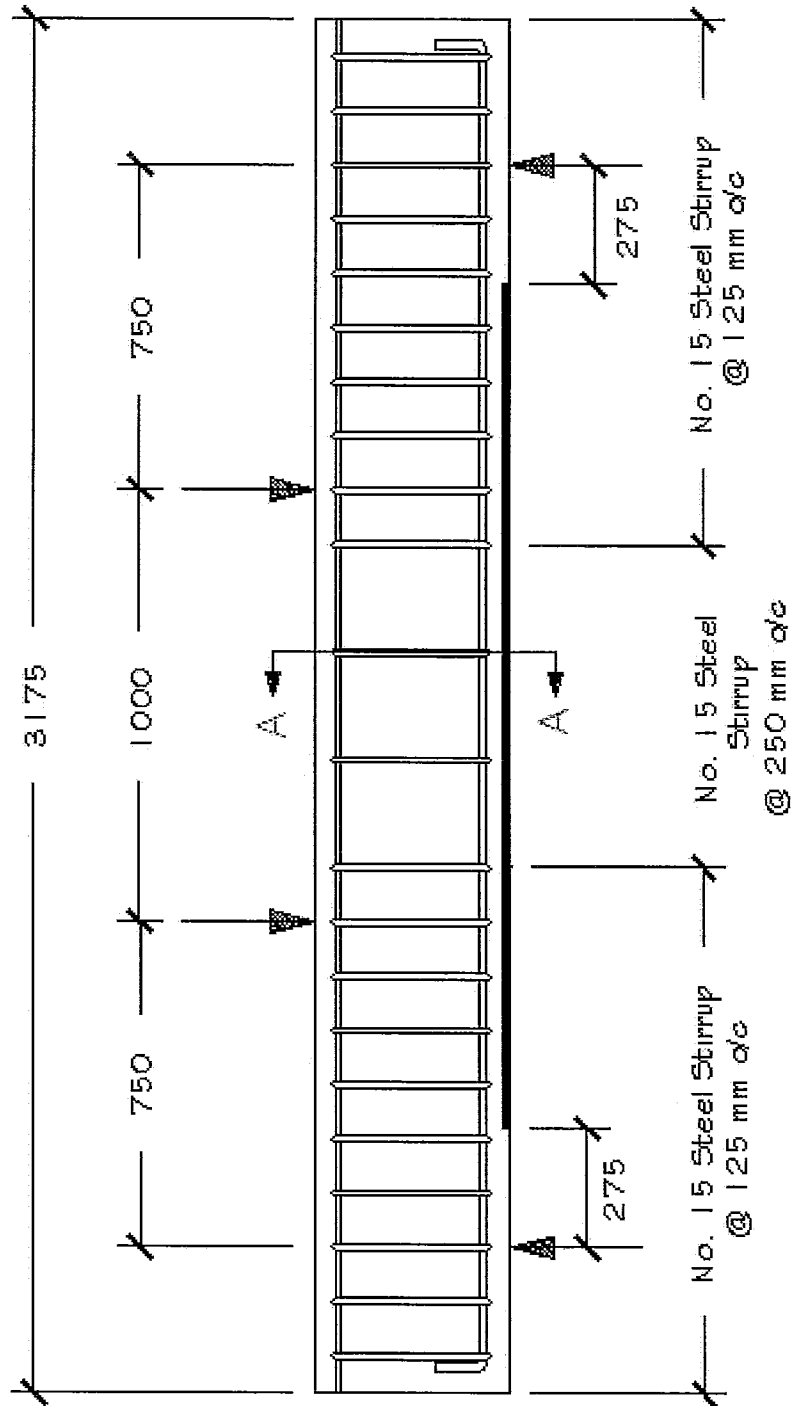
(a)



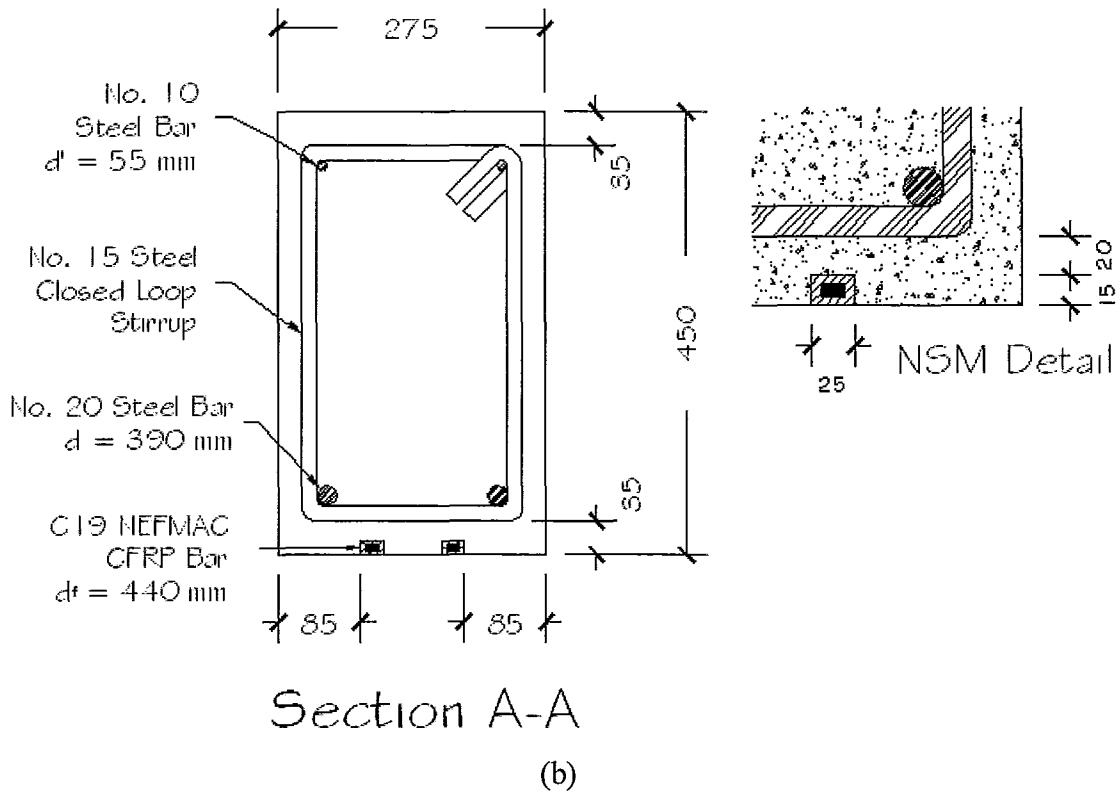
(b)

Note: All dimensions are in mm

**Figure 3.12: Control Beam (a) Profile Details, (b) Cross Sectional Details**

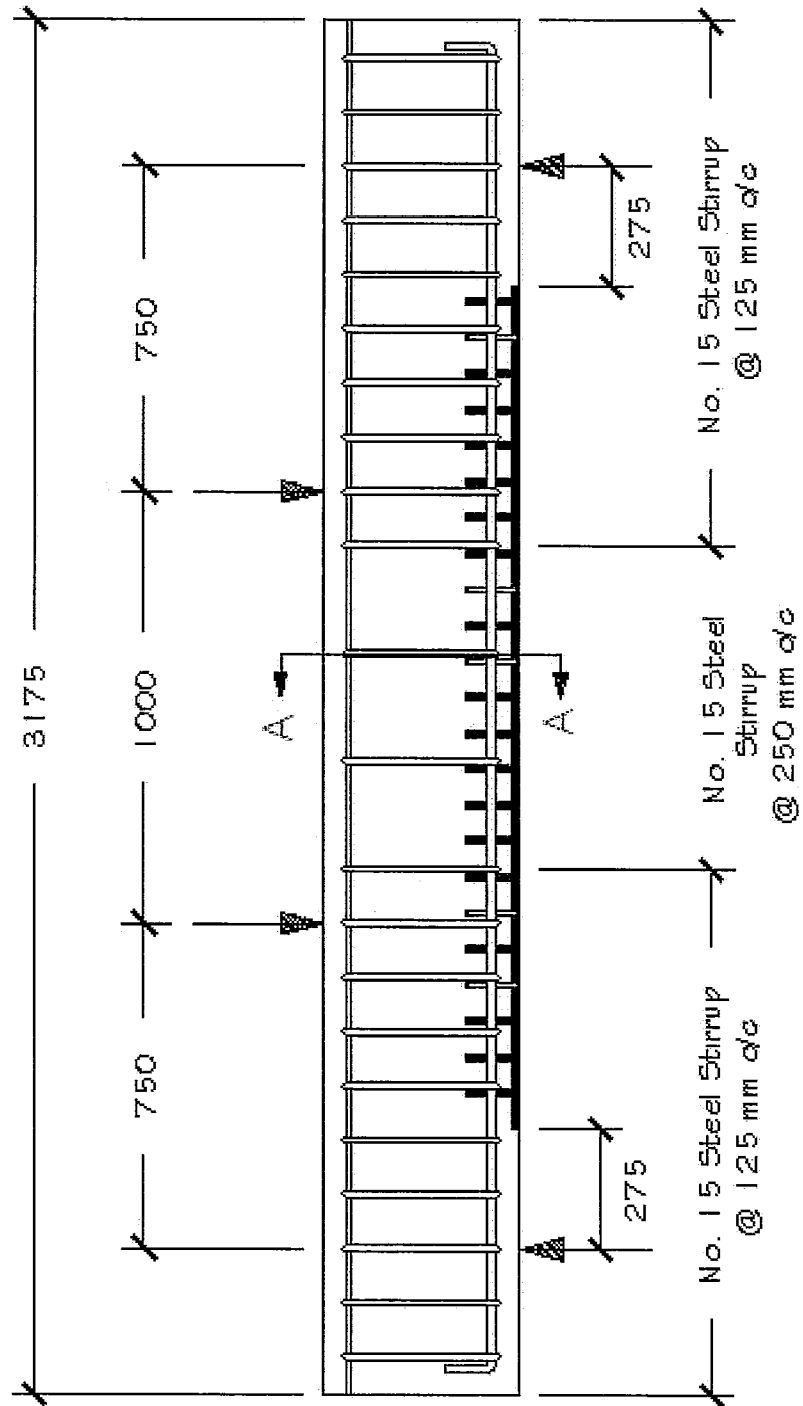


(a)

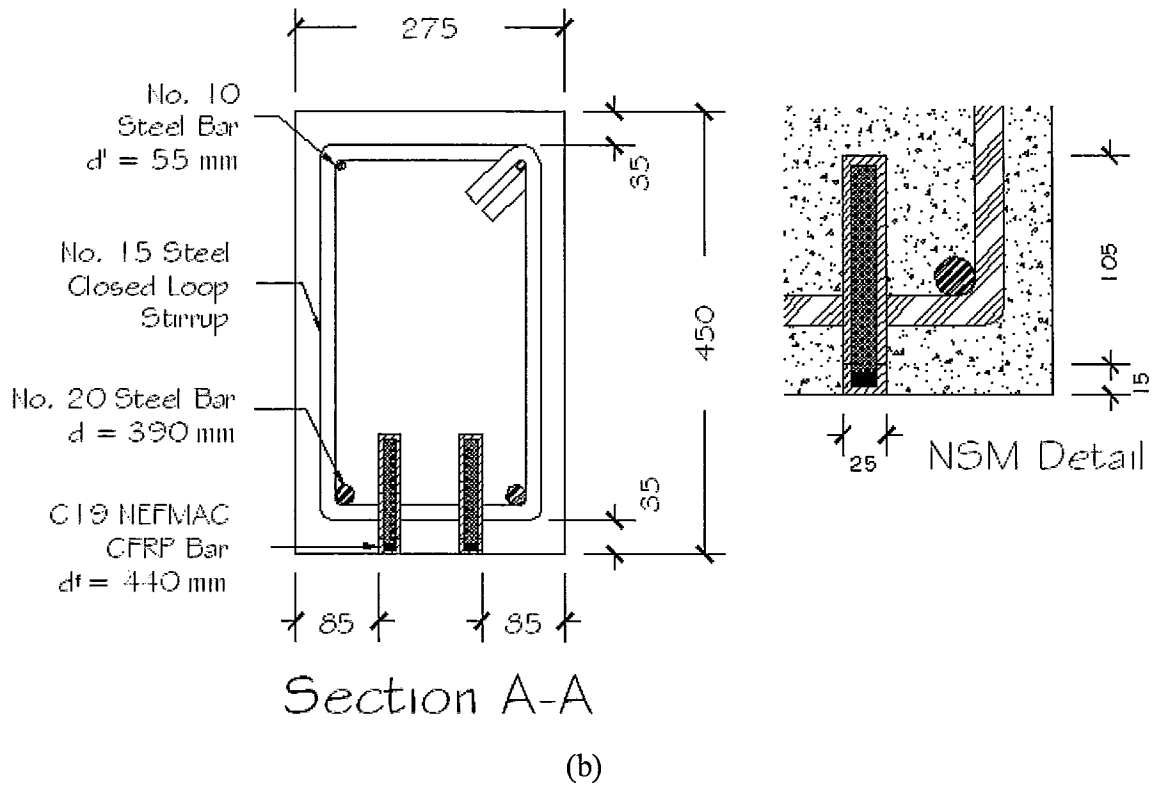


Note: All dimensions are in mm

*Figure 3.13: Type 1a and 1b (a) Profile Details, (b) Cross Sectional Details*

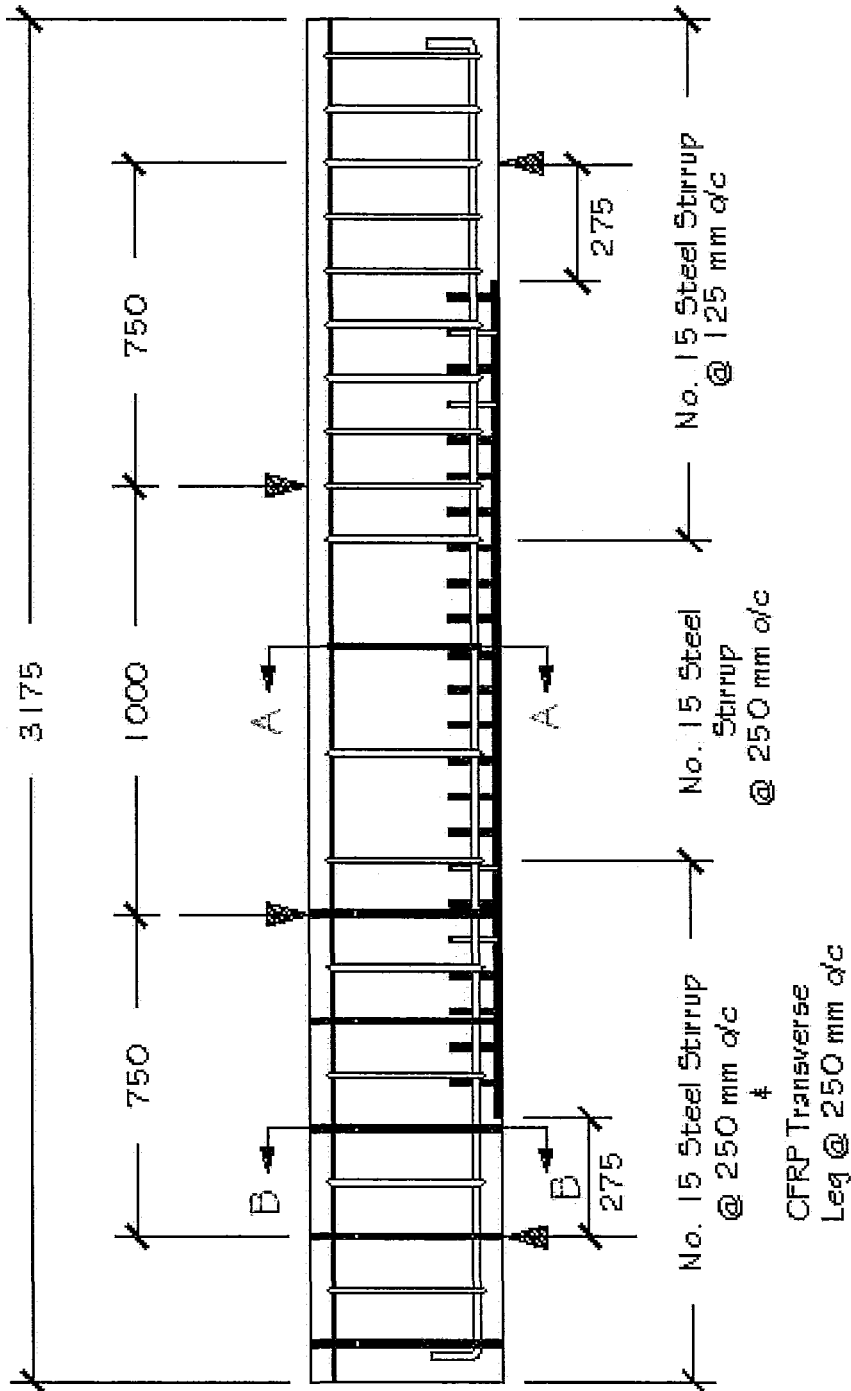


(a)

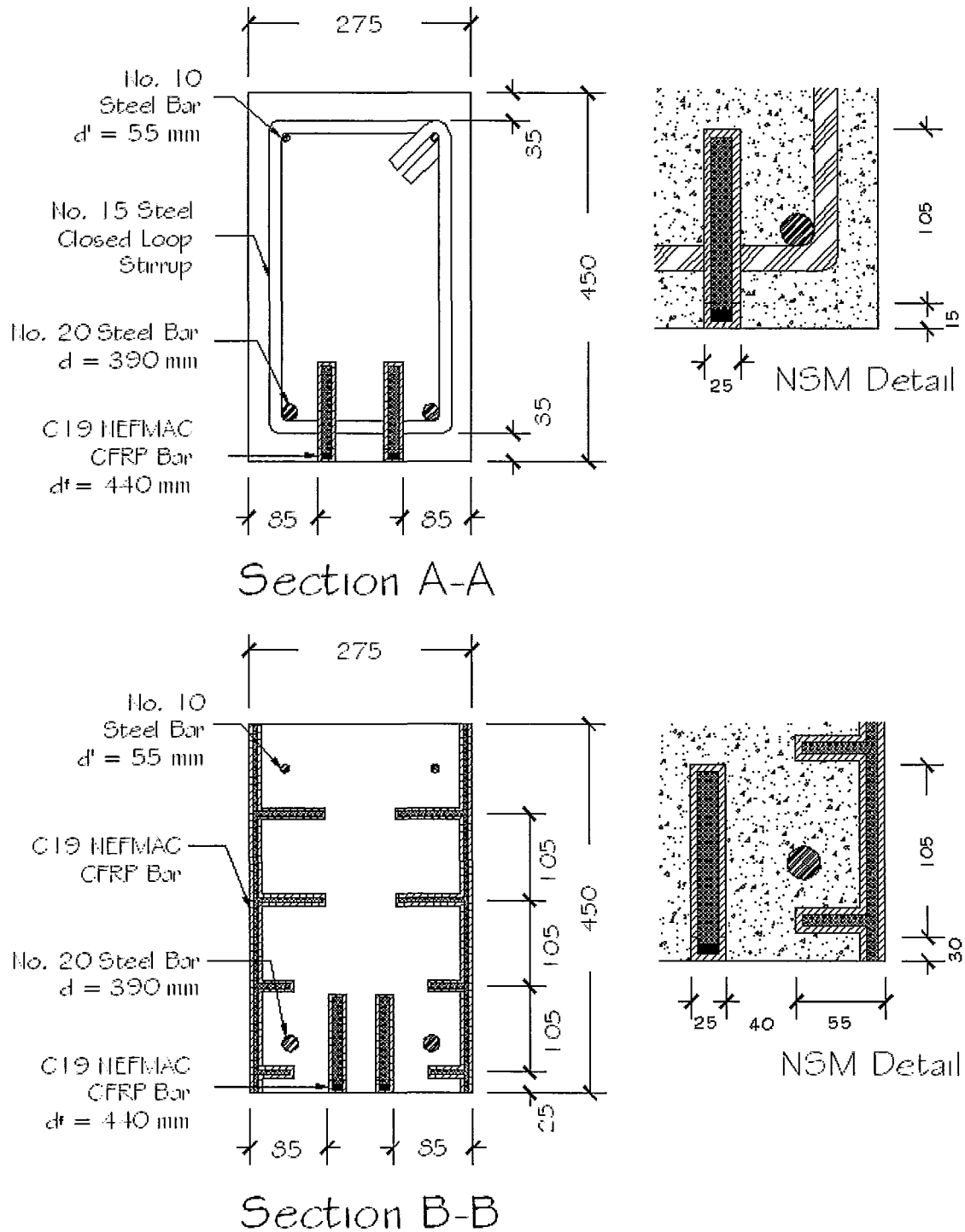


Note: All dimensions are in mm

**Figure 3.14: Type 2a and 2b (a) Profile Details, (b) Cross Sectional Details**



(a)



(b)

Note: All dimensions are in mm

Figure 3.15: Type 3a and 3b (a) Profile Details, (b) Cross Sectional Details

---

### **3.5. Construction of Test Beams**

The construction commenced with the assembling of the plywood forms. Seven forms were built to ensure that all the beams were cast using a single concrete mix and that all the beams were constructed at the same time. Prior to the construction of the reinforcement cages, the steel reinforcement was outfitted with strain gauges at designated locations. The deformed ribs on the steel reinforcement were removed where strain gauges were applied to ensure a smooth surface for attaching the gauge.

After the beams were cast and moist cured for ten days, the forms were removed twenty days after casting the concrete and the beams were air cured following the moist curing period. Using a saw with a diamond blade, grooves were cut along the soffit of the beams that were to be retrofitted with longitudinal NSM bars. Similar grooves were cut along the height of the beams to be retrofitted with the NSM transverse reinforcement. The anchor locations were then marked along the grooves and holes were drilled to the appropriate depth. If the internal shear reinforcement was struck by the concrete drill bit, the NEFMAC anchor was cut to the depth of the concrete cover.

Following the concrete cutting, the groove and the anchor holes were thoroughly cleaned using compressed air. The beams were air-cleaned multiple times to ensure a clean bonding surface. The grooves were then primed according to the manufacturer's specifications. The primer coating was permitted to dry until tack; approximately 12 to 24 hours from the time of application. The two-part epoxy was then mixed in accordance with the manufacturer specifications and half of the total groove volume was filled prior to the placement of the CFRP bars to reduce the likelihood of void spaces between the bar and the groove surface. During the application of both the primer and the two-component epoxy, the beams were oriented upside-down, with the grooves facing upward for ease of construction and to help the epoxy settle. Figure 3.16 through Figure 3.18 chronicle the construction of the NSM grooves and illustrate the process followed to prepare the CFRP strengthened beams.

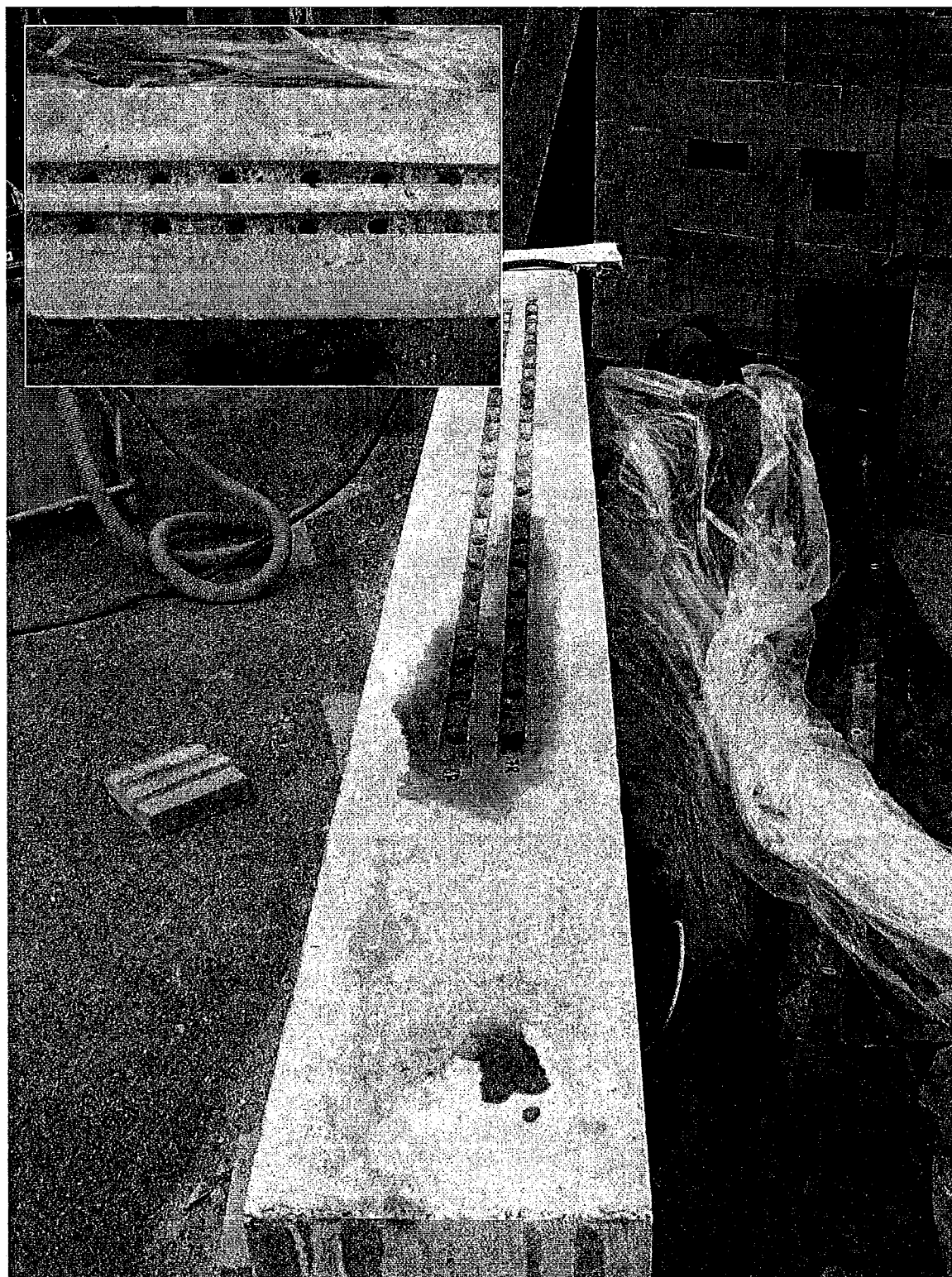


*Figure 3.16: Typical Longitudinal Grooves for Type 2 and 3 Beams*

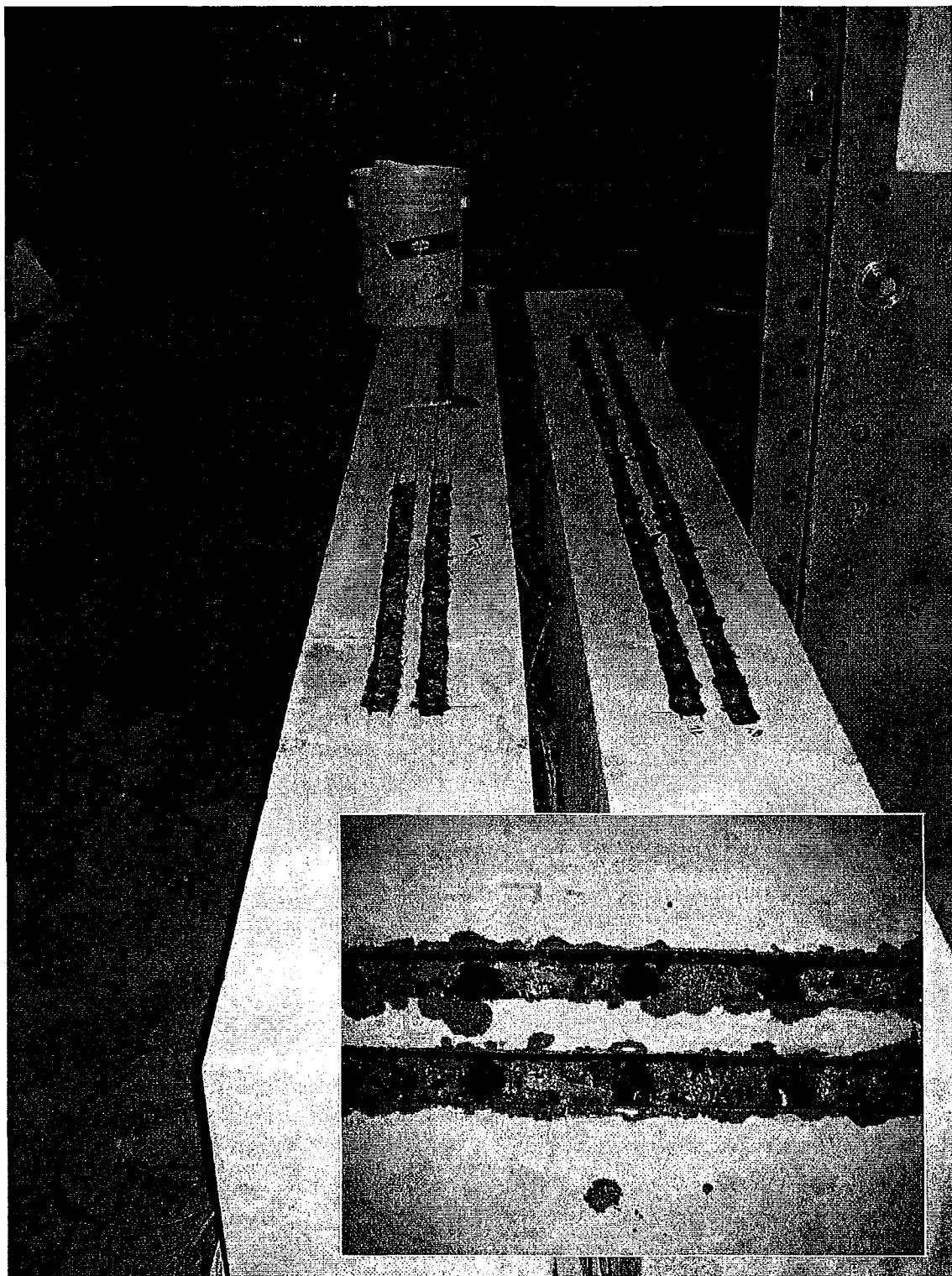


*Figure 3.17: Longitudinal Grooves during Primer Application*

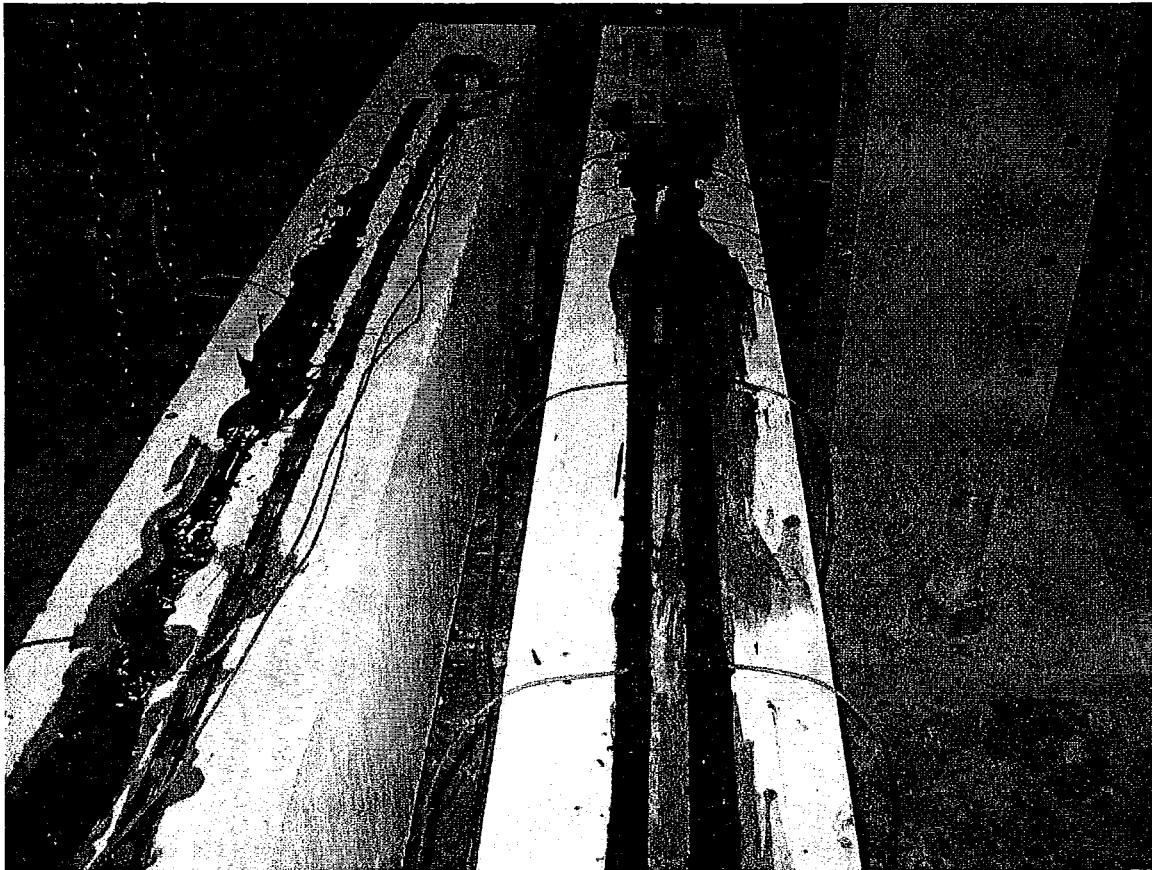


*Figure 3.18: Longitudinal Grooves During Epoxy Application and Final NSM Bars Disposition*

### **3.6. Test Equipment and Instrumentation**

For the internal steel reinforcing bars, strain gauges were attached along one of the primary tensile bars and along both legs of selected stirrups in all the seven beams. A single 5 mm foil strain gauge was applied at each location as shown in Figure 3.19. The five designated locations for the longitudinal tensile reinforcement includes: the mid-length of the reinforcement, at the location of the two point loads and at a distance,  $d = 390$  mm, from each support, where  $d$  is the effective depth of the beam.

In addition to the gauges on the reinforcing steel, gauges were also attached to the primary CFRP longitudinal reinforcement in type 1, type 2 and type 3 beams. The strain

gauges bonded to the CFRP were the same as those attached to the steel reinforcement. As shown in Figure 3.21 through Figure 3.23, the CFRP bars were strain gauged at the mid-length of the bar, at the locations of the point loads and at 200 mm from the bar ends. For Type 3 specimens strengthened with NSM transverse reinforcement, as illustrated in Figure 3.23, strain gauges were attached at the mid-length of each of the bars located at 250 and 500 mm from the closest support. Due to the rough texture of the NEFMAC CFRP bars, the finish was smoothed with sand disk prior to the application of the strain gauges to ensure uniform contact between the applied strain gauge and the CFRP surface.

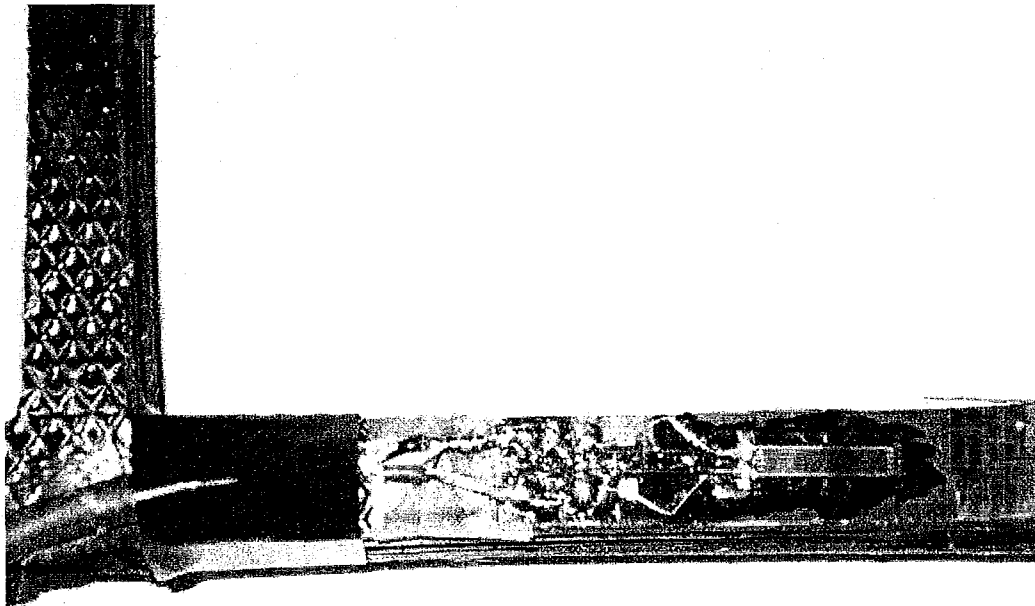


*Figure 3.19: Foil Strain Gauges Installed on CFRP Bar*

Displacements along the length of each beam were measured using string potentiometers placed at five locations under the beam. As Figure 3.24 shows, the locations include: the beam mid-point, under each of the applied loads and at mid-length of each shear span (i.e. 375 mm from each support).

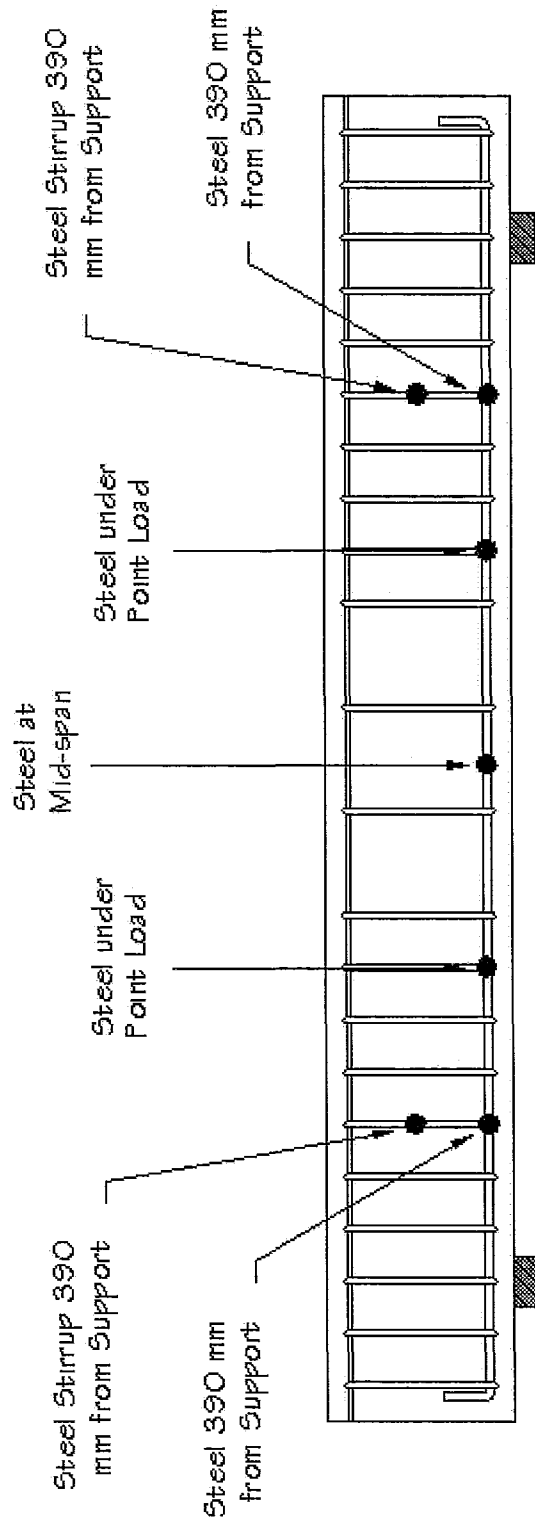


Figure 3.20: Strain Gauge Locations for Control Beam

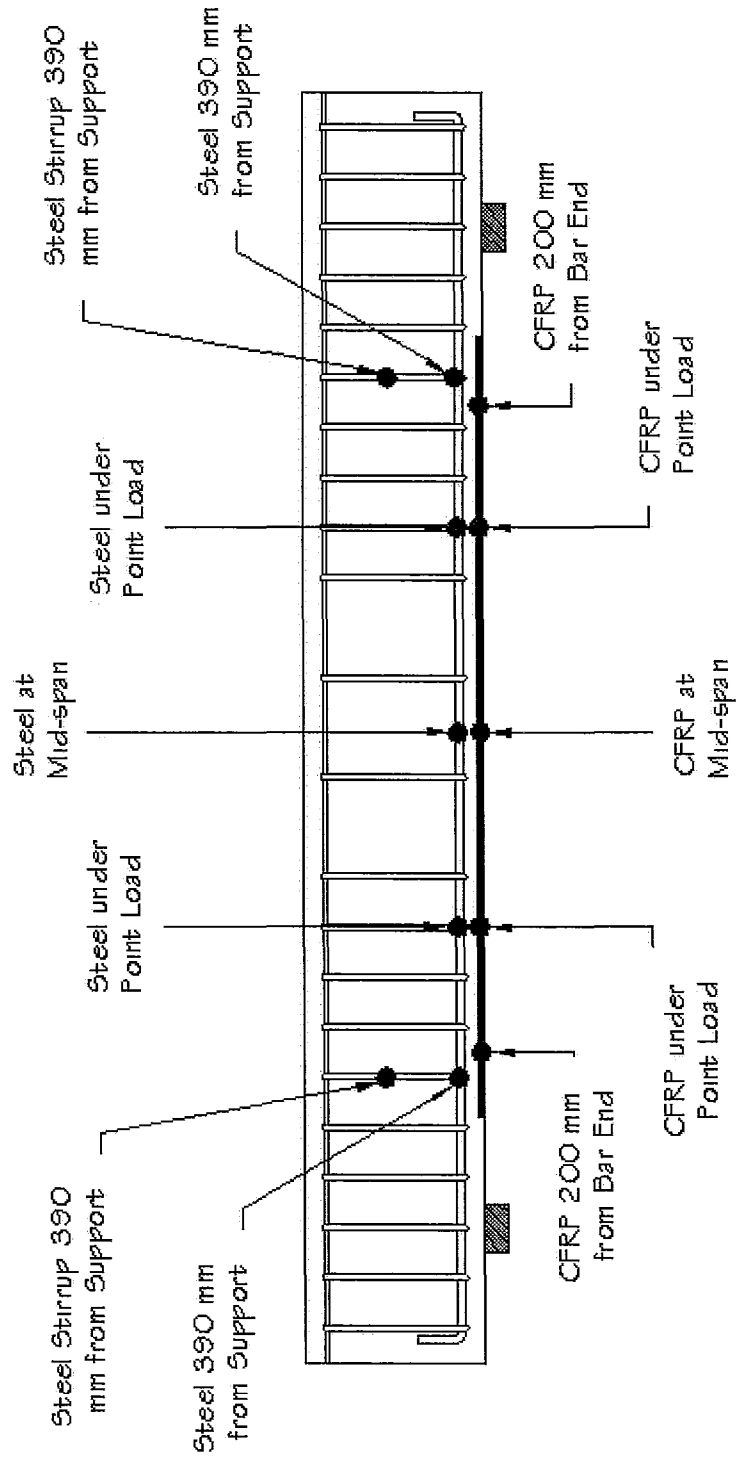


Figure 3.21: Strain Gauge Locations for Type 1 Beams

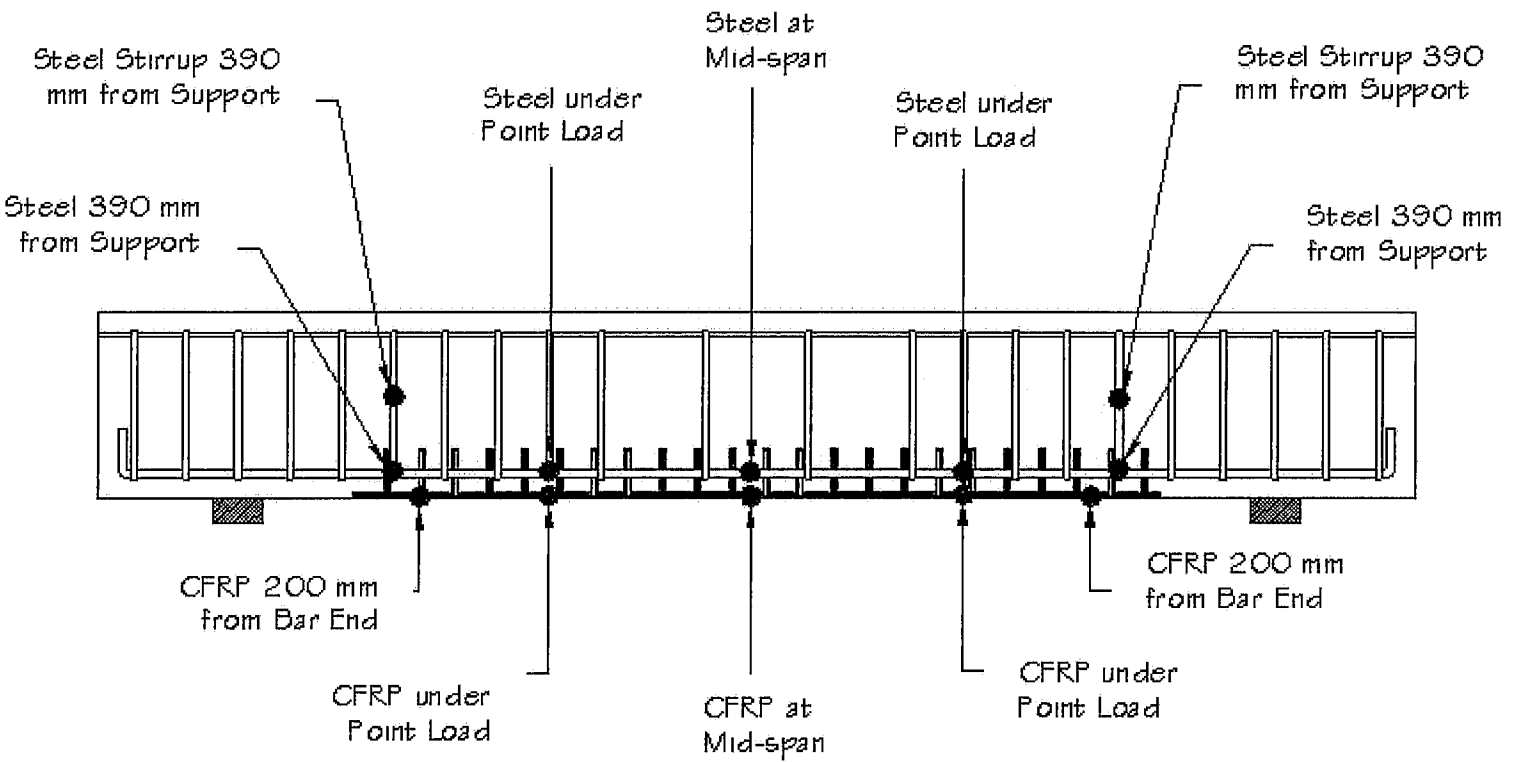


Figure 3.22: Strain Gauge Locations for Type 2 Beams

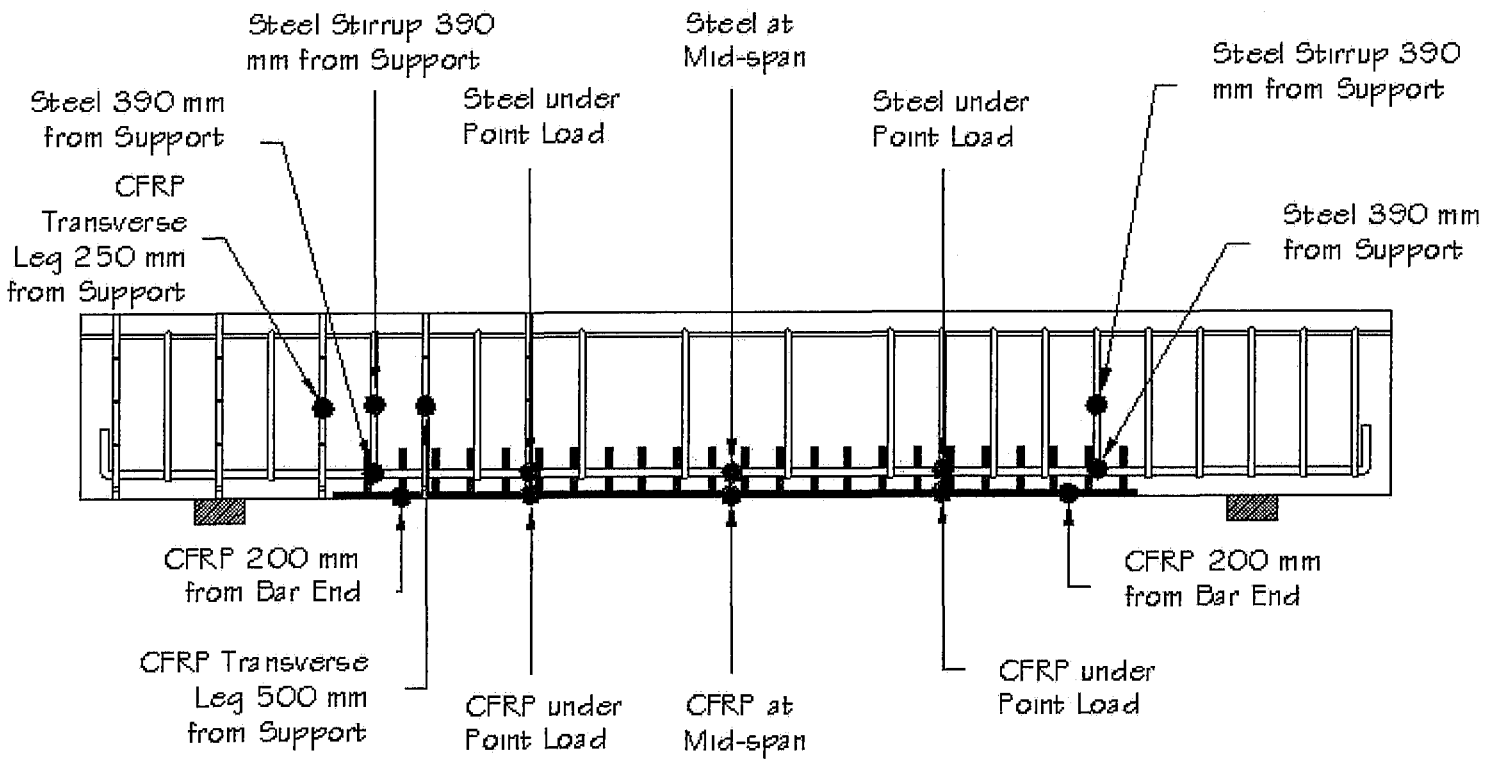
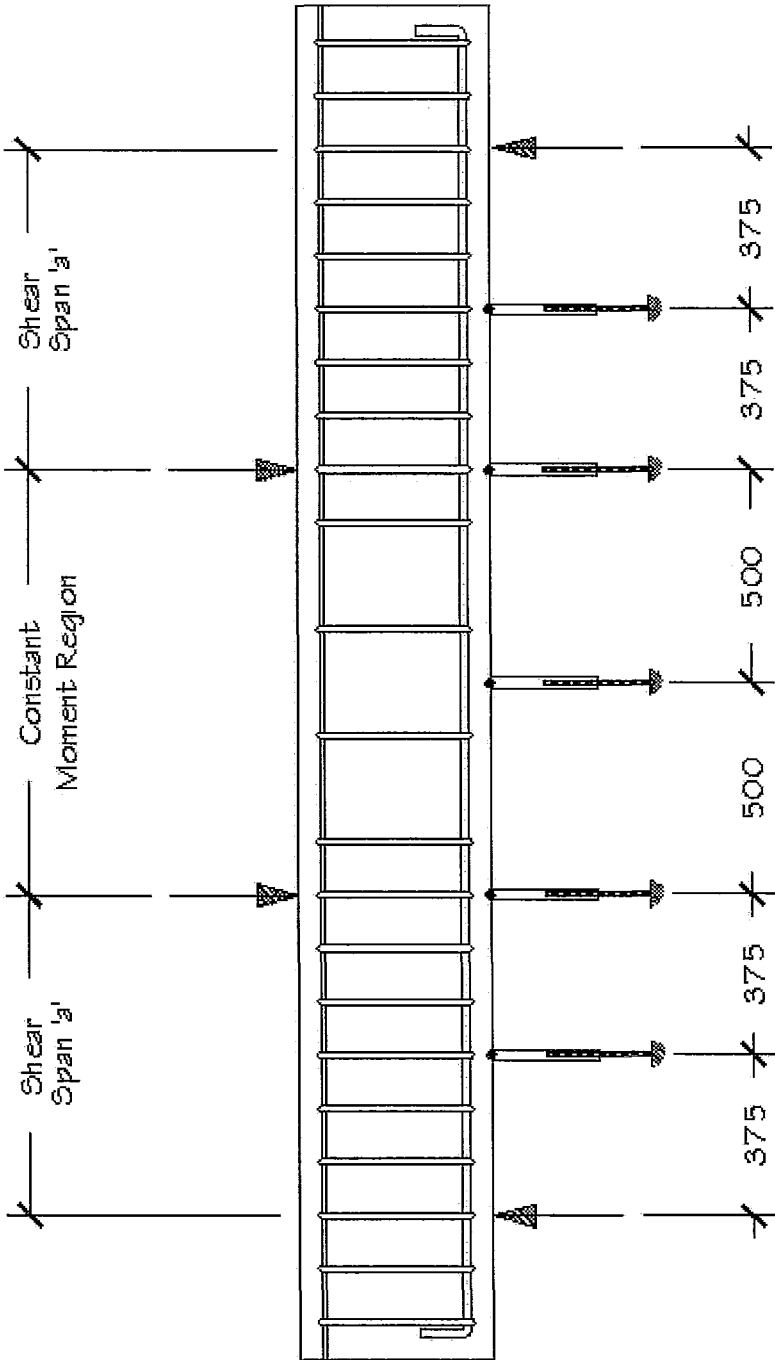


Figure 3.23: Strain Gauge Locations for Type 3 Beams



Note: All dimensions are in mm

Figure 3.24: Typical String Potentiometer Locations for all the Tested Beams

### 3.7. Test Setup

The tests were conducted in McMaster University's Applied Dynamic Laboratory (ADL). The test set-up is illustrated in Figure 3.25 and Figure 3.26. The loading jack was supported by two structural steel support columns and the columns were fastened to the laboratory RC strong floor. The test specimens were supported by steel chairs to permit them to deflect without any obstruction. The beams were loaded with a stiffened structural steel spreader beam which divided the single load from the jack into two equal concentrated loads. The load cell attached to the head of the jack piston or hydraulic cylinder monitored the applied load corresponding to a given downward displacement of the piston.

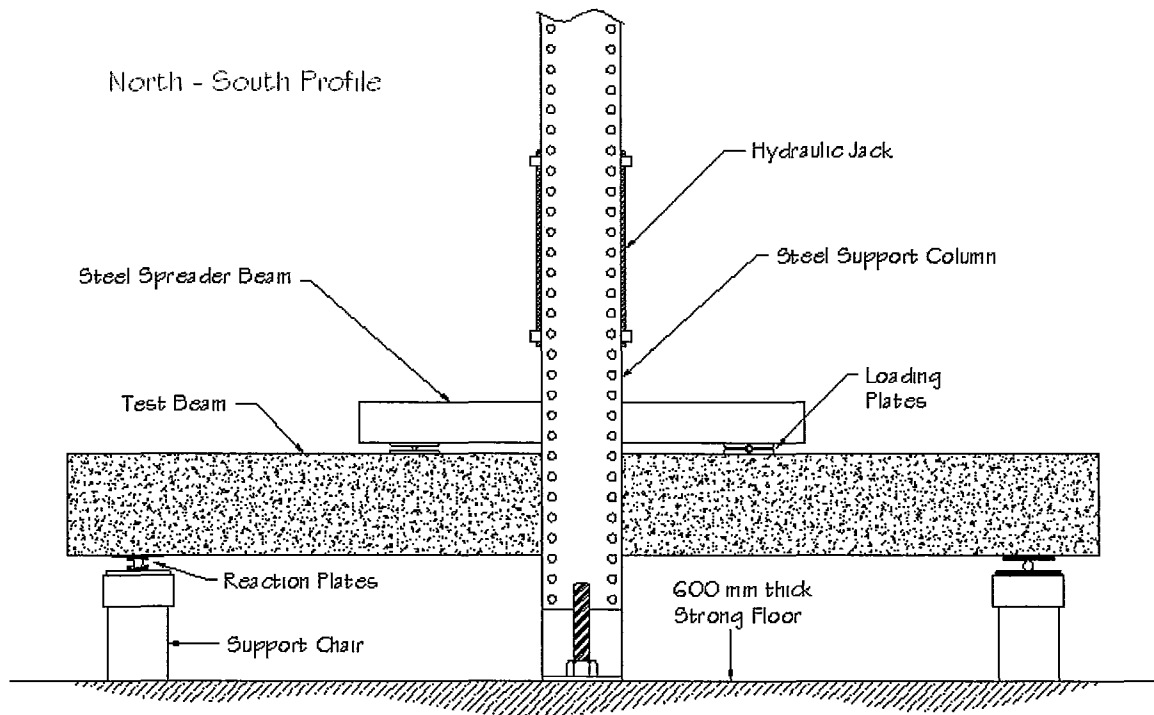


*Figure 3.25: Beams Test Set-up (North-South Profile)*

As discussed earlier, the test was performed using displacement control which permitted the recording of the descending branch of the load-displacement curve. The displacement of the piston head was recorded by the primary string potentiometer shown below and monitored by the system controller. The reaction plates at the beam supports, measured 150 by 275 mm in area while the loading plates, located between the specimen and the spreader beam, measured 190 by 275 mm. For both the reaction and loading plates, the 275 mm dimension was selected to match the cross sectional width of the beams to ensure a uniform loading distribution. The thicknesses of the plates varied according to fixity (pin or roller) of the plates, however the appropriate thicknesses were chosen to ensure that both the test specimen and the spreader beam were level and plumb when tested. The reaction and loading plates were bonded to the concrete with Hydrostone, a lime-based cementitious material, to ensure that the loading plates uniformly transferred the applied loads to the test specimen.

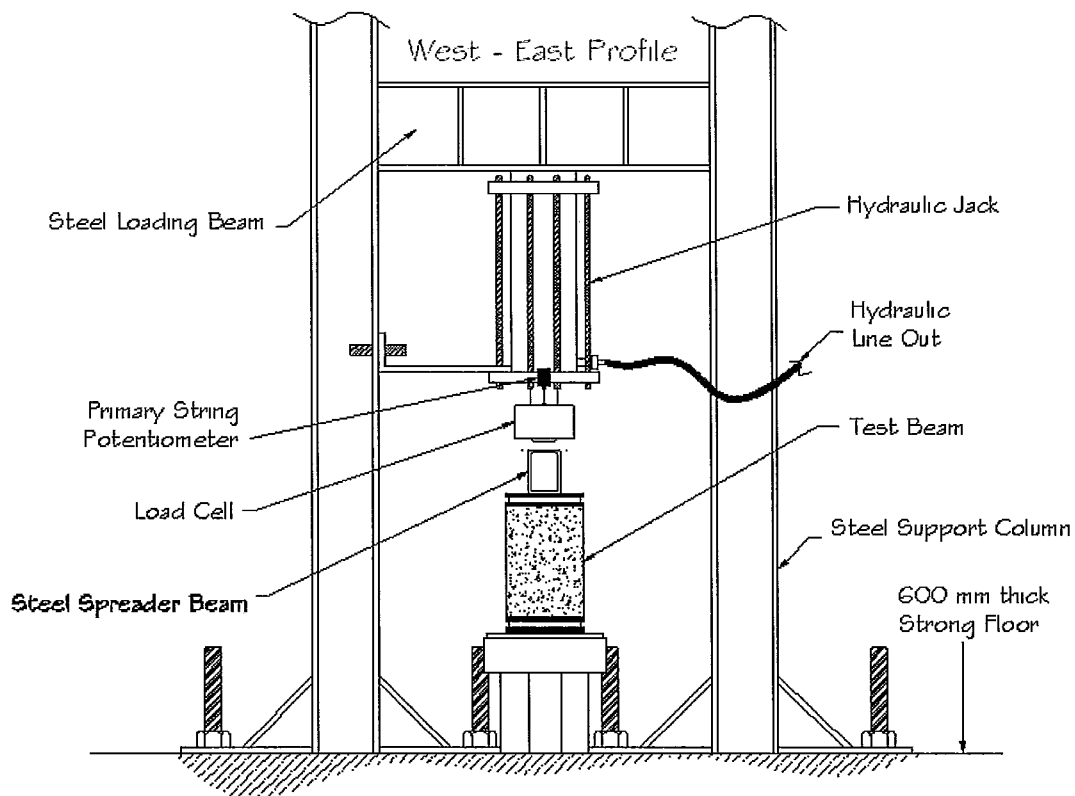


Figure 3.26: Beams Test Set-up (West-East Profile)

---

### **3.8. Loading and Data Acquisition**

To capture the descending branch of the load-displacement curve, the load was applied through displacement control. The rate of loading was set to 0.02 mm/sec for all seven tests and was controlled by a system controller which monitored the primary string potentiometer for the beam deflection. All data was collected using an automatic data acquisition and data was recorded in 2 second intervals during the first test but was later adjusted to 5 second intervals due to the excessive amount of data collected in the shorter interval. The data from all strain gauges, string potentiometers and the load cell were stored within a PC computer and subsequently exported to a MS Excel spreadsheet for analysis.

# Chapter 4

## Experimental Results

### **4.1. General**

The test beams were instrumented to carefully monitor their behaviour and deformations throughout the test. The strains along the tensile reinforcing steel, the NSM longitudinal reinforcement, the steel stirrups and the transverse NSM reinforcement were recorded by means of an automatic data acquisition system. In addition to the recorded strains, displacements along each beam were measured by means of string potentiometers to capture the beam deflected shape at various loading stages.

In this chapter the observed behaviour of the beams will be described with the aid of the collected data. The results in this chapter include: load-midspan displacement curves, the beam deflected shapes and strain variations at designated gauge locations along the reinforcement. As mentioned in the previous chapter, each strengthened beam had a duplicate beam tested to ensure repeatability of the recorded data; therefore, the results for the duplicate beams will be discussed concurrently.

### **4.2. Control Beam**

The control beam was designed to act as a reference for assessing the performance of the other test beams. It was designed to be under-reinforced with

reinforcement ratio of  $0.30\rho_b$ , where  $\rho_b$  is the balanced reinforcement ratio, and it was the first of the seven beams tested. The control beam was designed to have a similar moment capacity as the strengthened beams assuming full bond between the NSM bars and the concrete.

The test commenced by applying a monotonic displacement at a rate of 0.02 mm/sec. The first flexural cracks were noted near the midspan at a load of 91 kN, while the first shear crack appeared as an extension of an existing flexural crack in the western shear span at a load of 199 kN, as shown in Figure 4.1. Further increase of the load caused more flexural and shear cracks to develop while existing cracks widened. Within the load range of 570 to 585 kN, the concrete within the constant moment region appeared to experience crushing, but the beam reached a maximum load,  $P_{max}$ , of 595 kN.

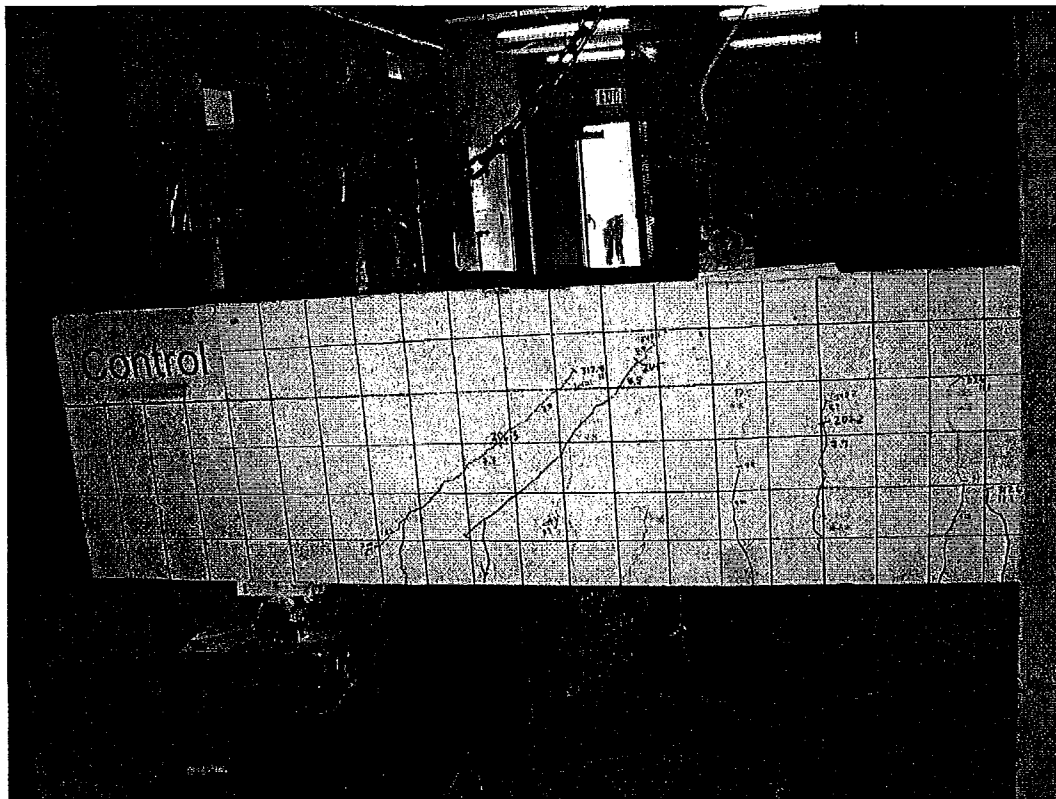


*Figure 4.1 Typical Crack Pattern along the Eastern Shear Span of the Control Beam at 50% of Maximum Load*

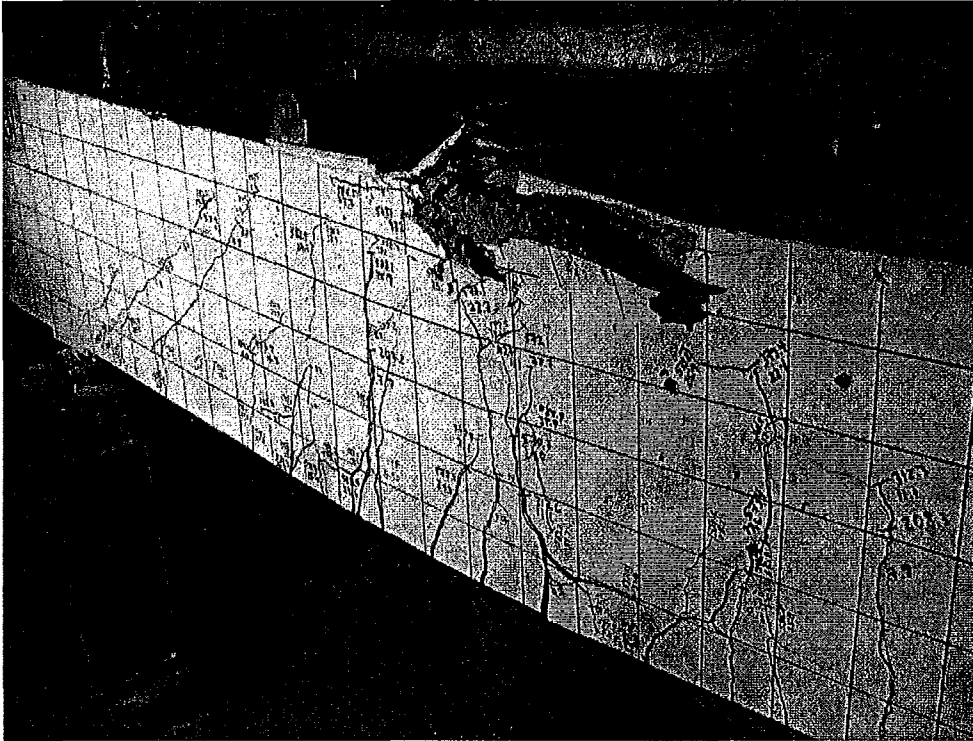


*Figure 4.2: Concrete Crushing in Constant Moment Region of the Control Beam*



*Figure 4.3: Buckled Compression Steel at Failure of the Control Beam*

The specimen eventually failed after the compression reinforcing bars buckled within the constant moment region, causing the surrounding concrete to separate from the lower part of the section. Figure 4.1, Figure 4.2 and Figure 4.3, respectively, show the typical crack pattern observed at 50%  $P_{max}$ , immediately after the peak load and at the eventual failure of the beam, manifested by the compression steel reinforcement buckling and the separation of the top concrete cover.

To gain deeper insight into the behaviour of this beam, its load-midspan deflection curve is plotted in Figure 4.4. The figure reveals ductile behavior and a maximum load of 596 kN which corresponds to an ultimate moment,  $M_u$ , of 224 kN·m. The maximum load was reached at a midspan deflection of 61 mm.

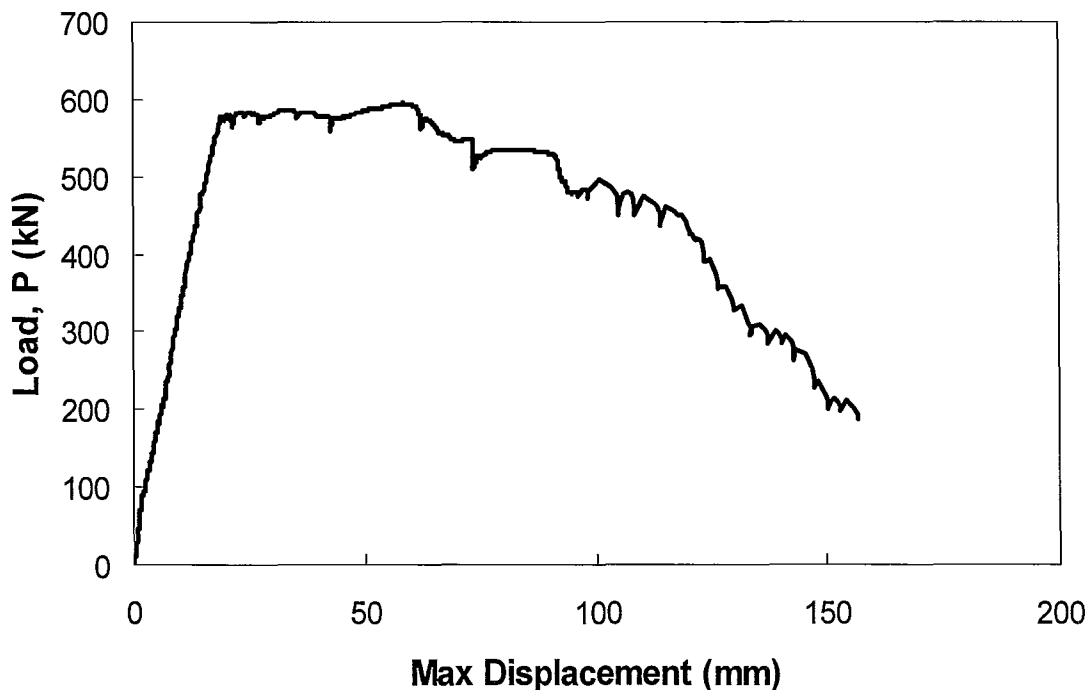


*Figure 4.4: Control Beam Load-Midspan Displacement*

Using the assumed steel and concrete properties, based on the uniform compressive stress rectangular block concept, the theoretical capacity of the control beam was calculated to be 192 kN·m. The theoretical capacity is lower than the observed

strength because the effects of strain hardening are ignored in the theoretical calculation and the actual yield strength of the reinforcement is significantly higher than the assumed value of 400 MPa. When the moment capacity is calculated based on the usual assumptions stipulated in the CSA Standard A23.3-04, the steel is considered elastic up to its yield strength and perfectly-plastic thereafter up to its rupture strain, but as reported in Chapter 3 (see page 32), the reinforcing steel used in the current test beams did not have a distinct yield plateau and had much higher strength than 400 MPa.

The deflected shape of the beam at various load levels is plotted in Figure 4.5. Deflection curves are shown for load levels corresponding to 20%, 40%, 60%, 80% and 100% of  $P_{max}$ . The figure generally exhibits symmetry about the beam midspan, indicating that the load was acting centrally and the two halves deformed practically the same.

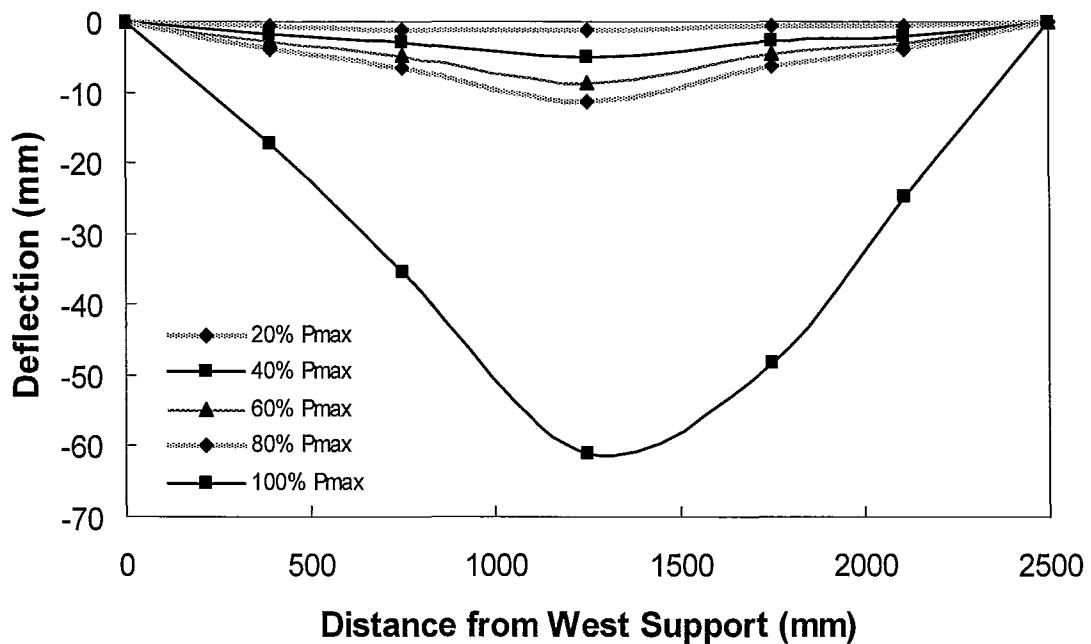
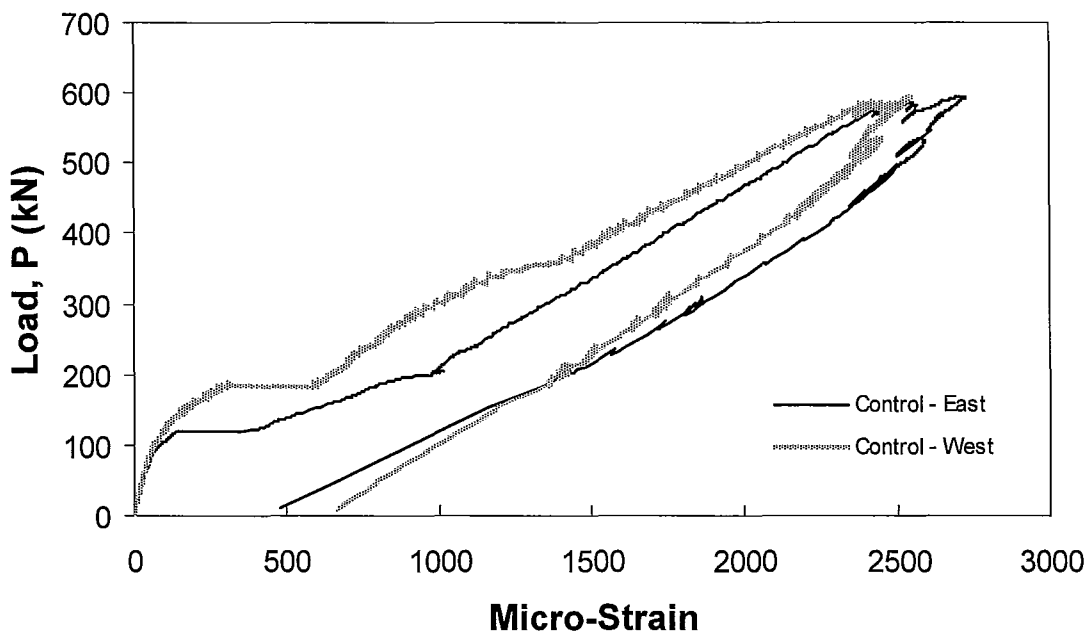


Figure 4.5: Control Beam Deflection

In addition to deflection, the strain variation in the reinforcement was monitored at designated locations along the beam. Figure 4.6 and Figure 4.7 present the recorded flexural steel strain variations 390 mm from each support and within the constant moment region, while Figure 4.8 illustrates the strain variations of the stirrups located 390 mm from each support. Figure 4.7 indicates that the steel at all three locations within the constant moment region reached its yield strength at 3000 micro-strain and then behaved plastically until beam failure. It is interesting to observe that the load-strain curves are exhibiting typical elasto-plastic response without strain hardening while the bare bar tensile coupon tests showed a more non-linear behaviour without a distinct yield point or yield plateau. This discrepancy is puzzling and casts a shadow on the accuracy



*Figure 4.6: Control Beam Longitudinal Steel Bar Strain 390 mm from Supports*

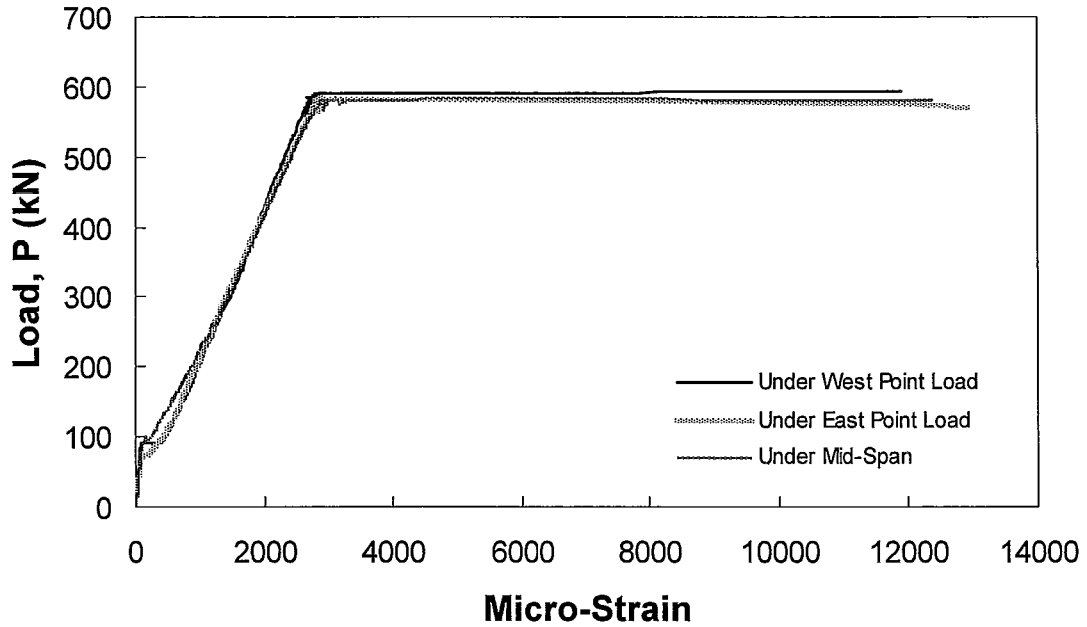


Figure 4.7: Control Beam Longitudinal Steel Bar Strain within Max. Moment Region

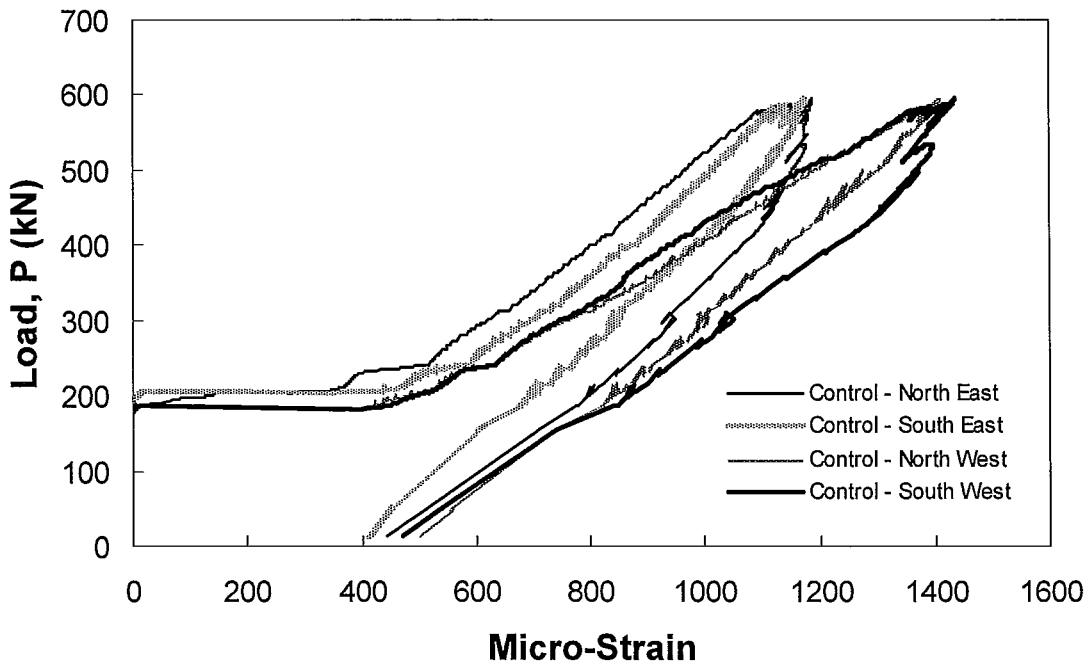


Figure 4.8: Control Beam Steel Stirrup Strain 390 mm from Supports

---

of the results obtained from the steel coupon tests. Figure 4.6 and Figure 4.8 indicate that neither the longitudinal nor the transverse steel at 390 mm from the supports yield and the strain values from the two symmetric locations in the east and west halves of the beam are in good agreement. Similarly, the recorded strains of the two legs of each stirrup are generally very close to each other. The stirrups reached a maximum strain of 1200 to 1450 micro-strain, which is well below their yield strength. It may be recalled that these beams were designed to have shear strength twice their moment capacity; therefore, the observed strain values are not unexpected.

### **4.3. Type 1 Beams**

Each Type 1 beam was strengthened with two NSM CFRP bars evenly spaced along the bottom of each beam. The beams had 50% less tensile steel reinforcement compared to the control beam and were designed to be under-reinforced. As mentioned earlier, the remaining 50% of the tensile steel and the additional NSM bars will yield a cross sectional moment capacity similar to the control beam, assuming full bond between the NSM bars and the concrete. Like the control specimen, type 1 beams were subjected to 4-point bending using displacement control.

The tests commenced by applying a monotonic displacement at a rate of 0.02 mm/sec. The first flexural cracks were noted near the midspan at load levels of 100 kN and 101 kN for beam 1a and 1b, respectively. The first shear cracks appeared as an extension of an existing flexural crack in both beams. In Beam 1a it appeared in the eastern shear span at a load 167 kN and in beam 1b in the western shear span at a load of 159 kN. Further increase of the load caused more flexural and shear cracks to develop while existing cracks widened. Both beams experienced premature NSM reinforcement delamination before the theoretical moment capacity of either beam could be reached. In both cases the reinforcement began to delaminate near the NSM bar ends at loads of 341 kN and 399 kN for beams 1a and 1b, respectively. Their corresponding ultimate moment capacities,  $M_u$ , were 153 kN·m and 150 kN·m. Although beam 1a began to delaminate at

---

a smaller load than 1b, both achieved similar ultimate capacity. Figure 4.9 and Figure 4.10 show that in both beams delamination initiated near the bar ends and continued to propagate toward the beam centre. In Figure 4.11 and Figure 4.12 the hardened epoxy in both cases remains attached to concrete and the NSM bars show no signs of damage upon visual inspection. Figure 4.13 and Figure 4.14 present the extent of the reinforcement delamination at failure. In both cases the NSM bars and most of the concrete cover separated from the beam, exposing the tensile steel reinforcement.

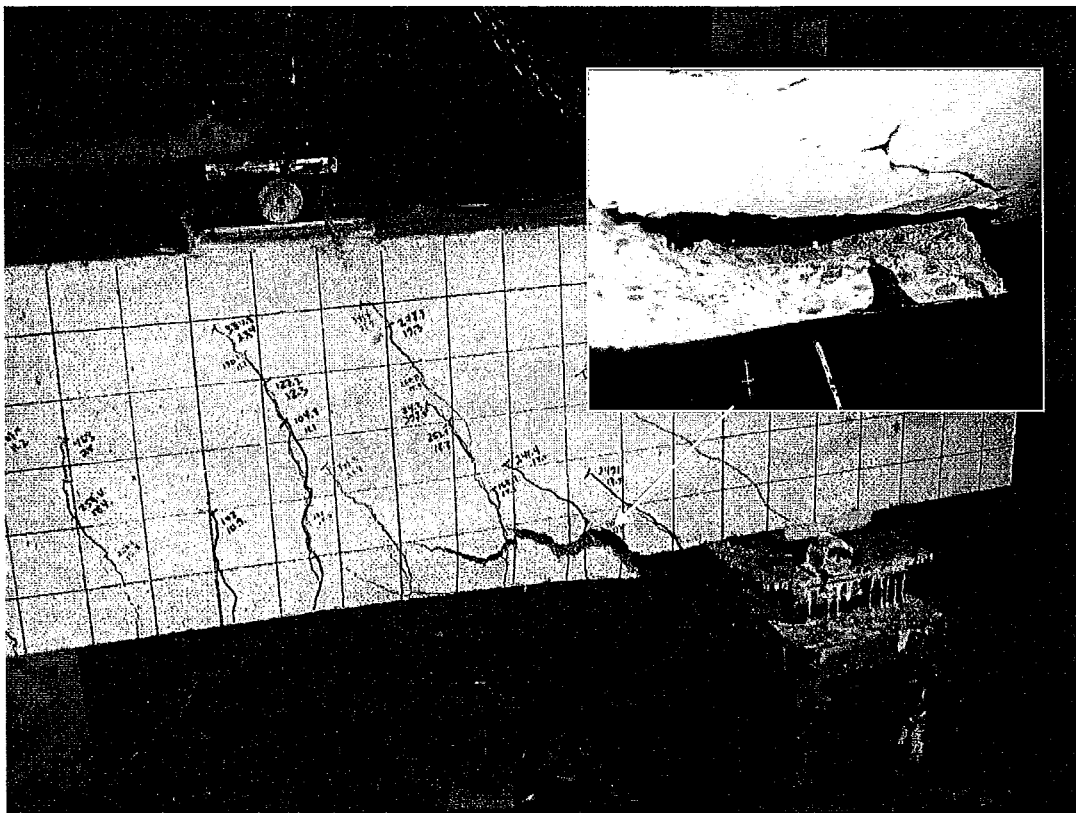


*Figure 4.9: Reinforcement Delamination Initiation for Beam 1a*

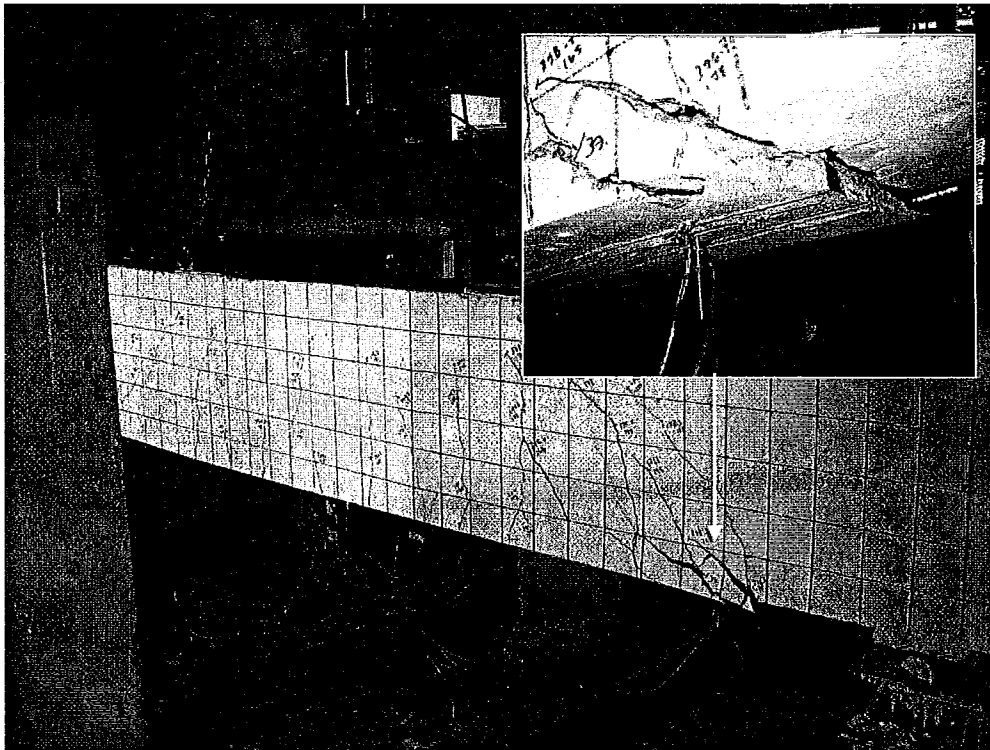


*Figure 4.10: Reinforcement Delamination Initiation for Beam 1b*

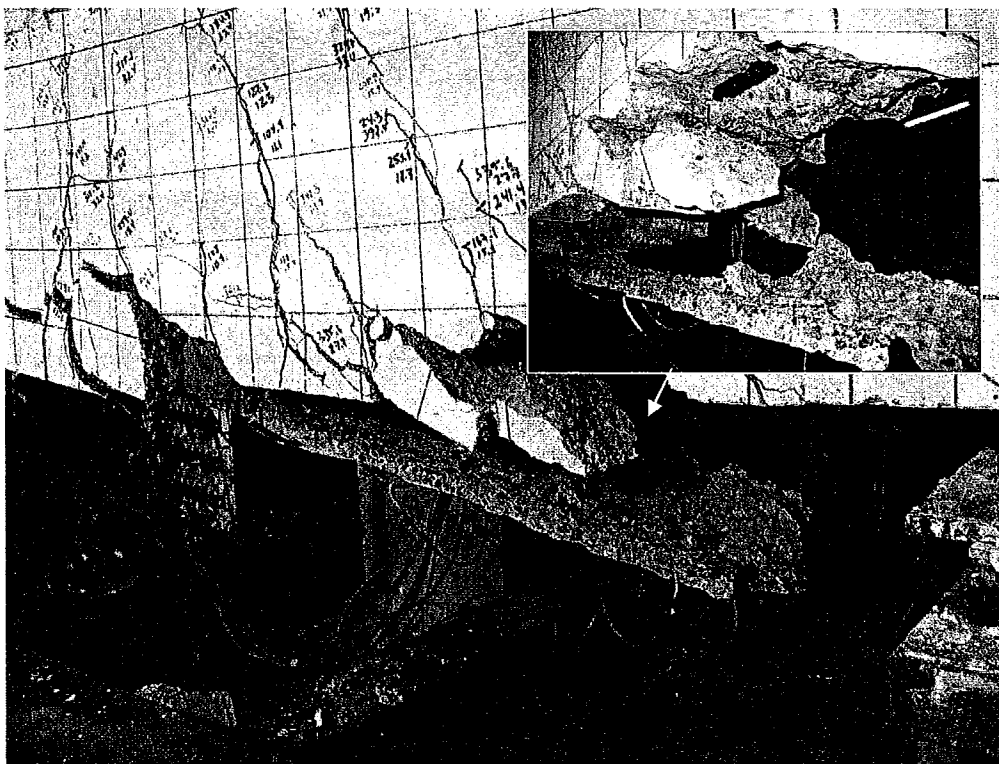


*Figure 4.11: Delaminated Reinforcement for Beam 1a*

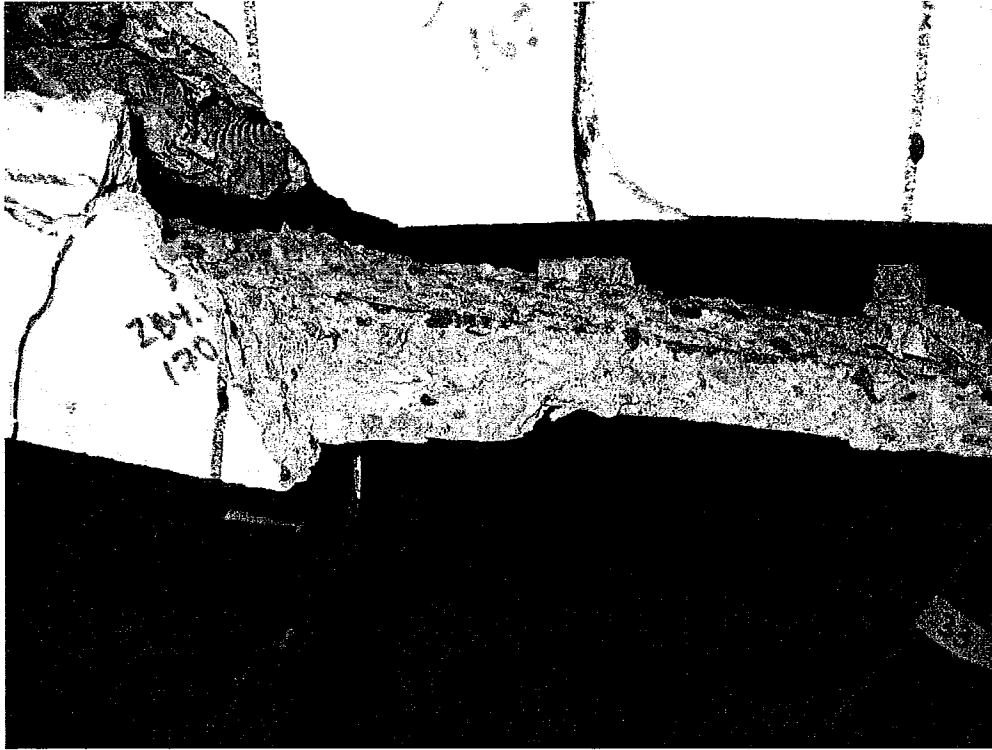


*Figure 4.12: Delaminated Reinforcement for Beam 1b*



*Figure 4.13: Delaminated Reinforcement for Beam 1a at Failure*

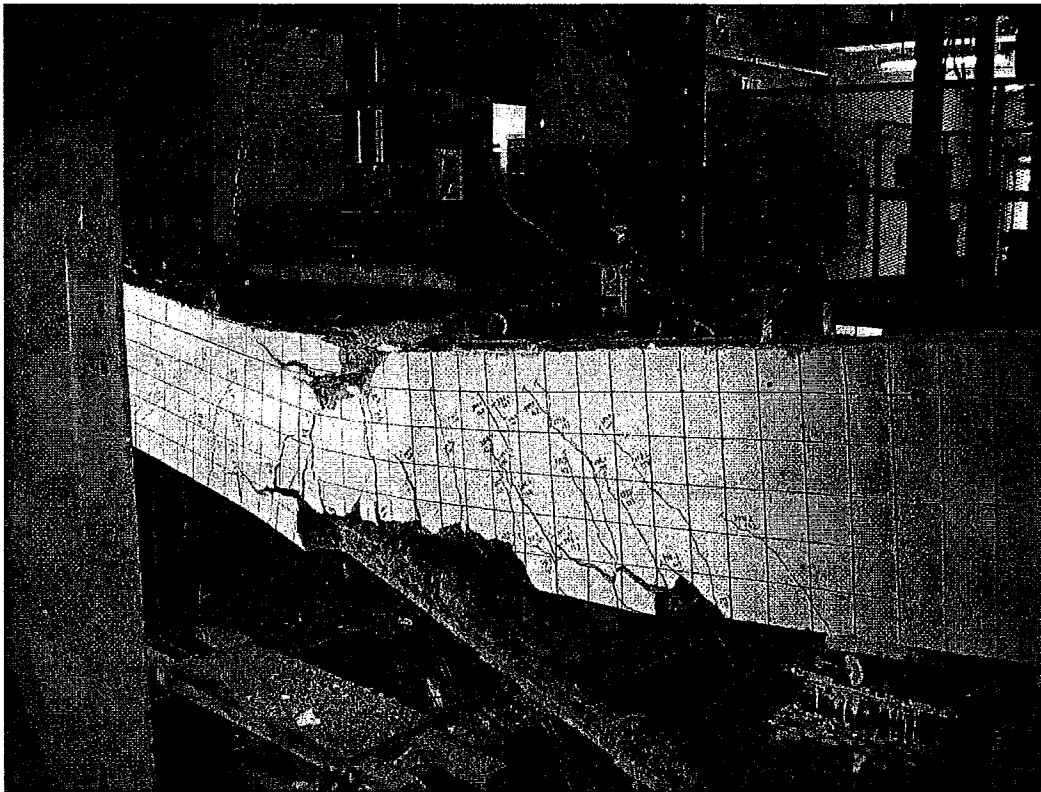


**Figure 4.14: Delaminated Reinforcement for Beam 1b at Failure**

To further examine the behaviour of these beams, their load-deflection curves are plotted in Figure 4.15 and both show good agreement with one another. The figures reveal a sharp decline in strength after the maximum load,  $P_{\max}$ , of 408 kN and 399 kN, which correspond to ultimate moments,  $M_u$ , of 153 kN·m and 150 kN·m, respectively. The maximum loads correspond to midspan displacements of 18 and 17 mm for beams 1a and 1b, respectively. The theoretical moment capacity of the type 1 beams was calculated to be 259 kN·m. The theoretical capacity is greater than the corresponding experimental values because the theoretical calculations assume no delamination and the NSM bars are assumed to be fully bonded up to failure.

The deflected shapes of the two beams are presented in Figure 4.16 and Figure 4.17. Deflection curves are shown for load levels corresponding to 20%, 40%, 60%, 80% and 100% of  $P_{\max}$ . The figures exhibit good symmetry indicating that the load was placed centrally and the observed response is characteristic of the beam behaviour. Note

the difference between the shapes of beam 1a and beam 1b, the former exhibits a smooth shape that is characteristic of a beam that has practically uniform flexural rigidity, while the latter shows a shape that is typical of a beam with variable flexural rigidity. According to Figure 4.17, the central portion of the beam within the constant moment region experienced significantly higher deflections relative to the corresponding region in Figure 4.16. The larger deflections can be attributed to more extensive cracking in the constant moment region of beam 1b.

The strain variation was monitored at designated locations along the main flexural resisting steel, the NSM CFRP bars and the internal stirrups as described in the previous chapter. Figure 4.18 illustrates the strain variation with the applied load in the main flexural steel reinforcement at 390 mm from the supports in beams 1a and 1b. The indicated location is approximately at the middle of the shear span. Notice that except for the steel on the west side of beam 1a, the maximum strain values at all other locations indicates that the steel has either yielded or is on the verge of yielding. This observation

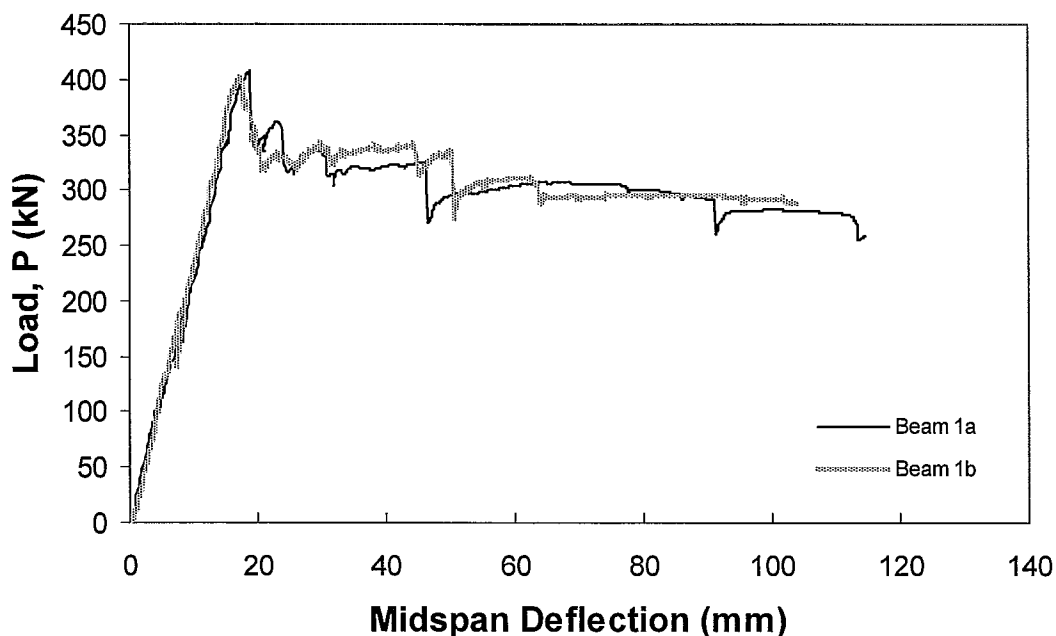


Figure 4.15: TYPE 1 Beams Load-Midspan Displacement

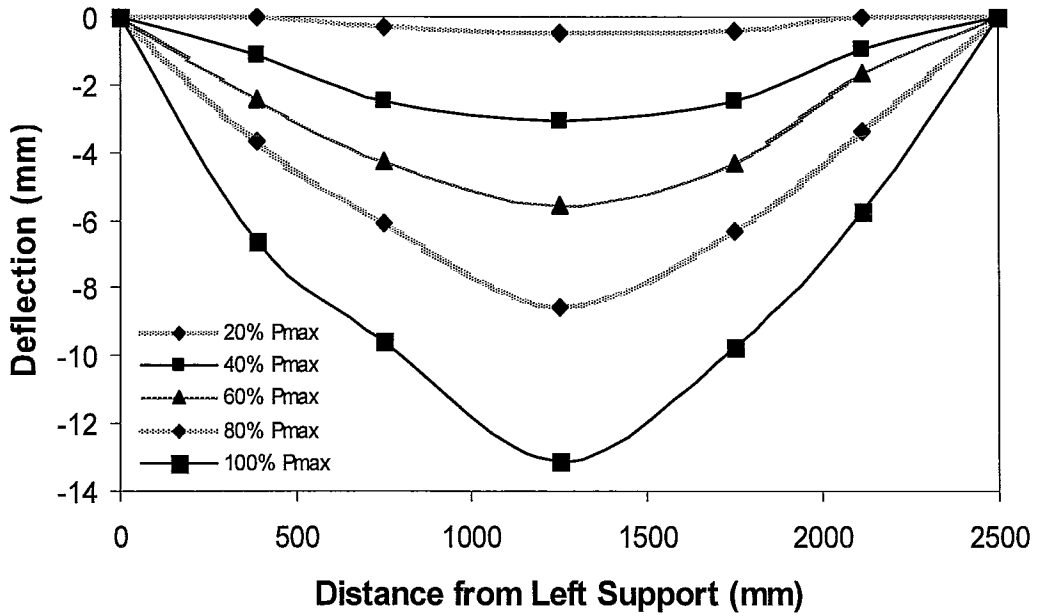


Figure 4.16: TYPE 1a Beam Deflection

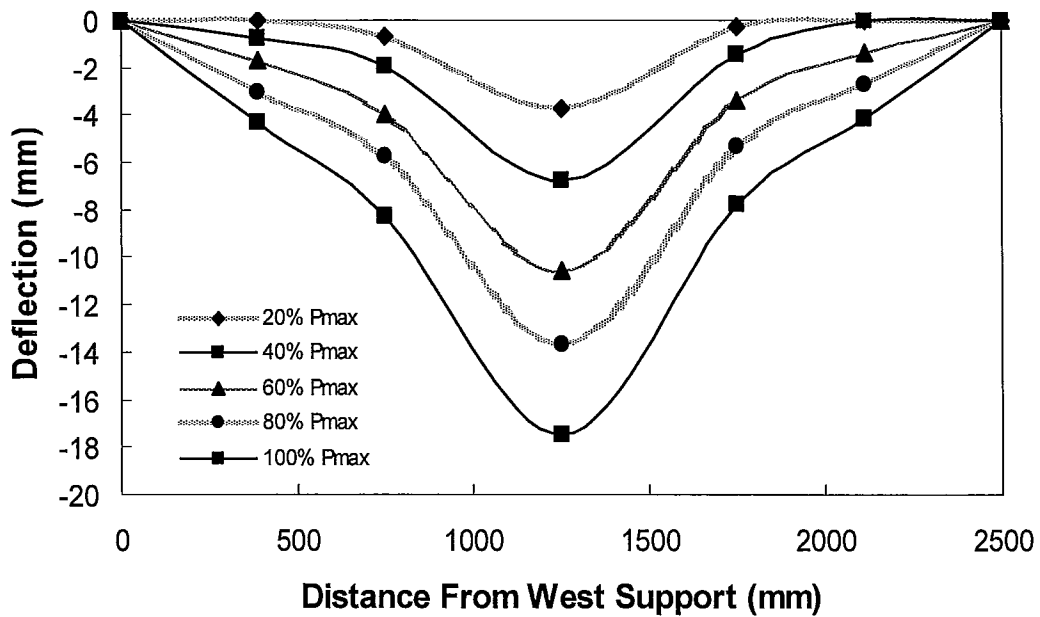
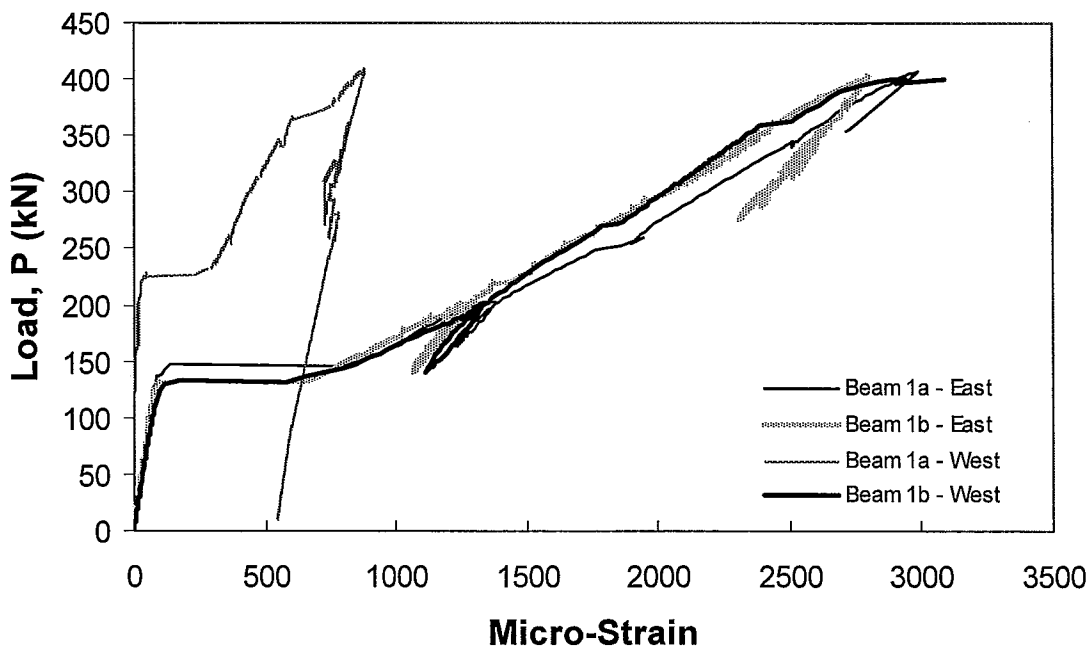


Figure 4.17: TYPE 1b Beam Deflection

is significant because the moment at this section is only 50% of the maximum moment acting on the beam; therefore, the maximum moment region must have experienced a large amount of plastic deformation.

Figure 4.19, Figure 4.20 and Figure 4.21 show the variation of strain in the main steel reinforcement and in the longitudinal NSM bars under the east and west point loads, respectively, for beams 1a and 1b. In reference to the observed behaviour of beam 1a, notice that the NSM bars experienced significant strain near ultimate load and reached 5000 micro-strain, which is approximately 40% of their strain capacity. Furthermore, as expected, these bars experienced larger strain than the steel reinforcement under the same load due to their farther distance from the neutral axis of the beam than the steel bars. Note that the sudden drop in the steel strain curves indicates the incidence of delamination of the NSM bars. Consequently, the height of this drop represents the



*Figure 4.18: Type 1 Beams Longitudinal Steel Strain 390 mm from Supports*

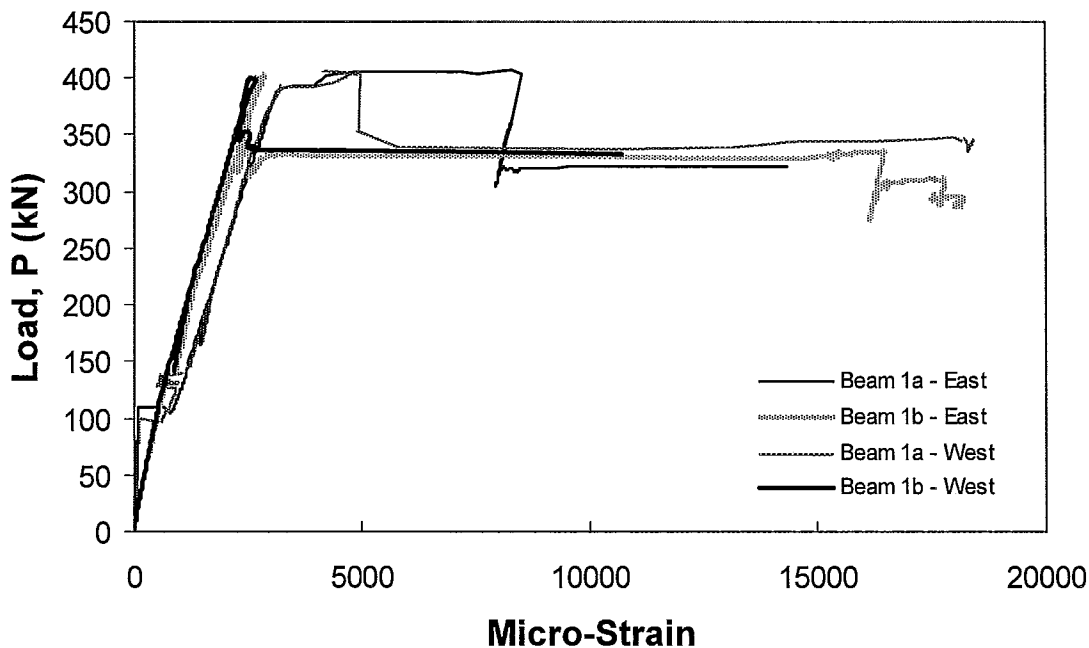


Figure 4.19: Type 1 Beams Longitudinal Steel Strain under Point Loads

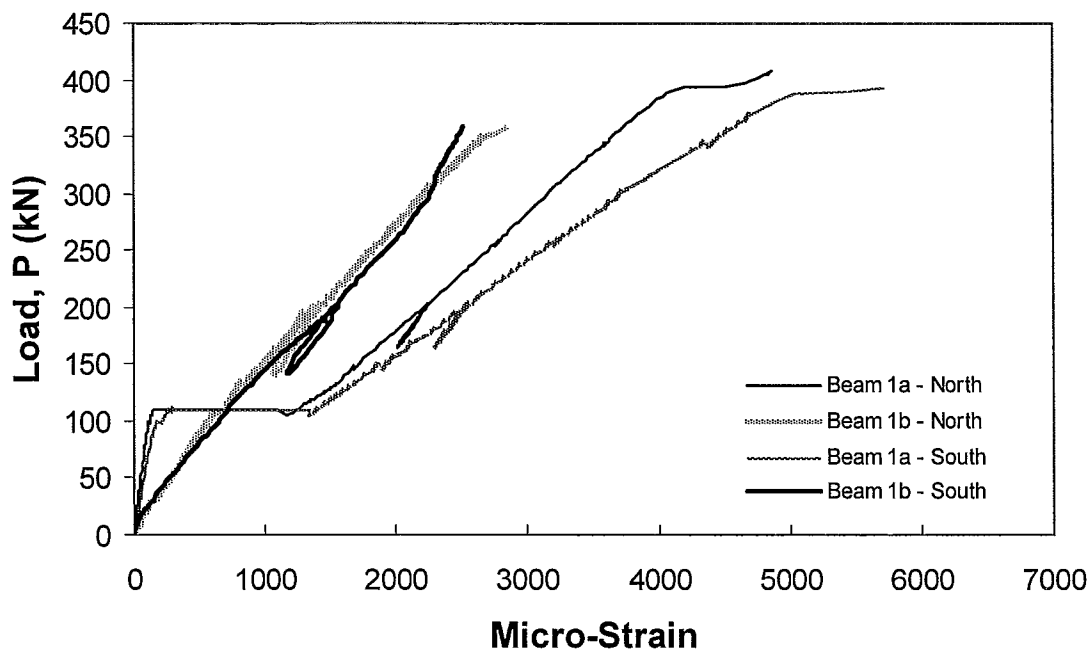
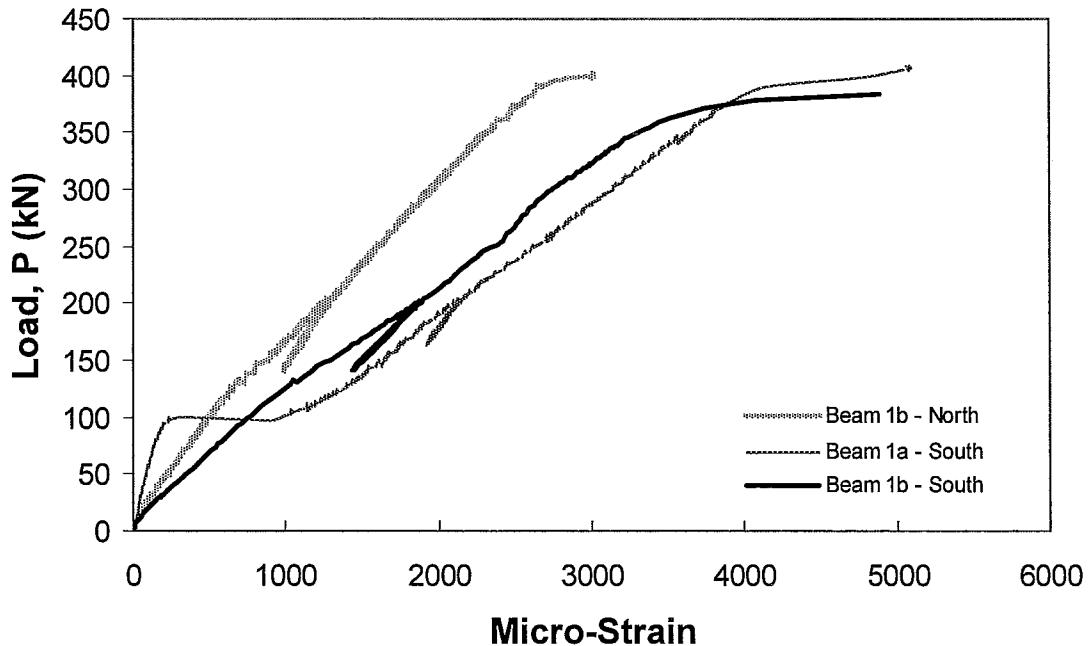


Figure 4.20: Type 1 Beams Longitudinal NSM Bars Strain under East Point Load



**Figure 4.21: Type 1 Beams Longitudinal NSM Bars Strain under West Point Load**

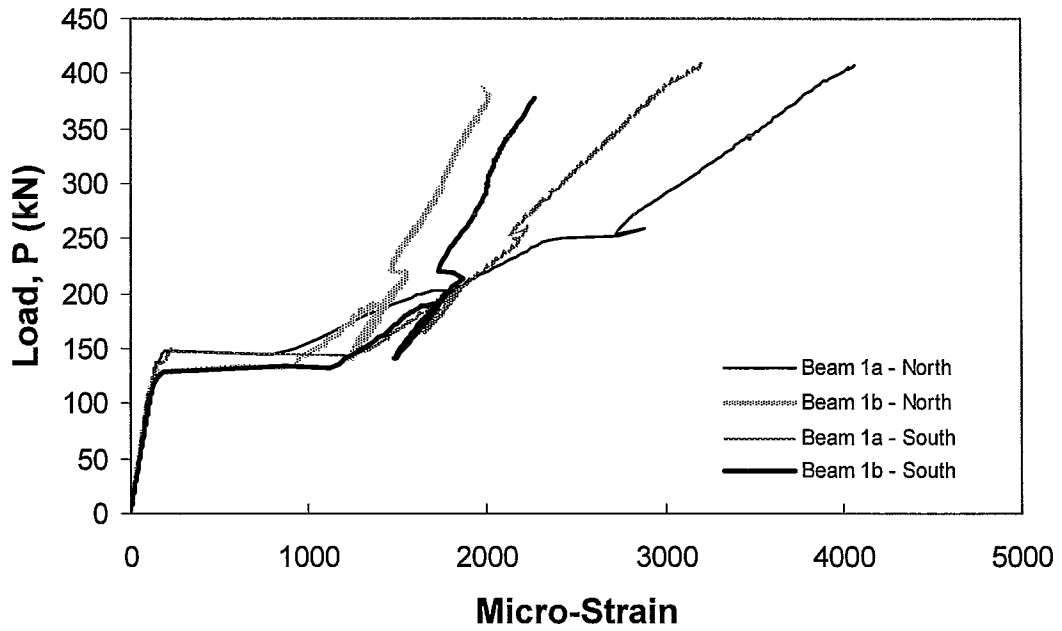
contribution of the NSM bars to the load carrying capacity of the member. Based on the strain variations in beam 1b as shown in Figure 4.19, Figure 4.20 and Figure 4.21, the beam also experienced sudden delamination. This type of behaviour is undesirable because it occurs suddenly and without adequate warning prior to its occurrence. One of the main reasons for the study of the anchored NSM bars in the current investigation is to explore if this sudden mode of failure can be averted. Based on strain variations in Figure 4.21 it appears the south NSM bar in beam 1b continued to remain bonded and resist the applied load despite the delamination of the north bar. This behaviour led to a relatively smaller drop in load compared to that in beam 1a.

Figure 4.19 also confirms the elasto-plastic response of the tensile steel which was also observed in the control beam. Unlike the ancillary tests conducted on steel bar coupons, which indicated a non-linear response, the flexural tests indicate elasto-plastic behaviour. This discrepancy is most likely due to the strain measurement equipment used

---

during the ancillary tests and the consistency of the results observed during the flexural tests verifies their validity. As a result in the next chapter, the tensile steel behaviour observed in the flexural tests will be used in the analysis and discussion to help explain the experimental results.

Figure 4.22 and Figure 4.23 show the strain variation in the two NSM bars for beams 1a and 1b, 200 mm from the bars east and west ends, respectively. For beam 1a, it can be observed that the bars experienced significant strain after the advent of cracking and in some cases exceeded 4000 micro-strain. It is interesting to observe the rather large increase in strain immediately after cracking at a load of approximately 150 kN. This large increase indicates that the ‘so-called’ tension-stiffening in beams with FRP reinforcement may not be as important as in steel reinforced members. Notice that the two bars in beam 1b behaved similarly albeit one bar seems to have undergone a little higher strain than the other. Similarly, the bars in the east and west ends undergo practically equal deformation at failure, which is in the vicinity of 2000 to 2500 micro-strain. Notice also that the large initial increase in the strain of these bars is caused by the advent of concrete cracking in the vicinity of the points where strains were measured. Once again, the relatively large jump in the strain indicates insufficient tension stiffening.



*Figure 4.22: Type 1 Beams Longitudinal NSM Bars Strain 200 mm from East Bar End*

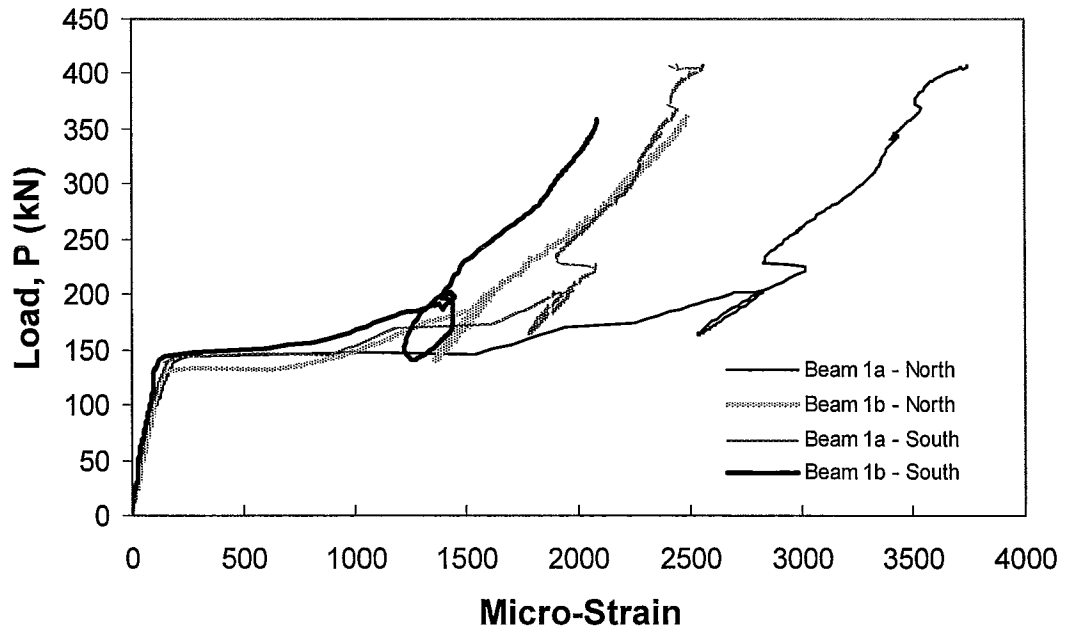


*Figure 4.23: Type 1 Beams Longitudinal NSM Bars Strain 200 mm from West Bar End*

The strain variations in the steel and NSM bar reinforcement at the midspan of beam 1a and 1b are shown in Figure 4.24 and Figure 4.25, respectively. For beam 1a, it is significant to observe the CFRP and the steel at this location experienced practically equal amount of strain although the NSM bars are expected to undergo approximately 10% more strain due to their greater relative distance from the neutral axis. Once delamination occurred, the NSM bars became ineffective, the resistance of the section dropped and the steel reinforcement experienced large plastic deformations, exceeding 15,000 micro-strain. For beam 1b, the CFRP bars reached strains exceeding 4000 micro-strain before delamination, where delamination is manifested by the drop in the load carrying capacity of the beam and the large plastic deformations experienced by the steel reinforcing bars.

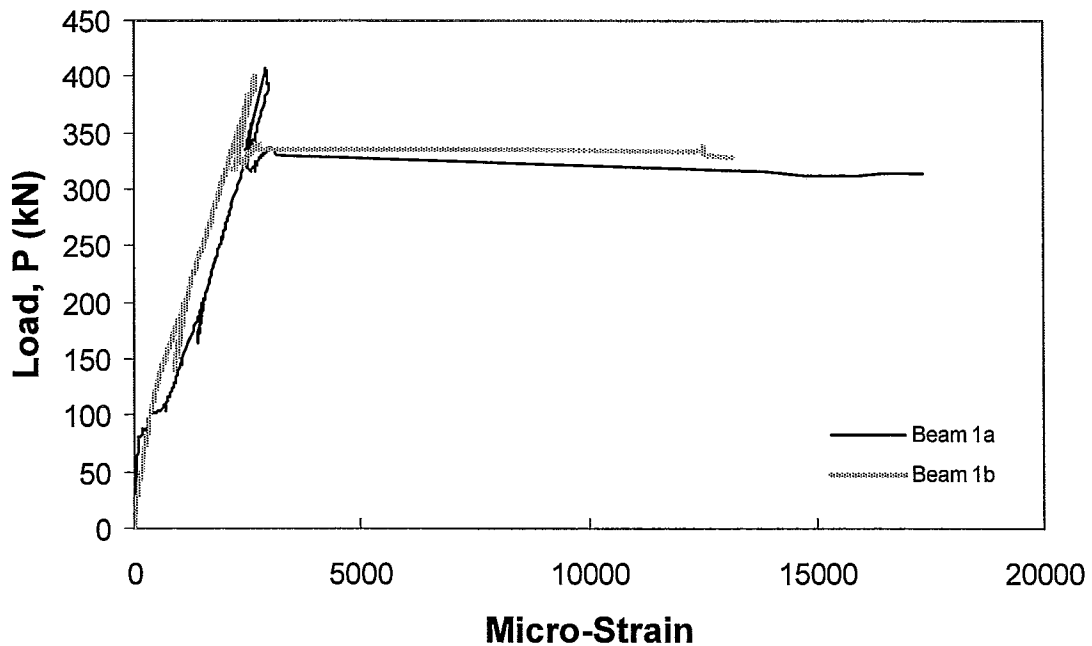


*Figure 4.24: Type 1 Beams Longitudinal Steel Strain at Mid-Span*

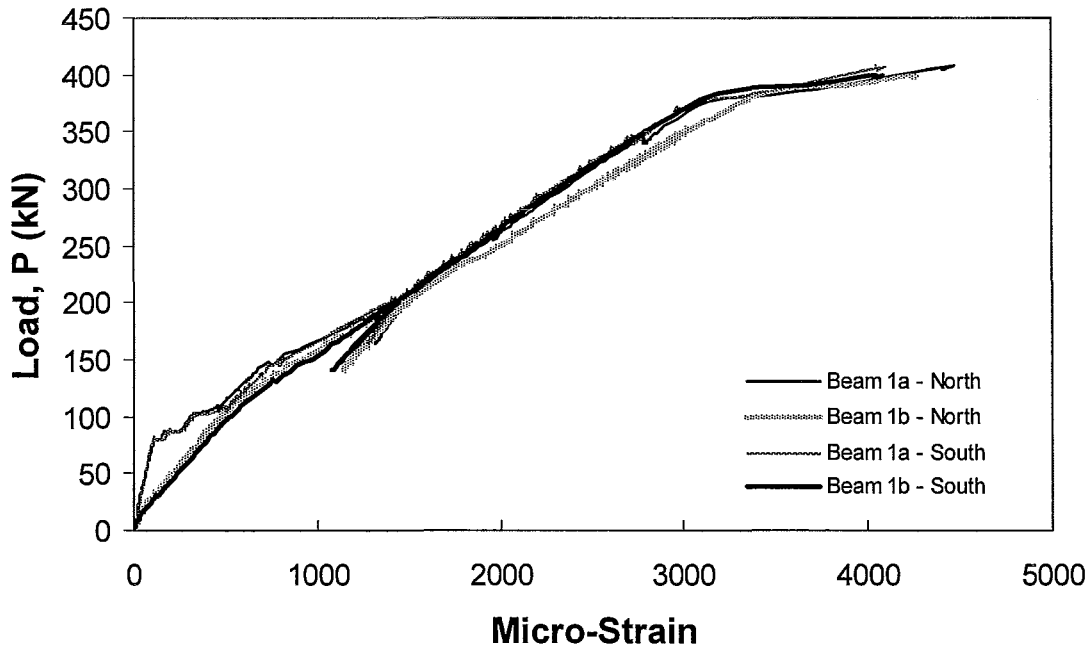


*Figure 4.25: Type 1 Beams Longitudinal CFRP Strain at Mid-Span*

As stated earlier, selected stirrups were strain gauged to measure their deformations. Figure 4.26 and Figure 4.27 show the variation of strain with the applied load in each leg of the steel stirrups located at a distance of 390 mm from the east and west supports, respectively. The stirrups appear to remain elastic although one leg of the stirrup in the western half of beam 1a indicates strain values greater than its yield strain. For beam 1b, all the recorded strain values are smaller than the yield strain of the stirrups, however, given that the beams were designed to have a shear capacity twice their bending capacity, the relatively large strain values recorded in the stirrups are somewhat unexpected. This may be partly due to the fact that the CFRP bars have much smaller axial rigidity than the steel bars and this reduction in axial rigidity of flexural reinforcement is known to cause a reduction in the shear resisted by the concrete, commonly referred to as  $V_c$  (McGregor and Bartlett, 2000).

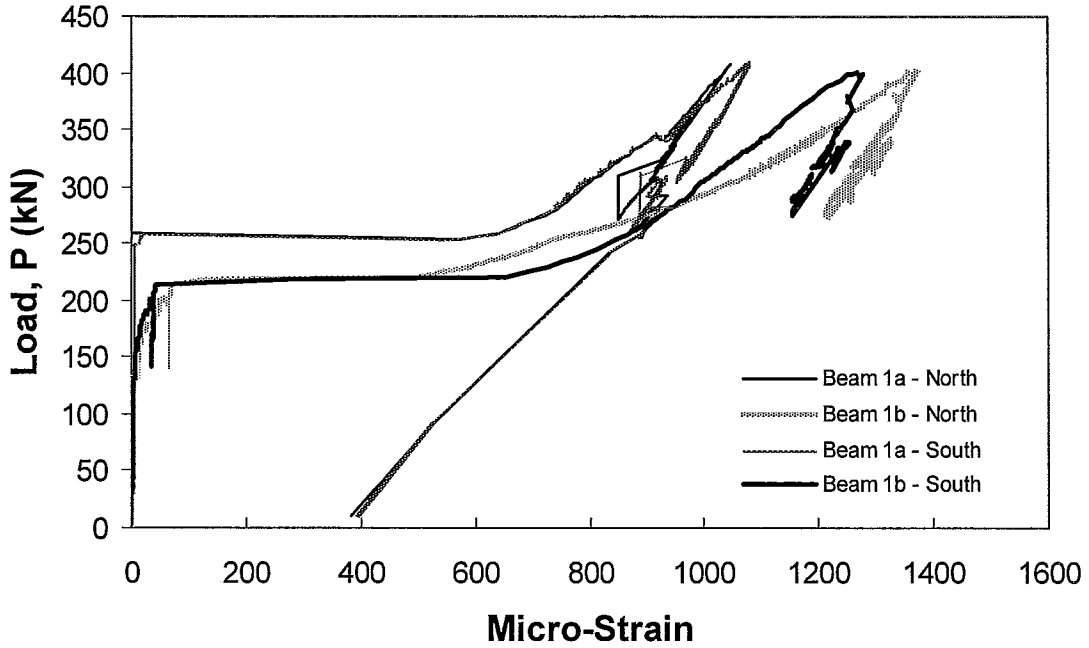


Figure 4.26: Type 1 Beams Steel Stirrup Strain 390 mm from East Support

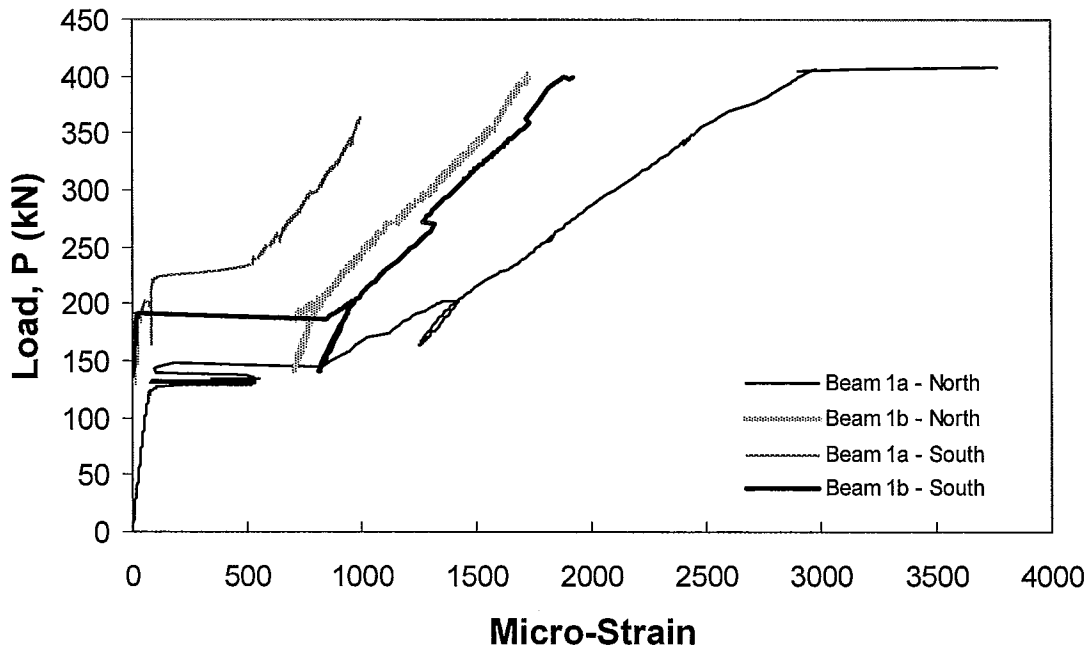


Figure 4.27: Type 1 Beams Steel Stirrup Strain 390 mm from West Support

---

#### 4.4. Type 2 Beams

The two type 2 beams, '2a' and '2b', were each strengthened with two NSM CFRP bars with integral anchors evenly spaced along their length. Like the type 1 beams, type 2 beams had 50% less tensile steel reinforcement compared to the control beam and were designed to be under-reinforced.

The tests commenced by applying a monotonic displacement at a rate of 0.02 mm/sec. The first flexural cracks were noted near the midspan at load levels of 103 kN and 101 kN in beams 2a and 2b, respectively. The first shear cracks appeared as an extension of an existing flexural crack for both beams. Both cracks appeared within the western shear span at a load of 140 kN in beam 2a and 162 kN in beam 2b. Further increase of the load caused more flexural and shear cracks to develop while existing cracks widened. Both beams experienced NSM reinforcement delamination before their theoretical moment capacity could be reached, however, both experienced an increase in strength compared to the type 1 beams. In both beams the NSM reinforcement began to delaminate near the bar ends, as in type 1 beams, at loads of 413 kN and 403 kN for beams 2a and 2b, respectively. Their corresponding ultimate moment capacities,  $M_u$ , were 168 kN·m and 174 kN·m.

Figure 4.28 and Figure 4.29 show that the NSM bars delaminated near their ends and the delamination continued to propagate toward the beam centre. In Figure 4.30 and Figure 4.31, one can see that the NSM reinforcement has delaminated from the beam and some anchors have sheared off. Figure 4.33 presents the close-up view of a sheared anchor in beam 2b. Figure 4.32 illustrates the extent of the reinforcement delamination at failure for beam 2a. In both cases the NSM bars together with most of the concrete cover separated from the beam, exposing the tensile steel reinforcement.

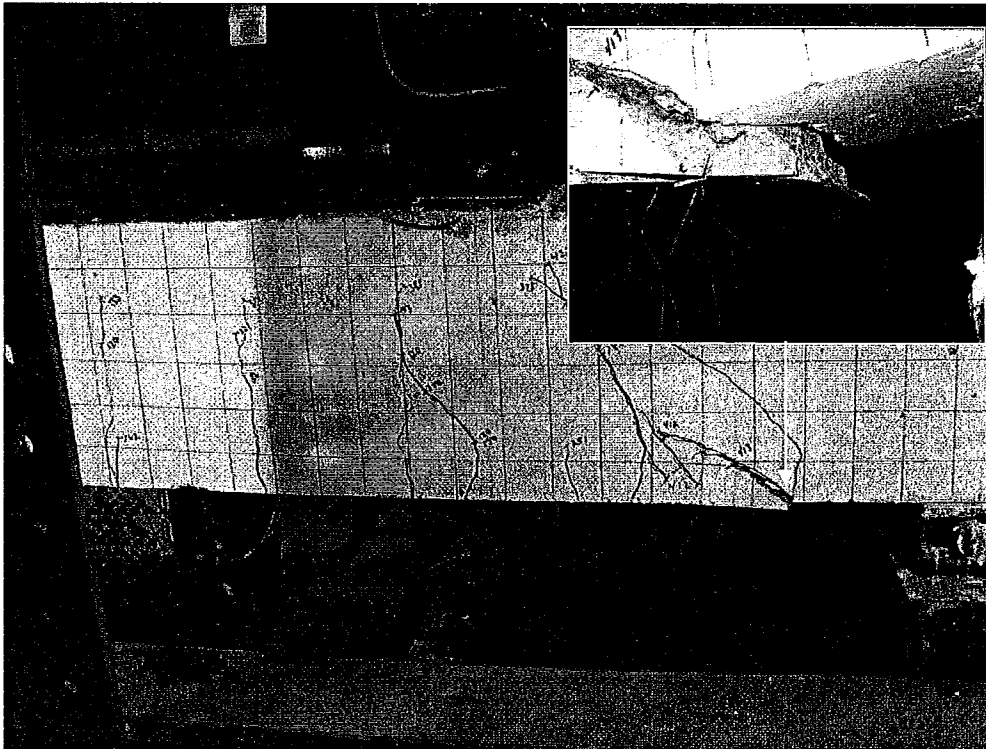


*Figure 4.28: Reinforcement Delamination Initiation in Beam 2a*

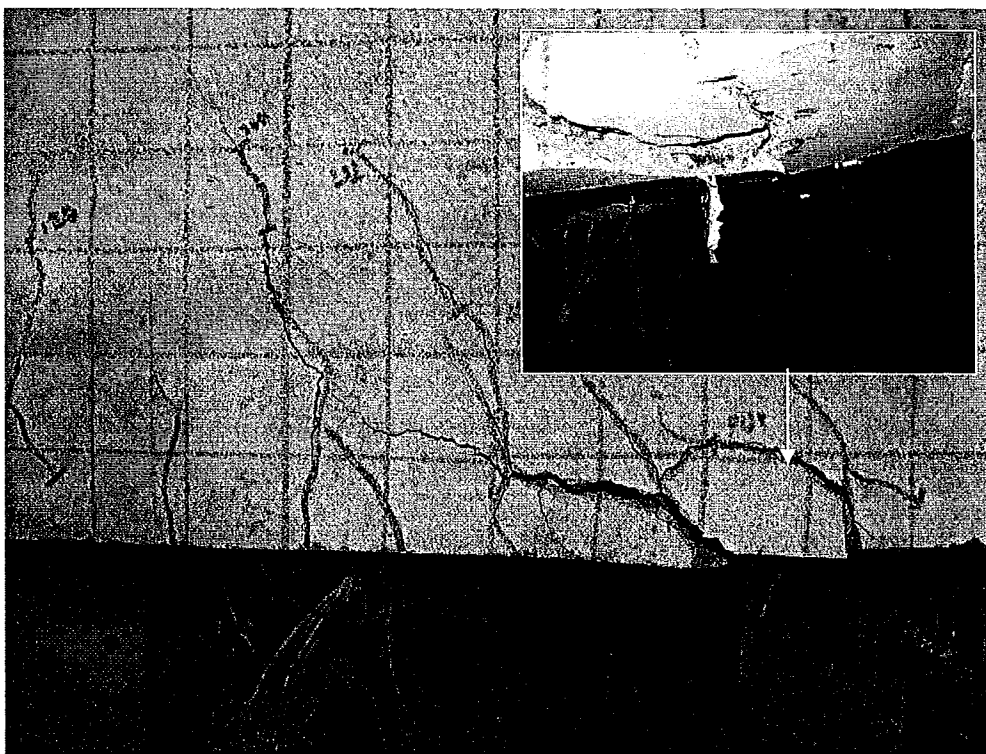


*Figure 4.29: Reinforcement Delamination Initiation in Beam 2b*

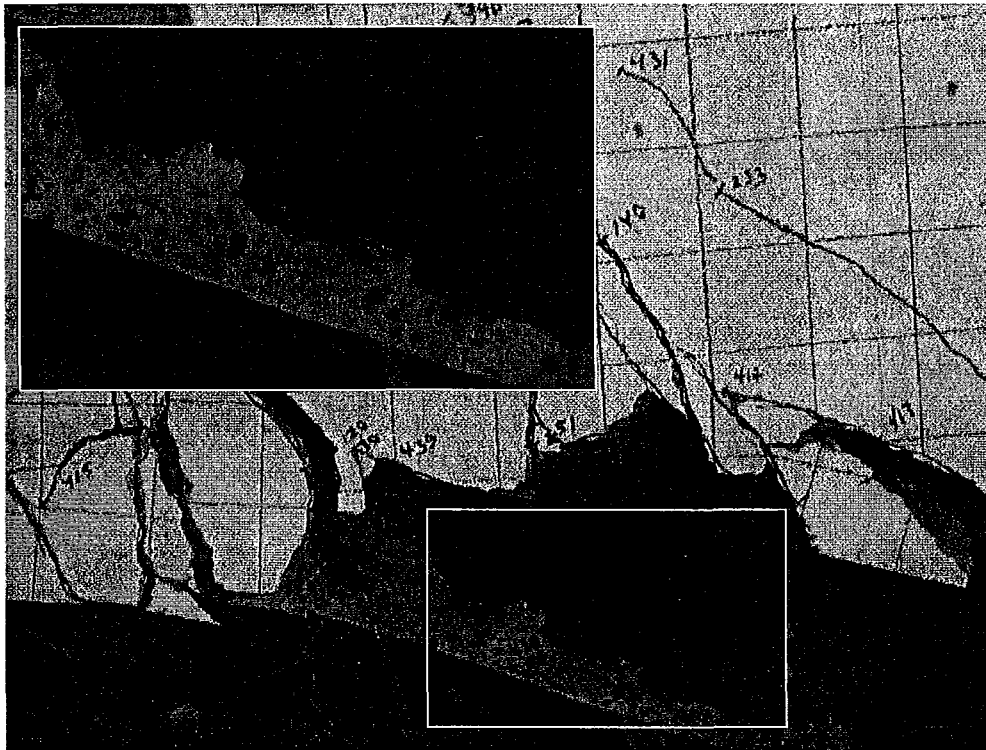


*Figure 4.30: Sheared Anchor Pegs along North CFRP Bar in Beam 2a*



*Figure 4.31: Sheared Anchor Pegs along North CFRP Bar in Beam 2b*

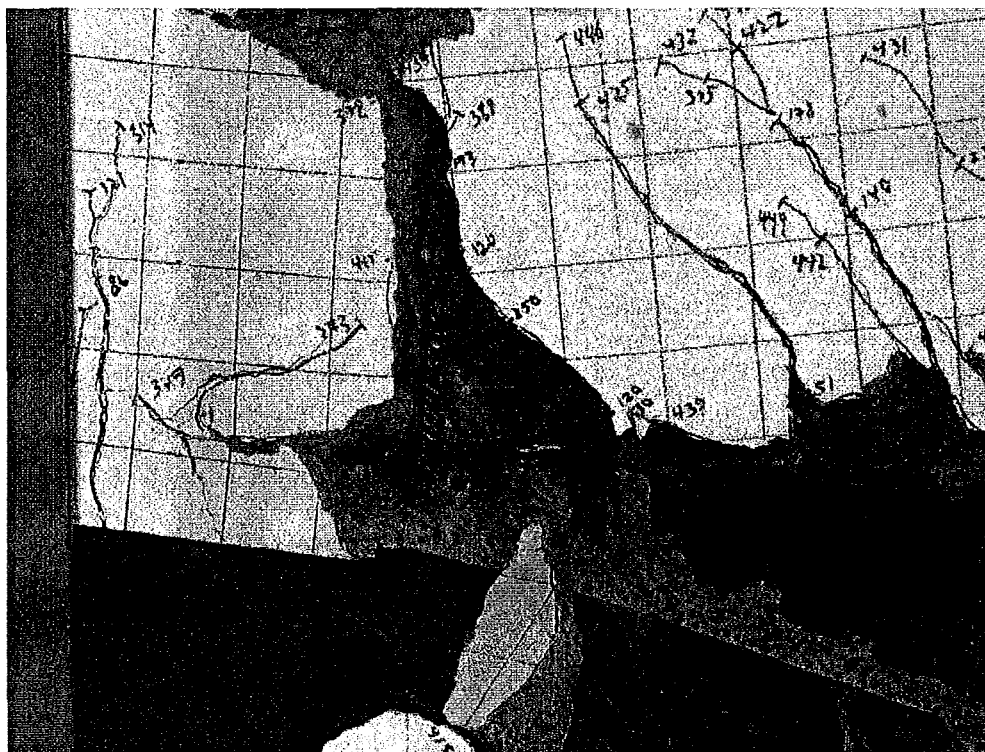


*Figure 4.32: Delaminated Reinforcement in Beam 2a at Failure*

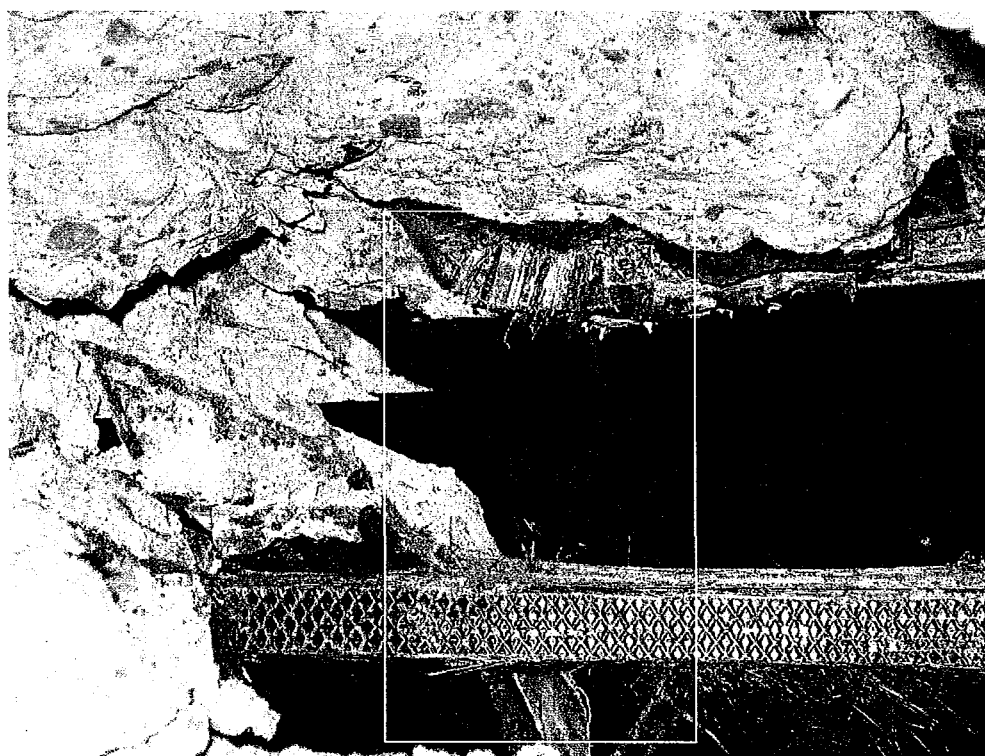


*Figure 4.33: Close-Up of Sheared Anchor in Beam 2b*

To further examine the behaviour of these beams, their load-midspan deflection diagrams are plotted in Figure 4.34. The figure reveals a more gentle decline in strength, compared to the type 1 beams, after maximum load,  $P_{max}$ , of 448 kN in beam 2a and 464 kN in beam 2b was reached, which corresponds to an ultimate moment,  $M_u$ , of 168 kN·m and 174 kN·m, respectively. The maximum loads were attained at midspan displacements of 22 and 19 mm for beams 2a and 2b, respectively. The theoretical capacity of the type 2 beams was calculated to be 260 kN·m which is the same as that of type 1 beams. The theoretical capacities of type 1 and type 2 beams do not differ because they are both based on the assumption of perfect bond between the concrete and the NSM bars. Although type 2 beams reached only 13% higher load on average compared to type 1 beams, their overall load-deflection behaviour is quite different. Unlike beams 1a and 1b, which exhibited a brittle response upon delamination, beams 2a and 2b exhibited a ductile response with a relatively small and gradual drop in maximum load up to failure. This is a rather desirable response because failure is accompanied by ample deformation without substantial loss in strength.

The beams deflected shapes are presented in Figure 4.35 and Figure 4.36. Deflection curves are shown for load levels corresponding to 20%, 40%, 60%, 80% and 100% of  $P_{max}$ . The figure illustrates good symmetry indicating that the load was placed centrally.

The strain variation was monitored at designated locations along the main flexural resisting steel, the NSM CFRP bars and the internal stirrups as described in the previous chapter. Figure 4.37 illustrates the strain variation with applied load in the main flexural steel reinforcement at 390 mm from the supports in beams 2a and 2b. The indicated location is approximately at the middle of the shear span. Notice that except for the steel in the western half of beam 2a, the maximum strain values at all other locations indicates that the steel has either yielded or was on the verge of yielding. This observation, as stated in the case of type 1 beams, is significant because the moment at this section is

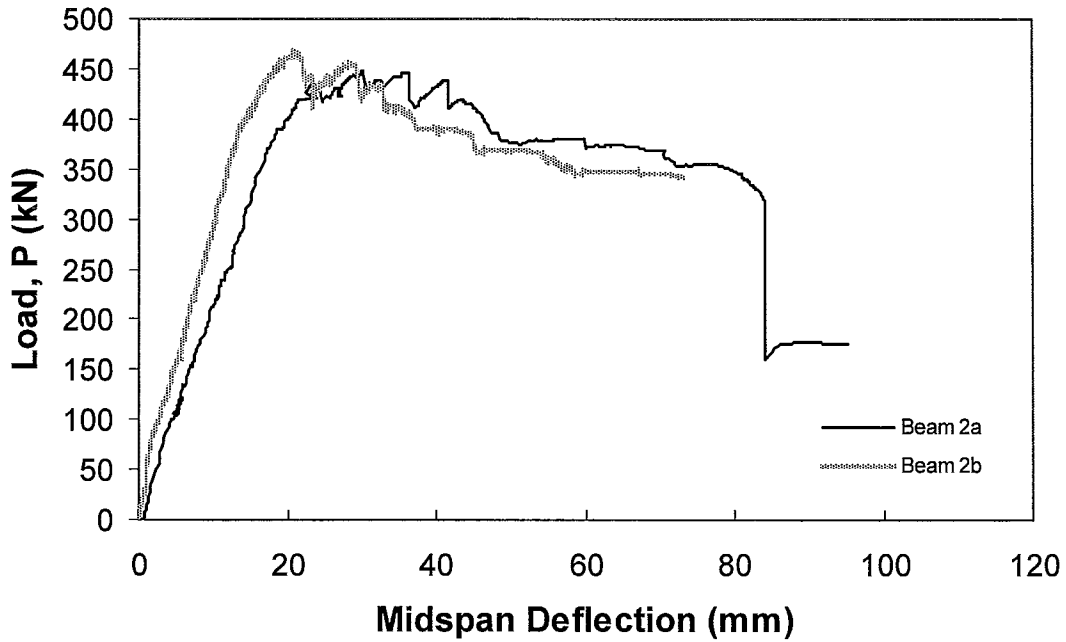


Figure 4.34: Type 2 Beams Load-Midspan Displacement

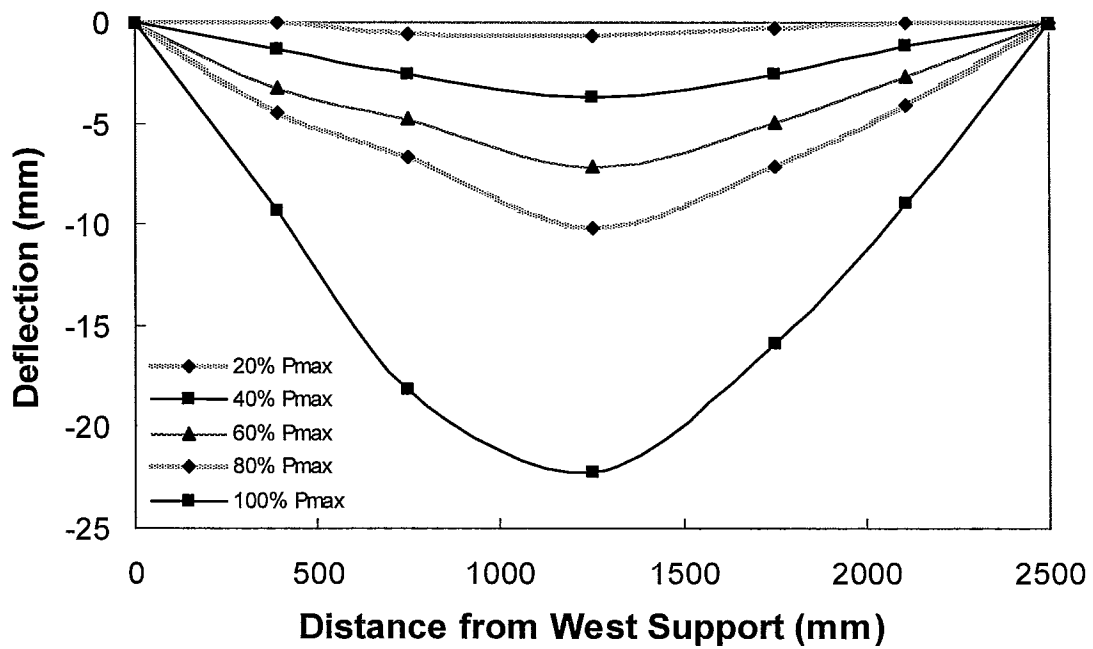


Figure 4.35: Type 2a Beam Deflection

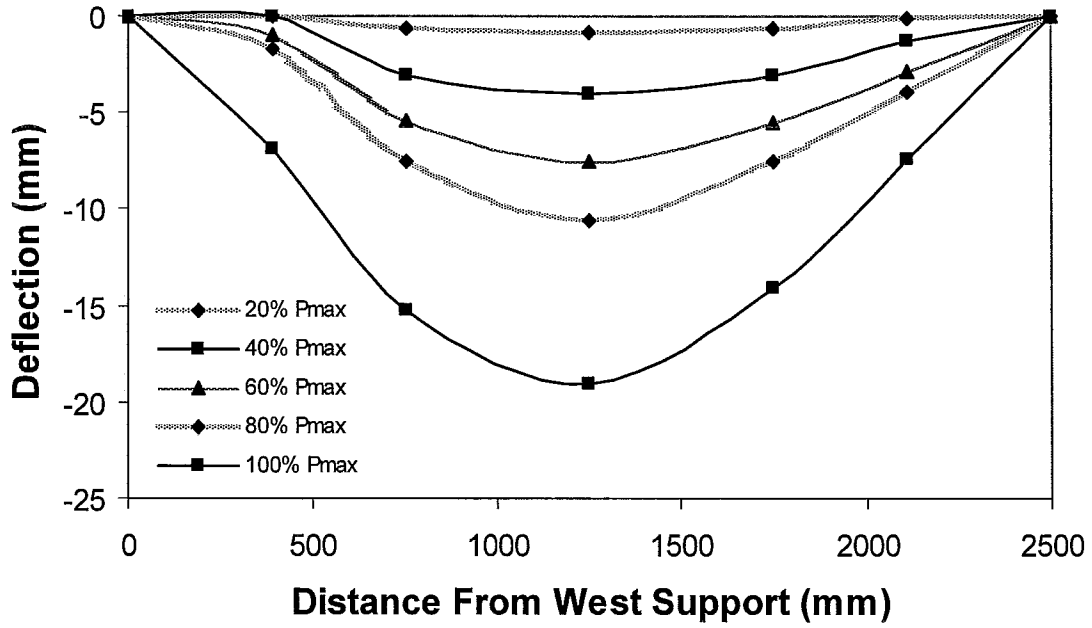


Figure 4.36: Type 2b Beam Deflection

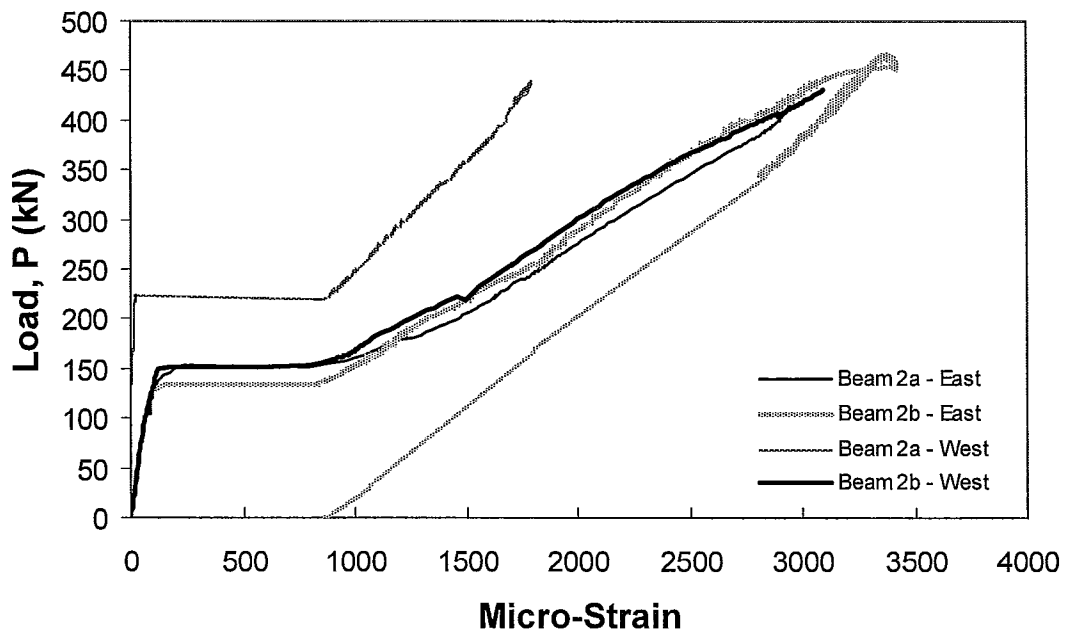


Figure 4.37: Type 2 Beams Longitudinal Steel Strain 390 mm from Supports

---

only 50% of the maximum moment acting on the beam; therefore, the maximum moment region must have experienced a large amount of plastic deformation.

Figure 4.38, Figure 4.39 and Figure 4.40 show the variation of strain in the main steel reinforcement and in the longitudinal NSM bars under the east and west point loads, respectively, for beams 2a and 2b. With reference to the observed behaviour of beam 2a, notice that the NSM bars experienced significant strain near ultimate load and reached an average of 7000 micro-strain, which is approximately 60% of their strain capacity whereas in type 1 beams they only reached roughly 40% of their ultimate strain capacity. The increase in strain is likely due to the anchoring of the bars, which resist the tendency for the bars to separate from the concrete beam and prevent longitudinal slipping at the concrete-bar interface. Furthermore, as expected, the NSM bars experience larger strain than the steel reinforcement under the same load due to their greater relative distance from the neutral axis of the beam. Note that unlike the sudden drop in the steel strain curves observed during the testing of beams 1a and 1b after delamination, type 2 beams exhibit little evidence of load drop with the onset of delamination. This behaviour is desirable as the beams continue to significantly deflect after delamination with relatively little negative effects on their overall strength.

Figure 4.41 and Figure 4.42 show the strain variation in the two NSM bars for beams 2a and 2b, 200 mm from the bars east and west ends, respectively. For beam 2a, it can be observed that these bars experience significant strain after the advent of cracking, reaching a maximum strain exceeding 4000 micro-strain. It is interesting to observe the rather large increase in strain immediately after cracking at a load of approximately 150 kN which is similar to the behaviour of type 1 beams. As stated before, this large increase indicates that the ‘so-called’ tension-stiffening in beams with FRP reinforcement may not be as important as in steel reinforced members. In beam 2b, notice that the two NSM bars behave similarly albeit the south bar seems to be undergoing a little higher

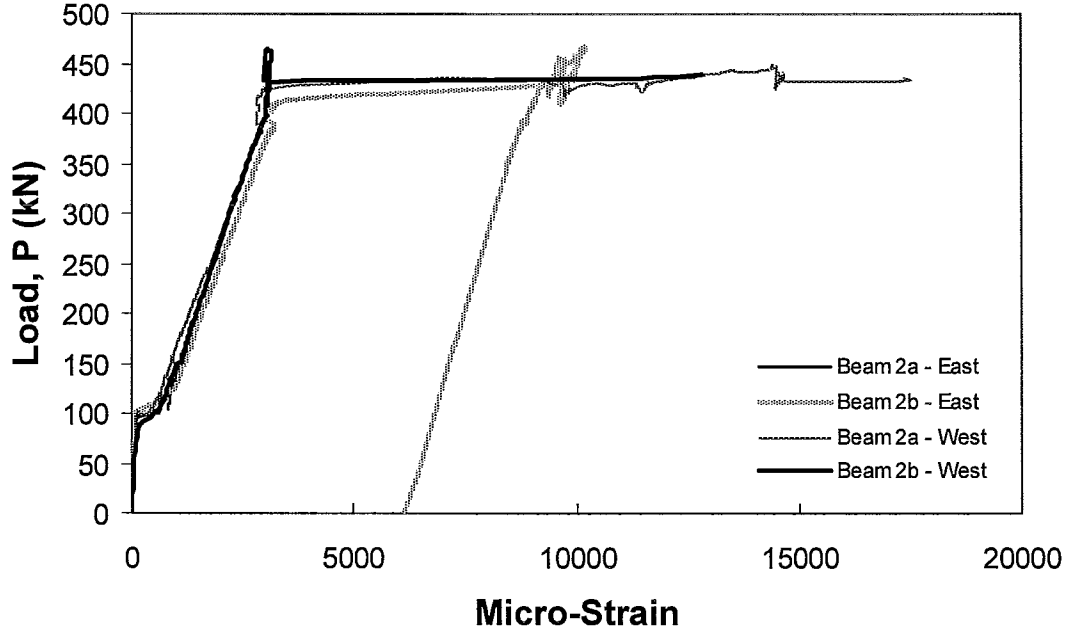


Figure 4.38: Type 2 Beams Longitudinal Steel Strain under Point Loads

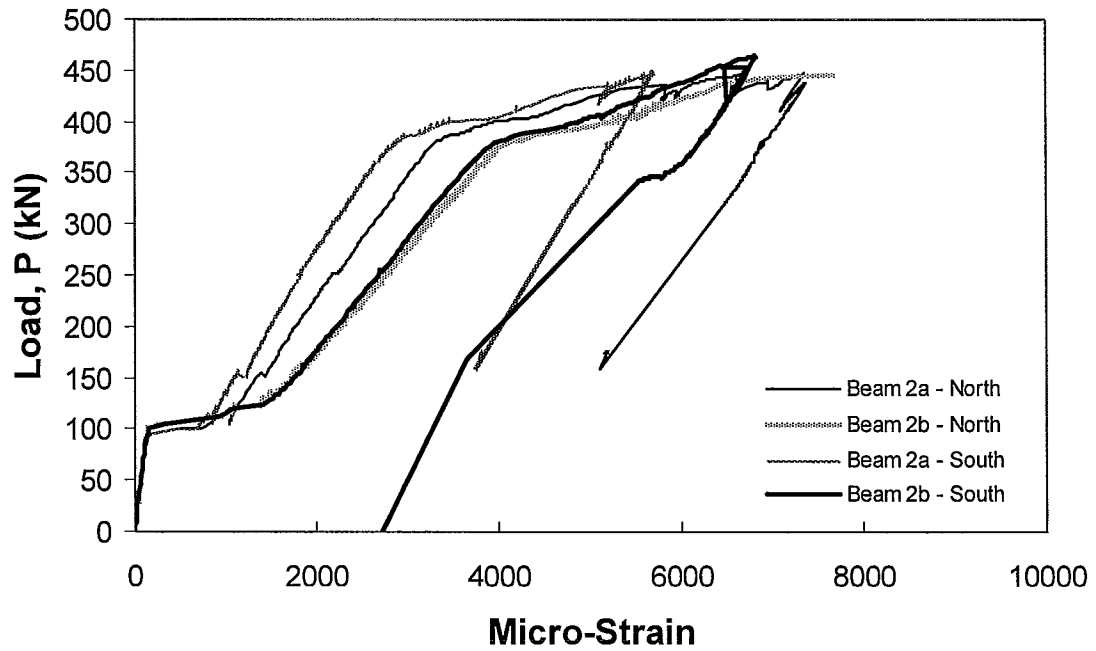
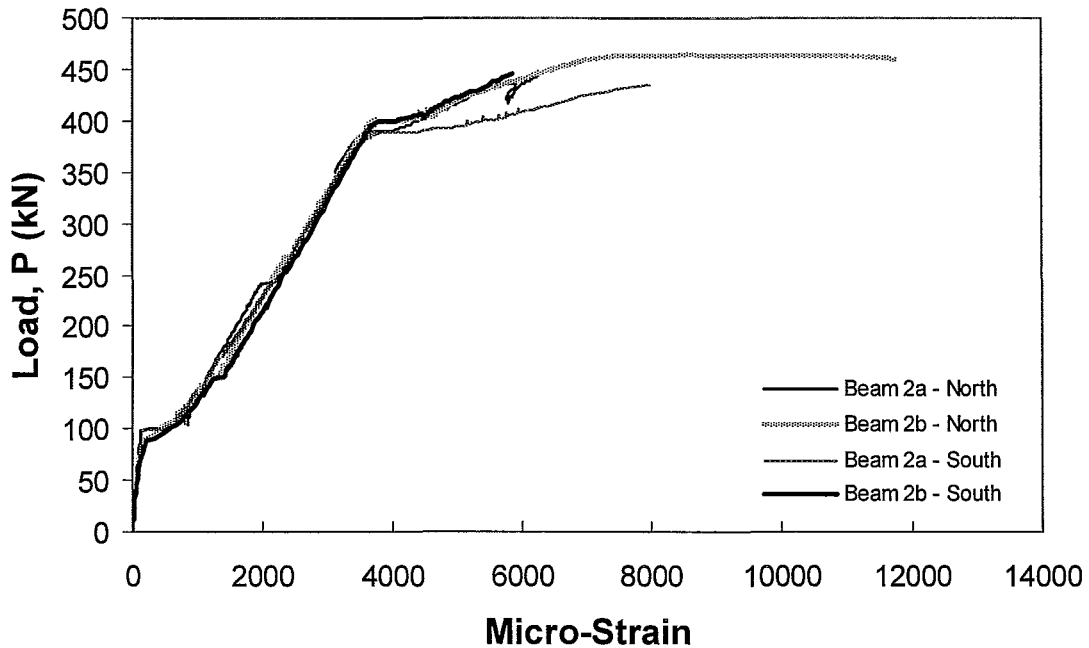


Figure 4.39: Type 2 Beams Longitudinal CFRP Strain under East Point Load



*Figure 4.40: Type 2 Beams Longitudinal CFRP Strain under West Point Load*

strain than the north bar in the east end. Similarly, the bars in the east and west ends undergo practically equal deformation at failure, which is in the range of 4000 to 5000 micro-strain. The strains of the type 2 beams near the bar ends reached nearly double the values observed in type 1 beams. Considering that this is the region where delamination is initiated, one can conclude that delamination is delayed by the anchors since the bars are able to reach higher strain levels. Additionally, and as noted previously, the large initial increase in the strain of these bars is caused by the advent of concrete cracking in the vicinity of the point where strain is measured.

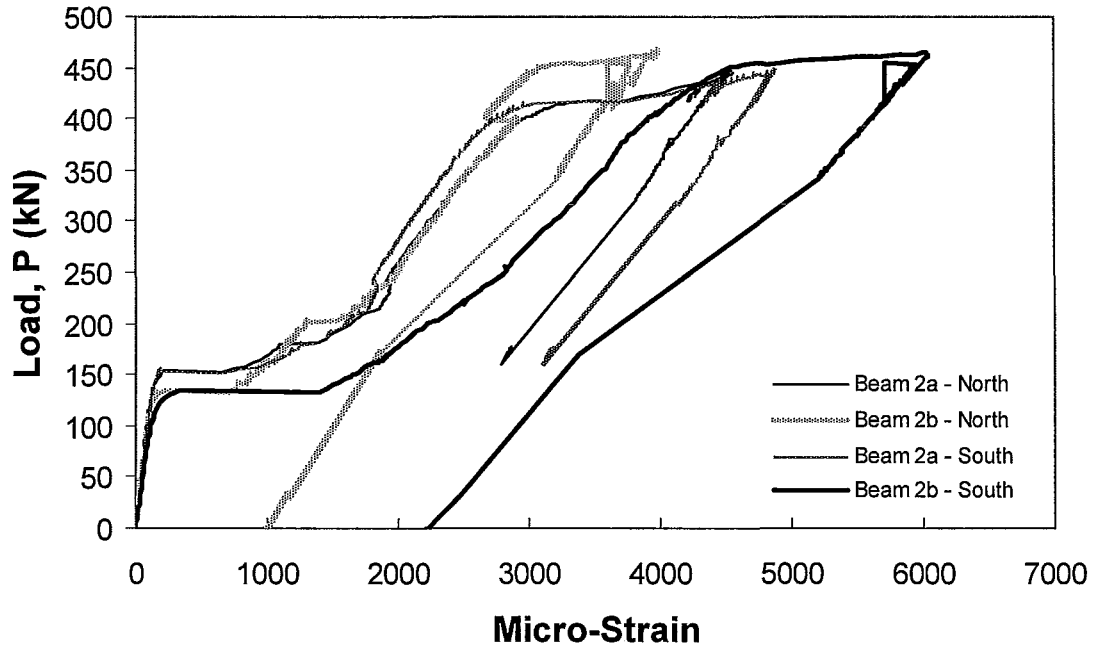


Figure 4.41: Type 2 Beams Longitudinal CFRP Strain 200 mm from East Bar End

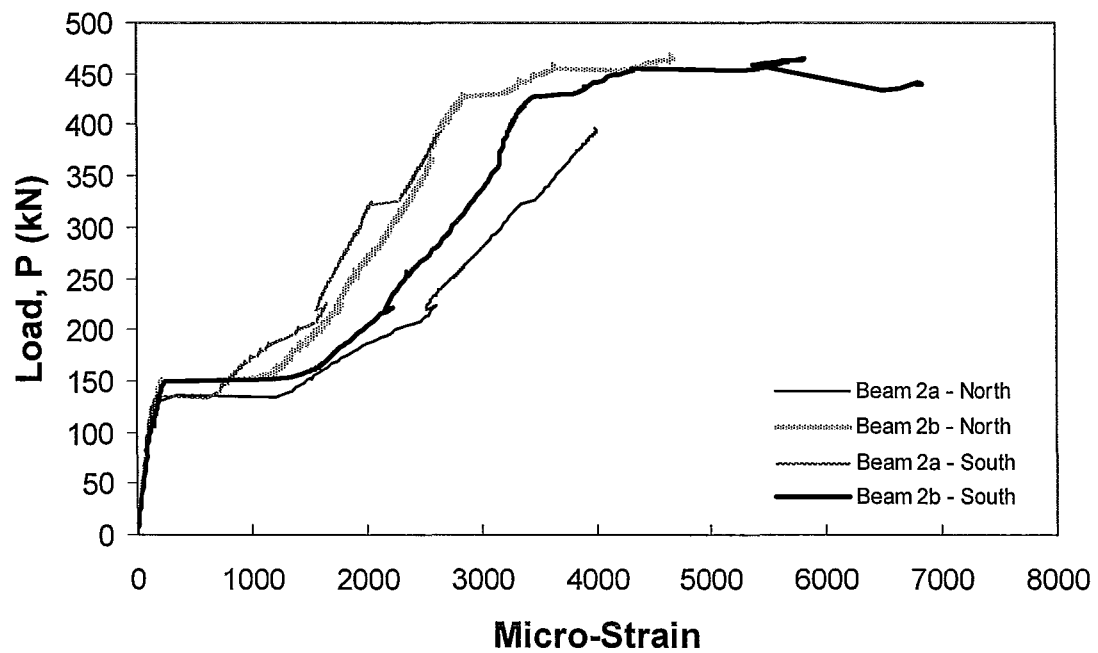
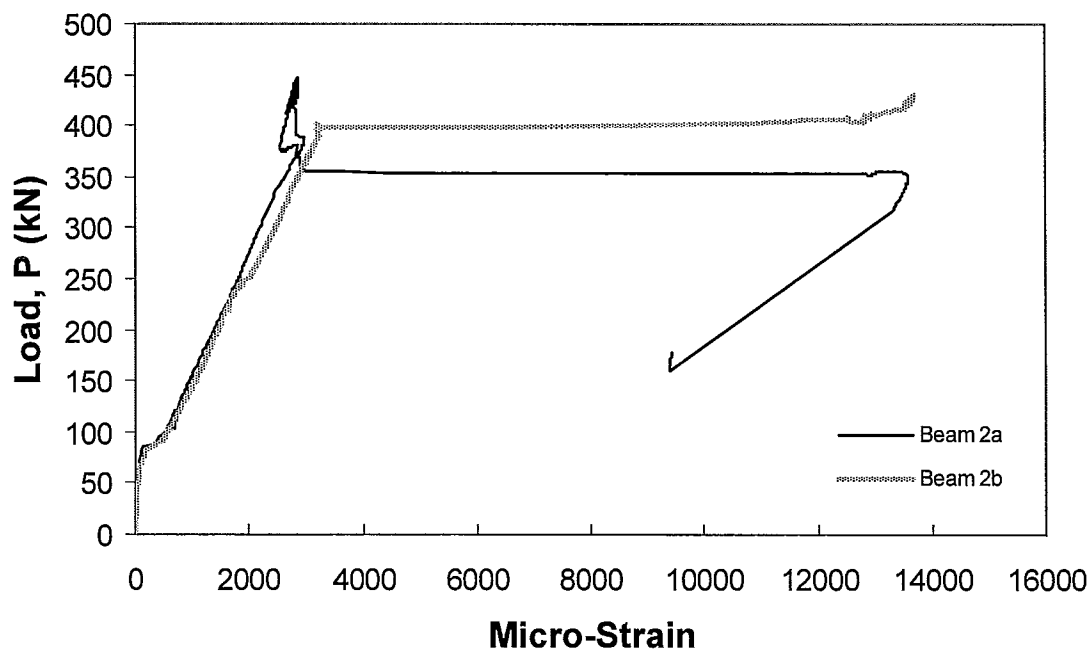
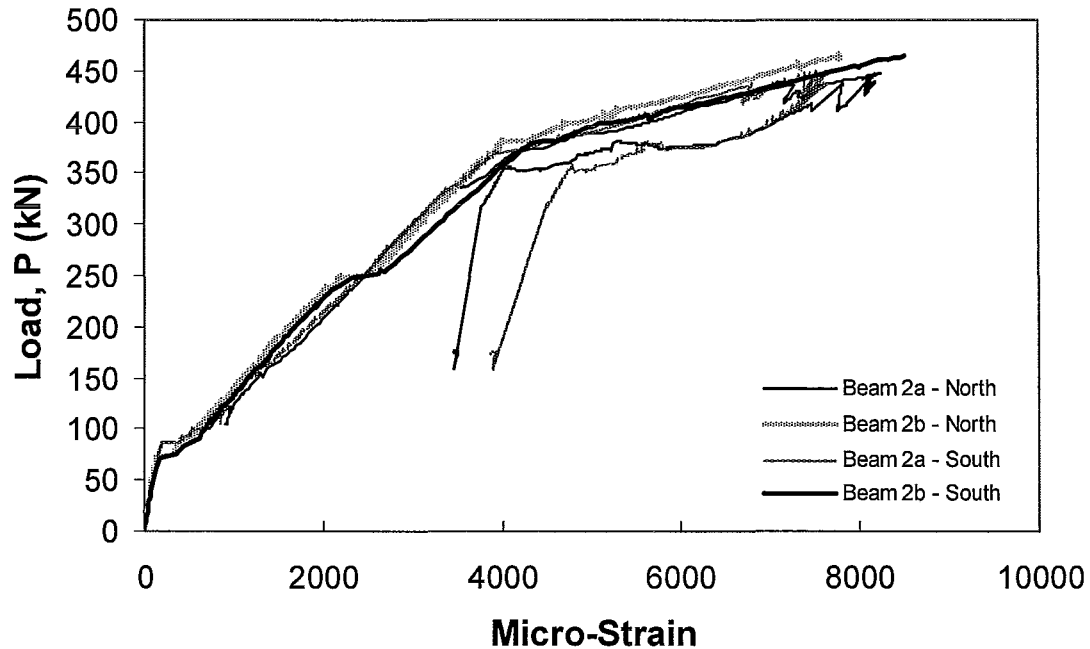


Figure 4.42: Type 2 Beams Longitudinal CFRP Strain 200 mm from West Bar End

The strain variation in the steel and NSM bar reinforcement at the mid-span of beam 2a and 2b is shown in Figure 4.43 and Figure 4.44. For beam 2a, one can observe that the FRP experienced larger strains than the steel reinforcement due to their greater relative distance from the neutral axis. Both NSM bars generally followed the same strain behaviour indicating symmetry. Once the delamination became extensive, the NSM bars became ineffective, the resistance of the section dropped and the steel reinforcement experienced large plastic deformations, exceeding 14,000 micro-strain. It is important to note that unlike the steel response observed under the east and west point loads, the steel response at midspan shows a drop in load similar to the behaviour observed in the type 1 beams. This behaviour does not follow the general trend of the steel reinforcement at other locations where upon delamination, the steel moved along the yield plateau without a significant drop in load. In beam 2b, the CFRP bars reached strain values exceeding 8000 micro-strain before delamination, which is nearly double the strain observed in the type 1 beams.



*Figure 4.43: Type 2 Beams Longitudinal Steel Strain at Mid-Span*



*Figure 4.44: Type 2 Beams Longitudinal CFRP Strain at Mid-Span*

Selected stirrups were strain gauged to measure their deformations. Figure 4.45 and Figure 4.46 show the variation of strain with the applied load in each leg of the steel stirrups located at a distance of 390 mm from the east and west supports, respectively. Stirrups in both beams appear to remain elastic throughout the testing, however the north leg in beam 2a experienced a maximum strain of approximately 3000 micro-strain. As noted during the type 1 beams discussion, the strain values are relatively high given that the beams were designed to have a shear capacity twice their bending capacity. Although yielding is not apparent in the latter figures, the stirrups recorded strain values indicating that they are on the verge of yielding. This may be partly due to the fact that the CFRP bars have much smaller axial rigidity than the steel bars and this reduction in axial rigidity of flexural reinforcement is known to cause a reduction in the shear resisted by the concrete.

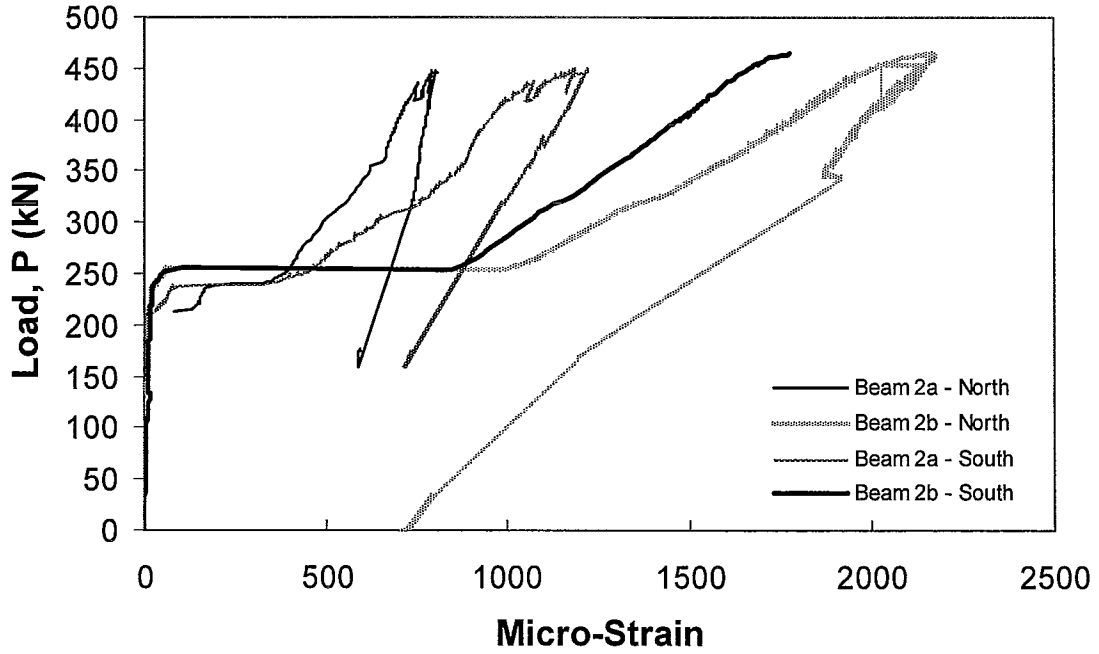


Figure 4.45: Type 2 Beams Steel Stirrup Strain 390 mm from East Support

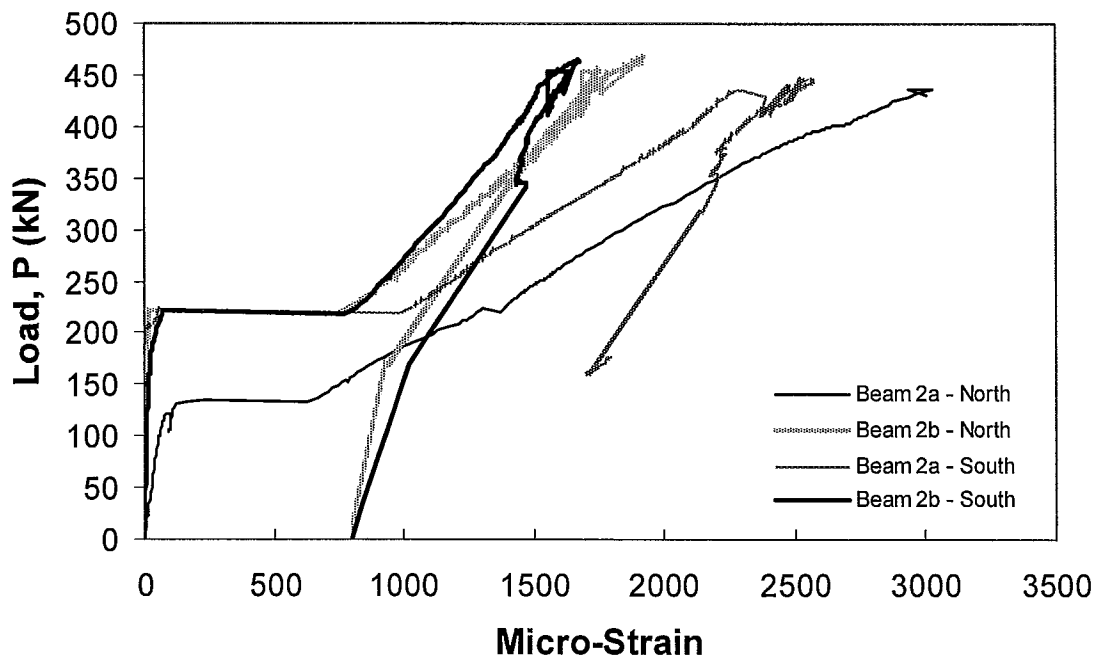


Figure 4.46: Type 2 Beams Steel Stirrup Strain 390 mm from West Support

#### 4.5. Type 3 Beams

The two type 3 beams were each strengthened with two NSM CFRP bars with integral anchors evenly spaced along their length. Like the type 1 and 2 beams, they had 50% less tensile steel reinforcement compared to the control beam and were designed to be under-reinforced. Additionally, the eastern shear span was strengthened with transverse anchored NSM bars in place of every-other internal steel stirrup.

The tests commenced by applying a monotonic displacement at a rate of 0.02 mm/sec. The first flexural cracks were noted near the midspan at load levels of 94 kN and 97 kN for beams 3a and 3b, respectively. The first shear cracks appeared as an extension of an existing flexural crack for both beams. Both cracks appeared within the eastern shear span at a load of 206 kN in beam 3a and 173 kN in beam 3b. Further increase of the load caused more flexural and shear cracks to develop while existing cracks widened. Both beams experienced premature NSM reinforcement delamination, similar to the other strengthened beams in this test program and before the theoretical moment capacity of the beams could be reached. However, both beams experienced increase of strength compared to the type 1 beams. Since both type 3 beams failed by cover delamination, the ultimate moment capacities were similar to the observed capacities of beams 2a and 2b. In both cases the NSM reinforcement began to delaminate near the bar ends, at loads of 388 kN for beam 3a and 382 kN for beam 3b. Their corresponding ultimate moment capacities,  $M_u$ , were 167 kN·m and 171 kN·m. Figure 4.47 and Figure 4.48 show the delamination near the bar ends for these beams. Figure 4.49 and Figure 4.50 show that as the beams delaminated the NSM anchors pulled from the beam core and in most cases fragments of concrete were pulled along with the anchors. Figure 4.51 and Figure 4.52 show the delaminated NSM reinforcement at failure.



*Figure 4.47: Reinforcement Delamination Initiation for Beam 3a*

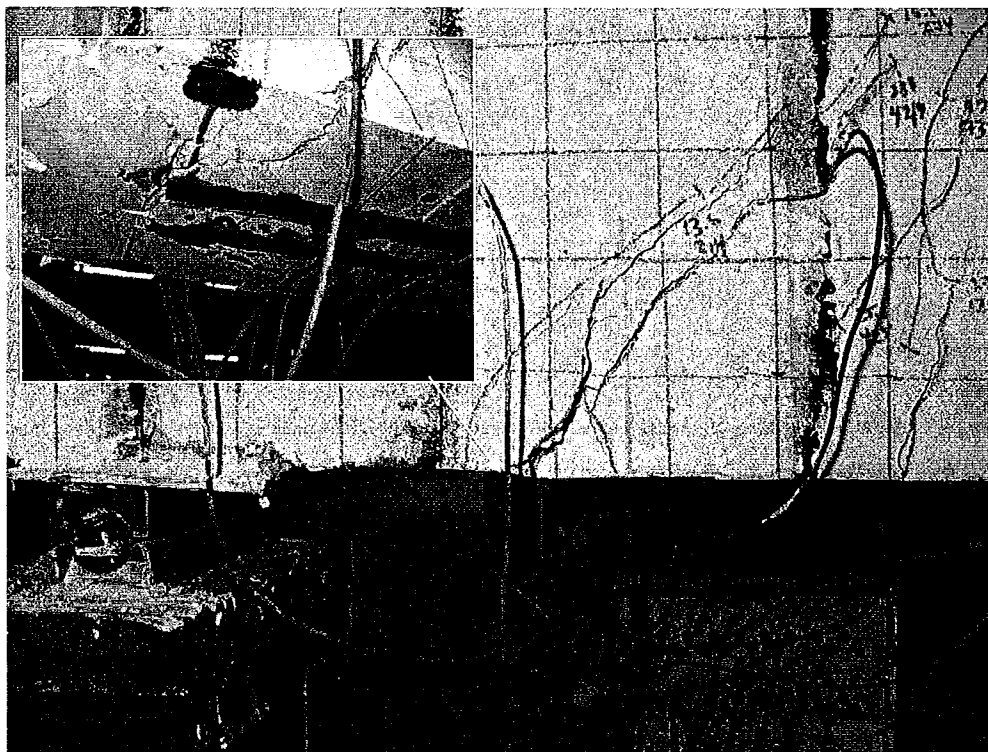


*Figure 4.48: Reinforcement Delamination Initiation for Beam 3b*

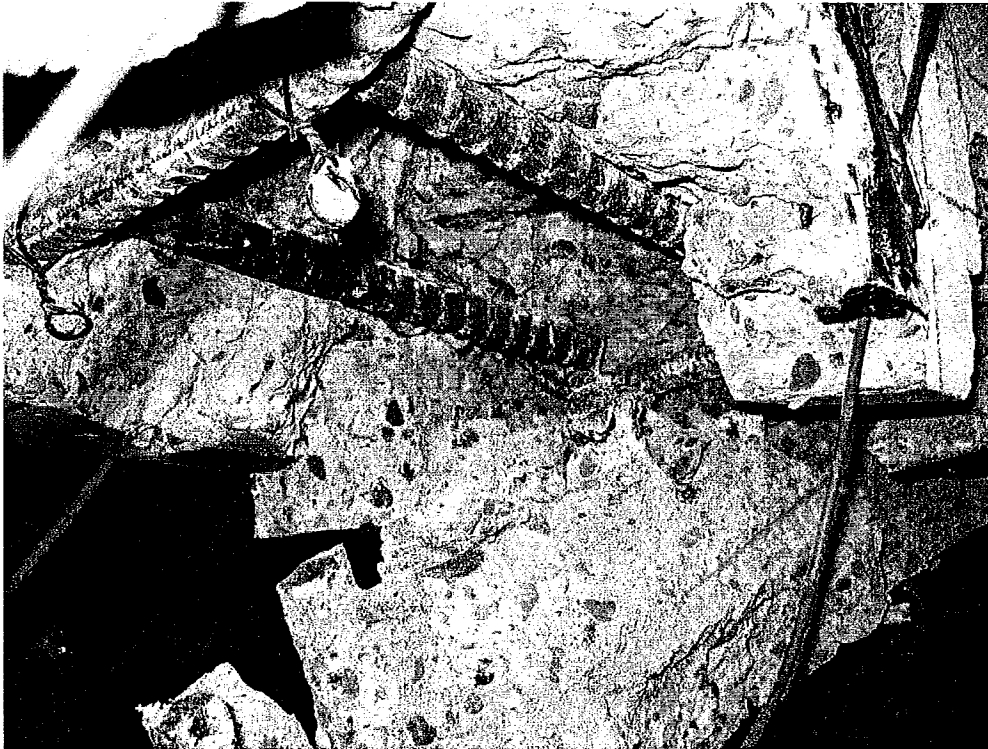


*Figure 4.49: Anchors Pulled from Concrete Core in Beam 3a*



*Figure 4.50: Anchors Pulled from Concrete Core in Beam 3b*

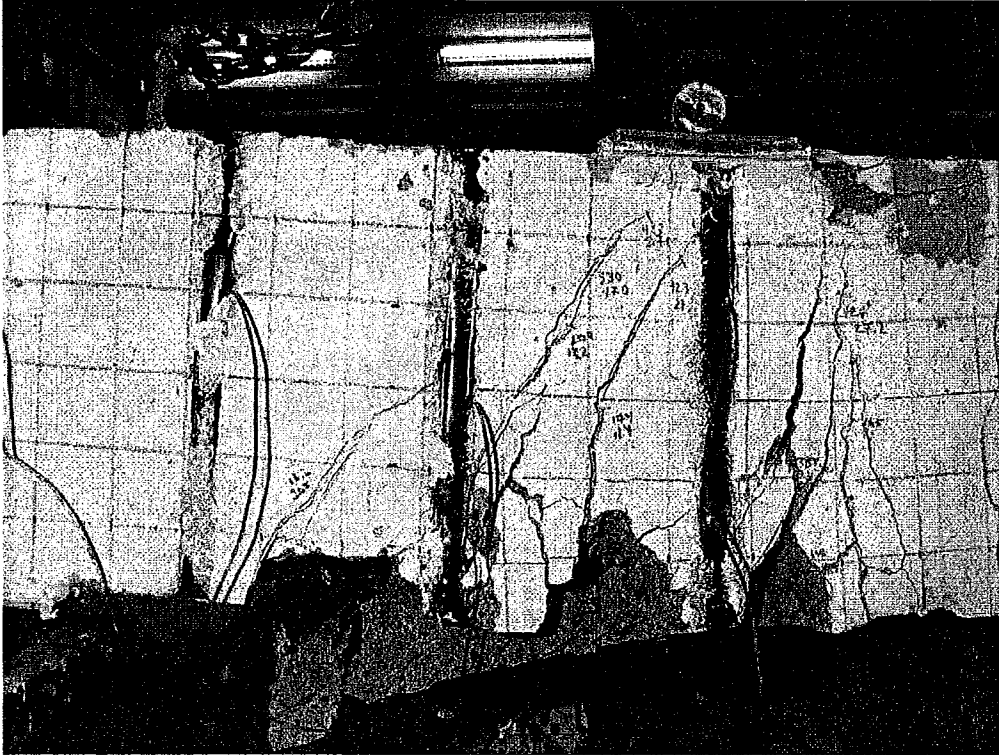


*Figure 4.51: Beam 3a at Failure due to NSM Reinforcement Delamination*



*Figure 4.52: Beam 3b at Failure due to NSM Reinforcement Delamination*

To further examine the behaviour of these beams, their load-midspan deflection diagrams are plotted in Figure 4.53. The figure illustrates similar behaviour to the type 2 beams as there is a more gentle decline in strength, compared to the type 1 beams, after a maximum load,  $P_{\max}$ , of 445 kN in beam 3a and 456 kN in beam 3b was reached, which corresponds to an ultimate moment,  $M_u$ , of 167 kN·m and 171 kN·m, respectively. Their moment capacities were similar to the capacities observed for the type 2 beams as both were identically strengthened in flexure and the same general behaviour was observed. The NSM shear strengthening bars in each of the type 3 beams resisted the applied shear without experiencing failure. The maximum loads were reached at midspan displacements of 26 and 21 mm for beams 3a and 3b, respectively. The theoretical capacities of the type 3 beams were calculated to be the same as the type 1 and 2 beams as perfect bond was assumed between the NSM bars and the concrete in all cases.

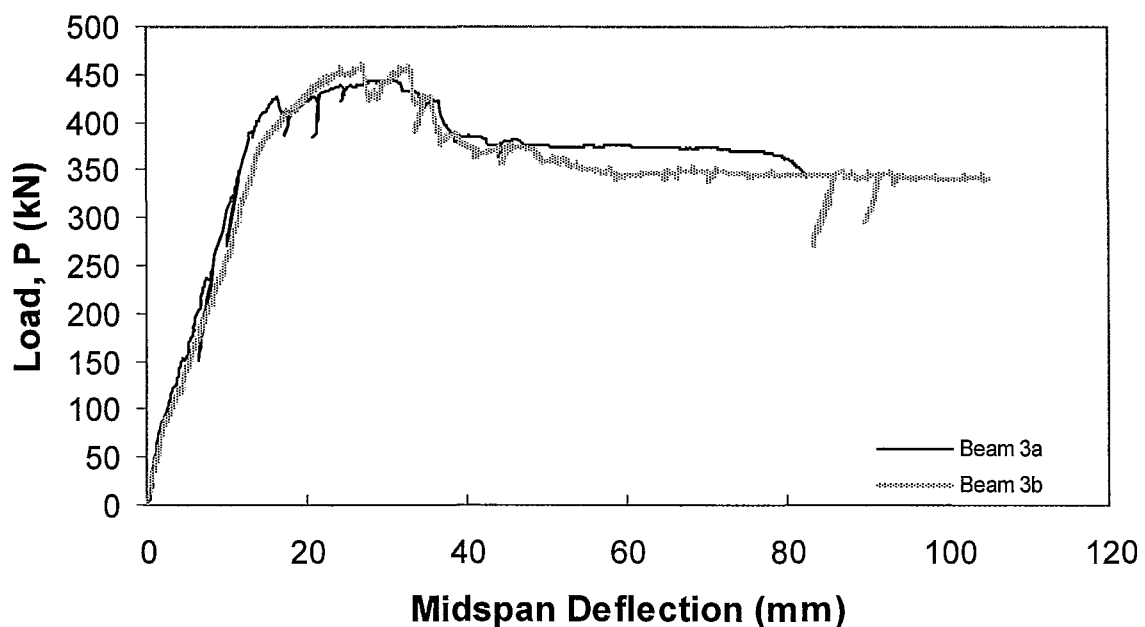


*Figure 4.53: Type 3 Beams Load-Midspan Displacement*

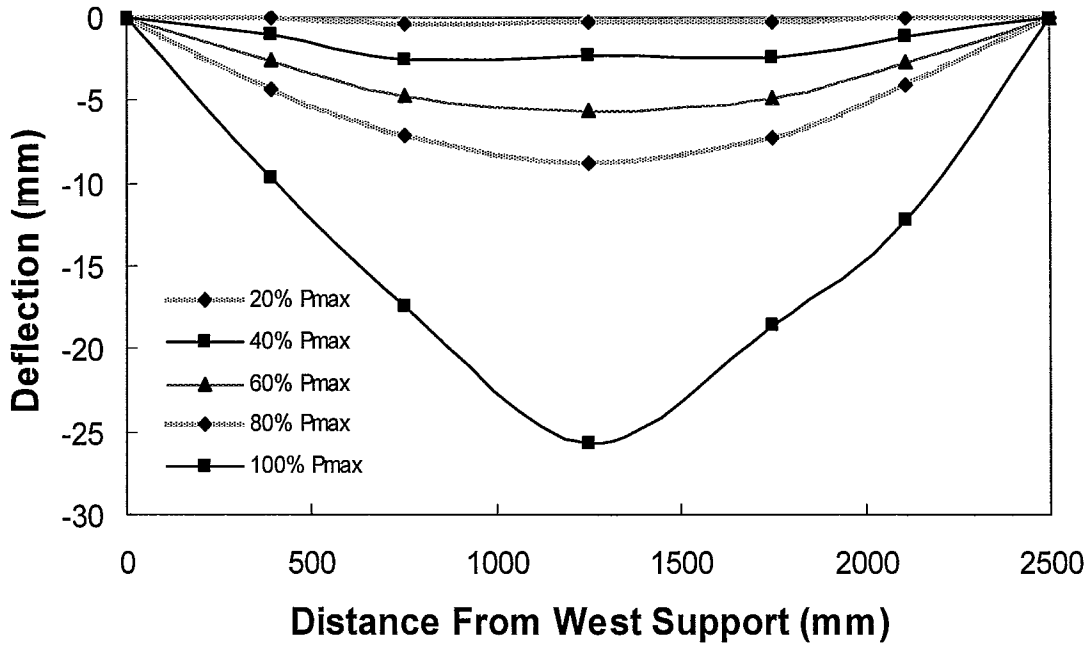


Figure 4.54: Type 3a Beam Deflection

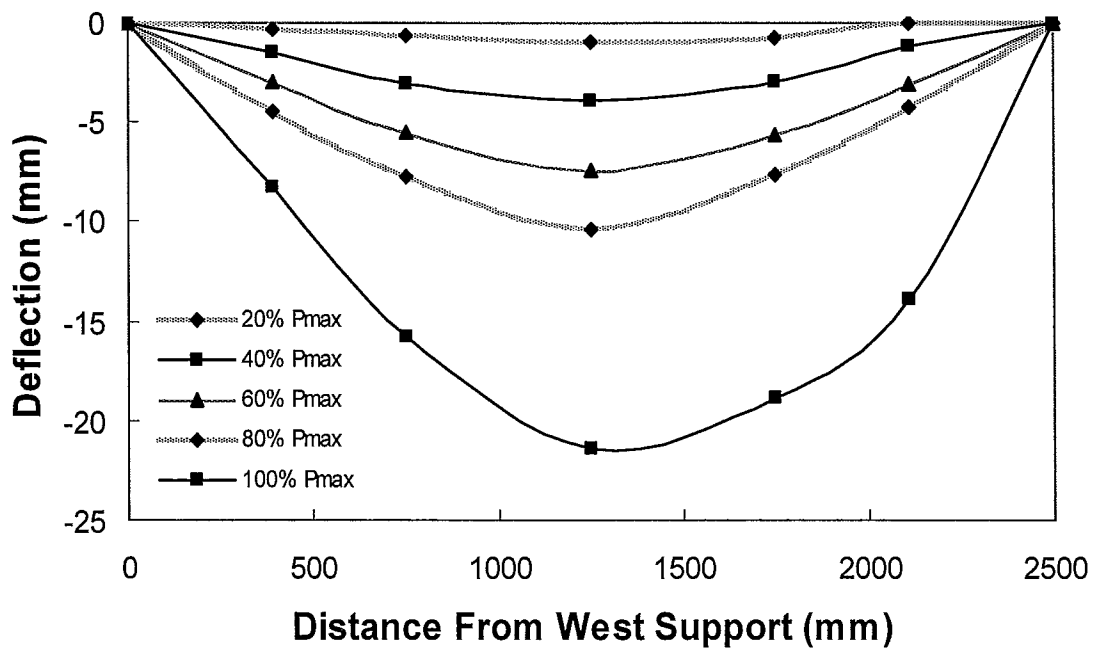


Figure 4.55: Type 3b Beam Deflection

---

The beams deflected shapes are presented in Figure 4.54 and Figure 4.55. Deflection curves are shown for load levels corresponding to 20%, 40%, 60%, 80% and 100% of  $P_{max}$ . The figure shows good symmetry indicating that the load was placed centrally.

The strain variation was monitored at designated locations along the main flexural steel, the NSM CFRP bars and the internal stirrups as described in the previous chapter. Figure 4.56 illustrates the strain variation with applied load in the main flexural steel reinforcement at 390 mm from the supports in beams 3a and 3b. The indicated location is approximately at the middle of the shear span. Notice that the maximum strain values at all the locations indicates that the steel has either yielded or is on the verge of yielding reaching 3000 micro-strain. Once again the moment at this section is only 50% of the maximum moment acting on the beam; therefore, the maximum moment region must have experienced a large amount of plastic deformation. Furthermore, in a similar steel reinforced beam such behaviour could not be observed because if the steel at this section were to yield, it would imply that the external moment at the section would be equal to the yielding moment. This in turn would require that the maximum moment acting on the beam would be double its yield moment, but this is not possible because the maximum or ultimate moment capacity of a steel reinforced beam is rarely more than 20 to 25% of its yield moment.

Figure 4.57, Figure 4.58 and Figure 4.59 show the variation of strain in the main steel reinforcement and in the longitudinal NSM bars under the east and west point loads, respectively, for beams 3a and 3b. With reference to the observed behaviour of beam 3a, notice that the NSM bars experienced significant strain near ultimate load and reached similar strain levels to beams 2a and 2b. The NSM bars achieved an average maximum strain of approximately 7500 micro-strain, which exceeds 60% of their strain capacity. Furthermore, and as expected, the NSM bars generally experienced larger strain than the steel reinforcement under the same load due to their relatively farther distance from the

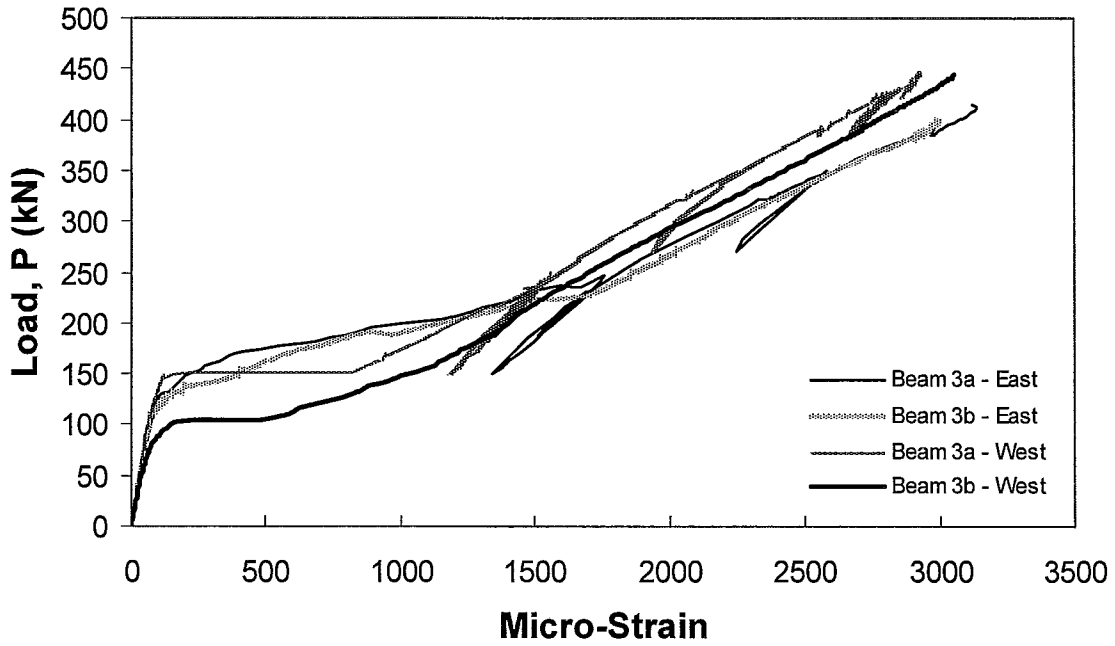


Figure 4.56: Type 3 Beams Longitudinal Steel Strain 390 mm from Supports

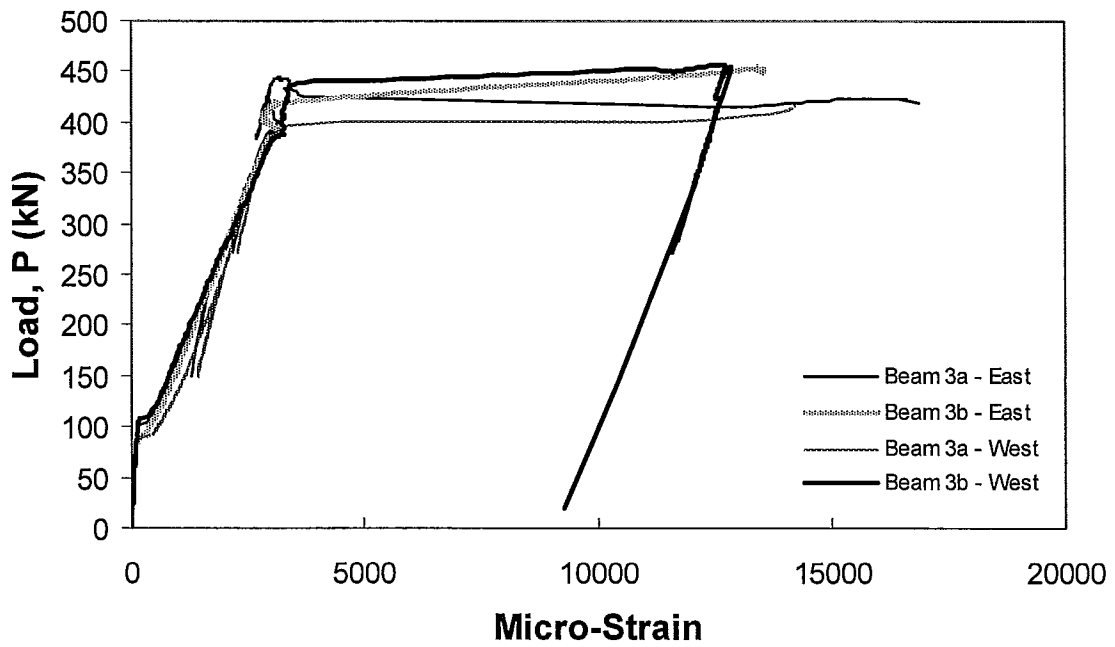


Figure 4.57: Type 3 Beams Longitudinal Steel Strain under Point Loads

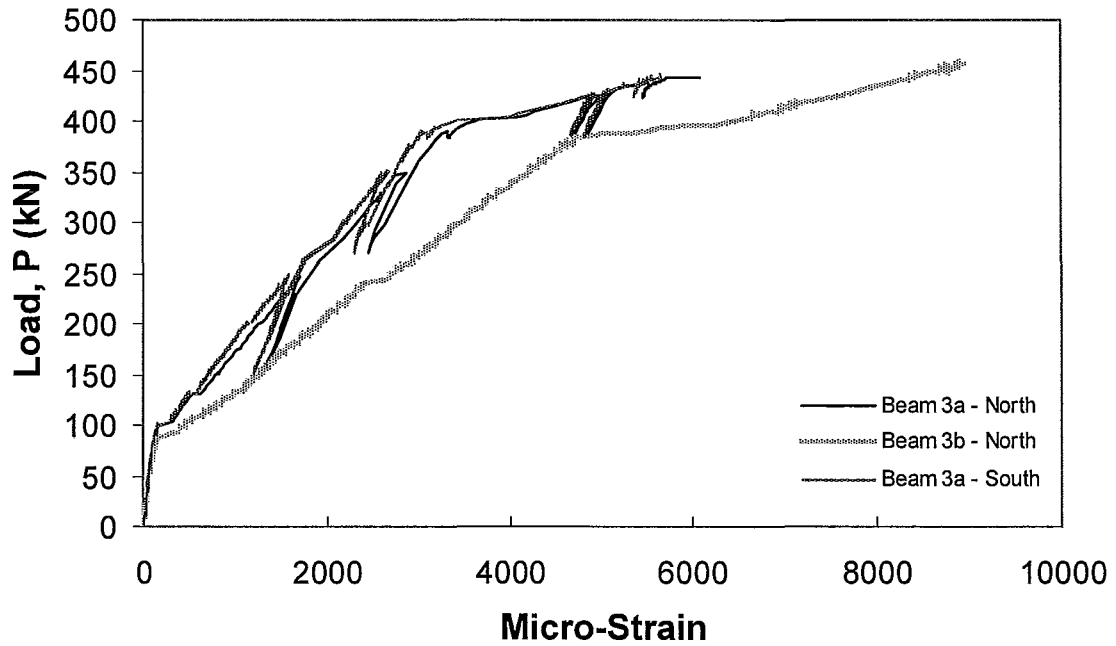


Figure 4.58: Type 3 Beams Longitudinal CFRP Strain under East Point Load

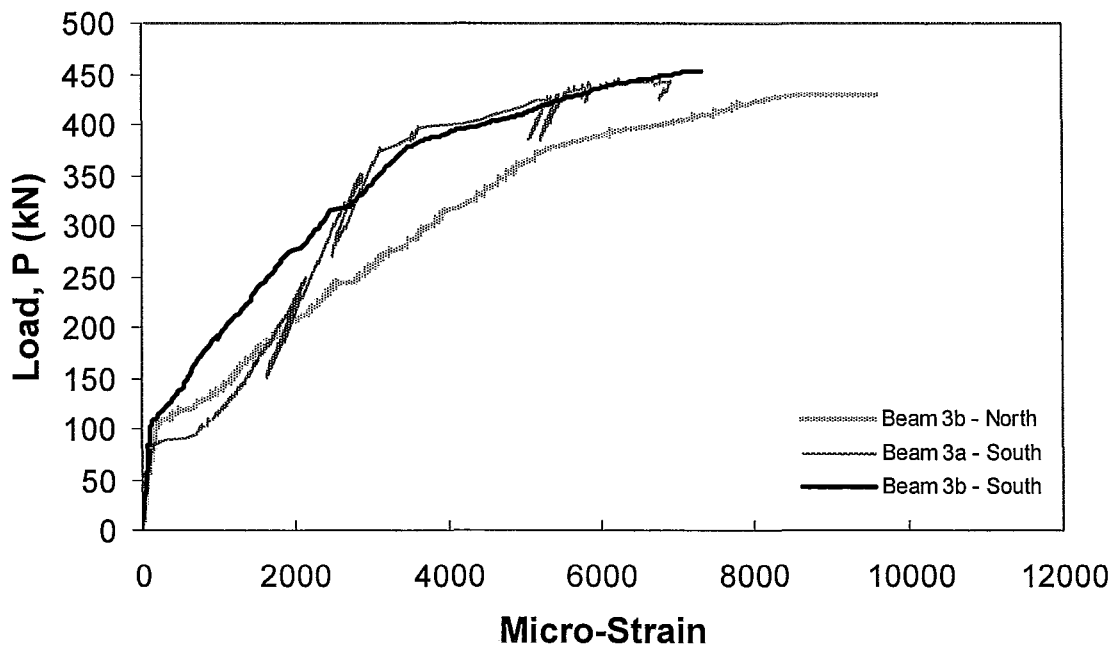


Figure 4.59: Type 3 Beams Longitudinal CFRP Strain under West Point Load

---

neutral axis of the beam, but the difference is not as significant as observed in the case of the other beams. Note that unlike the sudden drop in the steel strain curves of beams 1a and 1b immediately after delamination, type 3 beams show an insignificant load drop after the onset of delamination. This behaviour is desirable as the beams continue to deflect after delamination with relatively little effects on the beams overall strength.

Figure 4.60 and Figure 4.61 show the strain variation in the two NSM bars of beams 3a and 3b, at 200 mm from the bars east and west ends, respectively. For beam 3a, it can be observed that these bars experience significant strain after the advent of cracking and in some cases reach a maximum strain exceeding 4000 micro-strain, which is nearly the same as observed in type 2 beams. Observe the rather large increase in strain immediately after cracking at a load of approximately 150 kN. This large increase, as discussed earlier, indicates absence of tension-stiffening in beams with FRP reinforcement. The general behaviour of beam 3b is similar to that of beam 3a where the strain values reached 4,000 to 5,000 micro-strain. Unlike beams 1a and 1b, these strain values near the bar ends are nearly double the corresponding values in type 1 beams.

The strain variations in the steel and NSM bar reinforcement at the mid-span of beam 3a and 3b are shown in Figure 4.62 and Figure 4.63. The yield plateau is not shown in the following figures as the gauges were damaged during the test in the case of beam 3a and prior to testing in the case of beam 3b. Since both NSM bars generally followed the same strain behaviour, it indicates that the load was applied symmetrically. Once extensive delamination occurred, the NSM bars became ineffective and the resistance of the section dropped. For beam 3b, the CFRP bars reached strains exceeding 7500 micro-strain before delamination, which is nearly double the achieved strain observed in the type 1 beams.

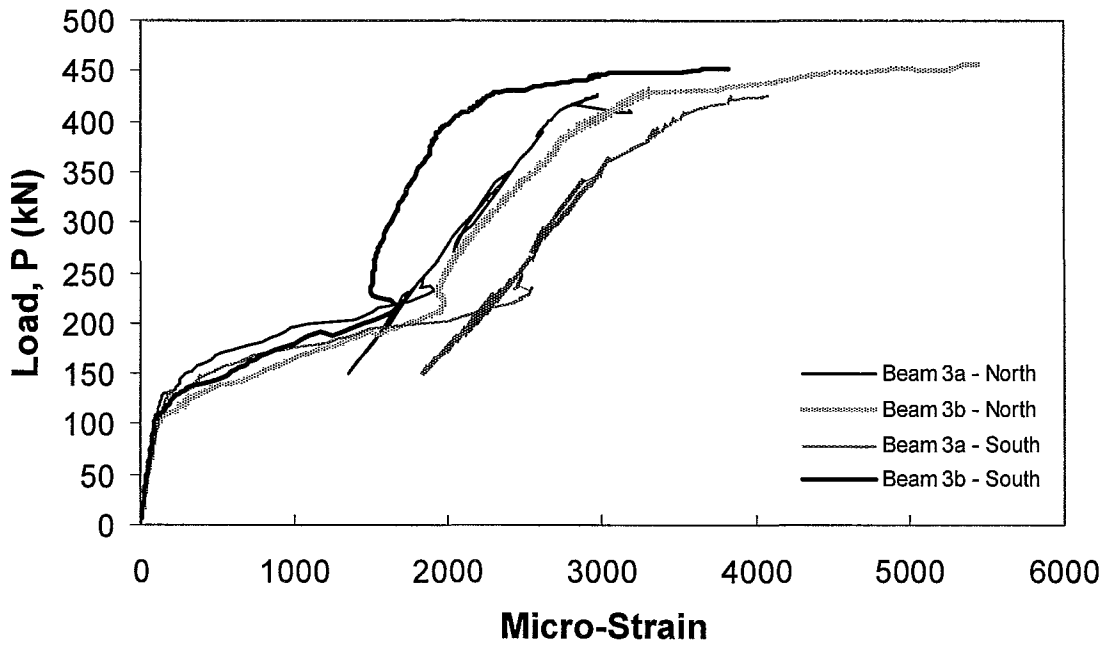


Figure 4.60: Type 3 Beams Longitudinal CFRP Strain 200 mm from East Bar End

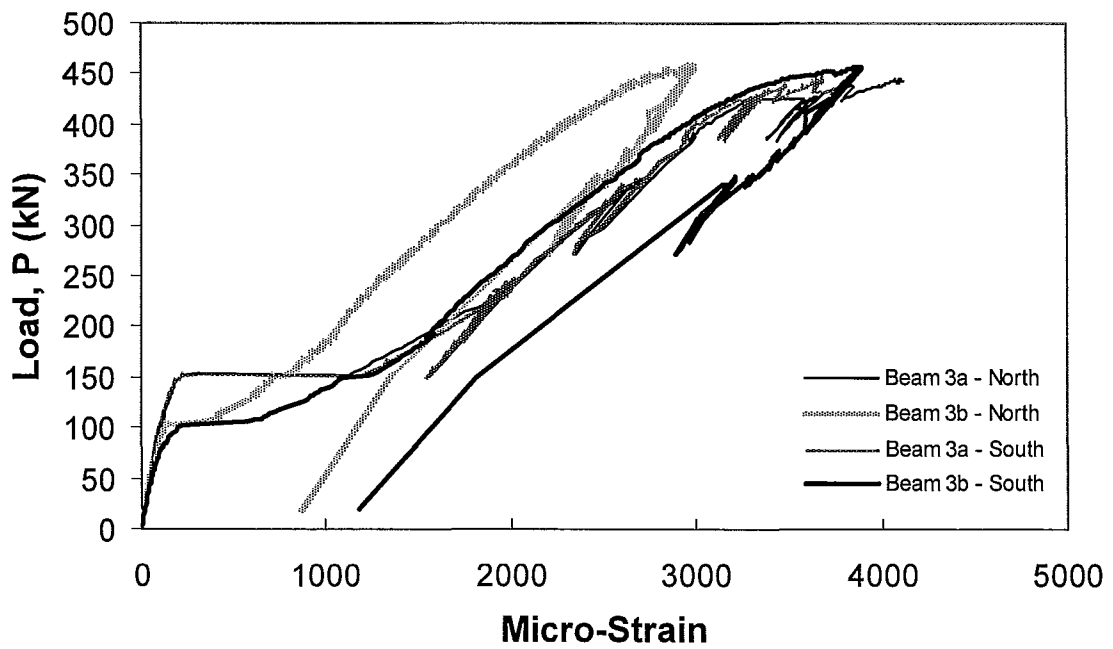


Figure 4.61: Type 3 Beams Longitudinal CFRP Strain 200 mm from West Bar End

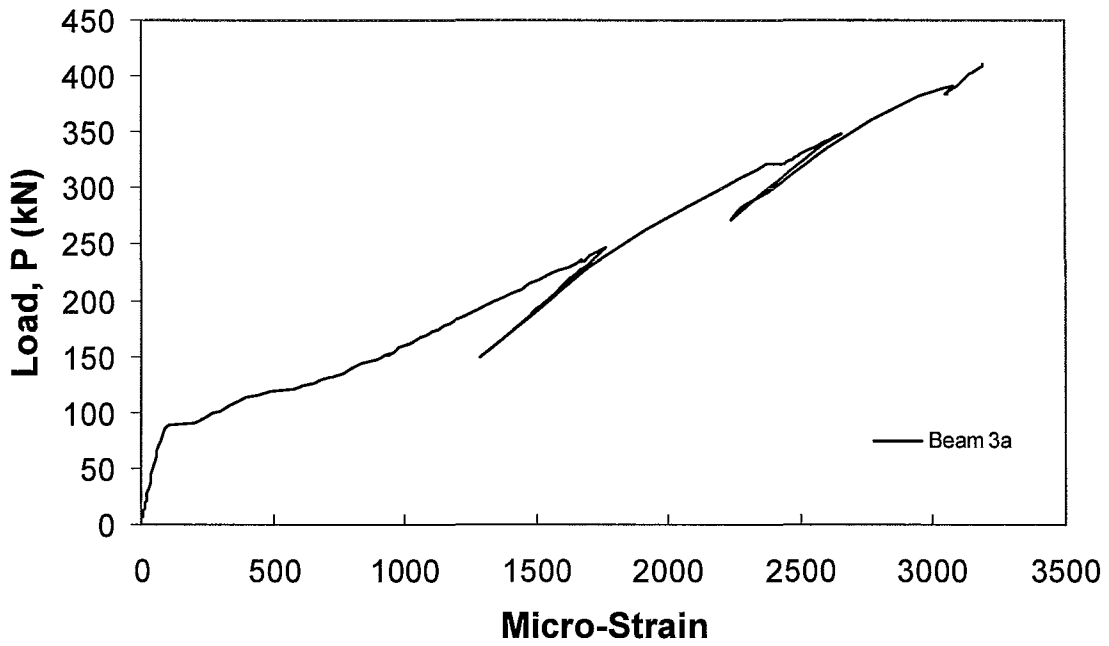


Figure 4.62: Type 3 Beams Longitudinal Steel Strain at Mid-Span

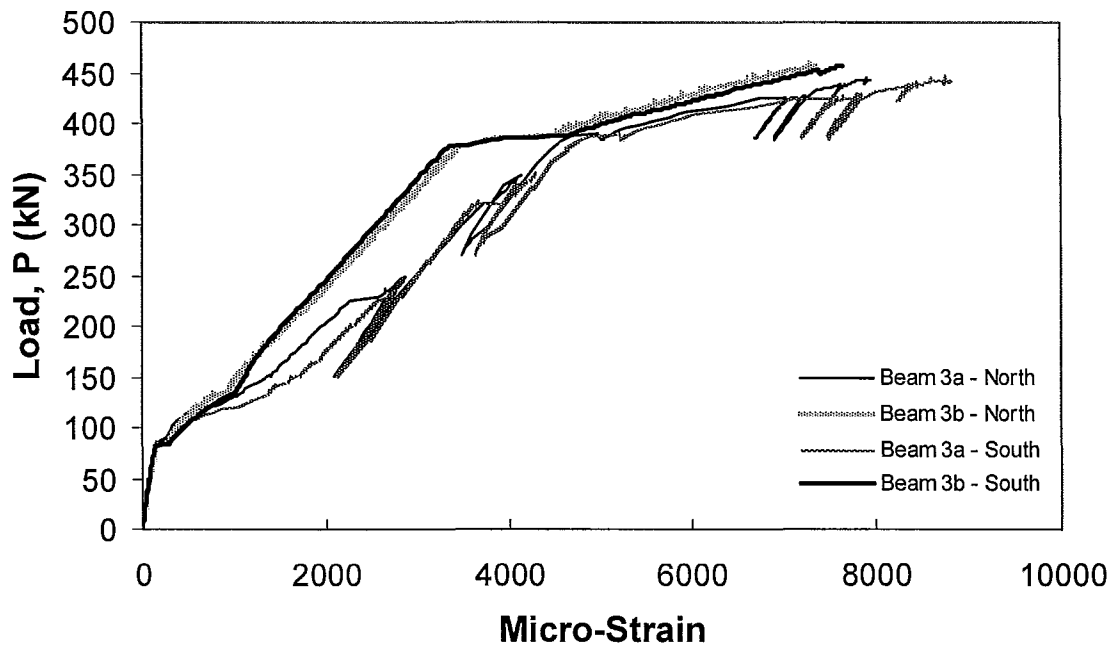


Figure 4.63: Type 3 Beams Longitudinal CFRP Strain at Mid-Span

Selected stirrups were strain gauged to measure their deformations. Figure 4.64 and Figure 4.65 show the variation of strain with the applied load in each leg of the steel stirrups located at a distance of 390 mm from the east and west supports, respectively. Stirrups in both beams 3a and 3b, appear to remain elastic throughout the testing. As noted during the discussion of the type 1 and 2 beams results, the strain values are relatively high given that the beams were designed to have a shear capacity twice their bending capacity.

Selected transverse NSM bars were gauged to measure their deformations. Figure 4.66 and Figure 4.67 show the variation of strain with the applied load in each NSM transverse bar located at distances of 250 and 500 mm from the east support. In both strengthened beams, the bar strains located at a distance 250 mm from the support illustrated extremely small strains, approximately 10%, of the strain in the internal stirrups located 390 mm from the support, and the NSM bars located 500 mm from the

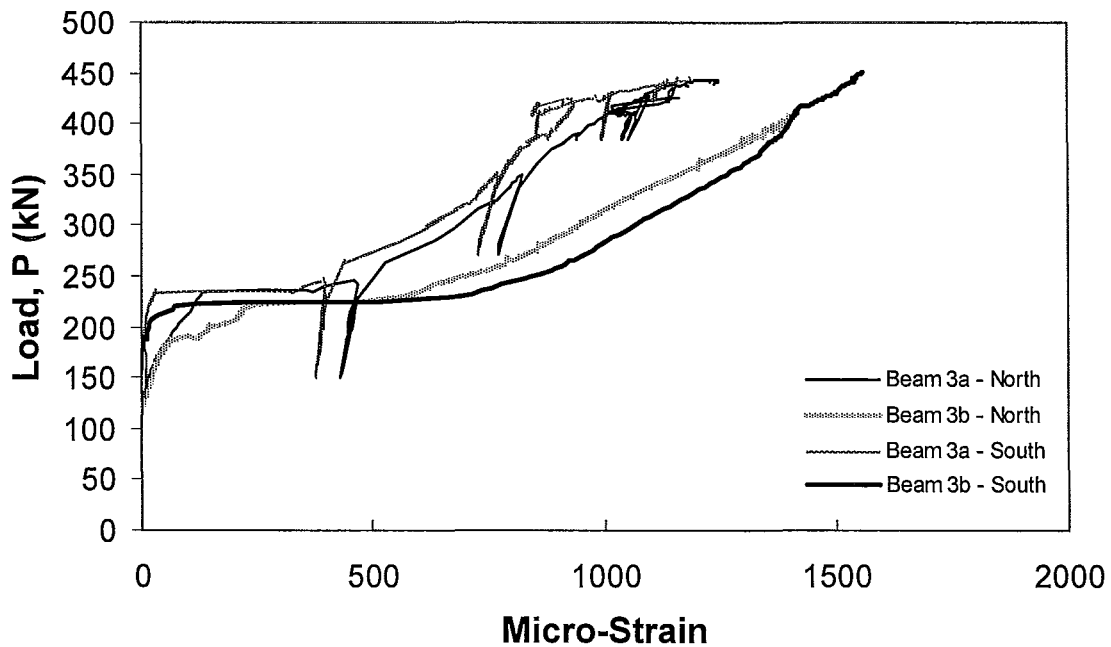
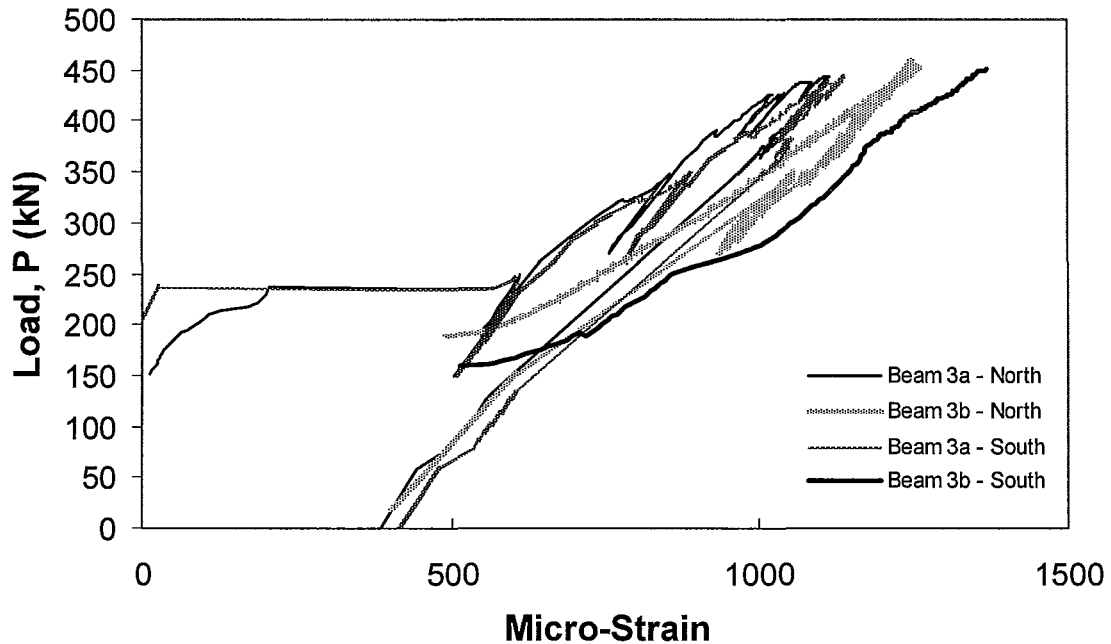


Figure 4.64: Type 3 Beams Steel Stirrup Strain 390 mm from East Support



*Figure 4.65: Type 3 Beams Steel Stirrup Strain 390 mm from West Support*

support. Whereas shear cracks formed 500 mm from the supports, they did not form at 250 mm and therefore the transverse NSM bars at 250 mm from the supports did not intercept diagonal cracks, which explains the unexpectedly low strain values in these bars. On the other hand, the maximum strain observed in the transverse NSM bars 500 mm from the support is practically the same as the maximum strain in the internal stirrups. Although the latter strain values are appreciable, they are still only 20% of the maximum strain capacity of the bars. Finally, it is important to point out that none of the transverse NSM bars delaminated.

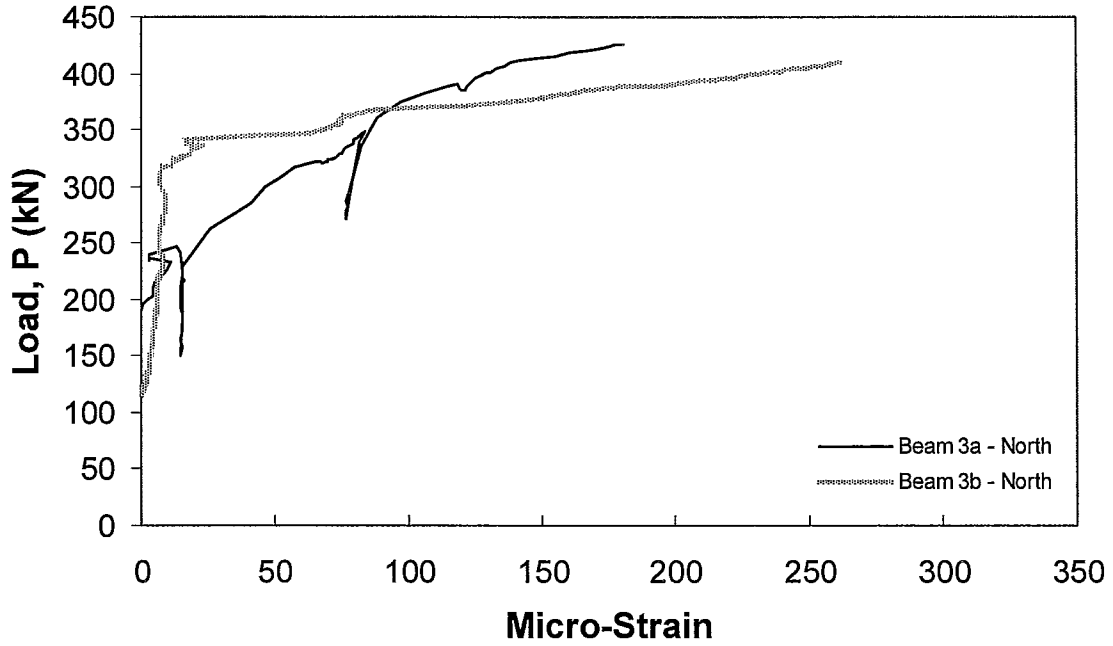


Figure 4.66: Type 3 Beams Transverse CFRP Strain 250 mm from East Support

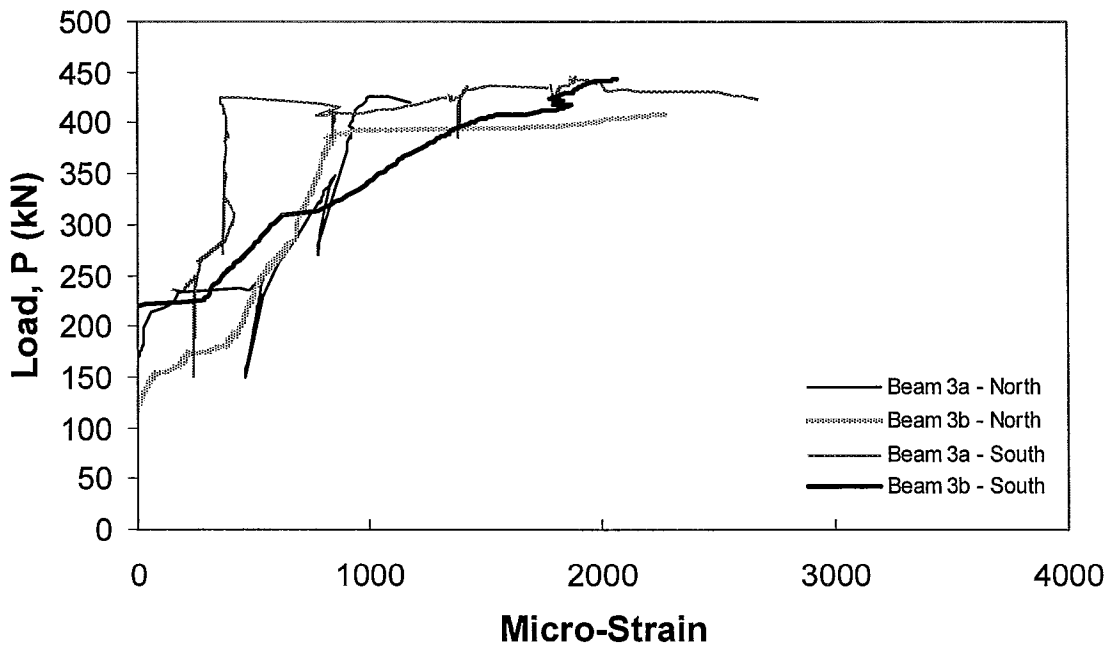
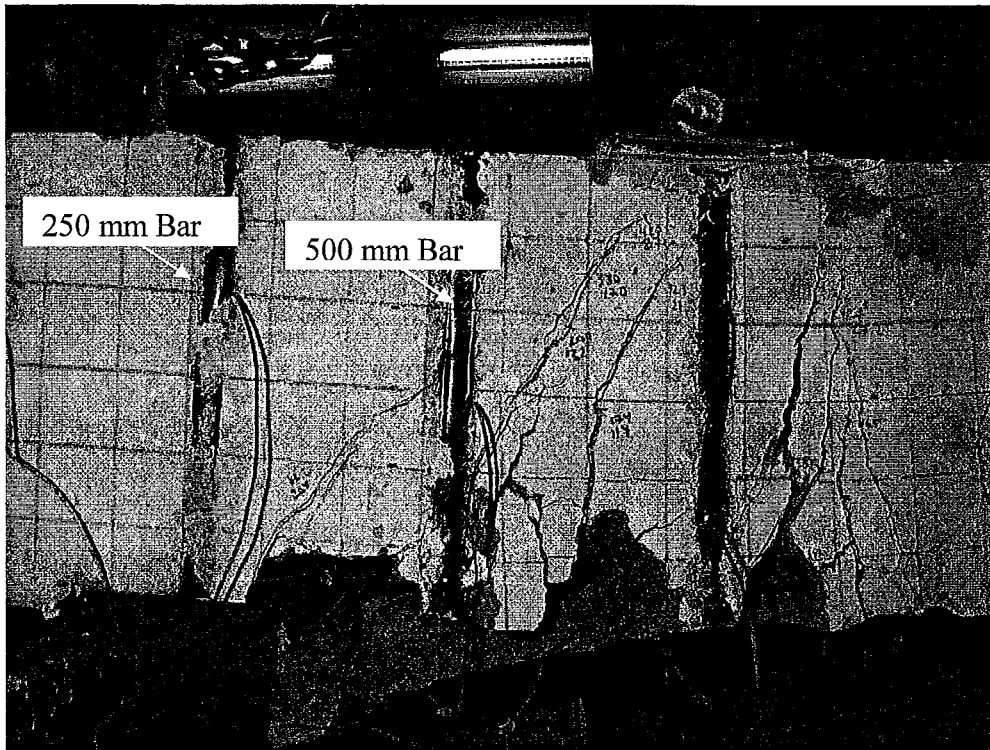
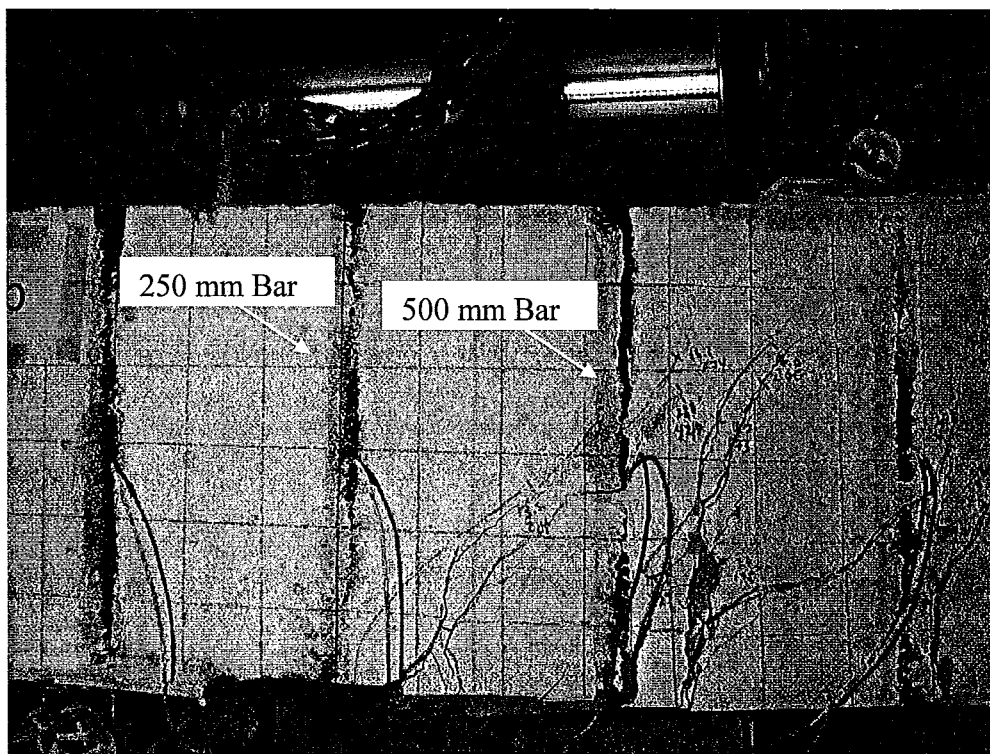


Figure 4.67: Type 3 Beams Transverse CFRP Strain 500 mm from East Support



*Figure 4.68: Intersecting Cracks along Transverse NSM Bars in Beam 3a*



*Figure 4.69: Intersecting Cracks along Transverse NSM Bars in Beam 3b*

#### 4.6. Summary of Results

All the NSM strengthened beams failed in flexure as designed. Table 4.1 summarizes the test data obtained from the load-midspan deflection curves. All the beams experienced first cracking load in the range of 88 to 101 kN. The strengthened beams without anchors, beams 1a and 1b, had lower delamination load than the beams with anchors. Additionally, the beams with the integral anchors all achieved higher ultimate load of approximately 50 kN or 13% compared to the NSM strengthened beams without anchors.

*Table 4.1: Summary of Experimental Testing*

Beam	Cracking Load (kN)	Delamination Load (kN)	Load Drop After Delamination (kN)	Ultimate Load (kN)	Type of Failure
Control	95	-	-	596	Tension Failure
1a	101	408	68	408	Tension Failure
1b	100	399	68	399	Tension Failure
2a	87	436	14	447	Tension Failure
2b	89	463	47	463	Tension Failure
3a	92	426	48	444	Tension Failure
3b	88	457	28	457	Tension Failure

In addition to the increased load carrying capacity, the anchored beams load deflection behaviour was different from that of the beams without anchors. The beams without anchors, or type 1 beams, continued to resist higher load until the onset of delamination, thereafter, where there was a sharp decline in their capacity as noted in Table 4.1. The strength of these beams continued to decline until the load was entirely carried by the internal steel and the beams failed when the compression zone experienced extreme crushing due to large deflections and curvature. On the other hand, the strengthened beams with anchors maintained their strength after the initial delamination of the NSM bars. The strength in all cases of the anchored beams remained relatively constant even after extensive delamination. Finally, the anchors pulled the concrete cover from the core of the beams causing the NSM bars to completely delaminate.

---

The observed maximum strain values in the flexural NSM bars were larger in the anchored beams compared to the beams without anchors. This characteristic was most apparent in the constant moment region where the tensile forces are largest; but even in the shear span, the anchored bars maximum strain achieved nearly twice the corresponding strain in the unanchored bars. Additionally, the strains in the NSM bars for all the strengthened beams, were larger than the strains in the steel reinforcement due to the relative distance between their associated depths and their relative distance from the neutral axis.

The type 3 beams strengthened with both NSM flexural and transverse bars failed in flexure. The transverse NSM bars strains reached similar strain levels to that observed in the internal stirrups; however, where shear or diagonal cracks did not cross the NSM transverse bars, the recorded strain values were quite low.

Finally, it was observed during the flexural tests that the primary longitudinal reinforcing steel was behaving differently than the bare bar coupons used in the ancillary tests. The ancillary tests presented in chapter three exhibit a non-linear stress-strain relationship without a distinct yield point or plateau, while the flexural tests indicate elasto-plastic response with a distinct yield point and plateau. It is probable that the problem originated in the ancillary tests where strain gauges were not used to measure the strain; instead an electric extensometer was used which was loosely fitted to the steel coupons. Due to the consistency of the flexural tests, the observed steel behaviour obtained in the flexural tests will be used in the analysis and discussions in the next chapter.

# Chapter 5

## Analysis and Discussion of Test Results

### **5.1. General**

The experimental results of the seven beams will be analyzed and discussed in this chapter. The ultimate moment capacity of each beam will be determined using a non-linear analysis computer program as well as the procedure stipulated in the CSA A23.3-04 for manual calculations and the results will be compared with the corresponding experimental data. The theoretical strength evaluations will be based on the assumption of perfect bond between the NSM bars and the concrete. Additionally, the behaviour of the NSM strengthened beams with the anchors will be compared to that of the beams without the anchors.

The cause of premature delamination in the six NSM strengthened test specimens will be examined through consideration of the interfacial shear and normal stresses along the NSM bars. The interfacial shear stresses calculated based on experimental data and through a closed-form solution developed by Täljsten (1997) will be compared to the shear stress limits for concrete specified by CSA A23.3-04. The resultant of the shear stresses acting on the horizontal failure plane will be determined and will be assumed to be resisted by the anchors. The resultant will be computed by using the experimental interfacial shear stresses and assuming a tributary area within the failure plane for each anchor. The peeling stresses, acting normal to the failure plane, will be estimated using

the procedure suggested by Täljsten (1997). The objective of determining both the interfacial shear and peeling stresses is to compare these stresses near the bar end at the onset of delamination with the corresponding stress combinations that would cause concrete failure. The ultimate objective of this exercise is to see whether the delamination load and its corresponding stresses could be predicted with a reasonable degree of accuracy.

Finally, a brief analysis will be presented to compare the use of the NSM CFRP shear strengthening system to the internal steel U-stirrups to assess the viability of using NSM bars as effective shear reinforcement.

## **5.2. *Ultimate Flexural Capacity***

The objective of using NSM CFRP reinforcing bars was to effectively utilize the high strength of the carbon bars to increase the flexural capacity of a deficient beam. The tests provided the actual flexural capacity of each test beam as well as its overall flexural behaviour. Table 5.1 summarizes the experimental ultimate moment capacities,  $M_u$ , of the seven beams and a fictitious test beam. The fictitious beam, referred to as Base in Table 5.1, represents the six strengthened beams without the application of NSM bars. In the present study the control beam was designed to have similar moment capacity as the NSM strengthened beams; however, it is typically the case in NSM research that the control beam has identical internal reinforcement configuration as the strengthened beams, less the NSM bars. Control specimens are designed in such a way to indicate the strength gained by the control specimen after the NSM bars are attached, therefore since this particular beam was not tested in the current study, it is a fictitious beam and its theoretical capacity is calculated. In addition, to the experimental ultimate moment values, the table also shows the beams theoretical moment capacities using the non-linear analysis software, Wizard, and hand calculations based on the procedure prescribed by the CSA Standard A23.3-04.

**Table 5.1: Experimental versus Theoretical Ultimate Moments of Tested Beams**

Beam	Experimental Capacities				Theoretical Ultimate Capacities			
	Delamination		Ultimate		Wizard ( $\epsilon_{cu} = 0.0035$ )		Manual ( $\epsilon_{cu} = 0.0035$ )	
	Moment (kN·m)	Load (kN)	Moment (kN·m)	Load (kN)	Moment (kN·m)	Load (kN)	Moment (kN·m)	Load (kN)
Base	-	-	-	-	119	317	118	314
Control	-	-	224	597	226	603	224	597
1a	153	408	153	408	258	688	259	691
1b	150	400	150	400	258	688	259	691
2a	164	437	168	448	259	691	260	693
2b	174	464	174	464	259	691	260	693
3a	160	427	167	445	260	693	261	696
3b	171	456	171	456	260	693	261	696

When computing the theoretical flexural capacities, full bond is assumed between the CFRP bars and the surrounding concrete. The calculations are based on the strain compatibility method and the assumption of plane sections remain plane. All the hand calculations are shown in detail in Appendix A and are revised based on the material strengths obtained from the ancillary tests with the exception of the steel properties. Recall that in the previous chapter the flexural tests indicated that the steel behaved elasto-plastically in contrast to the ancillary test results which indicated a non-linear behaviour reminiscent of high strength steel behaviour. In the calculations all the material reduction factors,  $\phi$ , were set to 1.0 as the calculations ignore random variations in material and geometric properties of the beams.

The non-linear analysis program, Wizard, was written by Abushoglin (1997). The program requires the user to define all material properties: concrete, reinforcing steel and strengthening CFRP. Key material properties are used to develop the relevant stress-strain relationships for each constituent material and these relations are utilized to analyze the specified RC beam under flexure. Wizard permits the user to set the maximum concrete strain,  $\epsilon_u$ , to any value, which is advantageous when comparing the effect of the

ACI (American Code) and CSA (Canadian Standards) specified ultimate concrete strains of 0.003 and 0.0035, respectively, on the beam strength. The ascending branch of the concrete compressive stress-strain relationship is defined by the Hognestad parabolic relationship up to the concrete ultimate strength and then descends linearly until the ultimate strain is achieved. The steel model permits the user to include the strain hardening region after the yield strength is exceeded. The FRP stress-strain relationship is assumed to be linear-elastic where the ultimate strength and strain are defined in accordance with the stiffness of the material. Although both calculations (Wizard and hand calculations) assume perfect bond between the CFRP bars and the concrete, Wizard incorporates the non-linear stress-strain relationship of the concrete and all the reinforcement whereas hand calculations use the equivalent rectangular stress block and its associated parameters to estimate the stresses in the concrete. Furthermore, in the hand calculations steel is treated as an elastic-perfectly plastic material.

From the results in Table 5.1 it is apparent that the hand calculations and Wizard calculated values for the strengthened beams agree with one another and are much greater than the moment capacities achieved in the tests. Note that the theoretical capacities are based on a maximum concrete strain of 0.0035 at failure. This difference between the theoretical and experimental moment capacities can be attributed to premature delamination of the NSM bars. Generally, the capacity reduction in the experiments, relative to the hand or Wizard's calculation is approximately 40% and 32% for beams without anchors (type 1 beams) and beams with anchors (type 2 and 3 beams), respectively. Therefore illustrating an 8% gain in strength when the integral anchors were added to the CFRP strengthening bars.

One measure of the effectiveness of the NSM strengthening method is the maximum strain that could be reached in the NSM bars before the failure of the beam. The ratio of this strain to the maximum strain capacity of the bar could be denoted as the efficiency index of the NSM system. The efficiency index is a good indicator of both the economic and structural efficiency of the strengthening method, provided the economics

---

are measured in terms of efficiency of material utilization rather than labour or other related costs. For instance, if too much external reinforcement is provided (i.e. more than necessary to balance the strength of the concrete compression block in the beams under bending) the maximum strain in the NSM bars would not reach their ultimate strain capacity, even if the bars remained fully bonded to the concrete until failure. Similarly, if the maximum strain in the bars just before delamination is well below their maximum strain capacity, the bars will not be efficiently utilized. With the above objectives in mind, Figure 5.1 through Figure 5.6 present the maximum strain recorded in each of the longitudinal CFRP strengthening bars. If a strain gauge was damaged during the construction of the beams or peeled off during the loading process, the erratic data recorded by such a gauge are omitted from the following analysis.

As stated in Chapter 3, the CFRP bars used in the present study have ultimate tensile strength and elastic modulus of 1200 MPa and 100GPa, respectively. Assuming the bars to be linear-elastic, their expected ultimate strain is 12,000 micro-strain. The latter figures show that none of the bars reached its specified ultimate strain. This is due to delamination of the NSM bars before reaching their ultimate strain. However, larger strain values were achieved in the NSM bars with the anchors, beams 2a through 3b, than the bars without the anchors (i.e. beam 1a and 1b). Beams 1a and 1b reached average maximum strains corresponding to 39% and 33% of the rupture/ ultimate CFRP bar strain, respectively, while beams 2a, 2b, 3a and 3b reached an average maximum strain corresponding to 60%, 67%, 59% and 69% of the rupture/ ultimate CFRP bar strain, respectively. Thus, the corresponding efficiency index for these beams are 0.39, 0.33, 0.60, 0.67, 0.59 and 0.69, respectively. The previously listed percentages were based on the average maximum strain recorded in both the north and south bars located within the constant/ maximum moment region. The anchors helped the longitudinal CFRP bars achieve greater strain by delaying the onset of delamination, which as discussed in the following section, is accomplished by resisting the interfacial shear stresses and the normal peeling stresses acting on the horizontal failure plane.

It is worthwhile to point out that in some cases the measured bar strains within the shear span are larger than those within the maximum moment region. This behaviour can be explained by the fact that the longitudinal bars are subjected to extra tension by the applied shear within the shear span. This behaviour can be easily explained by the so-called truss model (Park and Paulay, 1975).

Although all three beam types failed prematurely due to cover delamination, the beams with anchors behaved differently than those without the anchors. Figure 5.7 presents the recorded load-deflection diagrams for beams 1a, 2a and 3a. Since beams 1b, 2b and 3b were nominally the same as their companion type ‘a’ beams and in the previous chapter it was illustrated that their load-deflection curves were similar to that of the type ‘a’ replicate beams, the load-deflection curves of type ‘b’ beams were omitted from Figure 5.7. In the latter figure only the first 80 mm of the central deflection experienced by the beams is shown because thereafter delamination and full separation of the NSM reinforcement occurred, and the beams began to behave as typical RC beams. The theoretical moment capacity of the strengthened beams without the NSM reinforcement is approximately 118 kN·m, corresponding to a total applied load of 314 kN, as calculated using Wizard. In Figure 5.7 the load level of 339 kN lies between the loads at the ends of the curves for the beams with and without anchors. This verifies that the strengthened RC beams behave as the original unstrengthened RC beams after the NSM delamination.

Although the beams strengthened with the anchors only achieved approximately 8% to 14% higher ultimate moment than the beams without the anchors, a significant increase in ductility was achieved by the four beams with the anchors. This is evident in

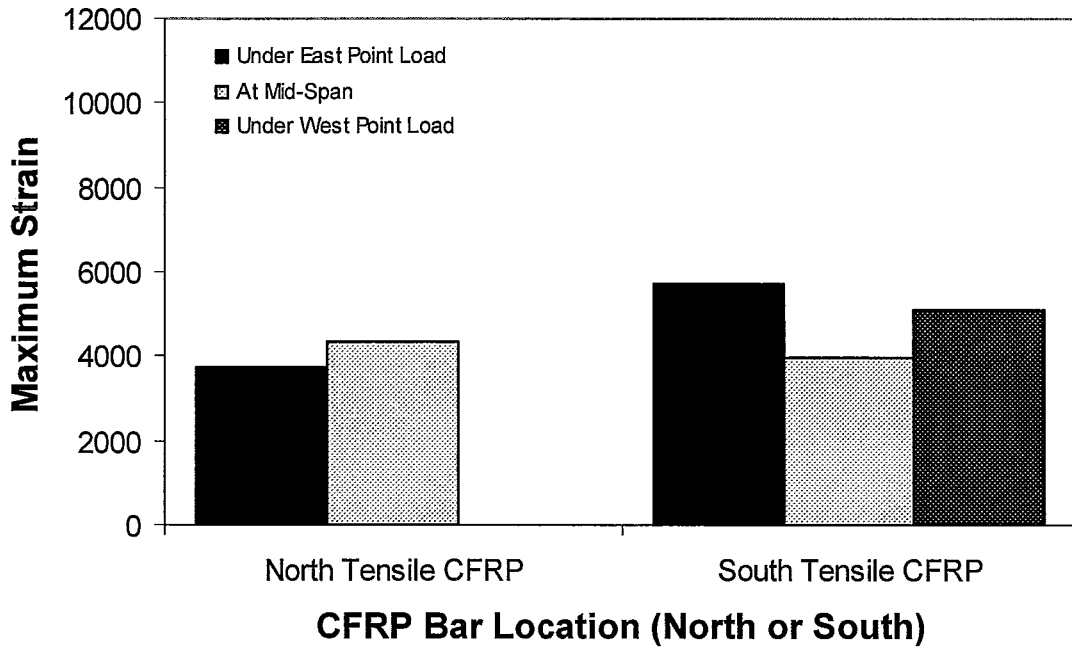


Figure 5.1: Maximum Recorded Strains in CFRP Bars in Beam 1a

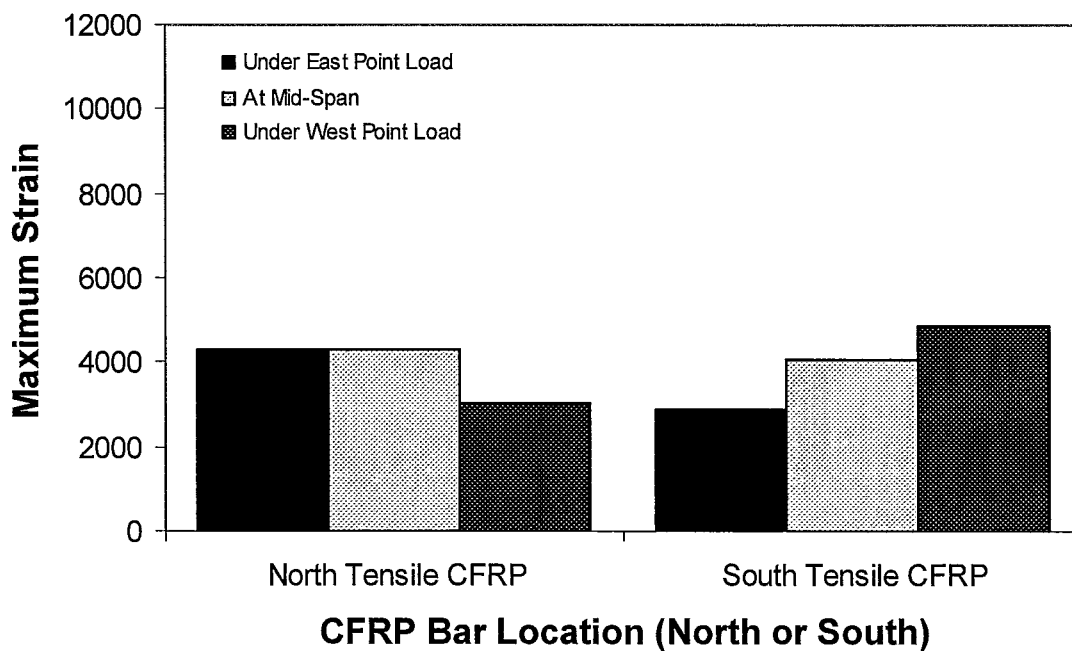


Figure 5.2: Maximum Recorded Strains in CFRP Bars in Beam 1b

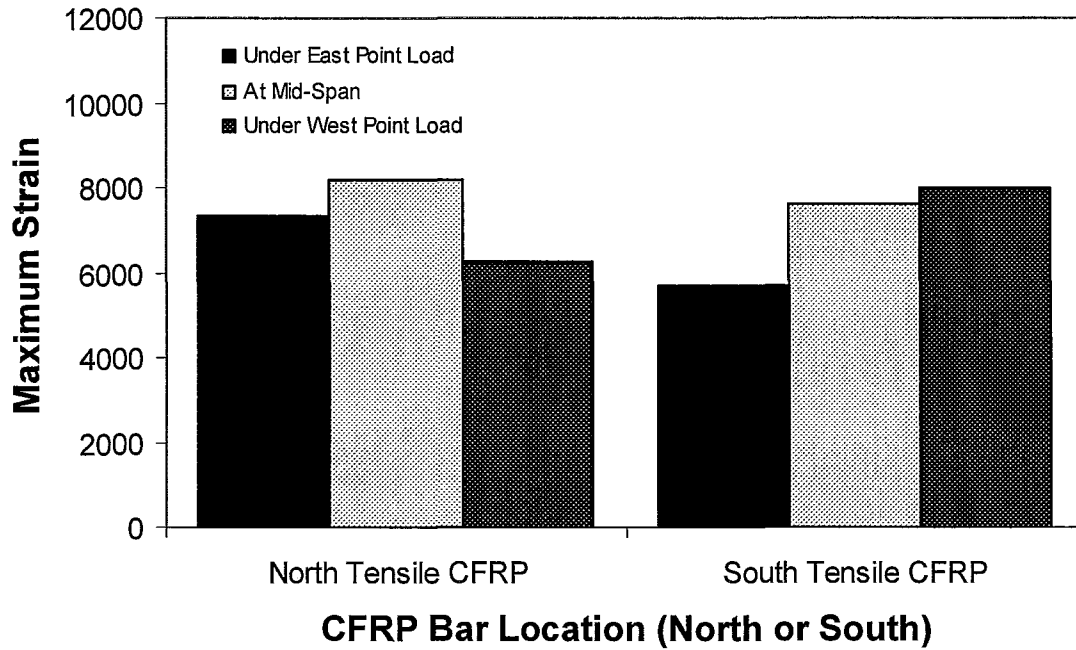


Figure 5.3: Maximum Recorded Strains in CFRP Bars in Beam 2a

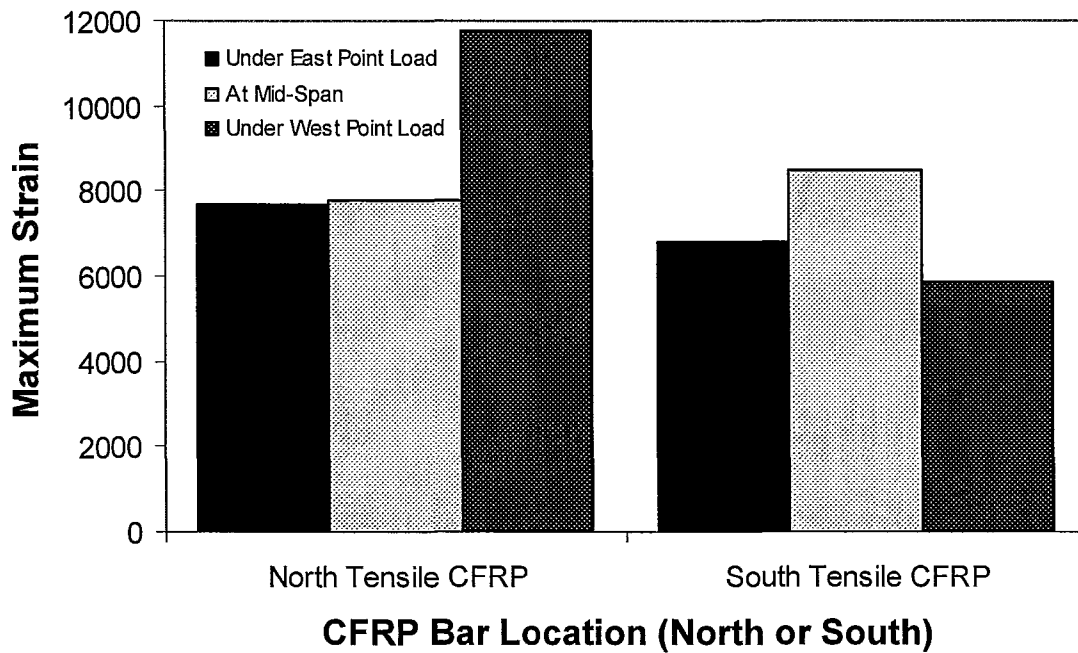


Figure 5.4: Maximum Recorded Strains in CFRP Bars in Beam 2b

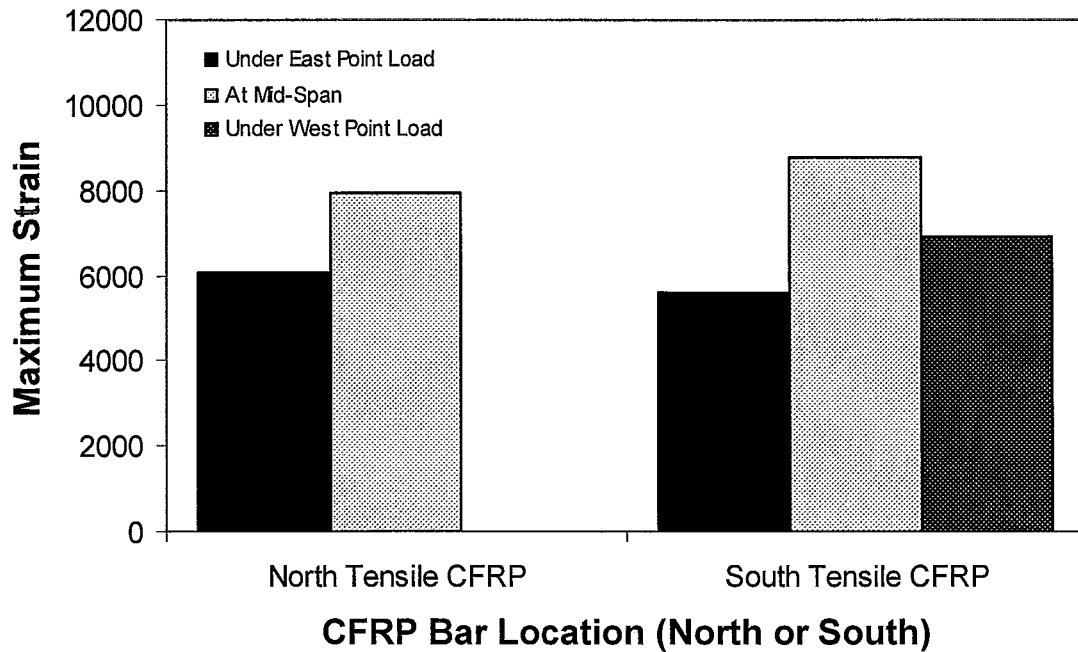


Figure 5.5: Maximum Recorded Strains in CFRP Bars in Beam 3a

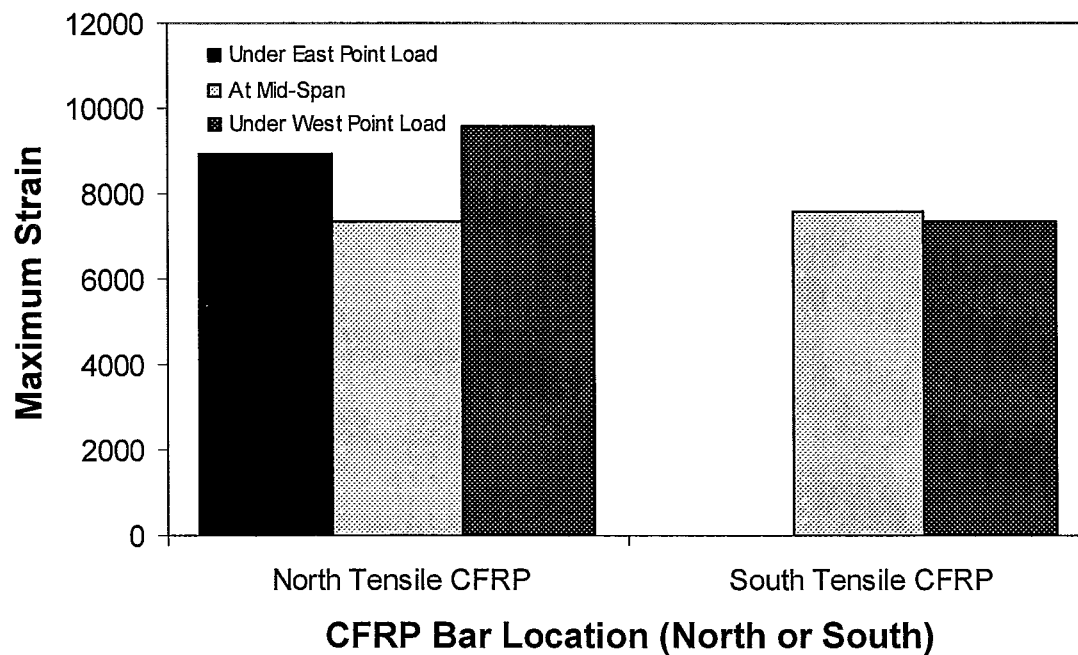


Figure 5.6: Maximum Recorded Strains in CFRP Bars in Beam 3b

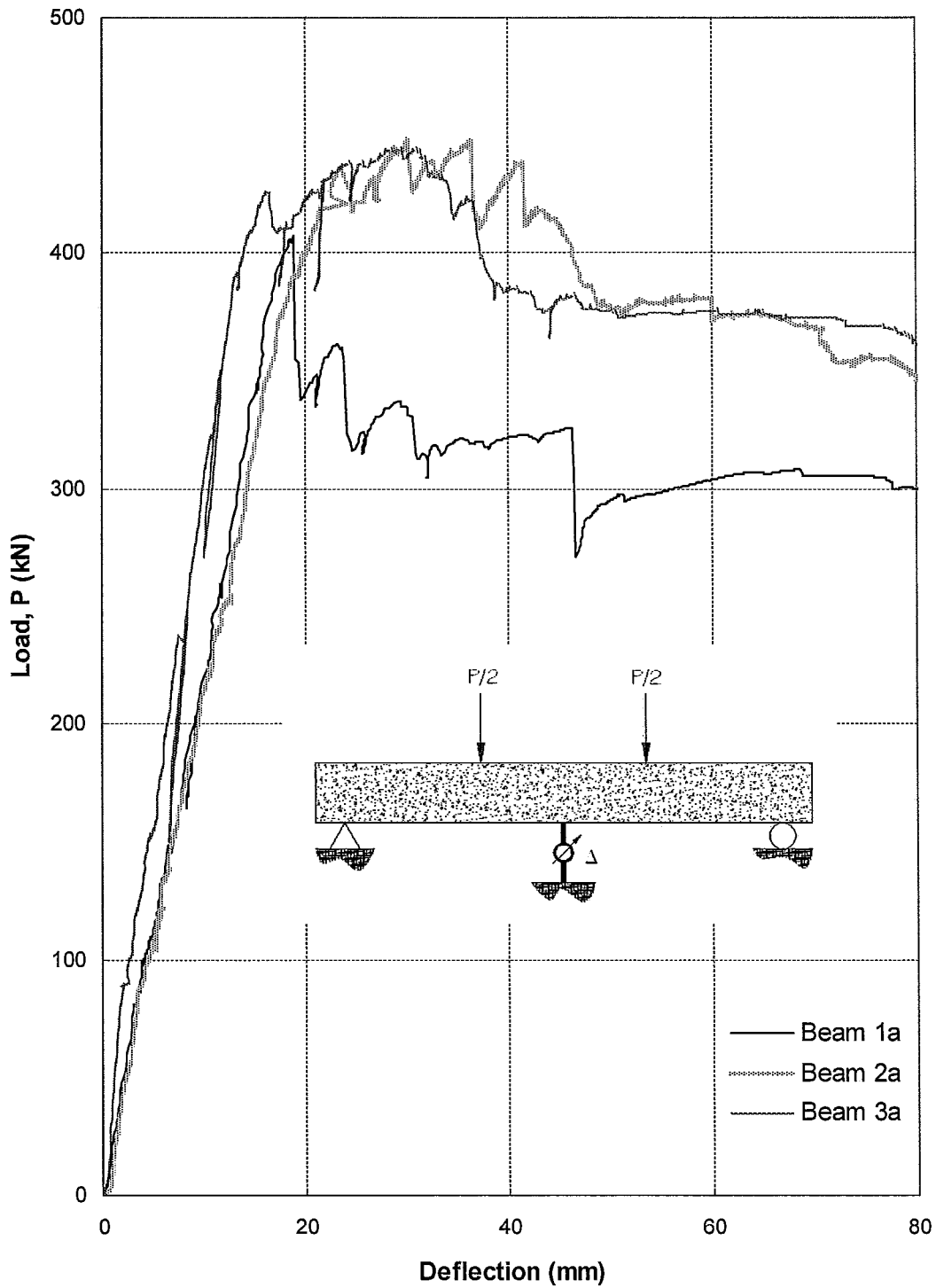


Figure 5.7: Load-Midspan Deflection for Beams 1a, 2a and 3a

Figure 5.7 where one observes that after beam 1a reached its ultimate load,  $P_u = 404$  kN, its resistance subsequently decreased sharply to 342 kN. This accounts for a decrease of over 15% in strength within an increase of 1.3 mm in displacement. On the other hand, beams 2a and 3a experienced some increase in strength after the onset of delamination. Delamination initiated in beams 2a and 3a at 437 kN and 427 kN, respectively, but they continued to gain strength thereafter. After the onset of delamination, beams 2a and 3a continue to deflect another 19 mm and 20 mm, respectively, before the NSM bars completely delaminate. Observe that the beams with the anchors have a higher residual strength even after the maximum deflection reached 80 mm.

Since in design strain-hardening is not generally considered, it can be argued that retro-fitting without anchors increased the beam load carrying capacity by at least a factor of  $\frac{404kN}{280kN} = 1.44$  while retrofitting with anchors increased it by at least a factor of  $\frac{447kN}{280kN} = 1.60$ . The numerator and denominator in the preceding ratios are the strength of the beams with and without NSM retro-fitting.

### 5.3. Interfacial Shear

Given the exceptional strength of the CFRP bars used to strengthen the test beams, the governing failure mechanism in every case was premature separation of the concrete cover. In every case the epoxy demonstrated excellent bond to the CFRP bar surface and to the concrete groove surfaces; however, the interfacial shear capacity of the concrete cover was exceeded causing the cover, with the NSM bars fully bonded to it, to detach from the concrete web. The failure occurred in the concrete between the internal longitudinal reinforcing steel and the grooves where substantial interfacial (longitudinal) shear and normal stresses can develop. Figure 5.8 schematically illustrates the normal or peeling stress and the interfacial shear stress distribution on the horizontal failure plane within the concrete cover. During testing, as discussed in the previous chapter, this plane failed typically in all the strengthened beams. The failure plane propagated from the bar

cut-off section toward the beam mid-length separating the cover from the rest of the beam. In the following sections these stresses will be examined and discussed in more detail.

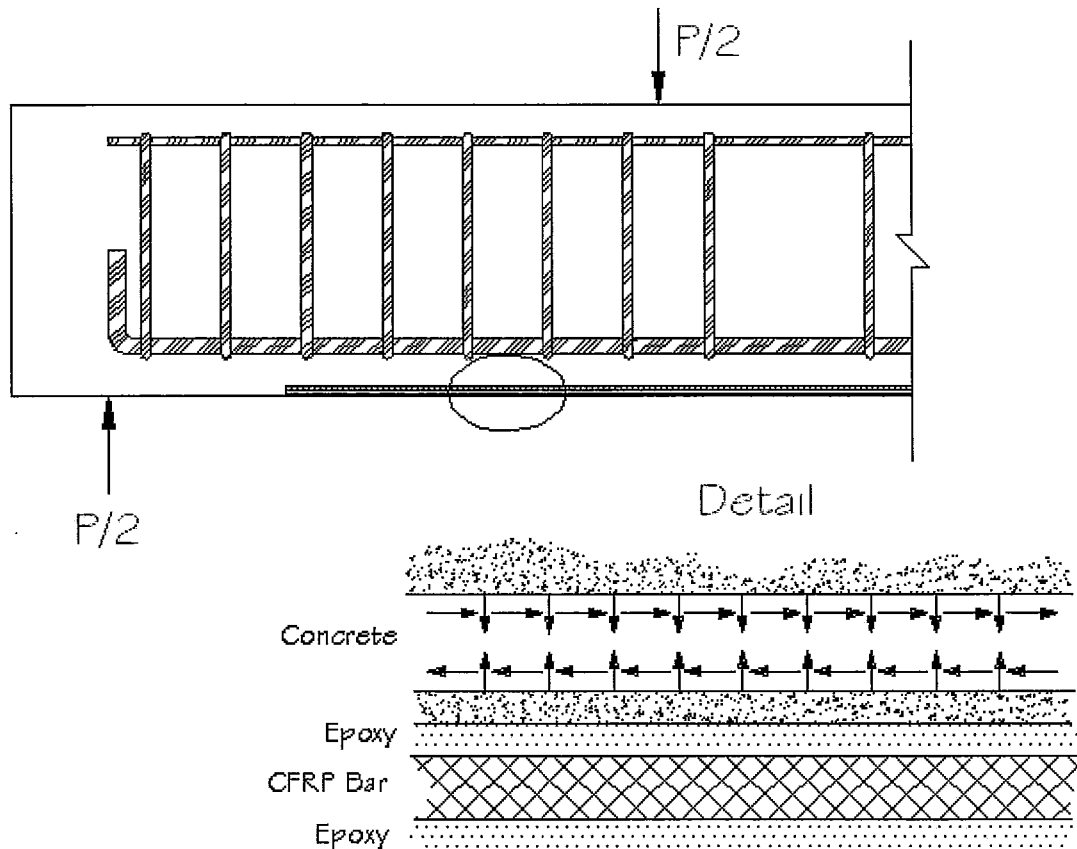


*Figure 5.8: Interfacial Shear and Normal Stress Distribution in the Concrete Cover*

### 5.3.1. Interfacial Shear Stresses based on Experimental Data

To relate the CFRP strains measured during the tests to the interfacial shear stresses,  $\tau_{xy}$ , consider the free-body diagram of an infinitesimal element of the CFRP bar in Figure 5.9. The bar is subjected to longitudinal forces,  $T_{fx}$ , along its x-axis due to the moment acting on the beam. The moment arm, as used in typical RC beam analysis, varies from cross-section to cross-section dependant on the moment acting on each section. Additionally, the stresses induced on the bonded CFRP bar perimeter,  $\tau_{xy}$  and  $\sigma_y$ ,

transmit the developed force in the bar,  $T_{fx}$ , to the surrounding epoxy and in turn to the RC beam. Together the steel and CFRP resist the applied moments.

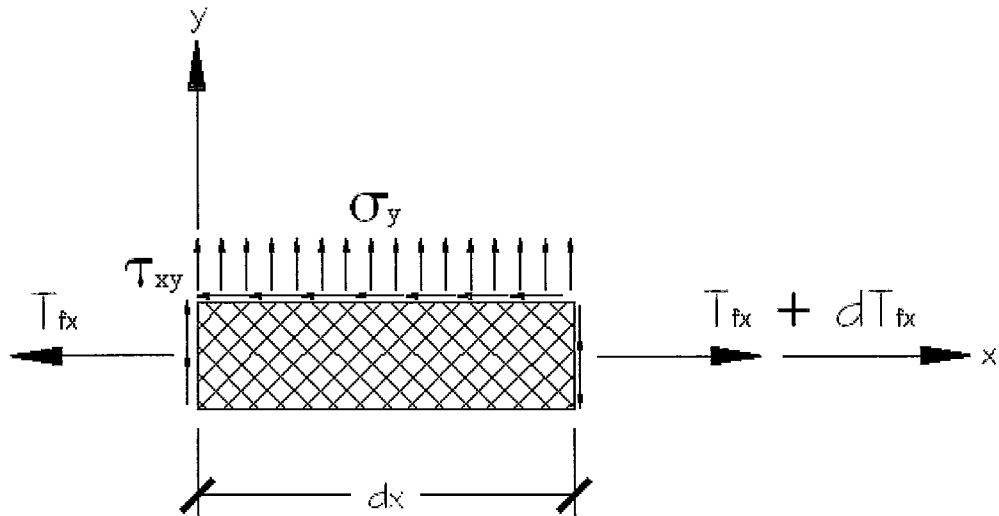


**Figure 5.9: Infinitesimal Element of CFRP Bar Free-Body Diagram**

Considering the equilibrium of the horizontal forces acting on the element in Figure 5.9,  $\sum F_x = 0$ ,

$$(T_{fx} + dT_{fx}) - T_{fx} - \tau_{xy} A_{bond} = 0 \quad (5.1)$$

or

$$dT_{fx} - \tau_{xy} l_p dx = 0 \quad (5.2)$$

where  $l_p$  is the portion of the perimeter of the CFRP bar cross-section bonded to the surrounding concrete. In the current tests the bars were bonded on three faces to the concrete, therefore,  $l_p$  is equal to 35 mm for a single bar. From Equation 5.2 it follows that

$$\frac{dT_{fx}}{dx} = \tau_{xy} l_p \quad (5.3)$$

Since CFRP is a linear elastic material until rupture, the bar longitudinal force can be related to its strain using Hooke's law,

$$T_{fx} = E_f \varepsilon_{fx} A_b \quad (5.4)$$

where  $E_f$  is the elastic modulus of the CFRP bar,  $A_b$  is its cross sectional area and  $\varepsilon_{fx}$  is its strain. Substituting for  $T_{fx}$  from equation 5.4 into equation 5.3, gives

$$\frac{d}{dx}(E_f \varepsilon_{fx} A_b) = \tau_{xy} l_p \quad (5.5)$$

$$\tau_{xy} = \frac{d\varepsilon_{fx}}{dx} \left( \frac{E_f A_b}{l_p} \right) \quad (5.6)$$

Equation 5.6 indicates that the shear stresses are a function of the CFRP bar strain gradient,  $\frac{d\varepsilon_{fx}}{dx}$ , along its length. We will estimate the gradient of the recorded strains by assuming a linear variation between any two consecutive points on the CFRP reinforcement and use Equation 5.6 to calculate the shear stresses along the length of the bar. The strains were not recorded at the ends of the CFRP bars, however, we can assume that the interfacial shear stresses will be zero at these locations due to the fact that the bar end is a free surface.

The following twelve figures, Figure 5.10 through Figure 5.21, illustrate the interfacial shear stresses calculated at the level of the NSM CFRP bars. These were calculated using the recorded experimental data and the relationship given in Equation 5.6. For the sake of clarity, the interfacial shear stresses for each beam are plotted in two separate figures. The first figure presents the interfacial shear at lower load levels, generally up to 40% of the ultimate load, and the second at higher load levels near failure or in some cases at the maximum recorded load level before some strain gauges became inoperable. The figures show the same general trend from one beam to the next. The interfacial shear stresses are maximum near the CFRP reinforcement ends, or within the shear spans and minimal in the constant moment region. This behaviour is similar to the standard elastic shear force diagram for a simply supported beam subjected to four-point bending.

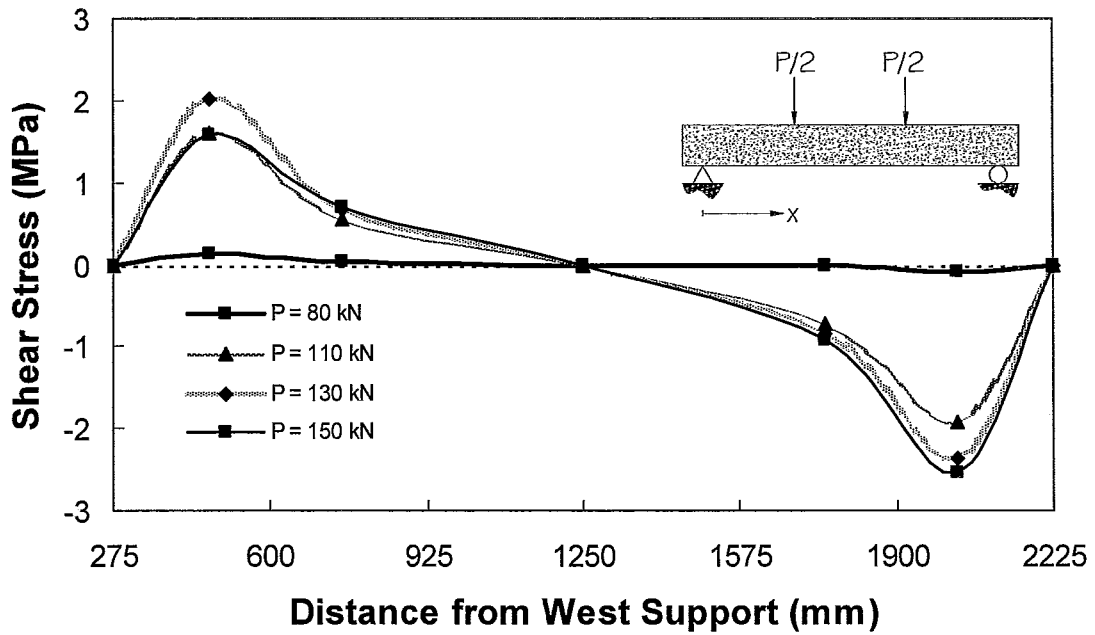


Figure 5.10: Shear Stress along the CFRP Reinforcement for Beam 1a

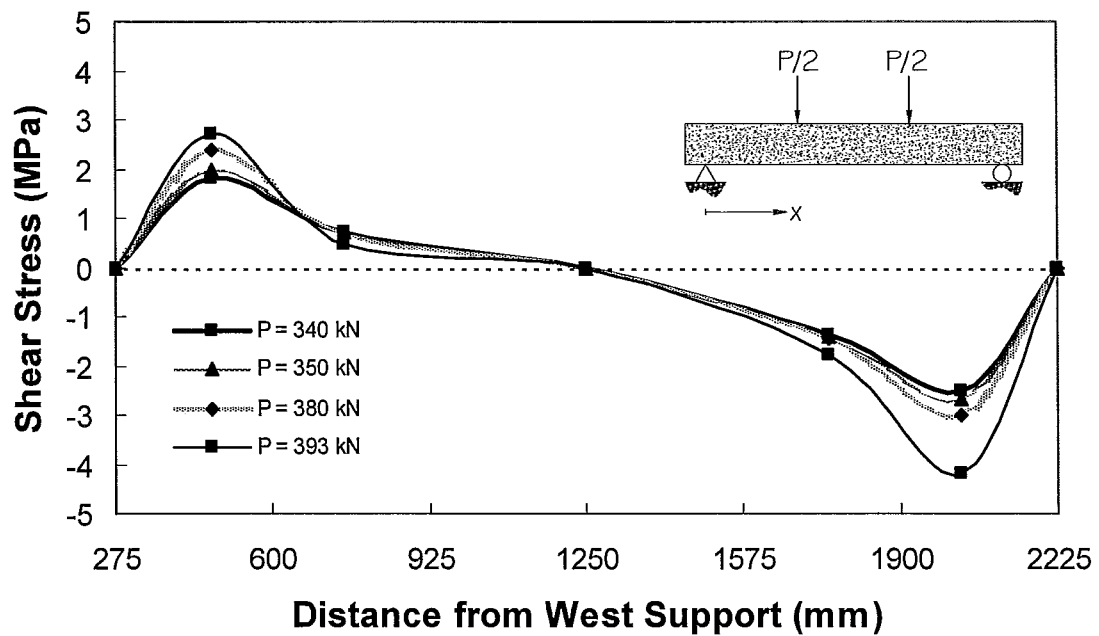


Figure 5.11: Shear Stress along the CFRP Reinforcement for Beam 1a

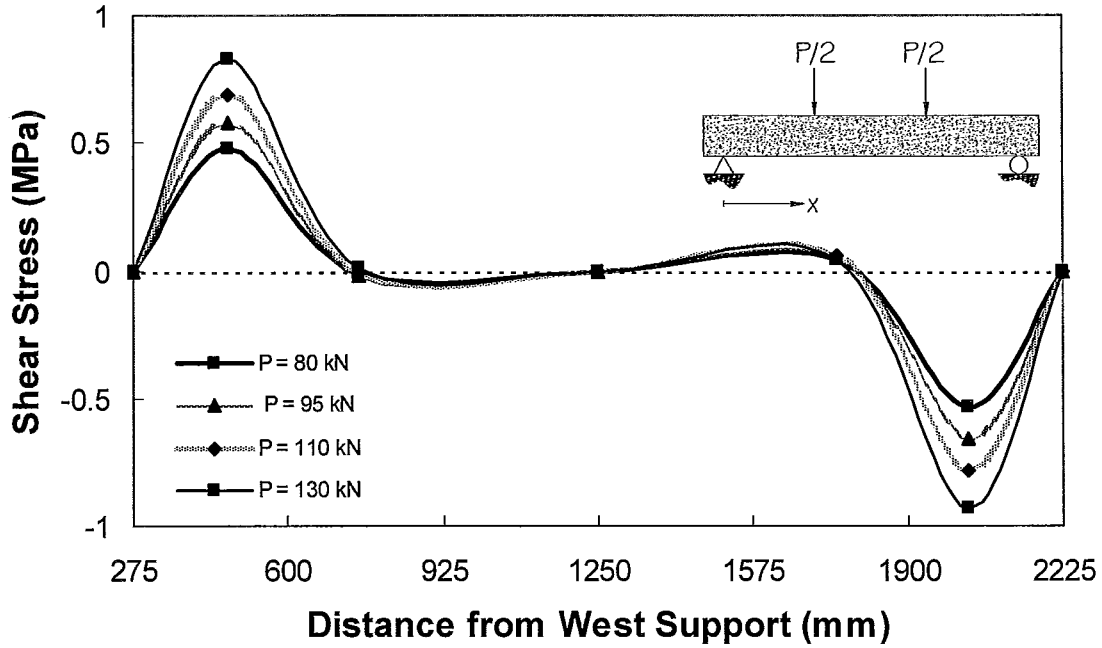


Figure 5.12: Shear Stress along the CFRP Reinforcement for Beam 1b

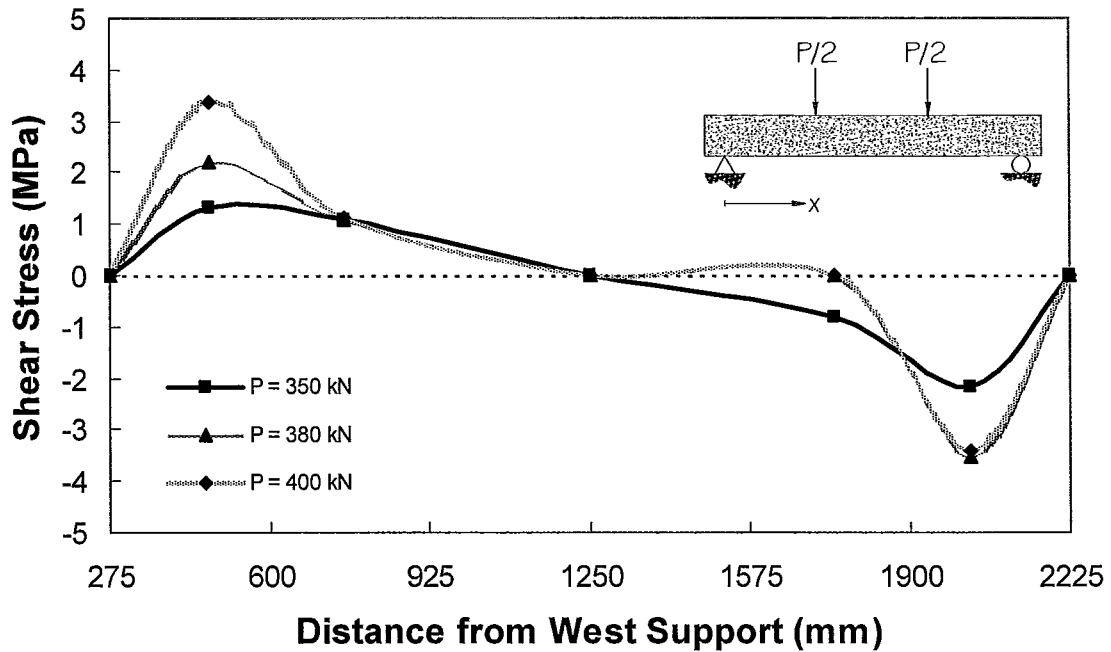


Figure 5.13: Shear Stress along the CFRP Reinforcement for Beam 1b

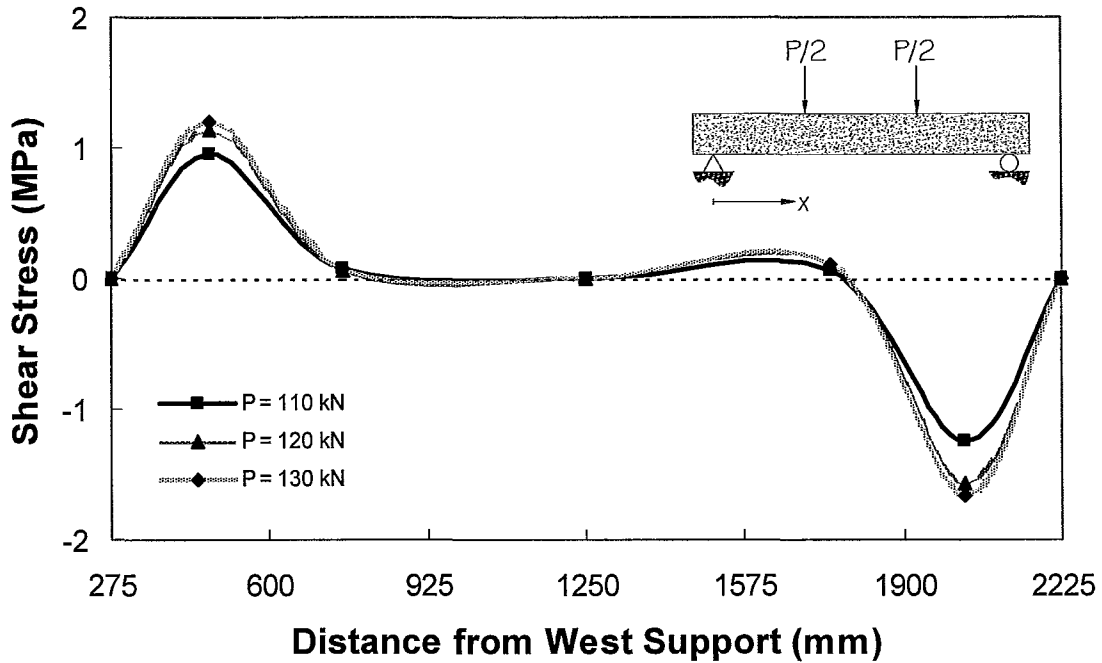


Figure 5.14: Shear Stress along the CFRP Reinforcement for Beam 2a

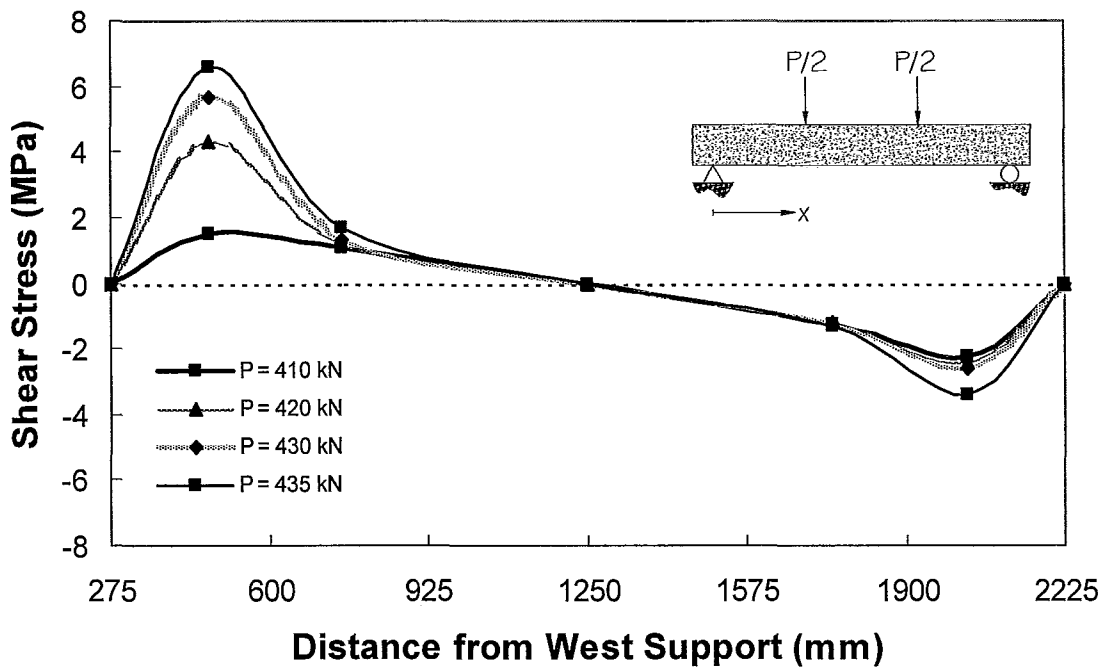


Figure 5.15: Shear Stress along the CFRP Reinforcement for Beam 2a

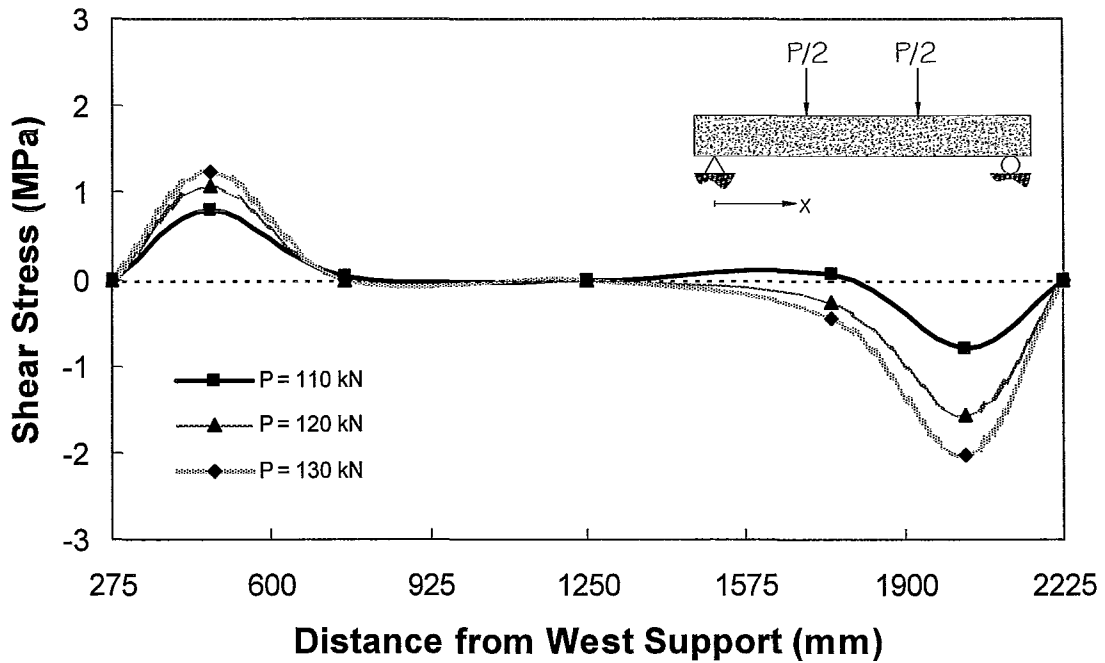


Figure 5.16: Shear Stress along the CFRP Reinforcement for Beam 2b

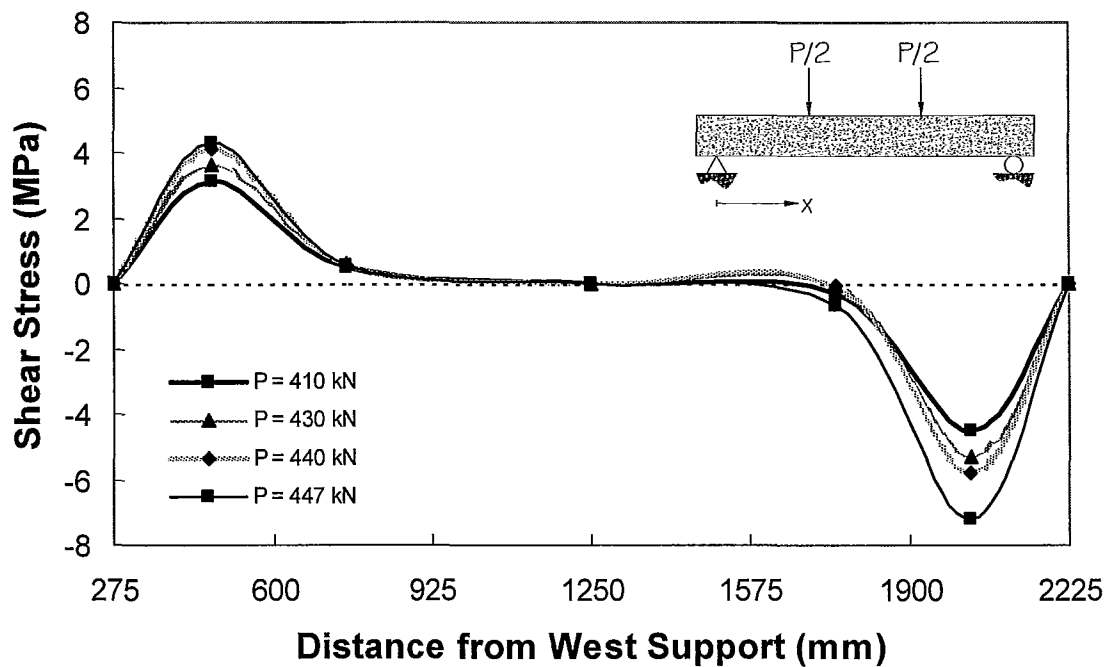


Figure 5.17: Shear Stress along the CFRP Reinforcement for Beam 2b

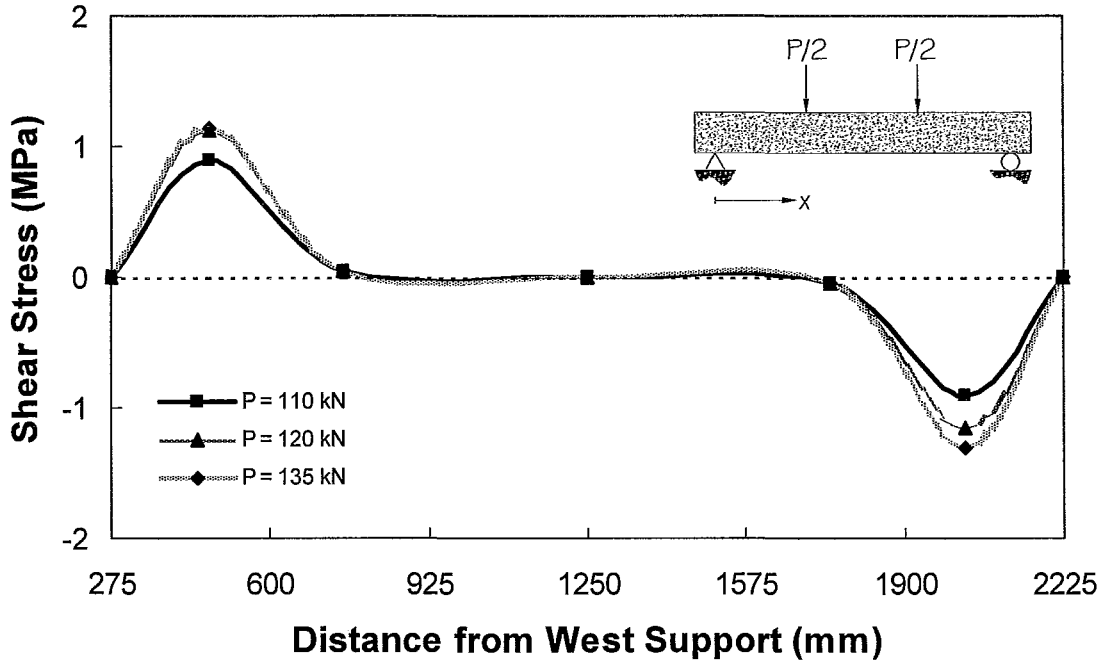


Figure 5.18: Shear Stress along the CFRP Reinforcement for Beam 3a

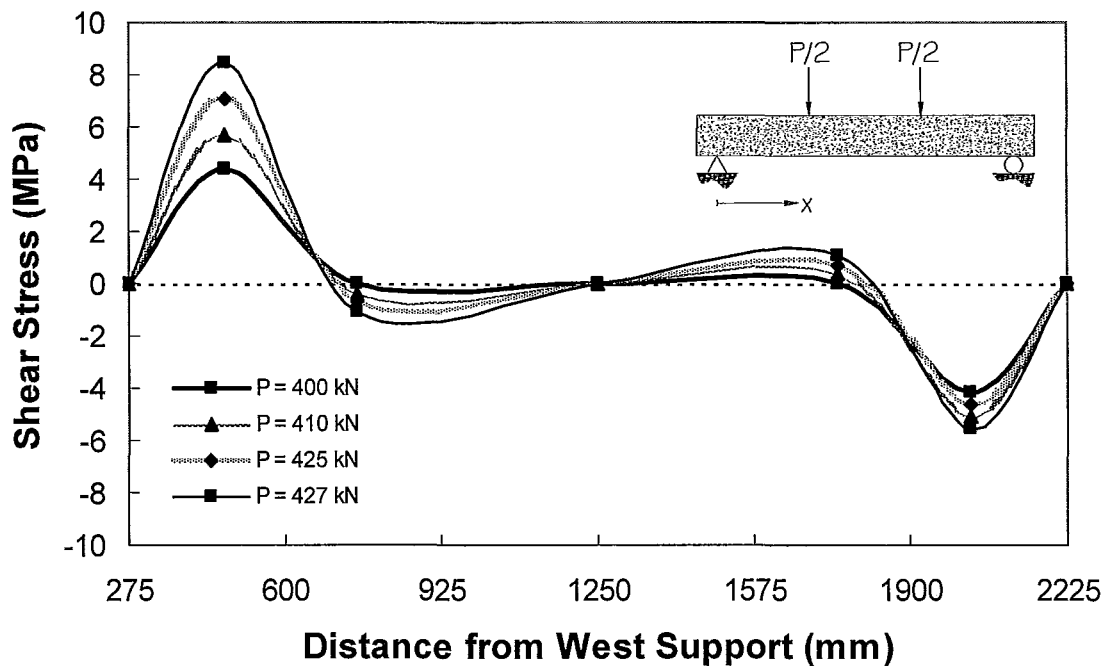


Figure 5.19: Shear Stress along the CFRP Reinforcement for Beam 3a

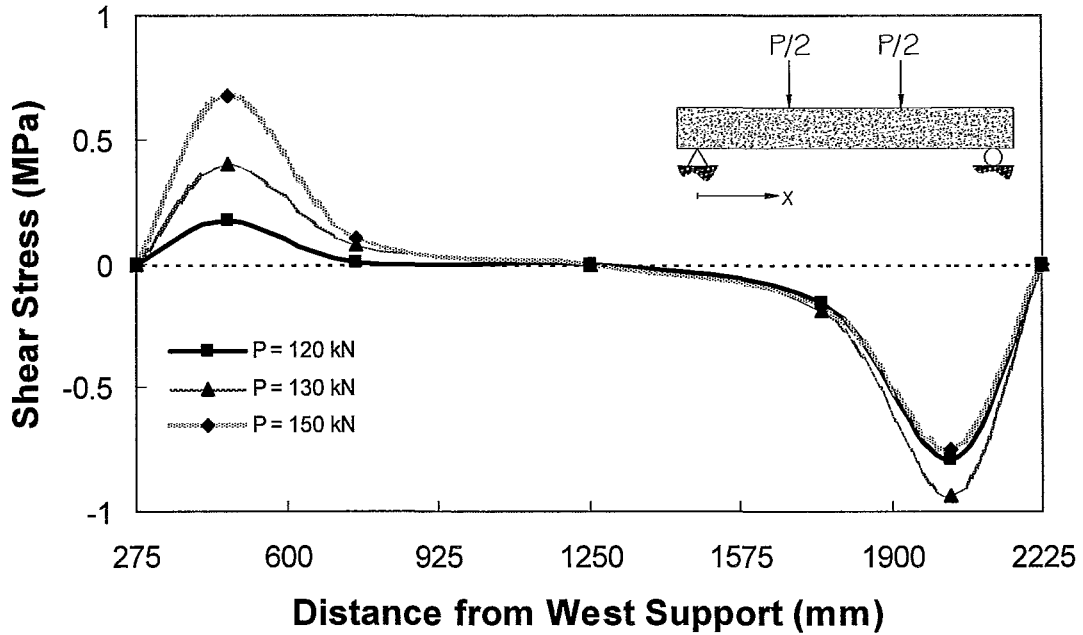


Figure 5.20: Shear Stress along the CFRP Reinforcement for Beam 3b

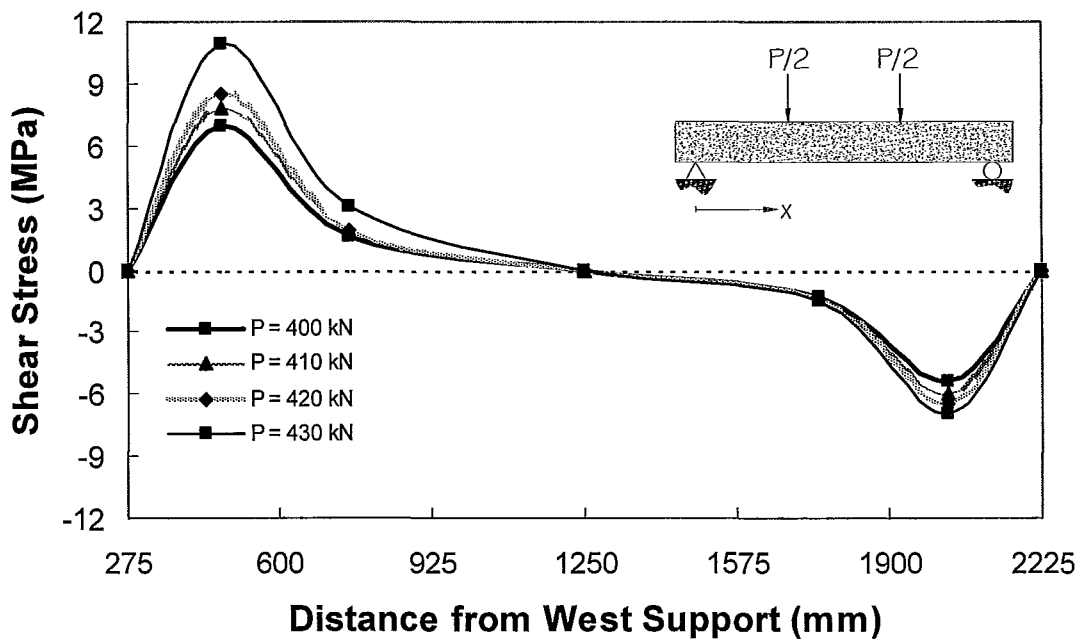


Figure 5.21: Shear Stress along the CFRP Reinforcement for Beam 3b

---

The variation of the experimental interfacial shear stresses is smooth along the length of the reinforcing bar due to the inelastic nature of the beams and is in contrast to the ‘sharp’ changes seen in the common shear force diagrams for a beam under four point bending. This may be in part due to the fact that the concrete between flexural cracks resists some tension, which in turn causes the force in the portion of reinforcing bar within the constant moment region to change, and this change in force is accompanied by interfacial shear stresses between the flexural cracks. The interfacial shear stress diagrams show substantial shear at the interface of the NSM bars and the epoxy and the adjoining concrete. It can be observed in Figure 5.10 through Figure 5.13 that this shear stress reached a maximum value of approximately 4.0 MPa in type 1 beams, while Figure 5.14 through Figure 5.17 show a maximum shear stress of over 8.0 MPa in type 2 beams. Similarly, Figure 5.18 through Figure 5.21 shows a maximum shear stress greater than 9.0 MPa in type 3 beams. The relative value of these shear stresses agree with the corresponding maximum strain values recorded in the NSM bars in the three types of beams. Thus, the anchor system allowed the NSM bars to resist significantly higher interfacial shear.

Table 5.2 summarizes the maximum interfacial shear stresses calculated based on the measured strain values. The table also gives the maximum load values corresponding to these stress values and the load at which delamination initiation was observed. If the maximum interfacial shear stress load precedes the delamination load, as in beams 1a, 2b and 3b, it is due to the fact that a strain gauge had become inoperable prior to reaching the delamination load. Among the five strain gauges along the length of the CFRP bar, if one gauge was damaged, the interfacial shear stresses at higher loads could not be plotted given the limited number of gauges along the length of the bar. The beams with anchors (beam 2a, 2b, 3a and 3b) developed higher interfacial shear stresses than the beams without anchors (beam 1a and 1b). The average maximum interfacial shear stresses amongst the four beams with anchors and the two beams without anchors are 8.3 and 4.0 MPa, respectively.

Table 5.2: Interfacial Shear Stress in Test Beams

Beam	Maximum Interfacial Shear Stresses (MPa)		Load (kN) Corresponding to:	
	Near Bar East End	Near Bar West End	Max. Interfacial Shear	Delamination
1a	4.2	2.7	393	408
1b	3.4	3.7	400	399
2a	3.4	6.6	435	436
2b	7.2	4.3	447	463
3a	5.5	8.4	427	426
3b	6.9	10.9	430	457

The maximum shear stress of 4.0 MPa is nearly equal to  $0.6\sqrt{f'_c}$ , where  $f'_c$  is the compressive strength of the concrete in test beams. For concrete under pure shear, the maximum shear stress is equal to the maximum tensile stress which occurs in the major principal direction. The CSA Standard A23.3-04 gives the flexural tensile strength of concrete to be  $0.6\sqrt{f'_c}$ . Thus the average maximum shear stress measured in type 1 beams is reasonable. The above estimate for concrete interfacial shear strength is also confirmed by the test results of Hofbeck et al. (1969) on push-off specimens who found the monolithic concrete interfacial shear strength to be 3.2 MPa for a concrete with a compressive strength of 27.6 MPa.

The difference between the high interfacial shear strength of the beams with and without anchors can be ascribed to the presence of the anchors. The anchors could resist shear by dowel action and by imposing some clamping action on the interface. The role of the clamping forces in increasing the interfacial shear strength is recognized by the shear friction provisions of the CSA Standard A23.3. Equations 5.7 and 5.8 below are given in the standard.

$$v_r = \lambda\phi_c(c + \mu\sigma) + \phi_s\rho_v f_y \cos\alpha_f \quad (5.7)$$

$$v_r = \lambda\phi_c k\sqrt{\sigma f'_c} + \phi_s\rho_v f_y \cos\alpha_f \quad (5.8)$$

where,

$v_r$  = factored shear resistance of the horizontal or failure plane

$\lambda$  = density of the concrete, taken as 1.0 for normal density concrete

$\phi_c$  = concrete material reduction factor taken as 0.65

$\phi_s$  = reinforcing steel material reduction factor taken as 0.85

$c$  = cohesive term taken as 1.00 MPa for concrete placed monolithically

$\mu$  = coefficient of friction taken as 1.40 MPa for concrete placed monolithically

$\sigma$  = compressive stress on the failure plane

$\rho_v$  = the ratio of the area of reinforcement crossing the failure plane to the total area of the failure plane

$f_y$  = yield strength of the steel intersecting the failure plane

$\alpha_f$  = the acute angle between the failure plane and the longitudinal axis of the steel crossing it

$k$  = factor accounting for cohesion taken as 0.6 for concrete placed monolithically

The first equation is based on a Mohr-Coulomb type failure, which is common in soil mechanics for deriving the shear strength of soils, and the second is based on an empirical model. Both are composed of two components: the contribution of the concrete based on cohesion at the failure interface and the amount of stress applied perpendicular to the plane causing frictional resistance; and the component of the reinforcement resultant directly resisting the applied load.

In the case of the beams in this experimental program no steel crossed the horizontal planes within the concrete cover, but in the beams with anchors, the anchors crossed the horizontal failure plane at right angles. This can increase the interface resistance after the initiation of delamination as the anchors would be able to supply the normal force to mobilize friction. If the frictional forces are less than the cohesion

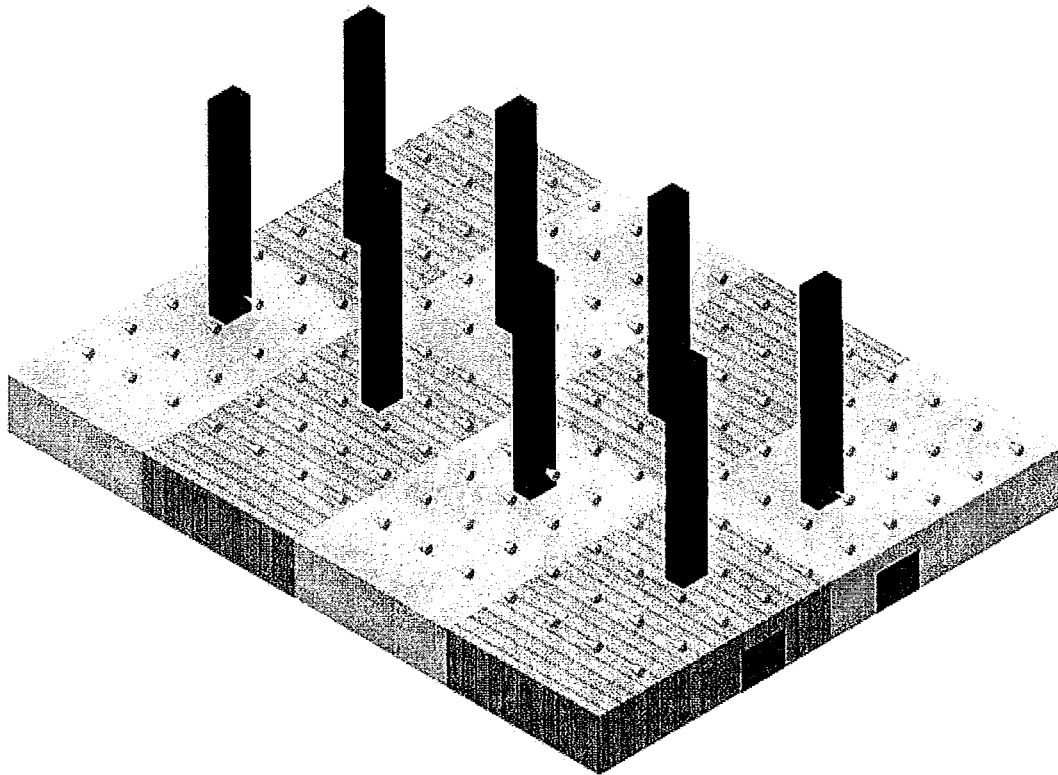
forces, the beam may fail as soon as delamination initiates, but if the frictional forces are greater, the beam will not fail at the onset of delamination.

In the present beams the anchors crossed the shear plane at 90 degrees, therefore the second term on the right hand side of Equations 5.7 and 5.8 can be set equal to zero. Furthermore  $\lambda = \phi_c = 1.0$  because the beams are made of normal density concrete with known strength. If we apply the above equations to the failure plane in the present test beams, with the failure plane being at the interface of the internal steel reinforcement and the concrete, then the maximum shear stress can be approximated by replacing  $l_p$  in Equation 5.6 by the width of the beam. For two bars  $l_p = 2 \times 35 \text{ mm per bar} = 70 \text{ mm}$  while the beam width is 275 mm. Therefore, the maximum shear stress  $\tau_{FP}$  acting on the failure would be the maximum shear as given in Table 5.2 multiplied by  $\frac{70\text{mm}}{275\text{mm}}$ . Based on this assumption  $\tau_{FP}$  values for the beams are shown in Table 5.3.

The approximate interfacial shear stresses in Table 5.3 are not very large, but the actual shear stresses may be higher due to fact that the net area resisting the interfacial shear stresses would be smaller because of the presence of stirrups. Furthermore, the internal steel reinforcement induces additional shear stresses on the adjoining concrete cover. Hence, strictly speaking delamination of the concrete cover is a function of both the internal and external reinforcement forces. However, a full analysis of this problem is beyond the scope of the present study; therefore, the current discussion is confined to the stresses caused by the presence of the NSM bars. Figure 5.22 schematically illustrates the failure plane surface and interfacial shear stresses that act upon it. Note that each anchor resists a portion of the total stress acting on the surface according to its tributary area.

*Table 5.3: Summary of Approximated Interfacial Shear Stresses along Failure Plane*

Beam	Max. Interfacial Shear Stress, $\tau_{xy}$ , along NSM Bar (MPa)	Approximated Interfacial Shear Stress, $\tau_{FP}$ , along Failure Plane (MPa)
1a	4.2	1.07
1b	3.4	0.87
2a	6.6	1.68
2b	7.2	1.83
3a	8.4	2.14
3b	10.9	2.77

*Figure 5.22: Interfacial Shear Stresses and Anchor Tributary Areas*

Since type 1 beams had no anchors, we can assume that the delamination initiation stress  $\tau_{FP}$  is approximately equal to the average  $\tau_{FP}$  of beams 1a and 1b and is equal to 0.87. This value is close to the 1.0 MPa suggested for shear resisted by cohesion in CSA A23.3-04. Once delamination initiates, resistance due to cohesion practically

vanishes and the resistance is primarily due to friction. Consequently, the  $\tau_{FP}$  values for beams 2 and 3 may be ascribed to friction. Hence, if we substitute these values for  $v_r$  in Equation 5.7, and assume  $\mu = 1.40$ , the corresponding normal stresses,  $\sigma_{FP}$  acting on the failure plane can be calculated as shown in Table 5.4. Given that the anchors have cross-sectional area equal to the bar cross-sectional area of  $150 \text{ mm}^2$  and are spaced at 85 mm along the beam, the reinforcement ratio of the shear plane is

$$\rho_{FP} = \frac{2 \times 150 \text{ mm}^2}{275 \text{ mm} \times 85 \text{ mm}} = 0.0128 \text{ or } 1.28\%. \text{ Consequently using the relationship,}$$

$$\sigma_{FP} = \rho_{FP} f_{FRP} \quad (5.9)$$

the anchor axial stress,  $f_{FRP}$ , can be calculated as shown in Table 5.4. These are relatively high stresses, but the actual stress may be lower because these stresses are calculated based on the assumption of negligible dowel action; in fact some shear would be transferred by dowel action.

**Table 5.4: Approximated Normal Stresses provided by NSM Anchors and the Corresponding Axial Stress in the Anchors**

Beam	Approximated Interfacial Shear Stress, $\tau_{FP}$ , along Failure Plane (MPa)	Approximated Normal Stress $\sigma_{FP}$ on Failure Plane (MPa)	Approximated Anchor Stress $f_{FRP}$ (MPa)
2a	1.68	1.20	93.5
2b	1.83	1.31	102.0
3a	2.14	1.53	119.0
3b	2.77	1.98	154.4

The anchor stresses in Table 5.4 are small compared to the actual strength of the anchors but it is unlikely that the anchors could resist much higher stresses unless their embedment length, measured from the failure plane to anchor free ends, is made much greater than their length in the present investigation. However, deeper embedment requires drilling deeper holes into the concrete web, which may be difficult. Further investigation is required to determine the consequences of such deep holes in the web of beams.

#### 5.4. Refined Analysis of Stresses at the NSM Bars-Concrete Interface

Numerous investigators (Roberts 1989, Malek et al. 1998, Täljsten 1997) have studied the stresses at the interface of externally bonded plates and concrete in which similar stresses develop at the concrete-plate interface as at the NSM bar-concrete interface. A well known conclusion of these studies is that over a short distance from the free end of the plate, significant tensile and shear stresses develop along the interface. Here we will present a summary of the method proposed by Täljsten to show how these stresses can be calculated.

To demonstrate the need for these stresses consider the beam in Figure 5.23 and the equilibrium of the portion of the concrete cover between the free end of the NSM bar and the section under the applied load. We can observe that the interfacial shear force,  $V_{FP}$ , and the tensile force,  $T_{FP}$ , in the NSM bars constitute a couple which must be balanced to satisfy equilibrium. This requires the interfacial normal forces,  $T_{FP}$  and  $C_{FP}$ , as self-equilibrating internal forces. Consequently, to be able to correctly predict the

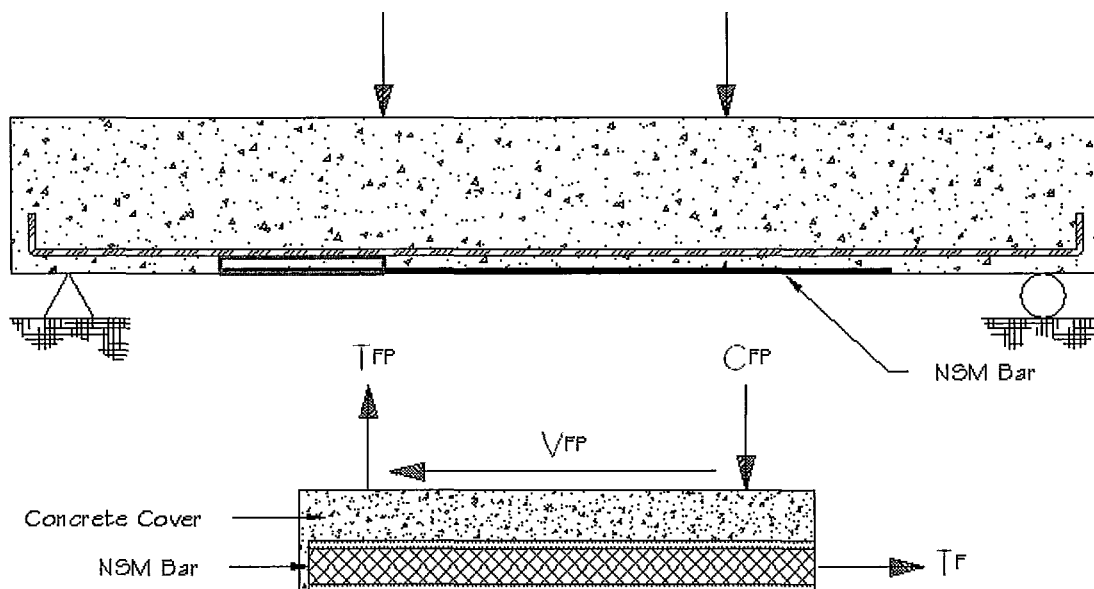


*Figure 5.23: Equilibrium of a NSM Strengthened RC Beam and its Concrete Cover*

delamination stresses, one must determine the shear and normal stresses corresponding to  $V_{FP}$  and  $T_{FP}$ . Closed-form solutions, such as those given by Täljsten, attempt to estimate the internal stresses whose resultants are  $V_{FP}$  and  $T_{FP}$ .

#### 5.4.1. Interfacial Shear Stresses Based on Refined Analysis

The objective of this section is to determine the interfacial shear stresses using an analytical closed-form solution developed by Täljsten (1997). The analysis was developed for beam strengthening using a bonded plate, however, the developed equation can be manipulated to estimate the interfacial shear stresses applied to the beams in this testing program.

The solution begins with the establishment of equilibrium of an infinitesimal element shown in Figure 5.24. The figure shows a segment of the bonded plate (adherent 2), the adhesive and the concrete web (adherent 1) to which the plate is bonded. To simplify the analysis, Täljsten initially neglected the bending moment in the plate which implies the interfacial normal or peeling stresses introduced later, to be negligible.

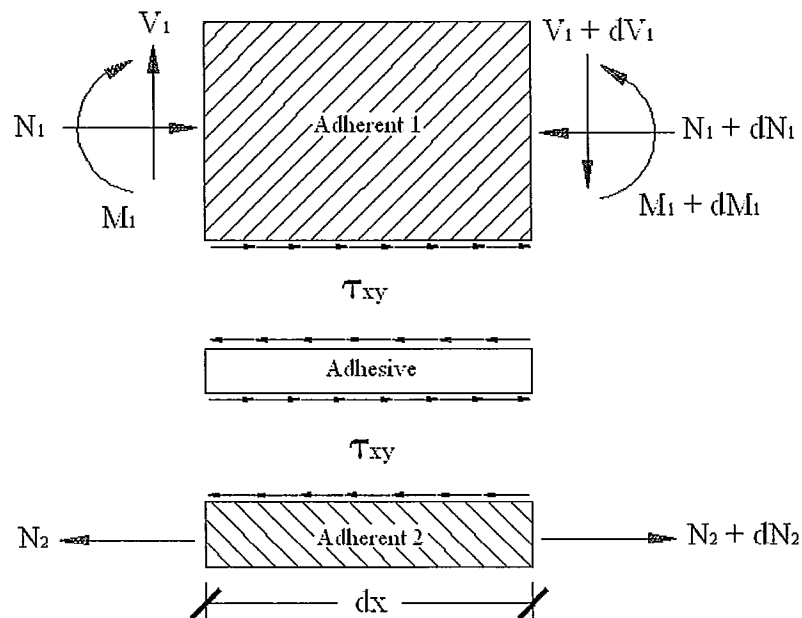


*Figure 5.24: Free-Body Diagram as a Basis for Täljsten Interfacial Stress*

From the equilibrium of forces in the x-direction  $\sum_i F_{xi} = 0$ ,

$$\frac{dM_1(x)}{dx} = V(x) - \tau_{xy}(x)b_2z_0 \quad (5.10)$$

where  $b_2$  and  $z_0$  are the width of the strengthening plate and the distance between the normal force,  $N_1$ , in adherent 1 and concrete/ adhesive interface, respectively. However, in the case of a NSM bar  $b_2$  shall be taken as the bond perimeter of the bar, referred to as  $l_p$  earlier in the chapter. Assuming linear-elasticity, Täljsten derived the following relation for the interfacial shear stress of a plate bonded to a slender beam loaded with a single concentrated point load,

$$\tau_{xy}(x) = \frac{G_a P}{2sE_1W_1} \frac{(2l + a - b)}{l + a} \frac{(a\lambda e^{-\lambda x} + 1)}{\lambda^2} \quad (5.11)$$

The parameters are defined as follows:

$s$  = thickness of the adhesive layer (m)

$P$  = point load (N)

$l$  = length (m)

$a$  = distance between support and end of steel plate (m)

$b$  = distance from the end of the steel plate to point load (m)

$G_a$  = shear modulus, adhesive (Pa)

$W_1$  = section modulus, adherent 1 ( $m^3$ )

$$\lambda = \frac{G_a b_2}{s} \left[ \frac{1}{E_2 A_2} + \frac{1}{E_1 A_1} + \frac{z_0}{E_1 W_1} \right] \text{ (1/m)}$$

$E_1, E_2$  = modulus of elasticity, adherent 1 and adherent 2, respectively (Pa)

$A_1, A_2$  = cross-sectional area, adherent 1 and adherent 2, respectively ( $m^2$ )

$z_0$  = distance from centroid of compression block in adherent 1 to adhesive (m)

$x$  = longitudinal coordinate with origin at the steel plate end (m)

$b_2$  = width of the strengthening plate (m)

Given that the maximum shear stress was observed near the ends of plate (i.e. by setting  $x$  equal to zero), the maximum shear stress is given by Equation 5.12,

$$\tau_{xy,\max} = \frac{G_a P}{2sE_1 W_1} \frac{(2l + a - b)}{l + a} \frac{(a\lambda + 1)}{\lambda^2} \quad (5.12)$$

In Equation 5.10 the term  $\frac{2l + a - b}{l + a}$  weights the value  $\frac{P}{2}$ , which is the magnitude of the reaction at the support, given that the concentrated load may be located anywhere along the length of the beam. In other words if the concentrated load acts centrally then the magnitude of the reaction will equal  $\frac{P}{2}$ . Recalling the symmetric four-point bending used in the current testing program, the magnitude of each reaction will equal  $\frac{P}{2}$  and the term  $\frac{2l + a - b}{l + a}$  becomes one. Therefore, for four-point bending, Equation 5.12 yields the following,

$$\tau_{xy}(x) = \frac{G_a P}{2sE_1 W_1} \frac{(a\lambda e^{-\lambda x} + 1)}{\lambda^2} \quad (5.13)$$

or

$$\tau_{xy,\max} = \frac{G_a P}{2sE_1 W_1} \frac{(a\lambda + 1)}{\lambda^2} \quad (5.14)$$

To estimate the non-linear behaviour of the RC beam at delamination, the stiffness coefficients listed in Equation 5.11 will be defined using the cracked moment of inertia,  $I_{cr}$ . The moment near the bar end exceeds the cracking moment,  $M_{cr}$ , therefore the stiffness of the beam will be reduced and the gross moment of inertia will not be used. Consequently, Equations 5.13 and 5.14 can be modified by replacing the section modulus of adherent 1,  $W_1$ , with the cracked section modulus of the RC beam,  $W_{1cr}$ . The modified form of the formula presented by Täljsten be,

$$\tau_{xy}(x) = \frac{G_a P}{2sE_1 W_{1cr}} \frac{(a\lambda e^{-\lambda x} + 1)}{\lambda^2} \quad (5.15)$$

or

$$\tau_{xy,\max} = \frac{G_a P}{2sE_1 W_{1cr}} \frac{(a\lambda + 1)}{\lambda^2} \quad (5.16)$$

Equation 5.15 is used in Figure 5.25 through Figure 5.27 to plot the shear stress along the length of the NSM CFRP bars. The distance shown in these figures is from the end of the bar to the location of the point load. Notice that at the bar end the interfacial shear stresses are maximum. In theory this cannot be true as no shearing stresses are present at the free surface. Nevertheless, Täljsten's closed-form equation does illustrate the same overall behaviour observed in the interfacial shear stress distributions obtained from the experimental data, with maximum shear stress occurring near the bar ends and diminishing to negligible shear stresses toward the mid-length of the bar.

Table 5.5 compares the maximum interfacial shear stress values calculated based on the measured strain values, as shown in Table 5.2, with the interfacial shear stresses computed through Täljsten's closed-form solution. The experimental values are based on strain values measured along the eastern half of the bar because these values appear more consistent than those along the western half.

*Table 5.5: Approximated vs. Täljsten Shear Stresses at Delamination*

Beam	Delamination Load (kN)	Interfacial Shear Stress (MPa)	
		Approximated $\tau_{FP}$ Based on Experimental Data	Calculated $\tau_{xy}$ Based on Täljsten Method
1a	408	4.2	4.02
1b	399	3.4	3.94
2a	436	3.4	4.24
2b	463	7.2	4.51
3a	426	5.5	4.11
3b	457	6.9	4.39

Although the agreement is not great in every case, the measured and predicted values are within the expected range. It should be pointed out that local strain values in cracked concrete can vary widely within a relatively small distance; therefore, the above differences are not unexpected. The normal stresses are discussed in the following section.

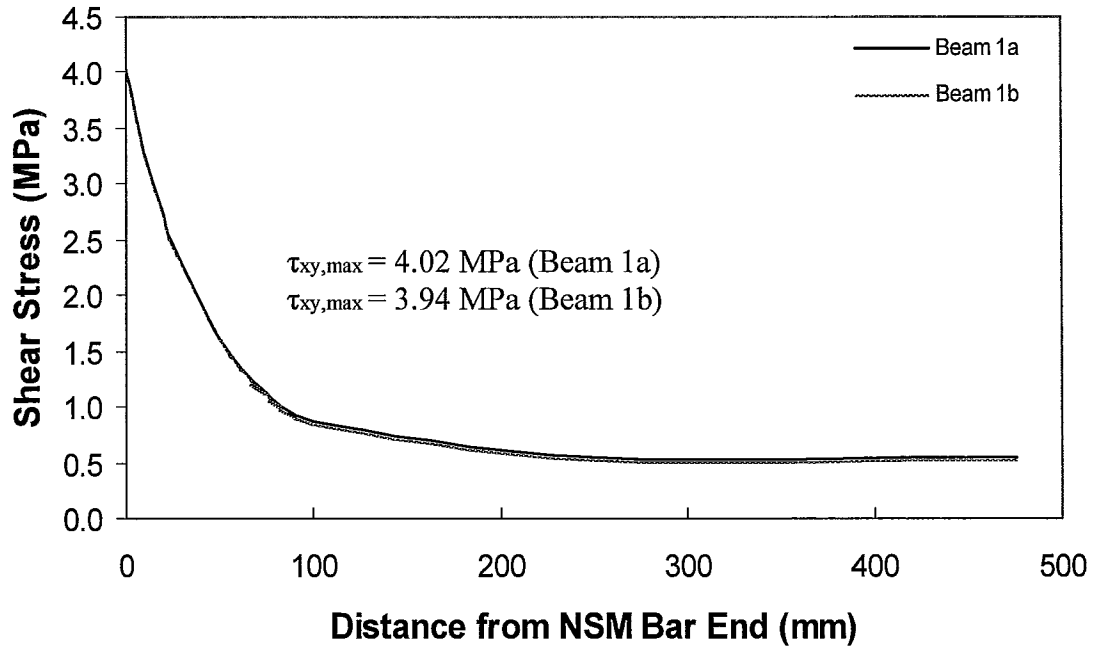


Figure 5.25: Interfacial Shear Stress along NSM Bar for Beams 1a and 1b

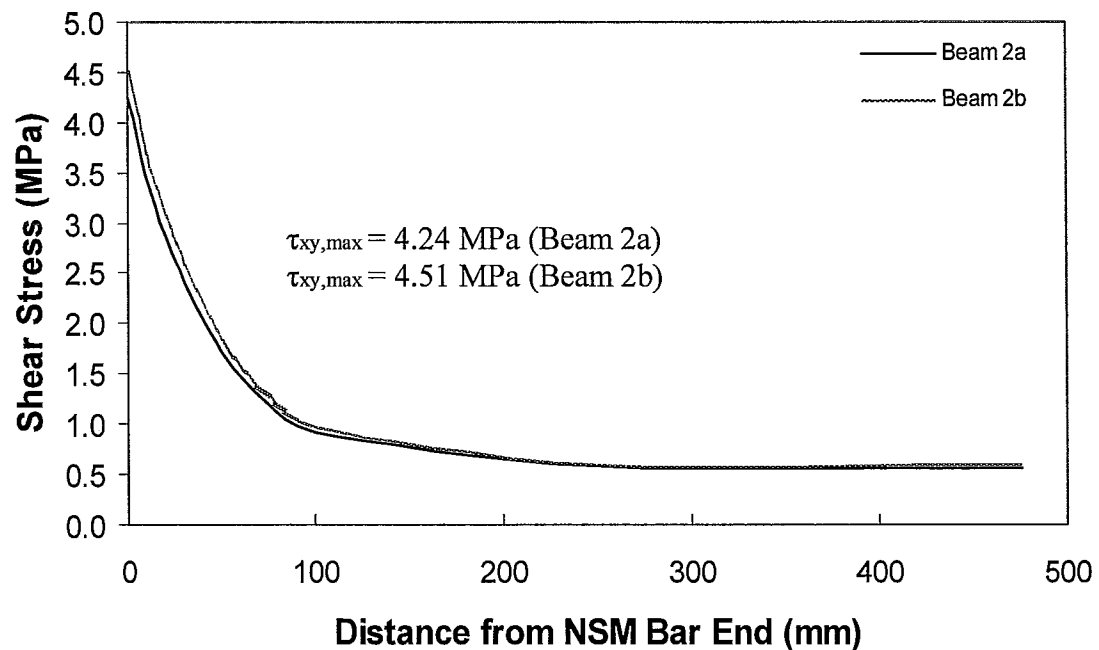


Figure 5.26: Interfacial Shear Stress along NSM Bar for Beams 2a and 2b

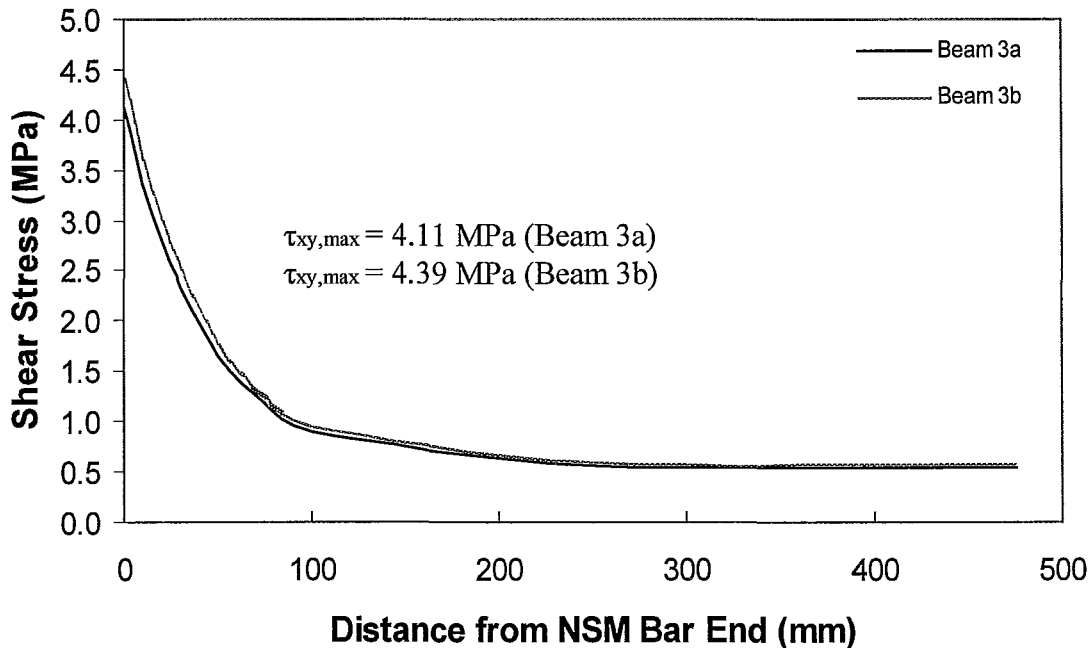


Figure 5.27: Interfacial Shear Stress along NSM Bar for Beams 3a and 3b

#### 5.4.2. Peeling or Normal Interfacial Stresses

Täljsten (1997) derived an expression for the interfacial peeling stress,  $\sigma_y$ , for a beam strengthened with a bonded plate. The formulation begins by considering the equilibrium of an infinitesimal element of the beam as shown in Figure 5.28, which include the peeling stress,  $\sigma_y$ . By reference to Figure 5.28, the following equilibrium equation can be written

$$\frac{dM_2}{dx} = V_2(x) - \tau_{xy}(x) \frac{b_2 t_2}{2} \quad (5.17)$$

where  $b_2$  and  $t_2$  are the width and the thickness of the strengthening plate, respectively. However, in the case of a NSM bar  $b_2$  and  $t_2$  shall be taken as the bond perimeter of the bar, referred to as  $l_p$  earlier in the chapter, and the thickness of the NSM bar, respectively.

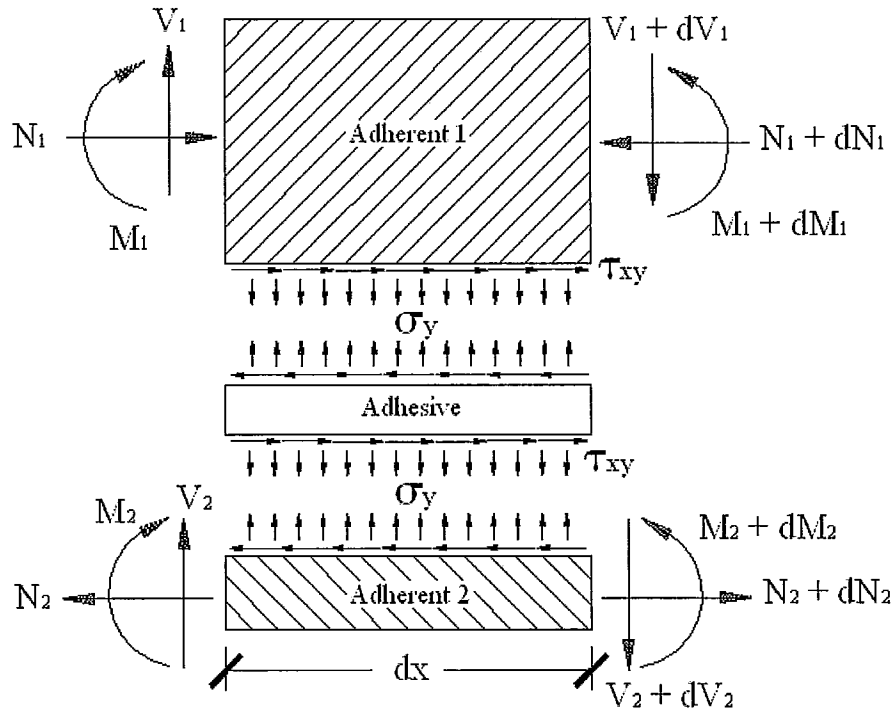


Figure 5.28: Free-Body Diagram as a Basis for Täljsten Peeling Stress

Using linear-elastic analysis, Täljsten derived the following relation for the peeling stress of a plate bonded to a beam,

$$\sigma_y(x) = \frac{E_a}{s} \left\{ \begin{aligned} & \frac{P}{4\beta^3} \frac{2l+a-b}{l+a} \left[ \frac{a\beta+1}{E_1 I_1} (1-\eta) + \frac{\beta\lambda^2 - \lambda^3}{(\lambda^4 + 4\beta^4)} \frac{ab_2}{sE_2 I_2} \right] e^{-\beta x} \cos \beta x \\ & \bullet \left[ \left( \frac{E_a \eta}{E_1 I_1 \lambda^2} + \frac{G_a t_2}{2E_1 W_1} \right) + \frac{G_a b_2 t_2}{2sE_2 I_2 E_1 W_1} \frac{a\lambda+1}{\lambda^2} \right] \\ & - \frac{P}{4\beta^2} \frac{2l+a-b}{l+a} \left[ \frac{a(1-\eta)}{E_1 I_1} + \frac{\lambda^2}{(\lambda^4 + 4\beta^4)} \frac{ab_2}{sE_2 I_2} \right] e^{-\beta x} \sin \beta x \\ & \bullet \left[ \left( \frac{E_a \eta}{E_1 I_1 \lambda^2} + \frac{G_a t_2}{2E_1 W_1} \right) \right] \\ & + \frac{P}{2E_1 I_1} \frac{2l+a-b}{l+a} \frac{\eta a}{\lambda^2} e^{-\lambda x} \\ & - \frac{P}{2sE_2 I_2 (\lambda^4 + 4\beta^4)} \frac{ab_2}{l+a} \frac{2l+a-b}{l+a} \left( \frac{E_a \eta}{E_1 I_1 \lambda^2} + \frac{G_a t_2}{2E_1 W_1} \right) e^{-\lambda x} \end{aligned} \right\} \quad (5.18)$$

The parameters in Equation 5.19 are defined as follows:

$E_a$  = modulus of elasticity, adhesive (Pa)

$s$  = thickness of the adhesive layer (m)

$P$  = point load (N)

$\beta$  = constant taken as  $\sqrt[4]{\frac{K}{4E_2I_2}}$  for slender beams (1/m)

$K$  = spring constant taken as  $\frac{E_a b_2}{s}$  (N/m<sup>2</sup>)

$l$  = length (m)

$a$  = distance between support and end of steel plate (m)

$b$  = distance from the end of the steel plate to point load (m)

$E_1, E_2$  = modulus of elasticity, adherent 1 and adherent 2, respectively (Pa)

$I_1, I_2$  = moment of inertia, adherent 1 and adherent 2, respectively (m<sup>4</sup>)

$\eta = \frac{G_a b_2 z_0}{s E_1 W_1 \lambda^2}$  (unitless)

$G_a$  = shear modulus, adhesive (Pa)

$b_2, t_2$  = width and thickness of the strengthening plate, respectively (m)

$z_0$  = lever arm from centroid of compression block in adherent 1 to adhesive (m)

$x$  = longitudinal coordinate with origin at the steel plate end (m)

$W_1$  = section modulus, adherent 1 (m<sup>3</sup>)

$\lambda = \frac{G_a b_2}{s} \left[ \frac{1}{E_2 A_2} + \frac{1}{E_1 A_1} + \frac{z_0}{E_1 W_1} \right]$  (1/m)

$A_1, A_2$  = cross-sectional area, adherent 1 and adherent 2, respectively (m<sup>2</sup>)

Since the maximum peeling stress occurs at the ends of plate, it can be determined by setting  $x$  equal to zero in Equation 5.19. Hence,

$$\sigma_{y,\max}(x) = \frac{E_a}{s} \left\{ \begin{aligned} & \frac{P}{4\beta^3} \frac{2l+a-b}{l+a} \left[ \frac{a\beta+1}{E_1 I_1} (1-\eta) + \frac{\beta\lambda^2 - \lambda^3}{(\lambda^4 + 4\beta^4)} \frac{ab_2}{sE_2 I_2} \right. \\ & \quad \left. \bullet \left( \frac{E_a \eta}{E_1 I_1 \lambda^2} + \frac{G_a t_2}{2E_1 W_1} \right) + \frac{G_a b_2 t_2}{2sE_2 I_2 E_1 W_1} \frac{a\lambda+1}{\lambda^2} \right] \\ & + \frac{P}{2E_1 I_1} \frac{2l+a-b}{l+a} \frac{\eta a}{\lambda^4} \\ & - \frac{P}{2sE_2 I_2 (\lambda^4 + 4\beta^4)} \frac{ab_2}{l+a} \frac{2l+a-b}{l+a} \left( \frac{E_a \eta}{E_1 I_1 \lambda^2} + \frac{G_a t_2}{2E_1 W_1} \right) \end{aligned} \right\} \quad (5.19)$$

Although this closed-form solution was based on an externally-bonded RC beam loaded with a single point load and assuming linear-elastic behaviour of the constituent materials, it can be manipulated to estimate the peeling stresses in the beams in the current experimental program.

In Equations 5.18 and 5.19 the term  $\frac{2l+a-b}{l+a}$  weights the value  $\frac{P}{2}$ . As discussed earlier, the term  $\frac{2l+a-b}{l+a}$  is equal to one for the current beams. Therefore, Equation 5.19 takes the following form for the four-point bending condition,

$$\sigma_{y,\max} = \frac{E_a}{s} \left\{ \begin{aligned} & \frac{P}{4\beta^3} \left[ \frac{a\beta+1}{E_1 I_1} (1-\eta) + \frac{\beta\lambda^2 - \lambda^3}{(\lambda^4 + 4\beta^4)} \frac{ab_2}{sE_2 I_2} \right. \\ & \quad \left. \bullet \left( \frac{E_a \eta}{E_1 I_1 \lambda^2} + \frac{G_a t_2}{2E_1 W_1} \right) + \frac{G_a b_2 t_2}{2sE_2 I_2 E_1 W_1} \frac{a\lambda+1}{\lambda^2} \right] \\ & + \frac{P}{2E_1 I_1} \frac{\eta a}{\lambda^4} - \frac{P}{2sE_2 I_2 (\lambda^4 + 4\beta^4)} \frac{ab_2}{l+a} \left( \frac{E_a \eta}{E_1 I_1 \lambda^2} + \frac{G_a t_2}{2E_1 W_1} \right) \end{aligned} \right\} \quad (5.20)$$

As discussed earlier the moment near the end of the NSM bars, where delamination initiates, exceeds the cracking moment,  $M_{cr}$ ; therefore the cracked moment of inertia,  $I_{cr}$ , will be used in the following calculations. The final form of the modified Täljsten expression will take the form shown in Equation 5.21.

$$\sigma_{y,\max} = \frac{E_a}{s} \left\{ \frac{P}{4\beta^3} \left[ \frac{a\beta + 1}{E_1 I_{1cr}} (1 - \eta) + \frac{\beta\lambda^2 - \lambda^3}{(\lambda^4 + 4\beta^4)} \frac{ab_2}{sE_2 I_2} \right] \cdot \left( \frac{E_a \eta}{E_1 I_{1cr} \lambda^2} + \frac{G_a t_2}{2E_1 W_{1cr}} \right) + \frac{G_a b_2 t_2}{2sE_2 I_2 E_1 W_{1cr}} \frac{a\lambda + 1}{\lambda^2} \right. \quad (5.21)$$

$$\left. + \frac{P}{2E_1 I_{1cr}} \frac{\eta a}{\lambda^4} - \frac{P}{2} \frac{ab_2}{sE_2 I_2 (\lambda^4 + 4\beta^4)} \left( \frac{E_a \eta}{E_1 I_{1cr} \lambda^2} + \frac{G_a t_2}{2E_1 W_{1cr}} \right) \right\}$$

Adhesive properties,  $G_a$ ,  $E_a$  and  $\nu$  will be taken as specified by the manufacturer as summarized below. Additionally, parameters  $K$ ,  $\beta$ ,  $\lambda$  and  $\eta$  were evaluated as follows:

$$E_a = 3034 \text{ MPa}$$

$$G_a = \frac{E_a}{2(1+\nu)} = \frac{3034 \text{ MPa}}{2(1+0.4)} = 1084 \text{ MPa}$$

$$K = \frac{E_a b_2}{s} = \frac{3034 \text{ MPa} \times 70 \text{ mm}}{5 \text{ mm}} = 42,476 \text{ MPa}$$

where  $b_2$  and  $s$  are taken as the

bonded length of the two NSM bars or  $2 \times l_p = 70 \text{ mm}^2$  and the thickness of the adhesion layer between the concrete groove surface and the NSM bar, respectively.

$$\beta = \sqrt[4]{\frac{K}{4E_2 I_2}} = \sqrt[4]{\frac{42476 \text{ MPa}}{4 \cdot 100 \text{ GPa} \cdot 2500 \times 10^{-6} \text{ m}^4}} = 80.7 / \text{m}$$

$$\lambda = \frac{G_a b_2}{s} \left[ \frac{1}{E_2 A_2} + \frac{1}{E_1 A_1} + \frac{z_0}{E_1 W_{1cr}} \right]$$

$$= \frac{1084 \text{ MPa} \times 70 \text{ mm}^2}{5 \text{ mm}} \left[ \frac{1}{100 \text{ GPa} \times 300 \text{ mm}^2} + \frac{1}{27958 \text{ MPa} \cdot 123750 \text{ mm}^2} + \frac{405 \text{ mm}}{27958 \cdot 5.23 \times 10^6 \text{ mm}^4} \right] = 23.5 / \text{m}$$

$$\eta = \frac{G_a b_2 z_0}{s E_1 W_{1cr} \lambda^2} = \frac{1084 \text{ MPa} \times 70 \text{ mm} \times 405 \text{ mm}}{5 \text{ mm} \cdot 27958 \text{ MPa} \cdot 5.23 \times 10^6 \text{ mm}^3 \cdot (23.5 / \text{m})^2} = 0.073$$

---

where the concrete strength,  $f'_c$ , was taken in this example as 38.6 MPa (concrete strength for control beam, and beams 1a and 1b) and the effective section modulus,  $W_{1cr}$ , was based on an applied moment at the NSM bar end causing delamination in beam 1a.

Figure 5.29, Figure 5.30 and Figure 5.31 show the interfacial peeling stresses computed using Equation 5.19. The curves are plotted from the bar end to the location of the point load. Note that generally each beam behaves similarly yielding a maximum peeling stress of approximately 3 MPa. Intuitively, the presence of the anchors in the type 2 and 3 beams should provide additional resistance to these stresses; however, the Täljsten equation does not directly account for the latter resistance. The effect of the anchors enter the closed-form expression through an increase in load causing delamination between the beams with anchors and without anchors. By reference to Figure 5.7 it was noted earlier that the advantages of the anchors were not realized until after delamination had been initiated, permitting the beams to deflect without losing substantial strength. The largest variation in delamination load was noted between beams 1b (no anchors) and beam 2b (with anchors) where there was only a 16% increase in capacity; therefore, it makes sense that the Täljsten equation generally yields the same maximum normal stresses for all the strengthened beams.

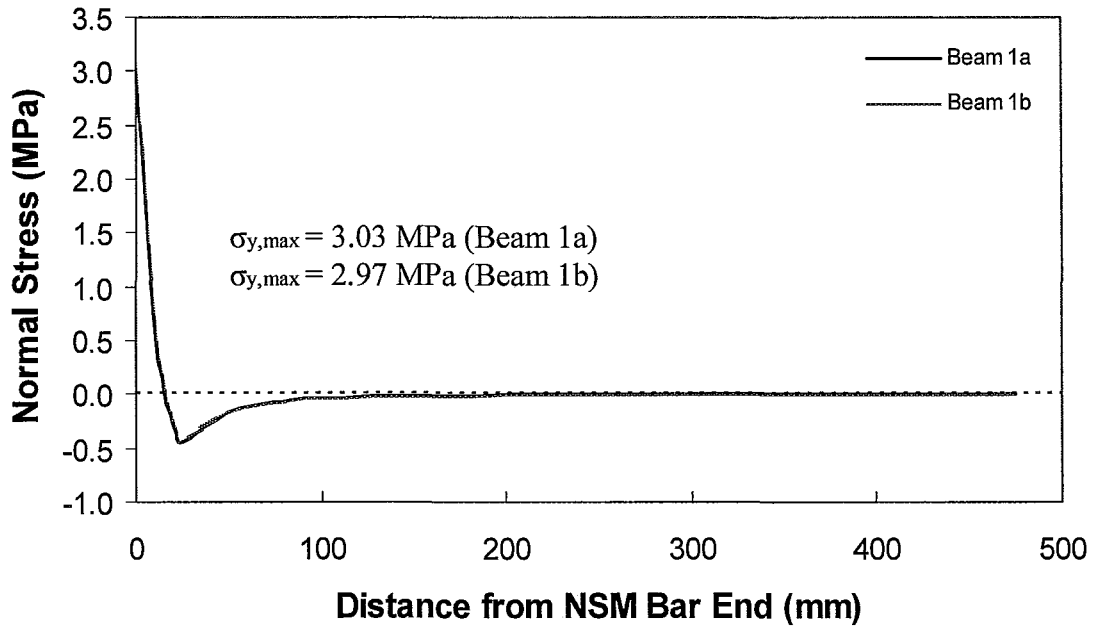


Figure 5.29: Interfacial Normal Stress along NSM Bar for Beams 1a and 1b

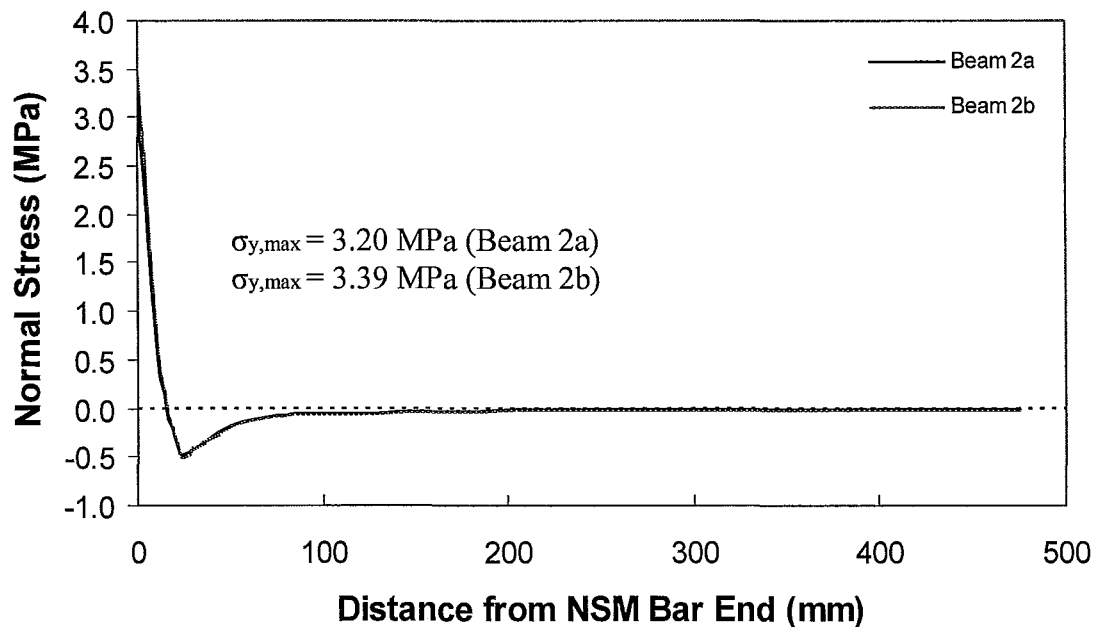


Figure 5.30: Interfacial Normal Stress along NSM Bar for Beams 2a and 2b

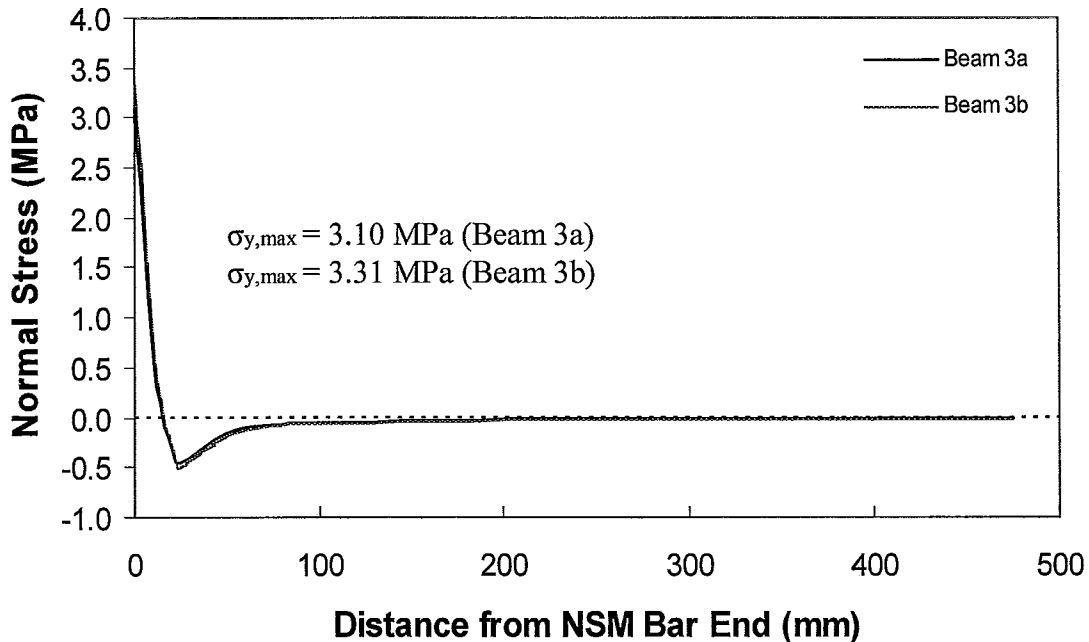


Figure 5.31: Interfacial Normal Stress along NSM Bar for Beams 3a and 3b

## 5.5. Concrete Cover Failure Analysis

The combination of the interfacial shear and peeling stresses and the longitudinal normal stress,  $\sigma_x$ , acting on the concrete cover near the end of the NSM bar would eventually lead to the failure of the concrete. To estimate the maximum magnitude of the stresses, and the corresponding applied load that would cause concrete failure, one can use either the Kupfer and Gerstle (1973) failure envelope or the Mohr-Coulomb failure criterion for concrete.

As shown in Figure 5.32, if we remove an infinitesimal concrete element near the bar end where delamination initiates, we can show the normal and shear stresses as well as the principle stresses acting on it. Near the bar ends, the state of stress is characterized by the interfacial shear stresses induced by the NSM bar on the concrete, the longitudinal

tensile stresses due to bending of the beam and the tensile peeling stresses acting normal to the interface.

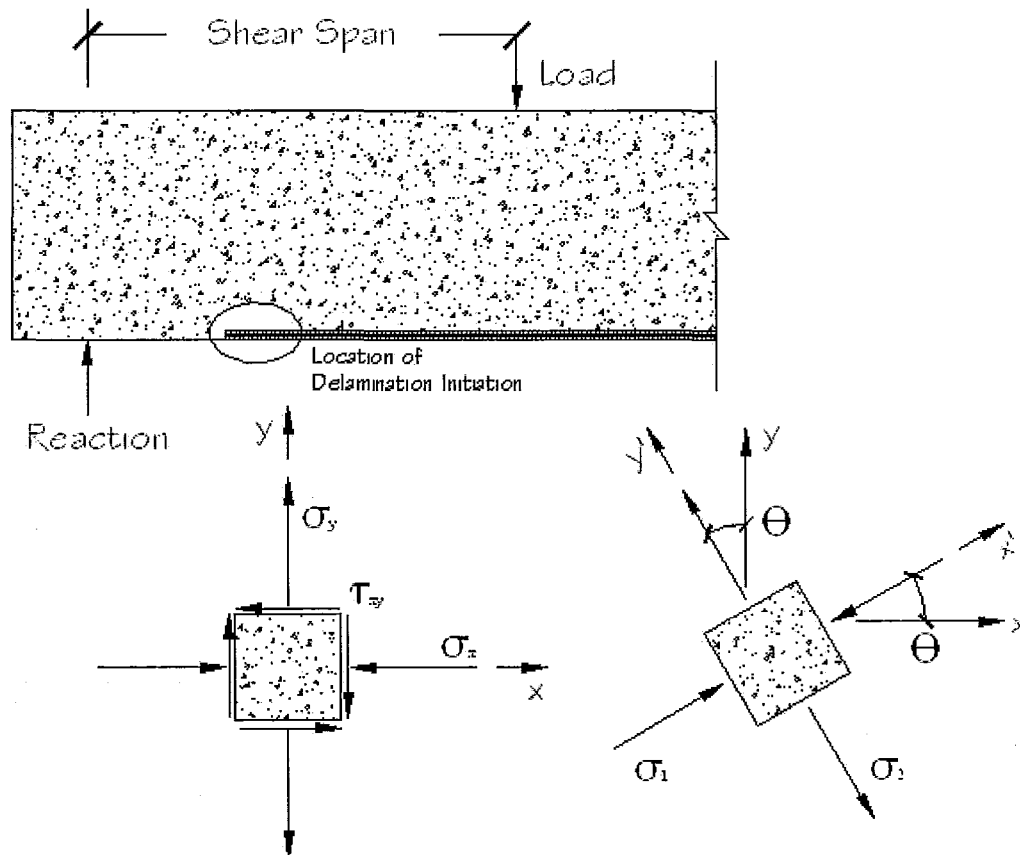


**Figure 5.32: Principle Stresses at Location of Delamination Initiation**

Although at the onset of delamination the RC beam may be cracked, therefore it would typically be assumed that concrete no longer resists tensile forces below the neutral axis, in reality between cracks tensile stresses do exist in concrete. Naturally, as these tensile stresses in the concrete increase, they exceed the modulus of rupture of concrete and cause flexural cracks. However, the concrete between the cracks would still be resisting tension. Since the bending moment at sections close to the ends of the bar exceeded the cracking moment of the beam cross sections, we will assume the properties associated with the cracked section to calculate  $\sigma_x$ . Between cracks we could expect a maximum tensile strength of  $f_r = 0.6\sqrt{f'_c}$ , where  $f_r$  is the modulus of rupture as

stipulated by the CSA A23.3-04. Table 5.6 summarizes the experimental and analytical shear and normal stresses as calculated by Täljsten's closed-form expression acting on the interface. Note that the stresses are assumed to be acting on the failure plane.

**Table 5.6: Concrete State of Stress near the Bar End and at the Onset of Delamination**

Beam	Delamination Load (kN)	Interfacial Shear Stress (MPa)		Peeling Stress (MPa)	Longitudinal Stress (MPa)
		Experimental Approximated $\tau_{xy}$	Täljsten Analytical $\tau_{xy}$	Täljsten Analytical $\sigma_y$	$\sigma_x$
1a	408	4.2	4.02	3.03	3.73
1b	399	3.4	3.94	2.97	3.73
2a	436	3.4	4.24	3.20	3.83
2b	463	7.2	4.51	3.39	3.83
3a	426	5.5	4.11	3.10	3.88
3b	457	6.9	4.39	3.31	3.88

The above stresses can be resolved into principal stresses. The orientation of the principal stress plane will be found using,

$$\tan 2\theta_p = \frac{2\tau_{xy}}{\sigma_x - \sigma_y} \quad (5.22)$$

and the principal stresses can be calculated using,

$$\sigma_1 = \frac{\sigma_x + \sigma_y}{2} + \sqrt{\left(\frac{\sigma_x - \sigma_y}{2}\right)^2 + \tau_{xy}^2} \quad (5.23)$$

$$\sigma_2 = \frac{\sigma_x + \sigma_y}{2} - \sqrt{\left(\frac{\sigma_x - \sigma_y}{2}\right)^2 + \tau_{xy}^2} \quad (5.24)$$

where  $\theta_p$ ,  $\sigma_1$ ,  $\sigma_2$  represent the angle of the principal planes orientation from the horizontal, the major principal stress and the minor principal stress, respectively. The positive sign convention of Equations 5.22 through 5.24 is taken as counter-clockwise for the angle  $\theta$ , tensile direction for the normal stresses and shear stresses act upwards on the

right surface of the element and downwards on the left. This sign convention is shown in Figure 5.33.

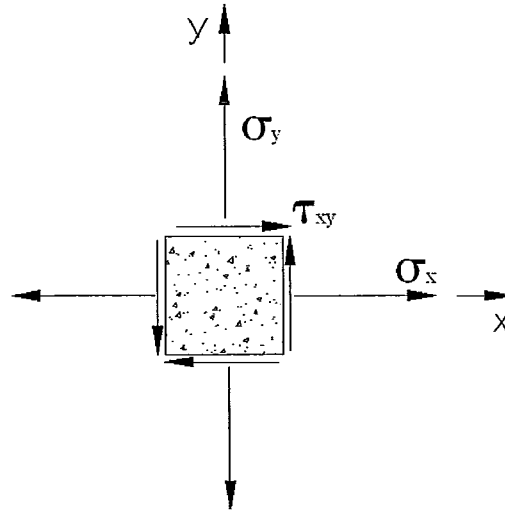


**Figure 5.33: Directions of Positive Stresses for Principal Stresses Calculation**

The calculated principal stresses are shown in Table 5.7 which will be used to check concrete failure. The biaxial failure envelope developed by Kupfer and Gerstle (1973) will be used for this purpose. The failure envelope is expressed in three regions as follows,

$$\text{Compression-Compression} \quad \left( \frac{\sigma_1}{f_{cu}} + \frac{\sigma_2}{f_{cu}} \right)^2 + \frac{\sigma_1}{f_{cu}} + 3.65 \frac{\sigma_2}{f_{cu}} = 0 \quad (5.25)$$

$$\text{Compression-Tension} \quad \frac{\sigma_2}{f_{tu}} = 1 + 0.80 \left( \frac{\sigma_1}{f_{cu}} \right) \quad (5.26)$$

$$\text{Tension-Tension} \quad f_{cu} = \sigma_2 = 0.64 \sqrt{f_{cu}^2} = \text{const.} \quad (5.27)$$

where  $f_{cu}$  and  $f_{tu}$  are the ultimate compressive strength and ultimate tensile strength of the concrete, respectively. As the principal stresses in each case involve tension and compression, only that portion of the envelope will be shown as defined by Equation 5.26. The results in Table 5.8 indicate whether the envelope limits were exceeded by the combination of the principal stresses acting on the concrete cover. Note that a concrete strength of 40 MPa was assumed to define the Kupfer-Gerstle failure envelope. Figure

5.34 shows the combination of the two principal stresses from each beam and the failure envelope corresponding to a concrete strength of 40 MPa. In every case, when comparing the interfacial shear stresses obtained through experimental testing and the analytical expression with the normal stresses calculated using Täljsten's equation, the results exceed the failure envelope. This of course indicates that the Kupfer and Gerstle failure criterion predicts concrete cover failure in every combination, which is in good agreement with the observed behaviour of the flexural tests.

*Table 5.7: Principal Stresses of Concrete at Delamination Initiation*

Beam	Based on Experimental Interfacial Shear Stress			Based on Analytical Interfacial Shear Stress		
	Plane Rotation $\theta_p$ (deg)	Horizontal $\sigma_1$ (MPa)	Vertical $\sigma_2$ (MPa)	Plane Rotation $\theta_p$ (deg)	Horizontal $\sigma_1$ (MPa)	Vertical $\sigma_2$ (MPa)
1a	-8.8	3.9	-3.0	-25.0	5.6	-4.9
1b	-7.2	3.8	-3.0	-24.8	5.5	-4.8
2a	-12.8	4.2	-3.2	-25.2	5.8	-5.2
2b	-13.5	4.3	-3.4	-25.7	6.0	-5.6
3a	-15.7	4.5	-3.1	-24.8	5.8	-5.0
3b	-18.8	4.8	-3.3	-25.3	6.0	-5.4

*Table 5.8: Prediction of Concrete Cover Failure based on the Kupfer and Gerstle Failure Envelope*

Beam	Based on Experimental Interfacial Shear Stress			Based on Analytical Interfacial Shear Stress		
	Horizontal $\sigma_1$ (MPa)	Vertical $\sigma_2$ (MPa)	Kupfer & Gerstle Failure Criterion	Horizontal $\sigma_1$ (MPa)	Vertical $\sigma_2$ (MPa)	Kupfer & Gerstle Failure Criterion
1a	3.9	-3.0	failed	5.6	-4.9	failed
1b	3.8	-3.0	failed	5.5	-4.8	failed
2a	4.2	-3.2	failed	5.8	-5.2	failed
2b	4.3	-3.4	failed	6.0	-5.6	failed
3a	4.5	-3.1	failed	5.8	-5.0	failed
3b	4.8	-3.3	failed	6.0	-5.4	failed

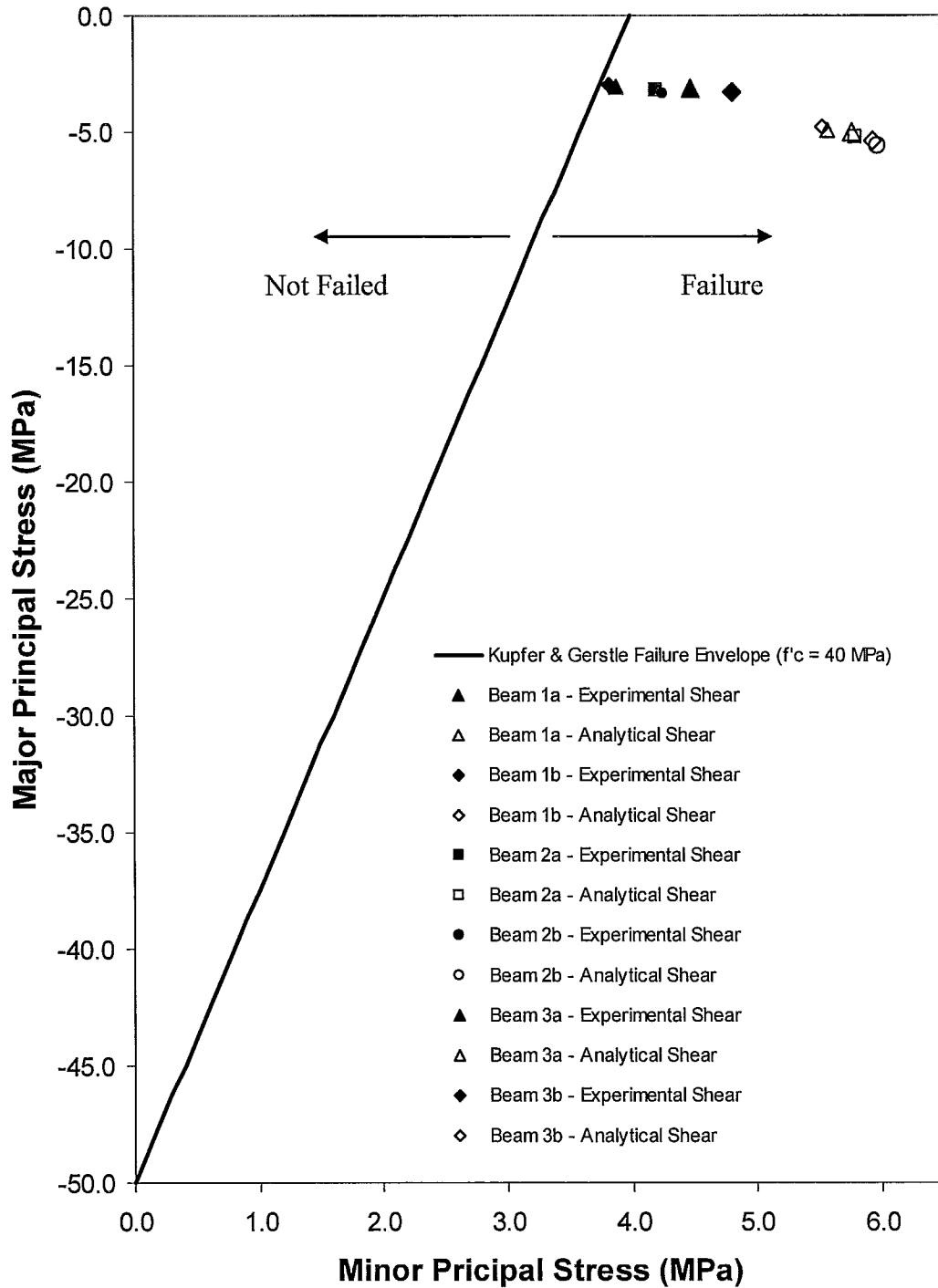


Figure 5.34: Kupfer and Gerstle Failure Envelope

In addition to the Kupfer and Gerstle failure envelope, the Mohr-Coulomb failure criterion can be used to check concrete failure near the bar ends as the actual shear resistance of unreinforced concrete is relatively small (Brosens and Van Gemert, 2001). The failure envelope is developed using the Mohr circle, corresponding to the different states of stress as shown in Figure 5.35 where a tangent, or envelope, can be drawn using a pure tensile and pure shear stress state as presented below.

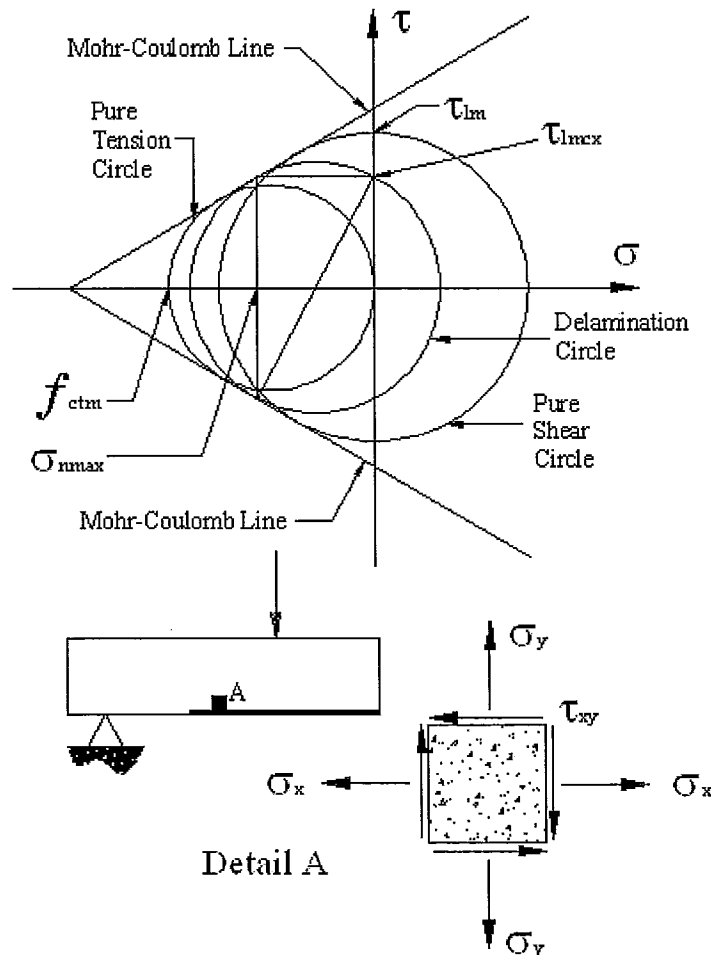


Figure 5.35: Mohr-Coulomb Failure Criterion

The Mohr-Coulomb failure criterion can then be defined as follows based on the assumption that  $\sigma_x \approx 0$ ,

$$\tau_{xy}^2 = Ff'_c f'_t - F(f'_c - f'_t)\sigma_y - F\sigma_y^2 \quad (5.28)$$

where

$$F = \frac{f'_c f'_t}{(f'_c + f'_t)^2}$$

Parameters  $f'_c$  and  $f'_t$  are the concrete compressive and tensile strength and  $\tau_{xy}$  and  $\sigma_y$  are the shear and normal stresses acting on the interface. If we assume  $f'_t \approx 0.1f'_c$ , then

$$F = \frac{f'_c{}^2}{(1.1f'_c)^2} = 0.083 \tag{5.29}$$

thus

$$\tau_{xy}{}^2 = (0.083 f'_c \times 0.1 f'_c) - 0.083(f'_c - 1.1 f'_c) \sigma_y - 0.083 \sigma_y{}^2 \tag{5.30}$$

or

$$\tau_{xy}{}^2 = 0.0083 f'_c{}^2 - 0.075 f'_c \sigma_y - 0.083 \sigma_y{}^2 \tag{5.31}$$

If we substitute peeling stresses from Table 5.6 into Equation 5.31, we can calculate the maximum shear stress,  $\tau_{xy}$ , needed to cause concrete failure at the interface. This shear stress can then be compared with the experimental shear stress,  $\tau_{FP}$ , and with shear stress calculated based on Täljsten’s method. If the calculated shear stress,  $\tau_{xy}$ , exceeds the stress  $\tau_{FP}$ , failure occurs, otherwise the interface is assumed not to fail. The results of these calculations are summarized in Table 5.9. For simplicity, the concrete strength is assumed 40 MPa for all the beams. Figure 5.36 illustrates all combinations of experimental and analytically calculated interfacial shear stresses with the interfacial

**Table 5.9: Prediction of Concrete Cover Failure Based on the Mohr-Coulomb Failure Envelope**

Beam	Based on Experimental Interfacial Shear Stress			Based on Analytical Interfacial Shear Stress		
	$\tau_{FP}$ (MPa)	$\sigma_y$ (MPa)	Mohr - Coulomb Failure Criterion	$\tau_{xy}$ (MPa)	$\sigma_y$ (MPa)	Mohr - Coulomb Failure Criterion
1a	1.07	-3.03	not failed	4.02	-3.03	failed
1b	0.87	-2.97	not failed	3.94	-2.97	failed
2a	1.68	-3.20	failed	4.24	-3.20	failed
2b	1.83	-3.39	failed	4.51	-3.39	failed
3a	2.14	-3.10	failed	4.11	-3.10	failed
3b	2.77	-3.31	failed	4.39	-3.31	failed

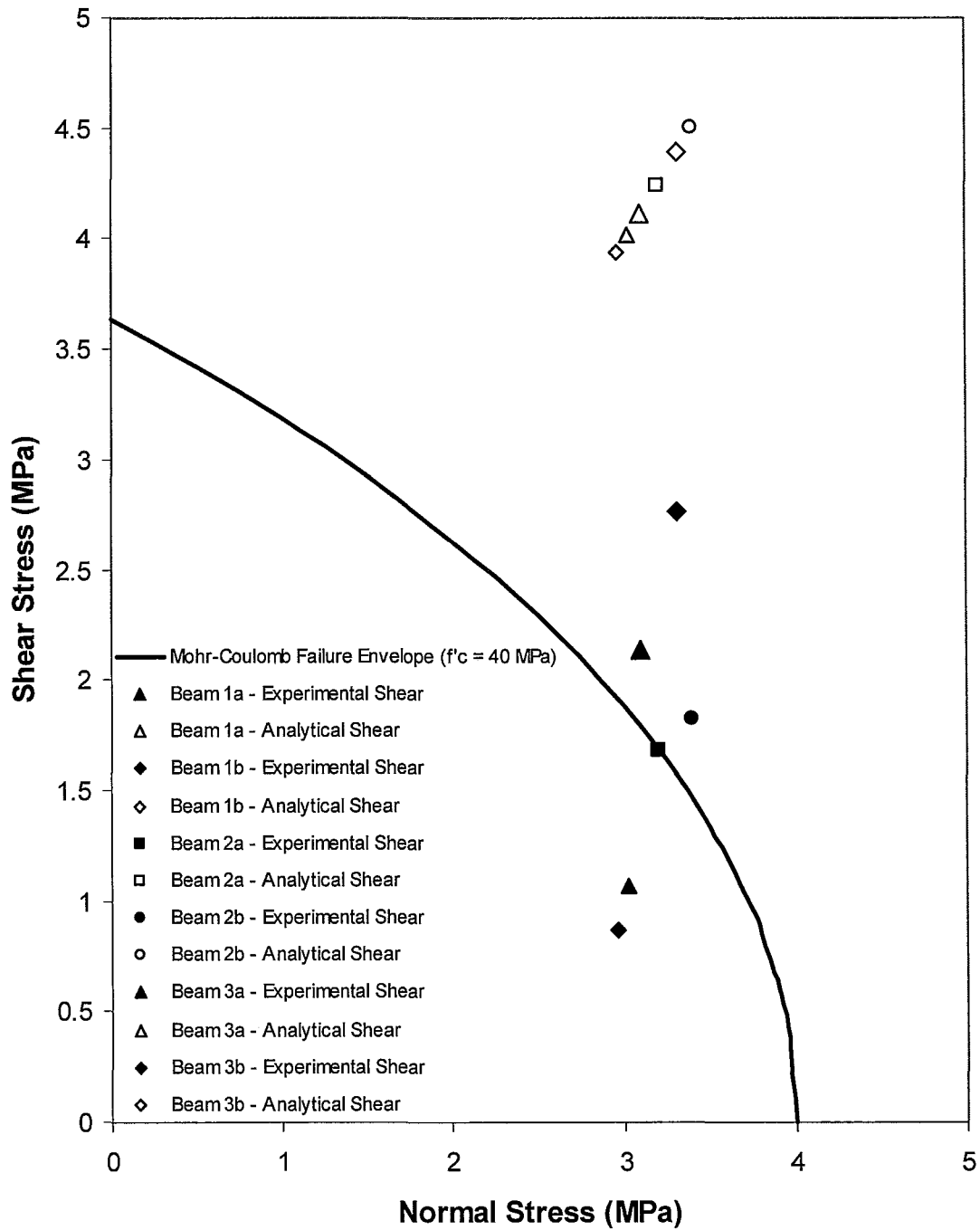
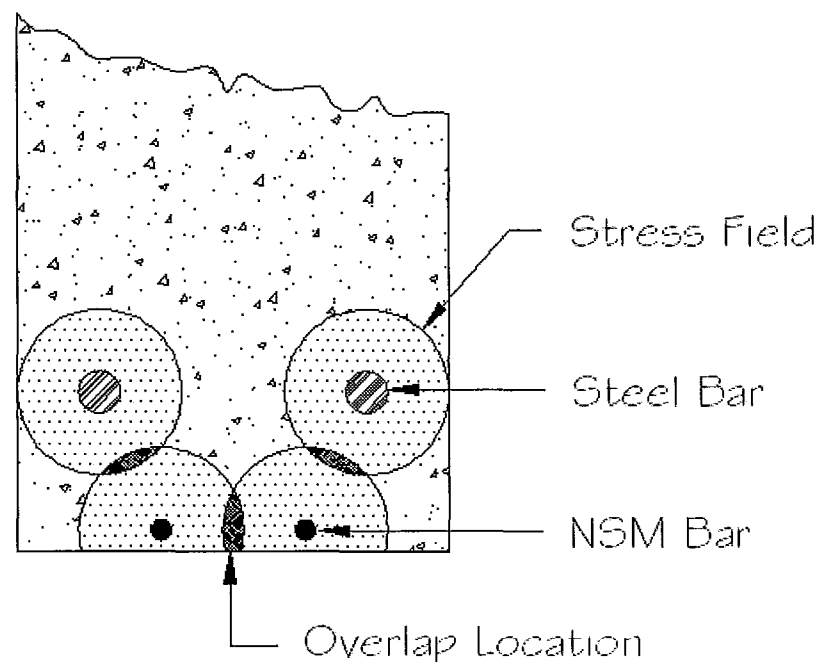


Figure 5.36: Mohr-Coulomb Failure Envelope

normal stresses calculated using Täljsten's closed-form solution. With the exception of beams 1a and 1b, where experimental interfacial shear stresses were used, all other combinations indicate that the concrete cover reached failure. Generally, the results of the Mohr-Coulomb failure criterion agree well with the results observed during testing and the Kupfer-Gerstle failure criterion. Note that the two beams which did not exceed the failure envelope are the unanchored beams, which due to relatively small longitudinal strain gradients along the NSM bar lengths, were unable to achieve higher interfacial shear strength. More importantly the previous analysis does not account for the additional interfacial shear stresses that are produced by the primary longitudinal steel. As shown in Figure 5.37, the bond stresses needed to develop the steel strength propagate into the concrete cover. These stress fields combined with the stress fields associated with developing the NSM reinforcement may overlap within the concrete cover and cause an additive effect, which is analogous to constructive interference amongst in-phase waves.



*Figure 5.37: Stress Concentrations due to Developing Stress Overlaps*

To examine the total tensile force at the NSM bar ends, consider Figure 5.38 (Brosens and Van Gemert, 2001). It illustrates the normal stress variation near the NSM bar end and follows Täljsten's closed-form solution for peeling stresses discussed earlier. At this location a tensile resultant,  $F_t$ , and a compressive resultant,  $F_c$ , are in equilibrium with one another. Notice how the tensile stress acts over a smaller length but is more intense than the compressive stresses that act over a much longer length. The length at which the tensile stresses act over is denoted as  $x_t$ , where

$$x_t = \frac{\pi}{4\beta} \quad (5.32)$$

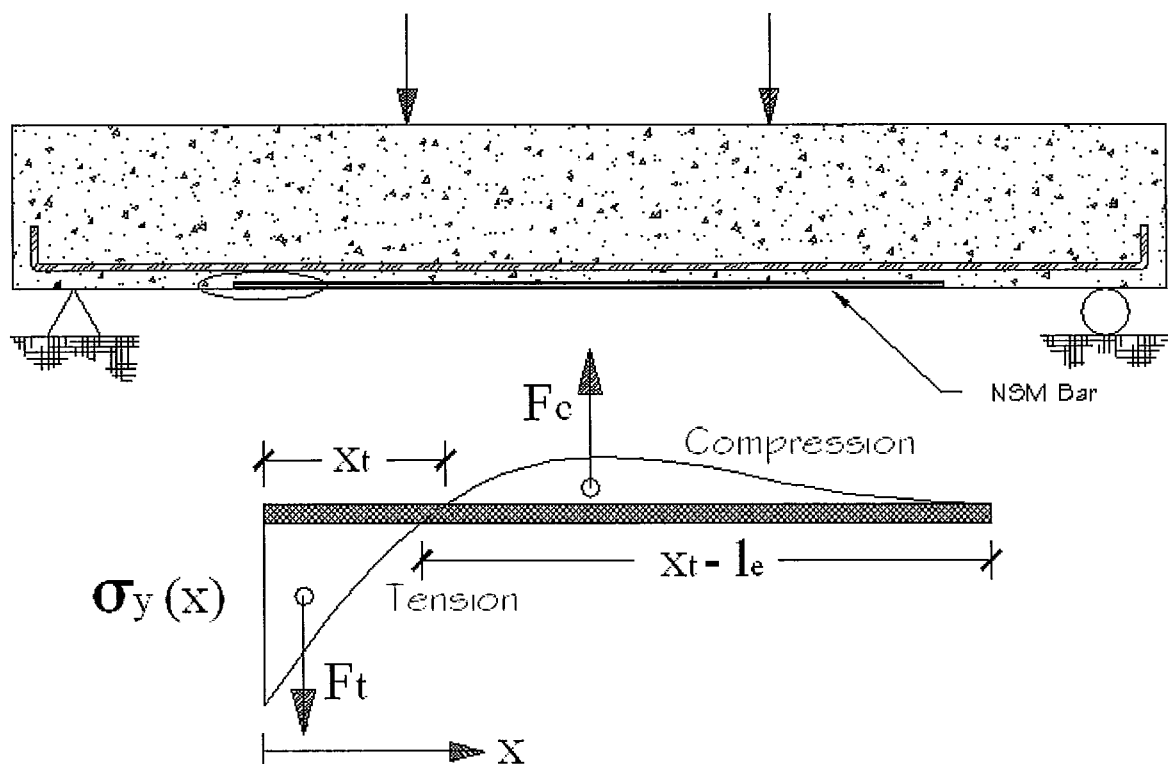


*Figure 5.38: Normal Stress Distribution at the NSM Bar End*

and as one may recall  $\beta$  is defined in Täljsten's expression as  $\beta = \sqrt[4]{\frac{E_a b_2}{4E_2 I_2 s}}$ . Figure 5.39 illustrates a typical normal stress variation based on Täljsten's expression. In this experimental program  $x_t$  is calculated as,

$$\beta = \sqrt[4]{\frac{E_a b_2}{4E_2 I_2 s}} = \sqrt[4]{\frac{3034 \text{MPa} \cdot 70 \text{mm}}{4 \cdot 100 \text{GPa} \cdot 2500 \text{mm}^4 \cdot 5 \text{mm}}} = 0.081 / \text{mm} \quad (5.33)$$

$$\Rightarrow x_t = \frac{\pi}{4\beta} = \frac{\pi}{4 \cdot 0.081} = 9.7 \text{mm} \approx 10 \text{mm}$$

where the value of  $x_t$  is common amongst all the strengthened beams.

The tensile segment of the curve can be approximated using a simple linear relationship as shown in Figure 5.39, which can be expressed using the following relationship,

$$\sigma_y(x) = \sigma_{y,\max} - \frac{\sigma_{y,\max}}{x_t} x \quad (5.34)$$

In both expressions  $x$  is taken from the bar end to  $x_t$ .

Therefore the tensile force,  $F_t$ , and from equilibrium the compressive force,  $F_c$ , can be determined using,

$$F_c = F_t = \int_0^{x_t} \sigma_y(x) \cdot A_{fcp} dx \quad (5.35)$$

where  $A_{fcp}$  is the total area of the CFRP bars located in the concrete cover in mm. Assuming that  $A_{fcp}$  is a constant and the tensile normal stress can be approximated with Equation 5.34, we can write Equation 5.36 as follows,

$$\text{Linear Approximation} \quad F_t \approx A_{fcp} \int_0^{x_t} \left( \sigma_{y,\max} - \frac{\sigma_{y,\max}}{x_t} x \right) dx \quad (5.36)$$

$$\Rightarrow F_t \approx A_{fcp} \left[ \sigma_{y,\max} x - \frac{\sigma_{y,\max}}{2x_t} x^2 \right]_0^{x_t}$$

$$F_t \approx \frac{1}{2} A_{fp} \sigma_{y,max} x_t \quad (5.37)$$

where for  $A_{fp}$  and  $x_t$  are common amongst all the strengthened beams, as mentioned earlier, and have values of 300 mm<sup>2</sup> and 10 mm, respectively. Therefore simplifying Equation 5.37 the tensile and compressive force near the NSM bar ends is approximately equal to  $1500\sigma_{y,max}$ , where the maximum vertical stress is determined using Täljsten's closed-form solution. Given these relationship we can calculate the tensile force,  $F_t$ , for all the beams which are summarized in Table 5.10.

**Table 5.10: Vertical Tensile/ Compressive Resultant Forces for Test Beams**

Beam	Maximum Normal Stress $\sigma_{y,max}$ (MPa)	Tensile/ Compressive Resultant (kN)
1a	3.0	4.5
1b	3.0	4.5
2a	3.2	4.8
2b	3.4	5.1
3a	3.1	4.7
3b	3.3	5.0

As seen in Table 5.10 the compressive and tensile resultants range from 4.5 to 5.1 kN. These resultant forces act perpendicular to the failure plane and are resisted by both the cohesion that exists in the concrete cover and the reinforcement that intersects it. In the current testing program, beams 2a through 3b have anchors which intersect the plane and carry a portion of the normal resultants whereas the beams 1a and 1b do not. Since these results are based on Täljsten's normal stress expression and the presence of the NSM anchors is not accounted for in the calculation, the tensile and compressive resultants are similar to one another regardless of the NSM bar configuration. Henceforth, the tensile force acting on the failure plane weakens the concrete cover as we have shown through failure analysis, while the compressive resultant increases the capacity of the local concrete due to confining effect. Since the tensile resultants act over a relative small length, 10 mm in the previous example, it is quite evident the significance of the end anchors during the application of the NSM bars. Although a maximum 5.1 kN

corresponds to 170 micro-strain in each of the 300 mm<sup>2</sup> NSM reinforcing anchors, assuming only one anchor from each bar will cross the plane within the distance  $x_i$ . One anchor would in practice be insufficient to prevent delamination, but if that anchor can hold a portion of the load and some delamination is allowed, the stress distribution within the interface will change and a new state of equilibrium will be established. In the new state, some of the stresses at the interface would be transferred to the adjacent anchors. Such detailed analysis is not within the scope of the present study, but is important for understanding the evolution of the delamination process.

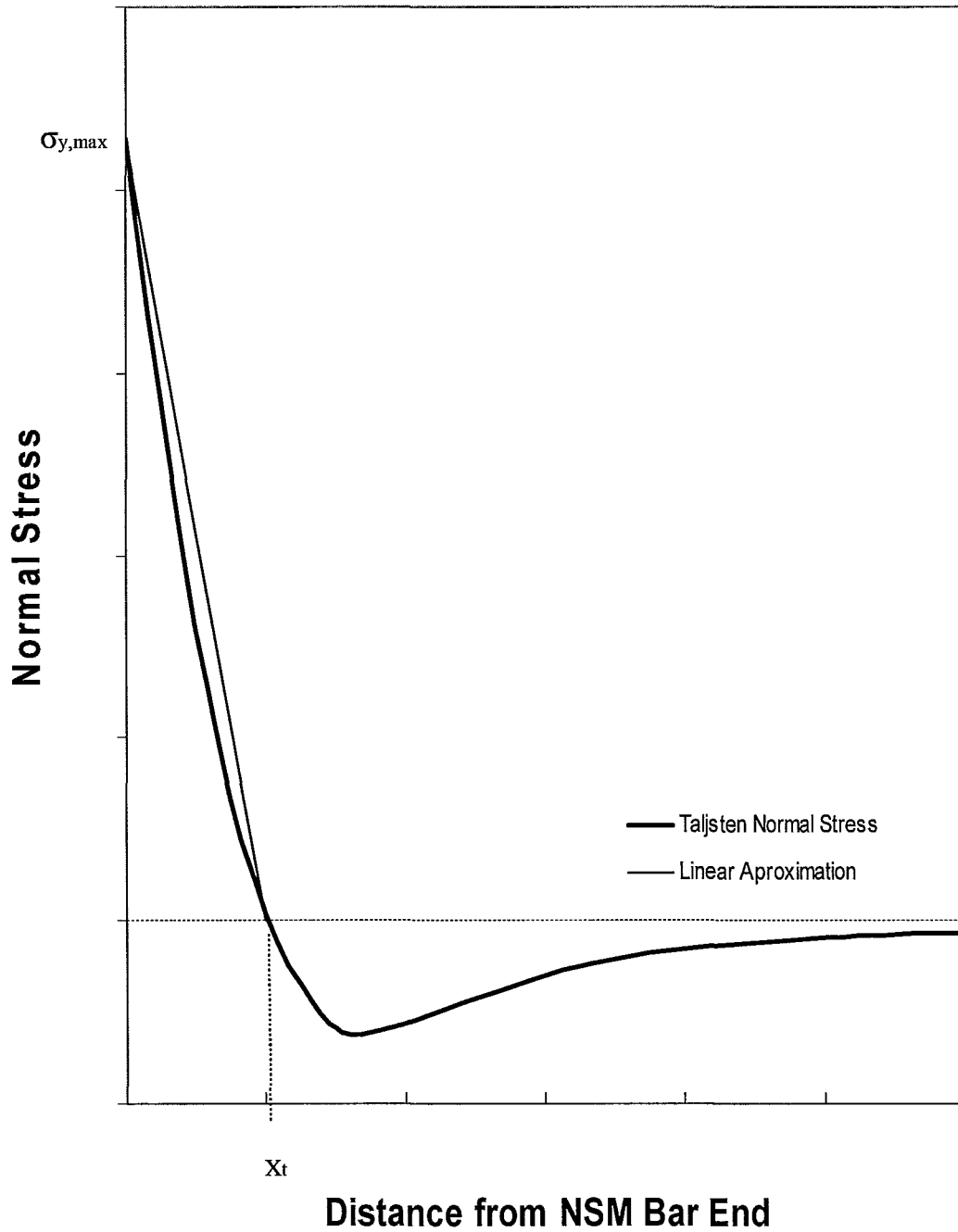


Figure 5.39: Tensile Stress Linear Approximation at NSM Bar End

---

## 5.6. Shear Strengthening using the NSM system

Like the issues encountered in flexural strengthening using NSM CFRP reinforcing bars, shear strengthening using a similar method has its own inherent challenges. For flexural strengthening the bars run along the beam axis, which for slender beams is much greater than the beam height. In flexural strengthening, the length of CFRP bars provide sufficient bond length to help develop the strength of the material; however, in shear strengthening a web, the length of the NSM bar is limited by the height of the beam. During the design of the experimental test specimens, all the beams were designed to fail in flexure and the idea of adding a NSM shear strengthening system was an exploratory topic. As discussed in chapter three, to ensure that the beams would not fail in shear they were designed to resist twice the maximum expected shear based on the empirical methods stipulated in the CSA A23.3-04. Thus in the type 3 beams, 3a and 3b, the objective of the shear strengthening system was to examine whether the CFRP NSM bars could be a viable replacement for the internal closed-loop steel stirrups.

Figure 5.40 and Figure 5.41 present the recorded maximum strains in the transverse reinforcement for beams 3a and 3b. It is apparent that the developed strains in the transverse reinforcement for the NSM CFRP bars are exceptionally small compared to the ultimate capacity of 12,000 micro-strain. The average strain in the CFRP is 1926 and 2929 micro-strain for beams 3a and 3b, respectively, at a 500 mm distance from the east support. These particular strain levels represent 16% and 24% of the CFRP ultimate strain. For both beams the longitudinal strain developed in the CFRP transverse reinforcement was negligible for the gauges located 250 mm from the east support as illustrated in the following two figures. On the other hand, the steel reinforcement located a distance of 390 mm from the east support never achieved its yield strain of approximately 2000 micro-strain. The behaviour of the under utilized transverse reinforcement, both steel and the CFRP, is due to the heavy shear reinforcement in the test specimens.

The design of the beams, based on the CSA A23.3-04 indicates that the shear corresponding to the flexural capacity can be satisfactorily resisted by No. 10 ( $A_s = 100 \text{ mm}^2$  per stirrup leg) closed-loop internal steel stirrups spaced at approximately 125 mm, but to ensure flexural failure, No. 15 ( $A_s = 200 \text{ mm}^2$  per stirrup leg) stirrups at 125 mm spacing were used. This substantially increased their shear capacity. When the NSM shear system was added, every other No. 15 internal stirrup was removed in the east shear span to accommodate the CFRP strengthening bars. Therefore, even without the additional CFRP strengthening bars the shear resistance of practically No. 15 internal stirrups at a spacing of 250 mm was sufficient to resist the applied shear; however, the relatively wide spacing might have caused complications if shear cracks had formed between adjacent stirrups. The objective as described earlier was to only examine if the CFRP NSM system is an acceptable replacement for the internal stirrups commonly used in beam design. Since both beams, 3a and 3b, failed in flexure and not in shear, we could assume that the CFRP strengthening method was an acceptable alternate reinforcing method for the achieved load levels and the designed internal shear capacity. To fully verify this statement, this shear strengthening system should be applied to beams designed to fail in shear, either alone or preferably in combination with internal reinforcement.

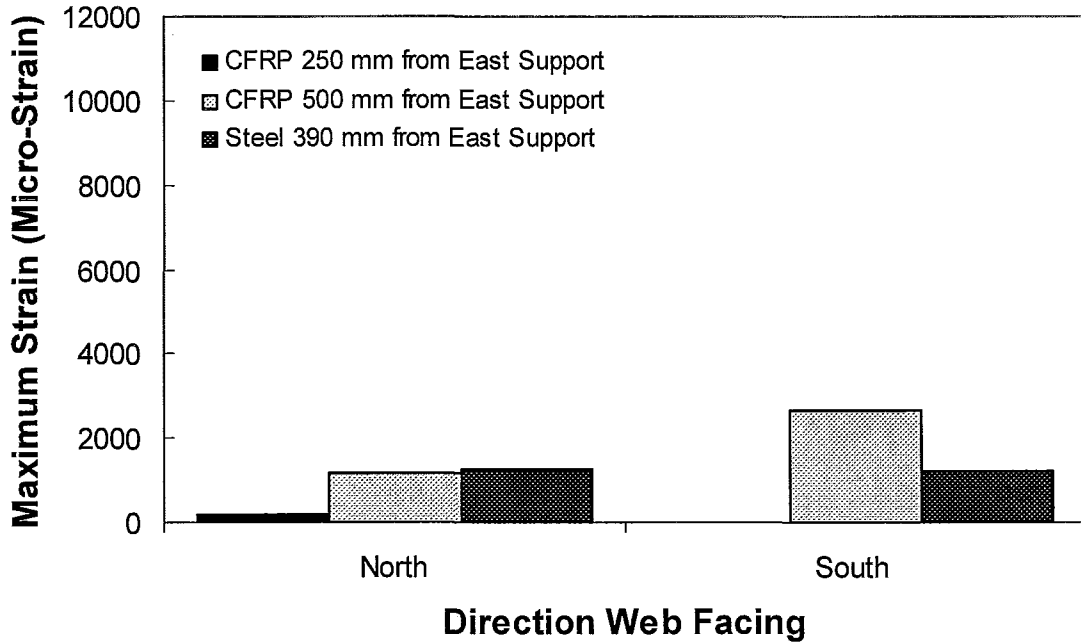


Figure 5.40: Strain Developed in Transverse Reinforcement for Beam 3a

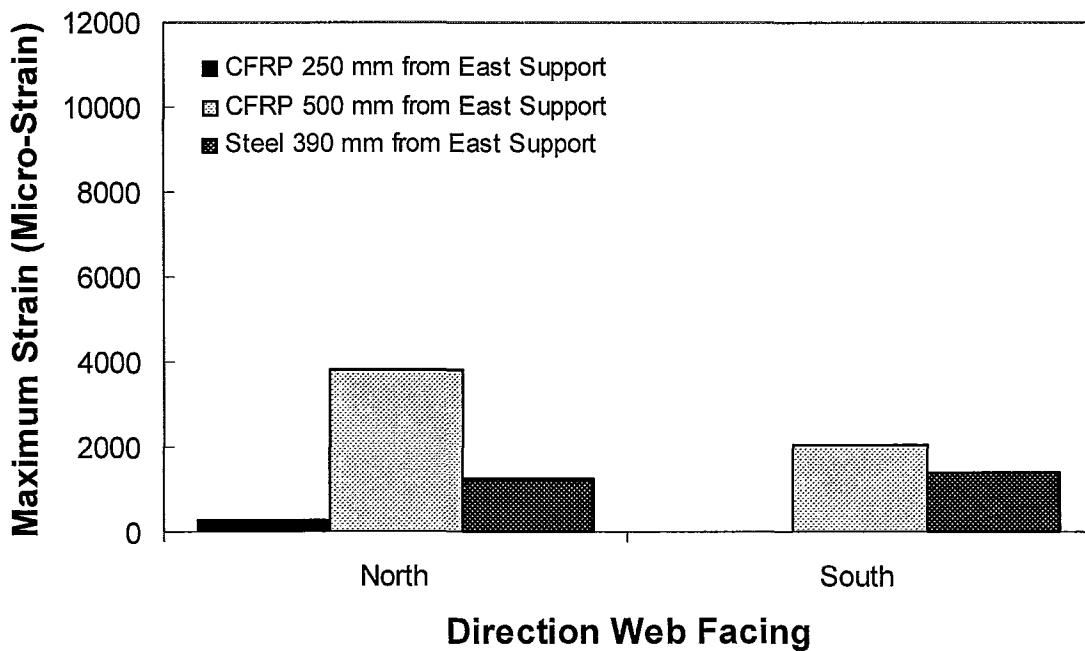


Figure 5.41: Strain Developed in Transverse Reinforcement for Beam 3b

# Chapter 6

## Summary, Conclusions & Recommendations

### **6.1. Summary**

Seven simply supported under reinforced RC beams were experimentally tested; six of the seven beams were strengthened using NSM CFRP bars while the remaining beam served as a control beam reinforced with internal steel only. Four of the strengthened beams were retrofitted with anchored CFRP bars extending into the core of the beam to delay the onset of delamination. The remaining two beams were strengthened with unanchored CFRP bars. All the beams were designed to fail in flexure to compare the behaviour of the beams with anchored NSM bars to that of the beams with unanchored NSM bars. As an exploratory study, two of the strengthened beams with anchored bars had every other internal steel stirrup removed and replaced with an anchored NSM CFRP bar grooved along the beam web to resist the applied shear forces. The replacement of internal stirrups with NSM bars was conducted along only one half of the beams to investigate whether the NSM technique is an acceptable for shear strengthening. All the beams were tested to failure in four-point bending over a span of 2500 mm, including shear span lengths of 750 mm and a region of constant moment of 1000 mm centered along the beam length.

The main objective of the study was to investigate the effectiveness of the new anchoring system to delay the onset of delamination due to interfacial stresses between the RC beam and the CFRP reinforcement. The CFRP bars were extracted from common NEFMAC grids which are intended to reinforce slab elements. The grids were cut for all three types of required NSM reinforcement: flexural reinforcement without anchors, flexural reinforcement with the integral anchors and the shear reinforcement with the integral anchors. The NSM reinforcement consisted of size C19 NEFMAC bars (nominal 10 mm by 15 mm cross sectional area) and were positioned within cut grooves along the beam's tensile faces; a similar procedure was followed to shear strengthen the two beams with anchored NEFMAC bars. The anchors were embedded within perpendicular grooves spaced at the NEFMAC standard grid width and extended into the core of the RC beam. The anchors were positioned along the primary longitudinal groove cut within the concrete cover. Due to the preliminary nature of the study and due to lack of design guidelines for the application of NSM strengthening systems, practical considerations regarding the NSM construction were based on recent experimental and analytical literature.

The tests were successfully completed under displacement controlled. The test beams failure loads were compared with their theoretical ultimate load capacities based on the method specified in the CSA A23.3-04 and using a non-linear software package named Wizard. Both calculations were based on an ultimate concrete strain of 0.0035 as commonly assumed in the Canadian Standard. In contrast to the ancillary tests, the reinforcing steel bars behaved elasto-plastically illustrating very little strain hardening, therefore calculations between Wizard and the manual calculations were similar to one another. Both procedures yielded similar capacities which were all larger than the capacities observed in the tests. All of the six strengthened beams failed prematurely due to the delamination of the NSM bars initiated near the bars ends. The beams retrofitted with anchored bars achieved approximately 8% higher moment than the beams without the anchors. Although the overall strength was not drastically increased, the achieved

strain in the NSM reinforcing bars increased by nearly two-fold and noticeably higher ductility was observed for the beams strengthened with anchored bars.

The stresses near the NSM bar ends where delamination initiated was analyzed. Generally, the combination of interfacial shear stresses and interfacial normal stresses exceeded the Kupfer and Gerstle and the Mohr-Coulomb failure criterion, exhibiting good agreement with the experimental observations. Interfacial shear stresses were obtained by both an approximate method based on experimental results and a closed-form analytical expression derived by Täljsten. Normal or peeling stresses, were calculated using Täljsten's theoretical expression.

The shear strengthening of RC beams using anchored NSM bars appeared to be successful. Although the beams had sufficient internal steel stirrups to resist the applied shear at flexural failure, their spacing did not satisfy the requirements of the CSA A23.3-04. The NSM bars were bonded between internal stirrups and provided sufficient resistance to cause the flexural NSM bars to delaminate from the concrete cover rather than the beams failing in shear.

## **6.2. Conclusions**

The following conclusions can be stated from the experimental testing and the analysis of the test results:

1. In every case, the delamination of the NSM strengthening system initiated in end regions of the bar and propagated toward the centre of the beam.
2. The initiation of delamination always caused a noticeable drop in the resistance. After the initial load drop, the beams strengthened with anchored NSM bars showed an increase in resistance while the beams strengthened with unanchored NSM bars experienced a 'sharp' decline in strength immediately following the onset of delamination.

3. The beams strengthened with anchored NSM CFRP bars exhibited excellent bond to the concrete. As the NSM bars separated from the RC beam, concrete from within the confined core was removed along with the anchors.
4. In every case the horizontal failure plane was located within the concrete cover and not at either the bar/ epoxy or epoxy/ concrete interfaces.
5. Beams with anchors generally had 8% higher moment capacity compared to the beams without anchors.
6. Beams with anchors exhibited an increase in ductility and experienced a larger deflection at failure compared to the beams without anchors.
7. Maximum strains were always greater in the anchored CFRP NSM reinforcing bars compared to the beams without anchors. The maximum strains ranged from 33 to 39 % and 59 to 69% for the beams without anchors and beams with anchors, respectively, of the bar's ultimate strain.
8. After the NSM bars delaminated from concrete cover, the load dropped and the beam behaved as a typical RC flexural element with the internal reinforcing steel resisting the applied load.
9. None of the strengthened beams achieved their theoretical capacity due to premature delamination of the NSM reinforcement.
10. Although the achieved strain in the NSM shear reinforcement was not significant due to the over design of the internal shear resisting system, the NSM shear reinforcement proved to be an acceptable substitute for internal steel stirrups.

11. Both concrete failure criteria, Kupfer and Gerstle, and Mohr-Coulomb, generally indicated concrete failure near the bar end when considering both the interfacial shear and normal stresses.

### **6.3. Recommendations for Future Work**

The following recommendations are discussed for future work:

1. Test beams with larger anchor spacing to determine the effect on the delamination load, ultimate strength and ductility of the beams strengthened with NSM CFRP bars.
  2. Remove anchors within the region of constant moment region to verify the insignificance of the anchors located within this zone of zero shear. Additionally, remove some of the anchors within the shear spans to observe the beam behaviour.
  3. Change the length of the anchors to establish an optimal embedment depth for them.
  4. Reduce the total area of NSM reinforcement used to investigate if a greater maximum strain can be achieved in the CFRP bars.
  5. Develop a complete design method for calculating the delamination load, ultimate capacity and ductility of beams strengthened with NSM FRP.
  6. Introduce test specimens with various bar development lengths for NSM FRP strengthened beams.
  7. Test beams without any internal stirrups and use the NSM shear reinforcement instead to validate the performance of the NSM shear reinforcement with anchors.
-

8. Test beams with NSM bars located above the internal steel reinforcement and place the bars on the vertical faces of the beam. Although this decreases the moment arm, it may allow the anchored NSM bars to reach full rupture.

# References

- Abushoglin, F. 1997. Computer-Aided Non Linear Analysis of Simple Beams and One-Way Slabs Reinforced by FRP and/or Steel Bars. M.Eng Thesis. Department of Civil and Environmental Engineering, Carleton University. Ottawa (ON). 150 p.
- [ACI] American Concrete Institute Technical Committee 440. 2002. Guide for the Design and Construction of Externally Bonded FRP Systems for Strengthening Concrete Structures. Farmington Hills (MI): American Concrete Institute. 45 p.
- [ASTM] American Society for Testing and Materials. 2006. Standard Test Method for Static Modulus of Elasticity and Poisson's Ratio of Concrete in Compression. West Conshohocken (PA): ASTM International. 5 p.
- Barros JAO and Fortes AS. 2004. Flexural strengthening of concrete beams with CFRP laminates bonded into slits. *Cement & Concrete Composites*. 27(2005): 471 – 480.
- Barros J, Sena-Cruz J, Dias S, Ferreira D and Fortes A. 2004. Near surface mounted CFRP-based technique for the strengthening of concrete structures. *Jornada Técnica en Honor a Ravindra Gettu*. October 5: 1 – 13.
- BASF. 2007. MB Primer II [Internet]. Shakopee (MN): BASF Construction Chemicals, LLC – Building Systems; [cited 2007 August] Available from: [http://files.buildsite.com/dbderived-f/masterbuilders/derived\\_files/derived300267.pdf](http://files.buildsite.com/dbderived-f/masterbuilders/derived_files/derived300267.pdf)
- BASF. 2007. MBrace® Saturant [Internet]. Shakopee (MN): BASF Construction Chemicals, LLC – Building Systems; [cited 2007 August] Available from: [http://files.buildsite.com/dbderived-f/masterbuilders/derived\\_files/derived300358.pdf](http://files.buildsite.com/dbderived-f/masterbuilders/derived_files/derived300358.pdf)
- Beer FP and Johnston ER. 1992. *Mechanics of Materials*. 2<sup>nd</sup> Edition. London (UK): McGraw-Hill Inc. 736 p.

- 
- Brosens K. and Van Gemert D. 2001. Strengthening of Concrete Structures with Externally Bonded Steel Plates or CFRP Laminates – Part 1: Specific Design Concepts. *WTA International Journal for Restoration of Buildings and Monuments*. 7(3-4): 367 – 402.
- Chen, WF. 1982. *Plasticity in Reinforced Concrete*. First Edition. New York (NY): McGraw-Hill Inc. 474 p.
- Choi HT, West JS and Soudki KA. 2008. Flexural Behaviour of Partially Bonded Near-Surface-Mounted CFRP Strengthened Concrete T-Beams. *Advanced Composite Materials in Bridges and Structures*. Winnipeg, Manitoba, Canada: September 22 – 24. 9 p.
- [CAC] Cement Association of Canada. 2004. *Design of Concrete Structures*. Ottawa (ON): Canadian Standards Association. 220 p.
- Collins MP and Mitchell D. 1991. *Prestressed Concrete Structures*. First Edition. Englewood Cliffs (NJ): Prentice-Hall Inc. 766 p.
- [CSA] Canadian Standards Association. 2002. *Design and Construction of Building Components with Fibre-Reinforcement Polymers*. CSA Standard S806-02. Rexdale (Toronto), Ontario.
- De Lorenzis L, Nanni A and La Tegola A. 2000. Strengthening of Reinforced Concrete Structures with Near Surface Mounted FRP Rods. *International Meeting on Composite Materials*. Milan, Italy: May 9 – 11. 8 p.
- De Lorenzis L and Nanni A. 2001. Shear Strengthening of Reinforced Concrete Beams with Near-Surface Mounted Fiber-Reinforced Polymer Rods. *ACI Structural Journal*. 98(1): 60 – 68.
- De Lorenzis L and Nanni A. 2002. Bond between Near-Surface Mounted Fiber-Reinforced Polymer Rods and Concrete in Structural Strengthening. *ACI Structural Journal*. 99(2): 123 – 132.
- De Lorenzis L, Lundgren K and Rizzo A. 2004. Anchorage Length of Near-Surface Mounted Fiber-Reinforced Polymer Bars for Concrete Strengthening – Experimental Investigation and Numerical Modeling. *ACI Structural Journal*. 101(2): 269 – 278.
- De Lorenzis L and Teng JG. 2006. Near-surface mounted FRP reinforcement: An emerging technique for strengthening structures. *Composites: Part B*. 38(2007): 119 – 143.
-

- 
- El-Hacha R and Rizkalla SH. 2004. Near-Surface-Mounted Fiber-Reinforced Polymer Reinforcements for Flexural Strengthening of Concrete Structures. *ACI Structural Journal*. 101(5): 717 – 726.
- Hassan TK and Rizkalla SH. 2003. Investigation of Bond in Concrete Structures Strengthened with Near Surface Mounted Carbon Fiber Reinforced Polymer Strips. *Journal of Composites for Construction*. 7(3): 248 – 257.
- Hassan TK and Rizkalla SH. 2004. Bond Mechanism of Near-Surface-Mounted Fiber-Reinforced Polymer Bars for Flexural Strengthening of Concrete Structures. *ACI Structural Journal*. 101(6): 830 – 839.
- Hofbeck JA, Ibrahim IO and Mattock, AH. 1969. Shear Transfer in Reinforced Concrete. *ACI Structural Journal*. 66 (2): 119 – 128.
- Jung WT, Park YH, Park JS, Kang JY and You YJ. 2005. Experimental Investigation on Flexural Behavior of RC Beams Strengthened by NSM CFRP Reinforcements. *ACI Structural Journal*. 230(2005): 795 – 806.
- Kang JY, Park YH, Park JS, You YJ and Jung WT. 2005. Analytical Evaluation of RC Beams Strengthened with Near Surface Mounted CFRP Laminates. *ACI Structural Journal*. 230(2005): 779 – 794.
- Karbhari, VM. 1994. Applications of Composites in Civil Engineering. *Advanced Manufacturing Technology for Polymer Composite Structures in Japan*. April (1994): chapter 3. Available from: [http://www.wtec.org/loyola/polymers/c4\\_s3.htm](http://www.wtec.org/loyola/polymers/c4_s3.htm).
- Kupfer, H and Gerstle, HK. 1973. Behaviour of Concrete under Biaxial Stresses. *Journal of Engineering Mechanics Division*. 99(EM4): 853 – 866.
- MacGregor JG and Bartlett FM. 2000. *Reinforced Concrete: Mechanics and Design*. 1<sup>st</sup> Canadian Edition. Toronto (ON): Pearson Education Canada Inc. 1042 p.
- Mallick, PK. 1988. *Fiber-Reinforced Composites: Materials, Manufacturing and Design*. First Edition. New York (NY): Marcel Dekker Inc. p. 353.
- Malek AM, Saadatmanesh H and Ehsani MR. 1998. Prediction of Failure Load of R/C Beams Strengthened with FRP Plate due to Stress Concentration at the Plate End. *ACI Structural Journal*. 95(1): 142 - 152.
- Moukwa M. and Barkey T. 1996. Performance of Thermoset Polymers in Mineral and Organic Acid Service. *Journal of Protective Coatings and Linings*. 13(7): 58 – 69.
-

- Park, R and Paulay, T. 1975. Reinforced Concrete Structures. New York (NY): Wiley. 800 p.
- Parretti R and Nanni A. 2004. Strengthening of RC Members Using Near-Surface Mounted FRP Composites: Design Overview. *Advances in Structural Engineering*. 7(6): 469 – 483.
- Perera WKKG, Ibell TJ, Darby AP and Denton SR. 2008. Anchorage and Behaviour of Near Surface Mounted Carbon Fibre Reinforced Polymer Bars. *Advanced Composite Materials in Bridges and Structures*. Winnipeg, Manitoba, Canada: September 22 – 24. 10 p.
- Roberts, TM. 1989. Approximate Analysis of Shear and Normal Stress Concentrations in the Adhesive Layer of Plated RC Beams. *The Structural Engineer*. 67(12): 229 – 233.
- Soliman SM, El-Salakawy E, Benmokrane B and Abdel Baky H. 2008. Experimental and Numerical Investigation of RC Beams Strengthened in Bending with Near Surface Mounted CFRP. *Advanced Composite Materials in Bridges and Structures*. Winnipeg, Manitoba, Canada: September 22 – 24. 10 p.
- Teng JG, De Lorenzis L, Wang B, Rong L, Wong TN and Lam L. 2006. Debonding Failures of RC Beams Strengthened with Near Surface Mounted CFRP Strips. *Journal of Composites for Construction*. 10(2): 92 – 105.
- Täljsten B. 1997. Strengthening of Beams by Plate Bonding. *Journal of Materials in Civil Engineering*. 9(4): 206 – 212.
- Yost JR, Gross SP, Dinehart DW and Mildenberg JJ. 2007. Flexural Behavior of Concrete Beams Strengthened with Near-Surface-Mounted CFRP Strips. *ACI Structural Journal*. 104(4): 430 – 437.

# Appendix A

## Design Calculations

### **A.1. General**

The following section will describe the detailed design calculations used to determine the internal and NSM reinforcement for each test specimen. The calculations are based on the provisions of the CSA A23.3-04 for RC design, and for the FRP on the recommendations of the ACI 440.2R-02. Although the ACI 440.2R-02 is a design guide for externally bonded FRP systems, due to the absence of specific guidelines for NSM strengthening, it is typical to adopt the same basic principles used to design externally bonded laminate systems. In addition to the ACI guidelines, two papers outlining the design of NSM systems were also used (Parretti and Nanni 2004; De Lorenzis and Teng 2006). The technical papers gave further insight into detailing NSM systems.

Initially the beams were designed using specified material properties, but material ancillary testing was performed to capture the actual stress-strain behaviour of each constituent material. The details and results of these tests were presented in chapter three. In contrast to the non-linear stress-strain behaviour observed in the steel reinforcement coupon tests during the ancillary tests, the beam tests revealed a stress-strain relation for reinforcement bars which was more elasto-plastic. As explained earlier, due to the consistency of this elasto-plastic behaviour in the flexural tests, the material properties of the reinforcing steel will be based on the beam tests results.

---

For calculating the design strength of a member, the CSA A23.3-04 specifies material reduction factors to account for the variability in material strength and the quality of the construction process. In the case of the seven test beams constructed for this experimental program, all material reduction factors were set to one. This permitted a more accurate estimate of the flexural capacity of the test specimens; nevertheless, in the shear design calculations the material reduction factors were included where seen fit to prevent shear failure.

Each beam, as discussed in chapter three, had total length and span of 3175 mm and 2500 mm, respectively. The length was chosen based on lab space limitations and past test experiments for near surface retrofits for slender beams. The cross sections of all the beams were 450 x 275 mm. The selection of the width of the web was influenced by the longitudinal steel and the CFRP reinforcement spacing. The height of the web was again based on previous test specimens reported in the literature and by the requirements of adequate shear capacity, ensuring flexural failure, and by the need for sufficient length to ensure a few anchors could be placed along the web height when using the CFRP shear strengthening system. All the beams were longitudinally reinforced, possessing similar theoretical moment capacity.

## ***A.2. Steel Material Properties Observed in Beam Testing***

The bare steel reinforcement coupon tests and the stress-strain relations observed during the beam tests contradict one another as described in chapters three and four. As discussed earlier, due to the consistency of the beam tests, the results of the ancillary tests for steel reinforcing bars will be discarded. The stress-strain relationships obtained from the coupon tests were measured with an electric extensometer, which was loosely fitted to the test specimen, increasing the probability of erroneous results.

Table A.1 summarizes the observed yield strains and associated yield load for each of the test beams. Additionally, Table A.2 presents the mean yield strain and mean yield load and their respective standard deviations for each test beam. The last row in

---

Table A.2 presents the mean strain and associated standard deviation across all beam specimens. Notice that the mean load and its standard deviation are not calculated as we cannot effectively compare the yield load of the control beam to those of the strengthened beams. Recall that the control beam contains double the amount of reinforcing steel compared to each of the six strengthened beams, therefore, the contribution of the steel in the control will inherently vary from the contribution of the steel in the strengthened beams.

**Table A.1: Summary of Steel Reinforcement Yield Strain from Beam Tests**

Beam	Under East Point Load		At Midspan		Under West Point Load	
	$\epsilon_y$ (Micro-Strain)	$P_y$ (kN)	$\epsilon_y$ (Micro-Strain)	$P_y$ (kN)	$\epsilon_y$ (Micro-Strain)	$P_y$ (kN)
control	2919	597	2878	597	2943	597
1a	3125	388	2880	404	3173	388
1b	2868	399	2651	399	2516	399
2a	2985	386	2902	370	2815	397
2b	3125	391	3206	398	3038	414
3a	2860	380	2815	376	2862	374
3b	2962	383	-	-	3019	381

**Table A.2: Summary of Yield Strain Statistics from Beam Tests**

Beam	Mean $\epsilon_y$	Standard Deviation, $\epsilon_y$	Mean $P_y$	Standard Deviation, $P_y$
control	2913	27	597	0
1a	3059	128	393	8
1b	2678	145	399	0
2a	2901	69	384	11
2b	3123	69	401	10
3a	2846	22	377	2
3b	2991	29	382	1
<b>All Samples</b>	<b>2927</b>	<b>163</b>	<b>-</b>	<b>-</b>

Based on the provisions of CSA A23.3-04 and the experimental moment capacity of the control beam we can back-calculate the yield strength of the reinforcing steel. Recall from Table 5.1 that the moment capacity of the control beam is 224 kN·m, and the following assumptions were incorporated in the back-calculation:

**a. Cross sectional geometric dimensions**

Height of the cross section,  $h = 450$  mm

Width of the cross,  $b = 275$  mm

**b. Tensile reinforcing steel detailing (compression steel neglected)**

Depth of the tensile reinforcing steel,  $d = 390$  mm

Area of the tensile reinforcing steel,  $A_s = 1200$  mm<sup>2</sup> (4 x No. 20 bars)

**c. Material properties based on ancillary tests (refer to chapter 3 for details)**

Concrete strength,  $f'_c = 38.6$  MPa (at time of testing)

Concrete material reduction factor  $\phi_c = 1.0$  (as discussed earlier)

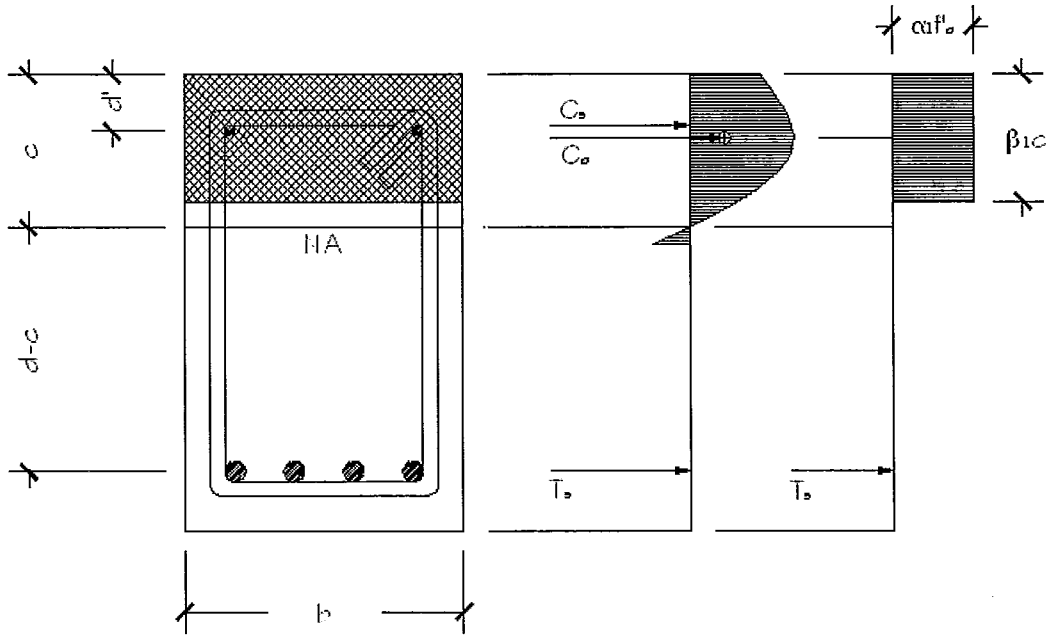
Steel material reduction factor, set to  $\phi_s = 1.0$  (as discussed earlier)

Figure A.2 illustrates the idealized compression stress rectangular block method stipulated in the CSA A23.3-04. The concrete stress-strain relationship is converted into an equivalent stress block, also known as the Whitney Stress Block, that is characterized by an intensity  $\alpha_1 f'_c$  acting uniformly over a depth  $\beta_1 c$ , where  $\alpha_1$  and  $\beta_1$  are parameters dependant on the amount of strain in the concrete. This equivalent stress block method is the basis for the following back calculations used to estimate the yield strength of the primary reinforcing steel and its corresponding elastic modulus knowing that the moment capacity of the control beam is 224 kN·m. The contribution of the compression steel will be neglected in the following calculations to reduce the number of considered parameters. Additionally, due to small area of the compressive bars relative to the amount of concrete area resisting compressive stresses, it is common to ignore such small amounts of compression steel. Taking moment with respect to the concrete resultant we find,

$$M_r = T_s \left( d - \frac{a}{2} \right) \quad (A.1)$$

or, taking moment equilibrium with respect to the primary steel resultant,

$$M_r = C_c \left( d - \frac{a}{2} \right) \tag{A.2}$$



**Figure A.1: Back Calculation using the Equivalent Stress Block Method**

where  $C_c$  and  $T_s$  are the resultant concrete and tensile steel forces, respectively. The resultants are given by

$$C_c = \phi_c (\alpha_1 f'_c) (\beta_1 c) b \tag{A.3}$$

$$T_s = \phi_s f_s A_s \tag{A.4}$$

where  $f_s$  represents the stress in the tensile steel and is assumed to behave elasto-plastically. To find the yield strength of the steel we will back-calculate from the yield strain, which is given as 2913 micro-strain on average, as shown in Table A.2. Substituting the resultants in Equation A.1 yields the following,

$$224 \text{ kN} \cdot \text{m} = \phi_s f_y A_s \left( d - \frac{\beta_1 c}{2} \right) \tag{A.5}$$

$$224kN \cdot m = f_y (1200mm^2) \left( 390mm - \frac{\beta_1 c}{2} \right) \quad (A.6)$$

$$224kN \cdot m = 468,000 f_y - 600 f_y \beta_1 c \quad (A.7)$$

$$\Rightarrow f_y = \frac{224kN \cdot m}{468,000 - 600 \beta_1 c} \quad (A.8)$$

and substituting the resultants in Equation A.2 yields the following,

$$224kN \cdot m = \phi_c (\alpha_1 f'_c) (\beta_1 c) b \cdot \left( d - \frac{\beta_1 c}{2} \right) \quad (A.9)$$

$$224kN \cdot m = \phi_c (\alpha_1 \cdot 38.6MPa) (\beta_1 c) (275mm) \cdot \left( 390mm - \frac{\beta_1 c}{2} \right) \quad (A.10)$$

$$224kN \cdot m = 4,139,850 \alpha_1 (\beta_1 c) - 5,307 \alpha_1 (\beta_1 c)^2 \quad (A.11)$$

$$\Rightarrow \alpha_1 = \frac{224kN \cdot m}{4,139,850 (\beta_1 c) - 5,307 (\beta_1 c)^2} \quad (A.12)$$

Using Equations A.8 and A.12 we can iterate to find the primary tensile steel yield strength and its modulus of elasticity. To simplify the integration associated with finding the stress-block parameters,  $\alpha_1$  and  $\beta_1$ , they were obtained through an integration table provided by Collins and Mitchell, 1991. The associated  $\alpha_1$  and  $\beta_1$  stress-block parameters were found to be 0.896 and 0.767, respectively (Collins and Mitchell, 1991). Knowing the two factors and the stress state of the concrete at 224 kN·m we can determine the steel yield stress and its modulus of elasticity as approximately 525 MPa and 178,750 MPa, respectively, assuming that the steel behaves perfectly elasto-plastically.

### A.3. Control Beam

The following assumptions were incorporated in the design calculations:

**a. Cross sectional geometric dimensions**

Height of the cross section,  $h = 450$  mm

Width of the cross,  $b = 275$  mm

**b. Tensile reinforcing steel detailing**

Depth of the tensile reinforcing steel,  $d = 390$  mm

Area of the tensile reinforcing steel,  $A_s = 1200$  mm<sup>2</sup> (4 x No. 20 bars)

Depth of the compression reinforcing steel,  $d' = 55$  mm

Area of the compression reinforcing steel,  $A'_s = 200$  mm<sup>2</sup> (2 x No. 10 bars)

**c. Shear reinforcing steel detailing**

Total area of transverse steel per stirrup,  $A_v = 400$  mm<sup>2</sup> (No. 15 closed loop internal steel stirrup)

**d. Material properties based on ancillary tests (refer to chapter 3 for details)**

Concrete strength,  $f'_c = 38.6$  MPa (at time of testing)

Steel yield strength,  $f_y = 525$  MPa (tensile reinforcement)

Steel yield strength,  $f_y = 569$  MPa (shear reinforcement)

Concrete material reduction factor, set to  $\phi_c = 1.0$  (as discussed earlier)

Steel material reduction factor, set to  $\phi_s = 1.0$  (as discussed earlier)

Concrete ultimate strain,  $\epsilon_{cu} = 0.0035$  (in accordance to the CSA A23.3-04)

Steel modulus of elasticity,  $E_s = 178,750$  MPa (tensile reinforcement)

Steel modulus of elasticity,  $E_s = 187,255$  MPa (shear reinforcement)

Figure A.2, illustrates the idealized concrete rectangular stress block specified by CSA A23.3-04. The concrete stress-strain relationship is converted into an equivalent stress block, also known as the Whitney Stress Block, that is characterized by an intensity  $\alpha_1 f'_c$  acting uniformly over a depth  $\beta_1 c$  when the maximum concrete strain,  $\epsilon_{cu}$ , is equal to 0.0035. This equivalent stress block method is the basis for the following calculations to determine the moment capacity of the assumed cross section.

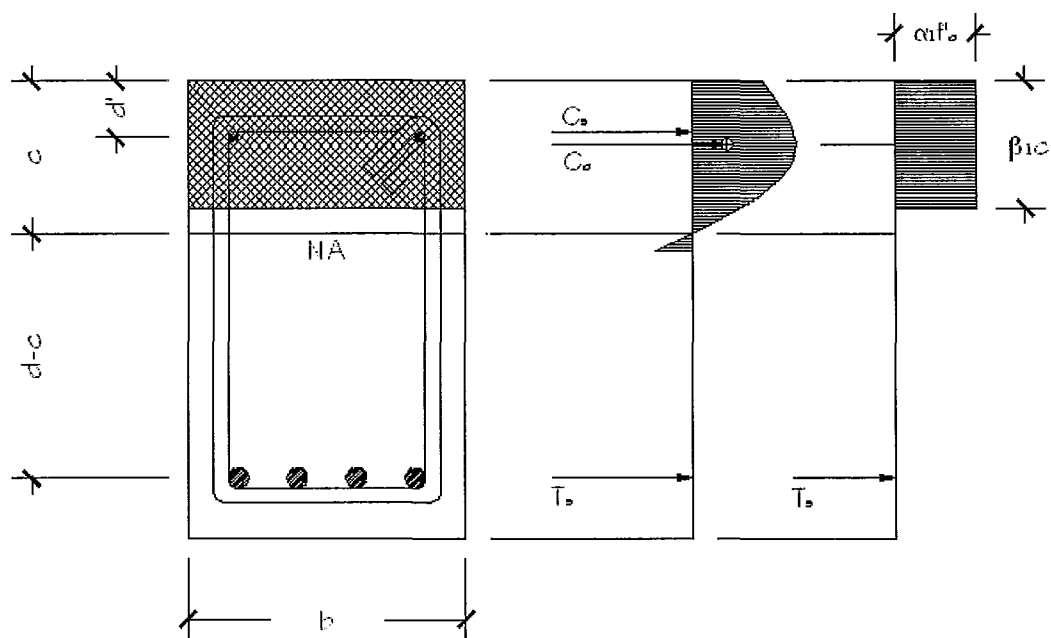


**Figure A.2: Equivalent Stress Block Method Design of Control Beam**

$$\sum_i F_x = 0 \tag{A.13}$$

$$C_c + C_s = T_s \tag{A.14}$$

where  $C_c$ ,  $C_s$  and  $T_s$  are the concrete, compression steel and tensile steel forces, respectively. The resultants are defined by the following:

$$C_c = \phi_c (\alpha_1 f'_c) (\beta_1 c) b \tag{A.15}$$

The equivalent stress block parameters,  $\alpha_1$  and  $\beta_1$ , are defined by the following according to the CSA A23.3-04:

$$\alpha_1 = 0.85 - 0.0015 f'_c \geq 0.67 \tag{A.16}$$

$$\beta_1 = 0.97 - 0.0025 f'_c \geq 0.67 \tag{A.17}$$

Therefore the parameters  $\alpha_1$  and  $\beta_1$  yield values of 0.79 and 0.87, respectively, and both values exceed the minimum value of 0.67. Both the steel reinforcement types, compressive and tensile, have resultants defined by the following:

$$C_s = \phi_s f'_s A'_s \tag{A.18}$$

$$T_s = \phi_s f_s A_s \quad (A.19)$$

where  $f'_s$  and  $f_s$  represent the stress in the compressive and the tensile steel, respectively, which are assumed to behave elasto-plastically. For the initial iteration, the compressive steel will not reach the yield strain and the tensile steel will be assumed to have past the yield strain as the concrete reaches its maximum failure strain. The following figure, Figure A.3, illustrates the strain distribution of the design cross section. In order to use strain compatibility along the height of the cross section, the fundamental concept that plane sections remain plane must hold true and is the basis for flexural analysis.

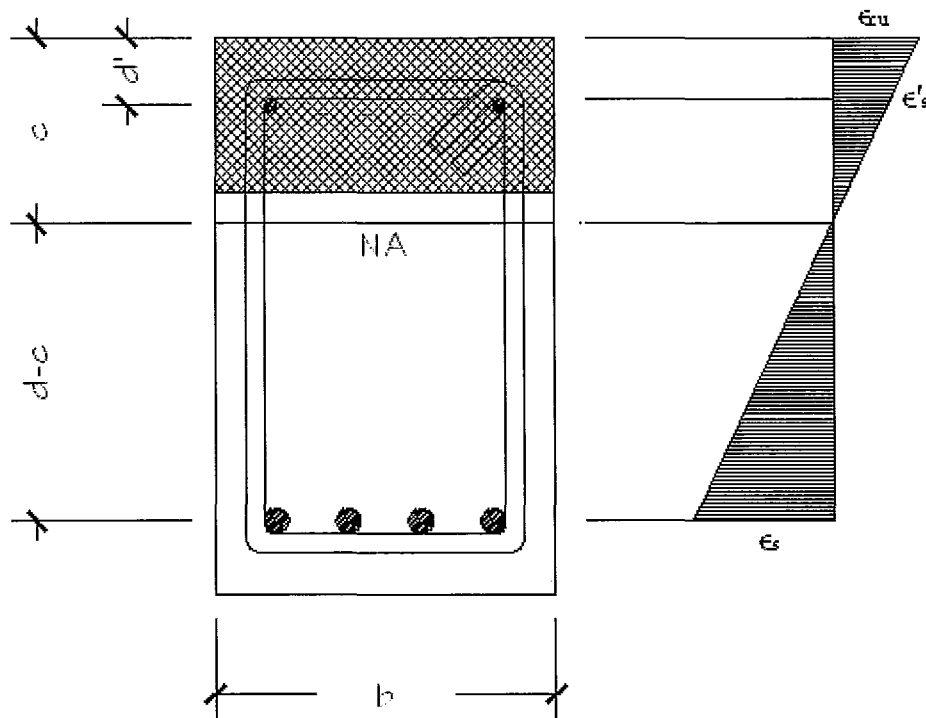


**Figure A.3: Strain Compatibility for Design of Control Beam**

The use of strain compatibility permits the calculation of strains across the entire cross section when two points are given. In the following ultimate analysis the maximum concrete strain given by the CSA A23.3-04 is given as 0.0035 at the extreme compression fibre which accounts for one point and the remaining second point is defined by the location of the neutral axis, or where the strain is equal to zero. This point is calculated

by utilizing equilibrium, which is stated in Equation A.14. To find the location of the neutral axis, Equations A.15 through A.19 are substituted into A.14.

$$\phi_c(\alpha_1 f'_c)(\beta_1 c)b + \phi_s f_s A'_s = \phi_s f_y A_s \quad (\text{A.20})$$

where the resultant concrete and steel forces are given by

$$C_c = 1.0 \cdot (0.79 \times 38.6 \text{ MPa})(0.87 \times c) \cdot 275 \text{ mm} = 7296c$$

$$C_s = 1.0 \cdot (E_s \varepsilon'_s) \cdot 200 \text{ mm}^2 = 35750000 \varepsilon'_s$$

$$T_s = 1.0 \cdot 525 \text{ MPa} \cdot 1200 \text{ mm}^2 = 630000$$

Inserting these forces into the equation of equilibrium gives

$$7296c + 35750000 \varepsilon'_s = 630000 \quad (\text{A.21})$$

Using strain compatibility to relate the strain in the compression steel to the depth of the neutral axis, we obtain the following

$$\frac{\varepsilon_{cu}}{c} = \frac{\varepsilon'_s}{c - d'} \quad (\text{A.22})$$

$$\Rightarrow \varepsilon'_s = \frac{c - 55}{c} \times 0.0035$$

Substituting Equation A.22 into A.21 yields the following quadratic equation

$$7296c + 35750000 \left( \frac{c - 55}{c} \times 0.0035 \right) = 630000 \quad (\text{A.23})$$

$$\Rightarrow 7296c + 125125 - \frac{6881875}{c} = 630000$$

Multiplying both sides of the equation by 'c' and gathering like terms,

$$\Rightarrow 7296c^2 - 504875c - 7264642 = 0 \quad (\text{A.24})$$

Solving the quadratic yields the following roots:  $c = 81.4 \text{ mm}$  and  $c = -12.2 \text{ mm}$ . Since the depth of the neutral axis must be greater than zero to have any physical meaning, the depth of the neutral axis,  $c$ , is taken as  $81.4 \text{ mm}$ . The assumptions regarding the compression steel not yielding and the tensile steel yielding must be verified using the calculated depth of the neutral axis and the strain compatibility. The concrete, tensile steel and compressive steel strains are now as follows:

$$\frac{\varepsilon_{cu}}{c} = \frac{\varepsilon'_s}{c - d'} = \frac{\varepsilon_s}{d - c} \quad (A.25)$$

$$\Rightarrow \varepsilon'_s = \left( \frac{c - d'}{c} \right) \varepsilon_{cu} = \left( \frac{81.4 - 55}{81.4} \right) \bullet 0.0035 = 0.0011 \leq \varepsilon_y \quad \text{OK!}$$

$$\Rightarrow \varepsilon_s = \left( \frac{d - c}{c} \right) \varepsilon_{cu} = \left( \frac{390 - 81.4}{81.4} \right) \bullet 0.0035 = 0.013 \geq \varepsilon_y \quad \text{OK!}$$

Therefore, the compression steel does not yield and the tensile steel yields as initially assumed. The moment capacity of the cross section can be calculated based on the depth of the neutral axis and the associated strains in the concrete, tensile steel and the compressive steel. Taking moments about the concrete resultant force leads to

$$M_u = C_s \left( d' - \frac{\beta_1 c}{2} \right) + T_s \left( d - \frac{\beta_1 c}{2} \right) \quad (A.26)$$

where,

$$C_s = 1.0 \bullet (E_s \varepsilon'_s) \bullet 200 \text{mm}^2 = 39.3 \text{kN}$$

$$T_s = 1.0 \bullet 525 \text{MPa} \bullet 1200 \text{mm}^2 = 630.0 \text{kN}$$

$$M_u = 39.3 \text{kN} \left( 55 \text{mm} - \frac{0.87 \bullet 81.4 \text{mm}}{2} \right) + 630.0 \text{kN} \left( 390 \text{mm} - \frac{0.87 \bullet 81.4 \text{mm}}{2} \right) \quad (A.27)$$

$$\Rightarrow M_u = 0.8 \text{kN} \bullet m + 223.3 \text{kN} \bullet m$$

$$\Rightarrow M_u = 224.1 \text{kN} \bullet m$$

Therefore, the moment capacity of the cross section is approximately 224 kN·m for the control beam. Given the moment capacity of the cross section we can determine the needed shear resistance assuming four-point bending, a span of 2500 mm and a constant moment region of 1000 mm. Using the elastic shear force and bending moment diagrams shown in the following figure, the shear corresponding to the flexural failure load can be determined.

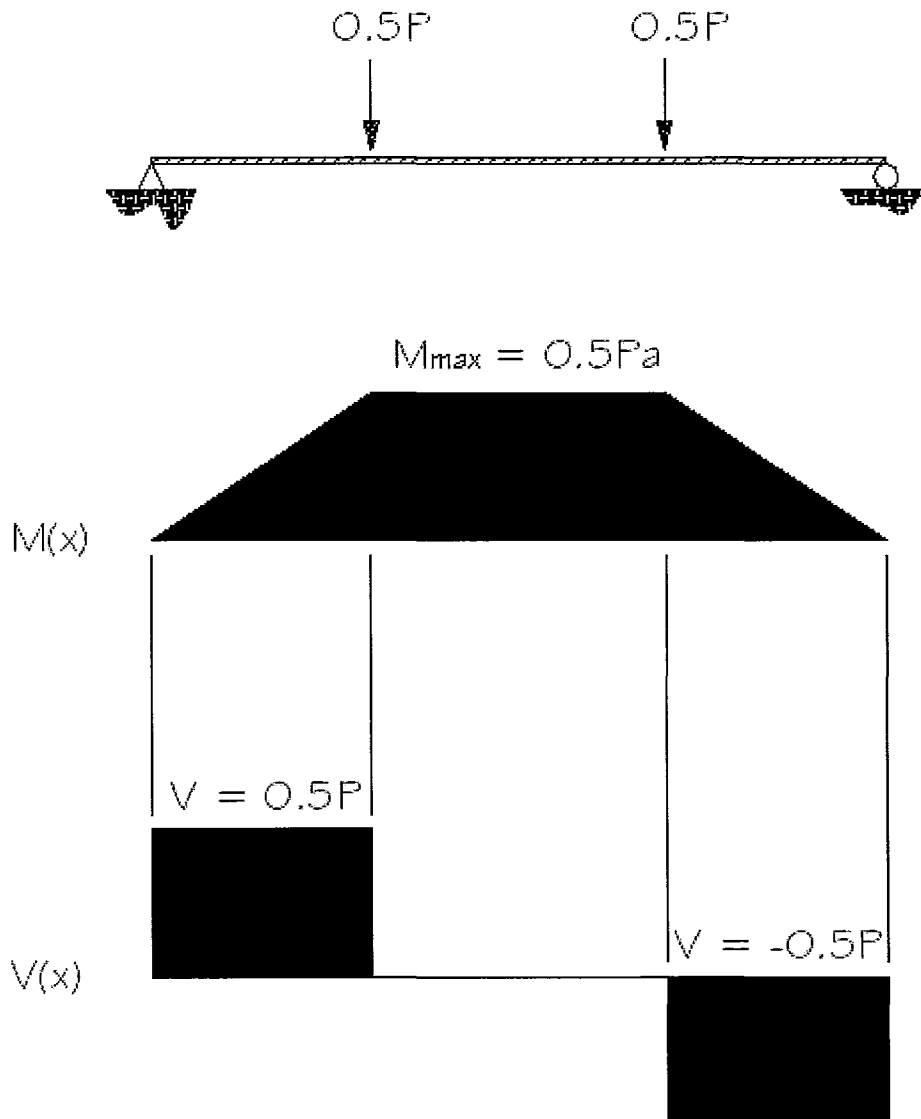


**Figure A.4: Elastic bending moment and shear diagrams for a simply-supported beam**

$$M_{\max} = \frac{1}{2} Pa \quad (\text{A.28})$$

where the length of the shear span on either side of the beam centre line is 750 mm.

Solving for  $P$ ,

$$\Rightarrow P = \frac{2 \times 224 \text{ kN} \cdot \text{m}}{0.750 \text{ m}} = 597 \text{ kN}$$

Substituting the calculated P of 549 kN into the following expression for shear as shown from Figure A.4,

$$V = \frac{1}{2}P \quad (\text{A.29})$$

$$\Rightarrow V = \frac{1}{2}(549\text{kN}) = 299\text{kN}$$

Therefore, we could expect an applied shear force of approximately 299 kN based on linear elastic analysis. Since all the beams, including the control beam, are to be designed to fail in flexure the simplified method according to the CSA A23.3-04 will be used to calculate a minimum spacing of the transverse reinforcement. The required spacing to satisfy the minimum area of shear reinforcement is calculated as follows:

$$A_v = 0.06\sqrt{f'_c} \frac{b_w s}{f_y} \quad (\text{A.30})$$

$$\Rightarrow s = A_v \left( \frac{f_y}{0.06\sqrt{f'_c} b_w} \right)$$

Assuming No. 15 closed U-stirrup ( $A_v = 2 \text{ legs} \times 200 \text{ mm}^2/\text{leg} = 400 \text{ mm}^2$ ),

$$\Rightarrow s = 400\text{mm}^2 \left( \frac{569\text{MPa}}{0.06\sqrt{38.6\text{MPa}} \cdot 275\text{mm}} \right)$$

$$s \leq 2220\text{mm}$$

To calculate the maximum allowable spacing permitted by the simplified method,

$$600 \text{ mm or } 0.7d \text{ if } \frac{V_f - \phi_p V_p}{b_w d} < 0.1\lambda\phi_c f'_c \text{ or} \quad (\text{A.31})$$

$$300 \text{ mm or } 0.35d \text{ if } \frac{V_f - \phi_p V_p}{b_w d} \geq 0.1\lambda\phi_c f'_c \quad (\text{A.32})$$

For  $0.1\lambda\phi_c f'_c = 2.3\text{MPa}$  and  $\frac{V_f - \phi_p V_p}{b_w d} = 2.8\text{MPa}$  the maximum allowable spacing is

the lesser of 300 mm or 0.35d yielding a value of 136.5 mm based on a tensile reinforcement depth of 390 mm. For the calculation of the  $0.1\lambda\phi_c f'_c$  term the material reduction factor for concrete was not set to unity to yield a conservative value ensuring

that the beam will fail in flexure and not shear. The maximum allowable spacing based on the estimated stirrup contributions are as follows:

$$V_r = V_c + V_s \quad (A.33)$$

where the applied shear,  $V_f$ , can be set equal to the resisting shear,  $V_r$ , of the beam,

$$V_r = V_f = 299kN \text{ but } V_r \leq V_c + 0.8\lambda\phi_c\sqrt{f'_c}b_wd \quad (A.34)$$

$$\Rightarrow 0.8\lambda\phi_c\sqrt{f'_c}b_wd = 320kN$$

$$\Rightarrow V_c = 0.2\lambda\phi_c\sqrt{f'_c}b_wd = 80kN$$

$$\Rightarrow V_r \leq 80kN + 320kN = 400kN \quad \text{OK!}$$

Again the material reduction factor for concrete was not set to unity to add safety to the shear design. From Equation A-21 we find that the steel contribution is,

$$V_s = V_r - V_c$$

$$V_s = 299kN - 80kN = 219kN$$

Therefore, calculating the spacing based on the shear resistance of the transverse steel

$$V_s = \frac{\phi_s A_v f_y d}{s} \quad (A.35)$$

$$\Rightarrow s = \frac{\phi_s A_v f_y d}{V_s}$$

$$\Rightarrow s = \frac{1.0 \cdot 400mm^2 \cdot 569MPa \cdot 390mm}{219kN} = 405mm$$

Therefore, the simplified method of CSA A23.3-04 gives three maximum allowable spacing configurations as calculated above. The governing spacing is approximately 137 mm, therefore the beam will be constructed using a 125 mm standard spacing. This spacing is highly conservative, however as discussed earlier the beams were designed to fail in flexure and the high factor of safety ensures adequate shear resistance.

#### A.4. CFRP Strengthened Beams

The following assumptions were incorporated in the design calculations:

##### a. Cross sectional geometric dimensions

---

Height of the cross section,  $h = 450$  mm

Width of the cross,  $b = 275$  mm

**b. Tensile reinforcing steel detailing**

Depth of the tensile reinforcing steel,  $d = 390$  mm

Area of the tensile reinforcing steel,  $A_s = 600$  mm<sup>2</sup> (2 x No. 20 bars)

Depth of the compression reinforcing steel,  $d' = 55$  mm

Area of the compression reinforcing steel,  $A'_s = 200$  mm<sup>2</sup> (2 x No. 10 bars)

**c. NSM CFRP detailing**

Depth of the NSM CFRP,  $d_f = 440$  mm

Area of the NSM CFRP,  $A_f = 300$  mm<sup>2</sup> (2 x C19 bars)

**d. Shear reinforcing steel detailing**

Area of transverse steel at shear span cross section,  $A_v = 400$  mm<sup>2</sup> (No. 15 closed loop internal steel stirrup)

**e. Material properties based on ancillary tests (refer to chapter 3 for details)**

Concrete strength,  $f'_c = 38.6$  MPa (type 1), 40.7 MPa (type 2) and 41.9 (type 3)

Steel yield strength,  $f_y = 525$  MPa (tensile reinforcement)

Steel yield strength,  $f_y = 569$  MPa (shear reinforcement)

CFRP rupture strain,  $f_u = 1200$  MPa

Concrete material reduction factor, set to  $\phi_c = 1.0$  (as discussed earlier)

Steel material reduction factor, set to  $\phi_s = 1.0$  (as discussed earlier)

CFRP material reduction factor, set to  $\phi_f = 1.0$  (as discussed earlier)

Concrete ultimate strain,  $\epsilon_{cu} = 0.0035$  (in accordance to the CSA A23.3-04)

Steel modulus of elasticity,  $E_s = 178,750$  MPa (tensile reinforcement)

Steel modulus of elasticity,  $E_s = 187,255$  MPa (shear reinforcement)

CFRP modulus of elasticity,  $E_f = 100,000$  MPa

The following figure, Figure A.5, illustrates the idealized concrete stress block of CSA A23.3-04. This equivalent stress block method, similar to that used for the control

beam analysis, is the basis for the following calculations to determine the moment capacity of the assumed cross section.

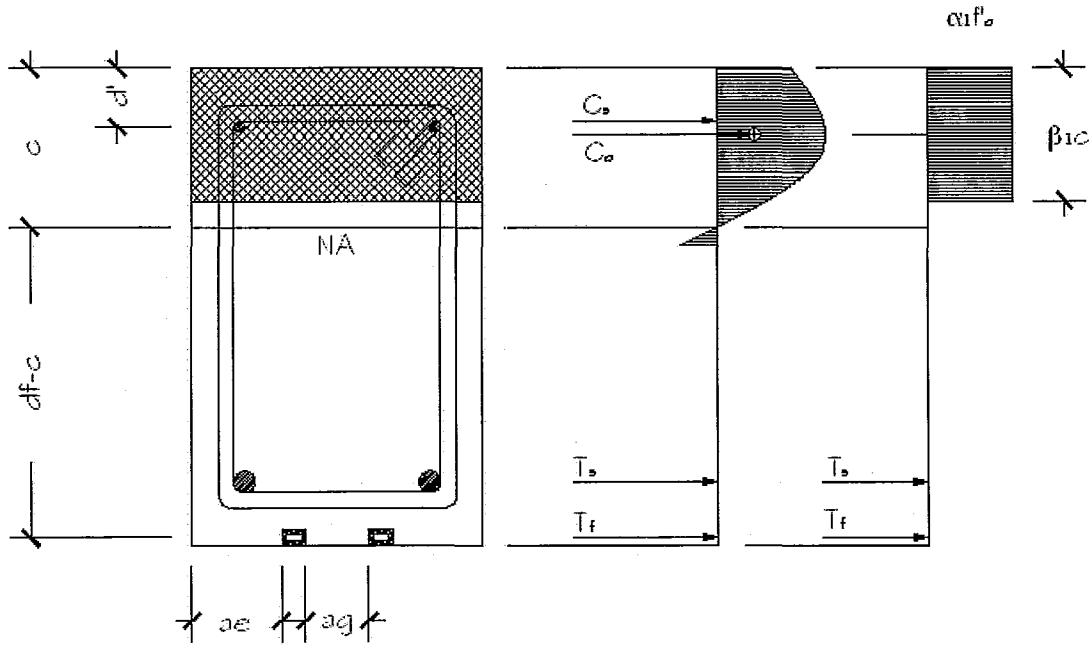


**Figure A.5: Equivalent Stress Block Method Design of Strengthened Beams**

$$\sum_i F_x = 0 \tag{A.36}$$

$$C_c + C_s = T_s \tag{A.37}$$

where  $C_c$ ,  $C_s$ ,  $T_s$  and  $T_f$  are the resolved concrete, compression steel, tensile steel and CFRP resultants, respectively. The resultants are defined by the following:

$$C_c = \phi_c (\alpha_1 f'_c) (\beta_1 c) b \tag{A.38}$$

As an initial assumption the concrete ultimate strain will not be reached, therefore the given values for  $\alpha_1$  and  $\beta_1$  will be obtained from a tables provided in Collins and Mitchell 1991. We will assume that the concrete strain at the top fibre will reach a strain of  $1.25\epsilon_c'$  which yields  $\alpha_1$  and  $\beta_1$  values of 0.896 and 0.767, respectively, where  $\epsilon_c'$  is the strain of the concrete at peak stress. For this example  $\epsilon_c'$  is taken as 0.002 and the stress block parameters,  $\alpha_1$  and  $\beta_1$ , will be assumed identical for the concrete strength of each

strengthened beam regardless of the small strength variation. The reinforcement forces are defined as follows:

$$C_s = \phi_s f'_s A'_s \tag{A.39}$$

$$T_s = \phi_s f_s A_s \tag{A.40}$$

$$T_f = \phi_f f_f A_f \tag{A.41}$$

where  $f'_s$ ,  $f_s$  and  $f_f$  represent the stress in the compressive steel, tensile steel and CFRP reinforcement, respectively. The steel reinforcing bars are assumed to behave elasto-plastically while the CFRP reinforcement is assumed to behave linear-elastically until rupture. For the initial iteration, the compressive steel will not reach its the yield strain, the tensile steel will be assumed to have past the yield strain and the CFRP bars will be assumed to have ruptured as the concrete reaches its maximum failure strain. The following figure, Figure A.6, illustrates the strain distribution of the cross section.

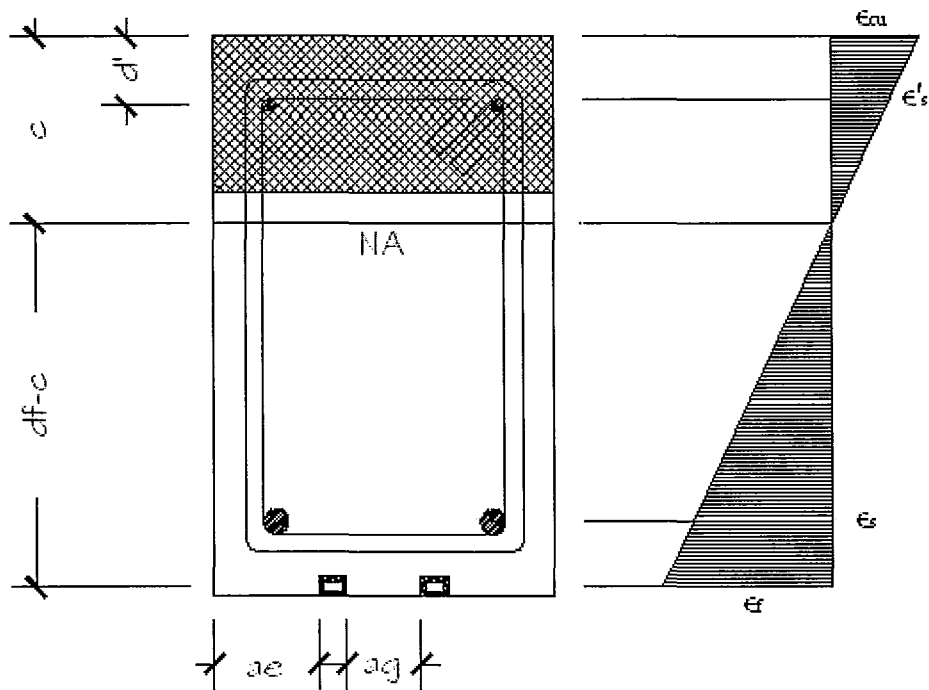


Figure A.6: Strain Compatibility for Design of Strengthened Beams

The use of strain compatibility permits the calculation of strains across the entire cross section when two points are given. In the following analysis the maximum concrete at the extreme compression fibre was assumed to reach  $0.0025$  ( $1.25\varepsilon_c$ ), which accounts for one point and the remaining second point is defined by the location of the neutral axis, or where the strain is equal to zero. This point is calculated with the use of cross sectional equilibrium, which is stated in Equation A.37. To find the location of the neutral axis, the following Equations A.38 through A.41 are substituted into A.37.

$$\phi_c(\alpha_1 f'_c)(\beta_1 c)b + \phi_s f_s A'_s = \phi_s f_y A_s + \phi_f f_u A_f \quad (\text{A.42})$$

where the resultant components are defined by,

$$C_c(f'_c = 38.6 \text{ MPa}) = 1.0 \cdot (0.896 \times 38.6 \text{ MPa})(0.767 \times c) \cdot 275 \text{ mm} = 7295c$$

$$C_c(f'_c = 40.7 \text{ MPa}) = 1.0 \cdot (0.896 \times 40.7 \text{ MPa})(0.767 \times c) \cdot 275 \text{ mm} = 7692c$$

$$C_c(f'_c = 41.9 \text{ MPa}) = 1.0 \cdot (0.896 \times 41.9 \text{ MPa})(0.767 \times c) \cdot 275 \text{ mm} = 7919c$$

$$C_s = 1.0 \cdot (E_s \varepsilon'_s) \cdot 200 \text{ mm}^2 = 35750000 \varepsilon'_s$$

$$T_s = 1.0 \cdot 525 \text{ MPa} \cdot 600 \text{ mm}^2 = 315000$$

$$T_f = 1.0 \cdot 1200 \text{ MPa} \cdot 300 \text{ mm}^2 = 360000$$

Substituting the values obtained by the resultant calculations for  $f'_c = 38.6$  MPa,

$$7295c + 35750000 \varepsilon'_s = 315000 + 360000 \quad (\text{A.43})$$

Substituting the values obtained by the resultant calculations for  $f'_c = 40.7$  MPa,

$$7692c + 35750000 \varepsilon'_s = 315000 + 360000 \quad (\text{A.44})$$

Substituting the values obtained by the resultant calculations for  $f'_c = 41.9$  MPa,

$$7919c + 35750000 \varepsilon'_s = 315000 + 360000 \quad (\text{A.45})$$

Using strain compatibility to relate the strain in the compression steel to the depth of the neutral axis. With reference to Figure A.6, we can write the following relationship,

$$\frac{\varepsilon_c}{c} = \frac{\varepsilon'_s}{c - d'} \quad (\text{A.46})$$

$$\Rightarrow \varepsilon'_s = \frac{c - 55}{c} \times 0.0025$$

Substituting Equation A.46 into the expressions described in A.43 through A.45 yields the following quadratics for the respective concrete strengths of 38.6, 40.7 and 41.9 MPa,

$$7295c + 35750000 \left( \frac{c-55}{c} \times 0.0025 \right) = 315000 + 360000 \quad (\text{A.47})$$

$$\Rightarrow 7295c + 89375 - \frac{4915625}{c} = 315000 + 360000$$

$$7692c + 35750000 \left( \frac{c-55}{c} \times 0.0025 \right) = 315000 + 360000 \quad (\text{A.48})$$

$$\Rightarrow 7692c + 89375 - \frac{4915625}{c} = 315000 + 360000$$

$$7919c + 35750000 \left( \frac{c-55}{c} \times 0.0025 \right) = 315000 + 360000 \quad (\text{A.49})$$

$$\Rightarrow 7919c + 89375 - \frac{4915625}{c} = 315000 + 360000$$

Multiplying both sides of the equation by 'c' and gathering like terms,

$$7295c^2 - 585625c - 4915625 = 0 \quad (\text{A.50})$$

$$7692c^2 - 585625c - 4915625 = 0 \quad (\text{A.51})$$

$$7919c^2 - 585625c - 4915625 = 0 \quad (\text{A.52})$$

Solving the quadratics yield the following roots:  $c = 87.9$  mm and  $c = -7.7$  mm for a concrete strength of 38.6 MPa;  $c = 83.8$  mm and  $c = -7.6$  mm for a concrete strength of 40.7 MPa;  $c = 81.6$  mm and  $c = -7.6$  mm for a concrete strength of 41.9 MPa. Since the depth of the neutral axis must be greater than zero to have any physical meaning, the depth of the neutral axis,  $c$ , is taken as 84.6 mm, 80.6 mm and 78.5 mm, for the respective concrete strengths. The assumptions regarding the compression steel not yielding, the tensile steel yielding, the CFRP bars rupturing and the top concrete fibre reaching a strain of approximately 0.0025 must all be verified using the obtained depth of the neutral axis and the strain compatibility in reference to Figure A.6. The concrete, tensile steel, compressive steel and FRP bars strain are calculated using

$$\frac{\varepsilon_c}{c} = \frac{\varepsilon'_s}{c-d'} = \frac{\varepsilon_s}{d-c} = \frac{\varepsilon_{fu}}{d_f-c} \quad (\text{A.53})$$

For a concrete strength of 38.6 MPa and setting the strain of the FRP to its ultimate,

$$\varepsilon'_s = \left( \frac{c - d'}{d_f - c} \right) \varepsilon_{fu} = \left( \frac{87.9 - 55}{440 - 87.9} \right) \bullet 0.012 = 0.001 \leq \varepsilon_y \quad \text{OK!}$$

$$\varepsilon_s = \left( \frac{d - c}{d_f - c} \right) \varepsilon_{fu} = \left( \frac{390 - 87.9}{440 - 87.9} \right) \bullet 0.012 = 0.010 \geq \varepsilon_y \quad \text{OK!}$$

$$\varepsilon_c = \left( \frac{c}{d_f - c} \right) \varepsilon_{fu} = \left( \frac{87.9}{440 - 87.9} \right) \bullet 0.012 = 0.028 \approx 0.0025 \quad \text{OK!}$$

For a concrete strength of 40.7 MPa,

$$\varepsilon'_s = \left( \frac{c - d'}{d_f - c} \right) \varepsilon_{fu} = \left( \frac{83.8 - 55}{440 - 83.8} \right) \bullet 0.012 = 0.0008 \leq \varepsilon_y \quad \text{OK!}$$

$$\varepsilon_s = \left( \frac{d - c}{d_f - c} \right) \varepsilon_{fu} = \left( \frac{390 - 83.8}{440 - 83.8} \right) \bullet 0.012 = 0.010 \geq \varepsilon_y \quad \text{OK!}$$

$$\varepsilon_c = \left( \frac{c}{d_f - c} \right) \varepsilon_{fu} = \left( \frac{83.8}{440 - 83.8} \right) \bullet 0.012 = 0.027 \approx 0.0025 \quad \text{OK!}$$

For a concrete strength of 41.9 MPa,

$$\varepsilon'_s = \left( \frac{c - d'}{d_f - c} \right) \varepsilon_{fu} = \left( \frac{81.6 - 55}{440 - 81.6} \right) \bullet 0.012 = 0.0008 \leq \varepsilon_y \quad \text{OK!}$$

$$\varepsilon_s = \left( \frac{d - c}{d_f - c} \right) \varepsilon_{fu} = \left( \frac{390 - 81.6}{440 - 81.6} \right) \bullet 0.012 = 0.010 \geq \varepsilon_y \quad \text{OK!}$$

$$\varepsilon_c = \left( \frac{c}{d_f - c} \right) \varepsilon_{fu} = \left( \frac{81.6}{440 - 81.6} \right) \bullet 0.012 = 0.026 \approx 0.0025 \quad \text{OK!}$$

Therefore all the assumptions were checked and assumed correctly for all three concrete strengths. The moment capacity of the strengthened cross sections can be calculated based on the depth of the neutral axis and the associated strains in the concrete, tensile

steel, compressive steel and FRP reinforcing bars. Taking moments around the concrete resultant yields the following equation knowing that the concrete resultant will act at a distance  $\frac{1}{2} \beta_1 c$  from the extreme compressive fibre,

$$M_u = C_s \left( d' - \frac{\beta_1 c}{2} \right) + T_s \left( d - \frac{\beta_1 c}{2} \right) + T_f \left( d_f - \frac{\beta_1 c}{2} \right) \quad (\text{A.54})$$

Where for a concrete strength of 38.6 MPa,

$$C_s = 1.0 \cdot (E_s \varepsilon'_s) \cdot 200 \text{mm}^2 = 35.8 \text{kN}$$

$$T_s = 1.0 \cdot 525 \text{MPa} \cdot 600 \text{mm}^2 = 315.0 \text{kN}$$

$$T_f = 1.0 \cdot 1200 \text{MPa} \cdot 300 \text{mm}^2 = 360.0 \text{kN}$$

$$M_u = 35.8 \text{kN} \left( 55 \text{mm} - \frac{0.767 \cdot 87.9 \text{mm}}{2} \right) + 315.0 \text{kN} \left( 390 \text{mm} - \frac{0.767 \cdot 87.9 \text{mm}}{2} \right) + 360.0 \text{kN} \left( 440 \text{mm} - \frac{0.767 \cdot 87.9 \text{mm}}{2} \right) \quad (\text{A.55})$$

$$\Rightarrow M_u = 0.8 \text{kN} \cdot m + 112.2 \text{kN} \cdot m + 146.3 \text{kN} \cdot m$$

$$\Rightarrow M_u = 259.3 \text{kN} \cdot m$$

Where for a concrete strength of 40.7 MPa,

$$C_s = 1.0 \cdot (E_s \varepsilon'_s) \cdot 200 \text{mm}^2 = 28.6 \text{kN}$$

$$T_s = 1.0 \cdot 525 \text{MPa} \cdot 600 \text{mm}^2 = 315.0 \text{kN}$$

$$T_f = 1.0 \cdot 1200 \text{MPa} \cdot 300 \text{mm}^2 = 360.0 \text{kN}$$

$$M_u = 28.6 \text{kN} \left( 55 \text{mm} - \frac{0.767 \cdot 83.8 \text{mm}}{2} \right) + 315.0 \text{kN} \left( 390 \text{mm} - \frac{0.767 \cdot 83.8 \text{mm}}{2} \right) + 360.0 \text{kN} \left( 440 \text{mm} - \frac{0.767 \cdot 83.8 \text{mm}}{2} \right) \quad (\text{A.56})$$

$$\Rightarrow M_u = 0.7 \text{kN} \cdot m + 112.7 \text{kN} \cdot m + 146.8 \text{kN} \cdot m$$

$$\Rightarrow M_u = 260.2 \text{kN} \cdot m$$

Where for a concrete strength of 41.9 MPa,

$$C_s = 1.0 \cdot (E_s \varepsilon'_s) \cdot 200 \text{mm}^2 = 28.6 \text{kN}$$

$$T_s = 1.0 \cdot 525 \text{ MPa} \cdot 600 \text{ mm}^2 = 315.0 \text{ kN}$$

$$T_f = 1.0 \cdot 1200 \text{ MPa} \cdot 300 \text{ mm}^2 = 360.0 \text{ kN}$$

$$M_u = 28.6 \text{ kN} \left( 55 \text{ mm} - \frac{0.767 \cdot 81.6 \text{ mm}}{2} \right) + 315.0 \text{ kN} \left( 390 \text{ mm} - \frac{0.767 \cdot 81.6 \text{ mm}}{2} \right) + 360.0 \text{ kN} \left( 440 \text{ mm} - \frac{0.767 \cdot 81.6 \text{ mm}}{2} \right) \quad (\text{A.57})$$

$$\Rightarrow M_u = 0.7 \text{ kN} \cdot m + 113.0 \text{ kN} \cdot m + 147.1 \text{ kN} \cdot m$$

$$\Rightarrow M_u = 260.8 \text{ kN} \cdot m$$

Therefore, the moment capacities of the cross sections are approximately 259 kN·m, 260kN·m and 261kN·m for the strengthened beams corresponding to their respective concrete strengths. Given that all the strengthened beams are designed to fail in flexure and the smallest recorded concrete strength recorded in all the strengthened beams was 38.6 MPa; a stirrup spacing of 125 mm can be used as designed for the control beam.

